An Energy Diffusion Model for Interior Acoustics with Structural Coupling Using the Laplace Transform Boundary Element Solution

Joseph M. Corcoran

Dissertation submitted to the faculty of the Virginia Polytechnic Institute and State University in partial fulfillment of the requirements for the degree of

Doctor of Philosophy
In
Mechanical Engineering

Ricardo A. Burdisso
Georg Reichard
Michael J. Roan
Pablo A. Tarazaga
Robert L. West

May 7, 2013
Blacksburg, Virginia

Keywords: Acoustic diffusion, boundary element method, Laplace transform, numerical inverse Laplace transform, structural-acoustic coupling

An Energy Diffusion Model for Interior Acoustics with Structural Coupling Using the Laplace Transform Boundary Element Solution

Joseph M. Corcoran

ABSTRACT

Knowledge of the indoor propagation of sound has many important applications including acoustic prediction in homes, office buildings, stores, and schools, and the design of concert halls, auditoriums, classrooms, and factories. At low frequencies, interior acoustics are analyzed with the wave equation, but significant computational expense imposes an upper frequency limit. Thus, energy methods are often sought for high frequency analysis. However, conventional energy methods are significantly limited by vast simplifications or computational costs. Therefore, new improvements are still being sought.

The basis of this dissertation is a recently developed mathematical model for interior acoustics known as the acoustic diffusion model. The model extends statistical methods in high frequency acoustics to predict the spatial distribution of acoustic energy in the volume over time as a diffusion process. Previously, solutions to the acoustic diffusion model have been limited to one dimensional (1-D) analytical solutions and to the use of the finite element method (FEM).

This dissertation focuses on a new, efficient method for solving the acoustic diffusion model based on a boundary element method (BEM) solution using the Laplace transform. First, a Laplace domain solution to the diffusion model is obtained using the BEM. Then, a numerical inverse Laplace transform is used to efficiently compute the time domain response. The diffusion boundary element-Laplace transform solution (BE-LTS) is validated through comparisons with Sabine theory, ray tracing, and a diffusion FEM solution. All methods demonstrate excellent agreement for three increasingly complex acoustic volumes and the computational efficiency of the BE-LTS is exposed.

Structural coupling is then incorporated in the diffusion BE-LTS using two methods. First, a simple transmission coefficient separating two acoustic volumes is implemented. Second, a structural power flow model represents the coupling partition separating acoustic volumes. The validation of these methods is successfully performed in an example through comparisons with statistical theory, a diffusion FEM solution, ray tracing, and experimental data.

Finally, the diffusion model and the BE-LTS are shown to possess capabilities beyond that of room acoustics. The acoustic transmission through a heat exchanger, acoustic foam, and mufflers is successfully modeled using the diffusion BE-LTS and compared to experimental data.

Dedication

To my wife, Rachel, for her infinite love, unwavering support, and personal sacrifice. I couldn't have done it without you.

Acknowledgements

I would like to thank my advisor, Dr. Ricardo Burdisso, for his great mentorship. The opportunities and advice that he has provided have greatly shaped my life.

Thank you to my committee for their assistance and valuable suggestions which have significantly improved my research.

The Mechanical Engineering Department staff at Virginia Tech deserve special acknowledgement, especially Gail Coe and Cathy Hill. They do a first-rate job of making everyone's life easier in the department.

Thank you to my friends who break up the monotony of the work schedule and provide my mind with valuable recharge time.

Lastly, I would like to thank my family. My parents, Paul Corcoran, Karen Corcoran, and Karen Hatzenbuhler, and sisters have always freely given their love and advice. My grandparents, James and Jeanne Corcoran and Leroy Forness, helped me so much with their love and generosity as I worked towards my degrees and started my family. My new family, Bob, Elizabeth, and Michael Harris, have been nothing but loving and supportive and are always willing to help me in any way they can. Finally, a special thank you to my wife, Rachel. I could not have accomplished this without her love, her support, and the sacrifices she made to help me.

Chapter 1: Introduction

1.1   Research Overview

The indoor propagation of sound, referred to as architectural acoustics or room acoustics, is an important branch of acoustics to study and understand. Humans spend much of their time indoors, whether at home, at work, or in school, so it comes as no surprise that noise is commonly experienced inside. Room acoustics has been studied for many years; traditional mathematical models include the wave equation, geometrical acoustics, and statistical analysis. Typical interior acoustic analysis methods are summarized in the flowchart in Figure 1.1. New improvements are still being made in its study today, particularly in the mid to high frequency range.
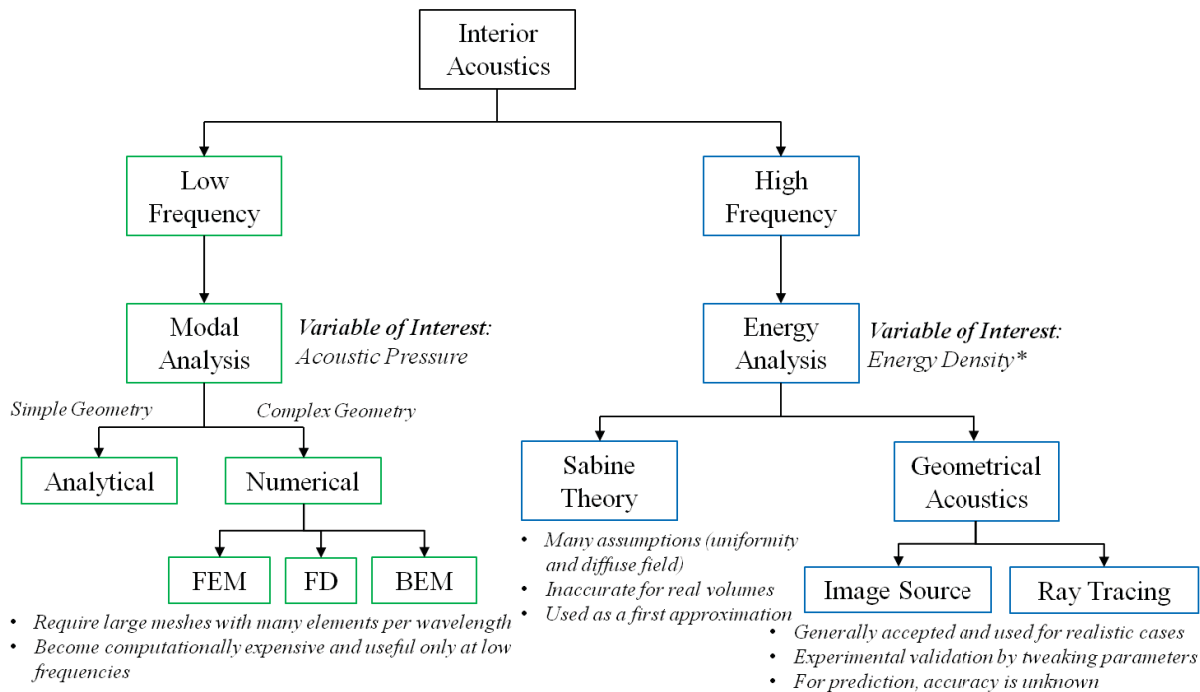
Figure 1.1: Typical methods of interior acoustic analysis.

Sound is created when small disturbances in the average air pressure propagate through the air as waves. Therefore, the most fundamental mathematical model of sound propagation is given by the three dimensional acoustic wave equation. The wave equation is a partial differential equation which can be solved analytically for only very simple room geometries (Kinsler et al., 2000). The wave equation in any room more complex than a simple geometric

volume must be solved numerically using methods like the Finite Element Method (FEM), the Boundary Element Method (BEM), or the Finite Difference (FD) technique. Whether it is performed analytically or numerically, the solution to the acoustic wave equation is very computationally intensive, thus only applicable at low frequencies.

Predicting sound indoors is also commonly carried out using techniques in geometrical acoustics, e.g. the image source method (Allen and Berkley, 1979) or ray tracing (Farina, 1995). However, the physics are simplified using these techniques by treating sound waves as rays which is not physically correct, especially at low frequencies. Though at higher frequencies, sound waves do exhibit ray-like behavior. Although accurate prediction of indoor sound is possible with these techniques, they typically require a significant number of computations, i.e. splitting the source into a very large number of rays or using an extreme number of image sources. Also, geometrical acoustics relies heavily on input acoustic properties of materials, e.g. absorption and scattering coefficients, which are inherently difficult to measure and vary depending on the frequency of the sound. Most commonly, measurements are made in conjunction with the use of geometric acoustic techniques to determine these material properties and accurately predict sound indoors.

Statistical analyses are also common methods of predicting indoor acoustics. In these analyses, only the sound energy is examined and it is assumed to be uniform throughout the room. Therefore, these techniques are only useful at high frequencies when there are no effects of individual resonant modes, if the spatial distribution of sound is unimportant, and in only certain types of rooms (Bies and Hansen, 2003). The types of rooms are restricted to relatively small rooms in which the reflective surfaces are not too distant from one another and no dimension of the room is so large that air absorption becomes important (Bies and Hansen, 2003). One room example which violates these restrictions is a long, flat room which requires alternative analysis.

More recently, statistical analyses have been extended to remove the uniform distribution restriction. In 1997, Picaut et al. proposed a new approach to room acoustics based on diffusion theory, introducing an acoustic diffusion coefficient. The idea is based on the analogue of the

scattering of acoustic energy in a room to the motion of a particle in a gas colliding with other particles as in classical diffusion theory as demonstrated in Figure 1.2.

(a) (b)
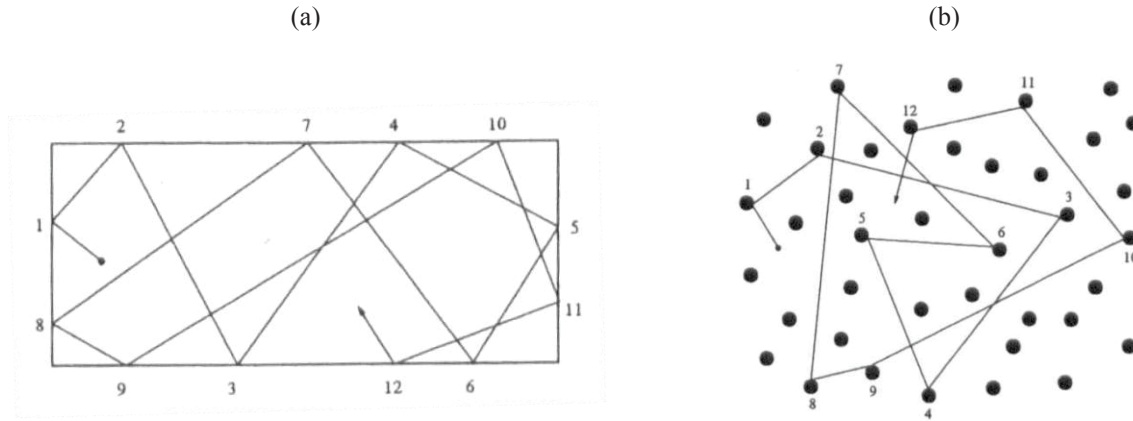
Figure 1.2: Motion of a (a) ray of acoustic energy propagating in a room and (b) gas particle colliding with other particles demonstrating the analogue of acoustic diffusion to classical particle diffusion (Picaut et al., 1997) [fair use].

The original diffusion equation for room acoustics is then obtained given by

$$\frac{\partial \psi(\mathbf{r},t)}{\partial t} = D\nabla^2 \psi(\mathbf{r},t) - \sigma \psi(\mathbf{r},t) \qquad 1.1$$

where $\psi(\mathbf{r},t)$ is the energy density at position $\mathbf{r}$ and time t. The diffusion coefficient is $D = \frac{\lambda c}{3}$ with the mean free path, λ, the average distance the particle travels between two wall collisions or a sound wave travels between two wall reflections, given by $\lambda = \frac{4V_r}{S_r}$ for a room of volume, V_r, and surface area, S_r. The attenuation coefficient is $\sigma = \frac{c\bar{\alpha}S}{4V} = \frac{c\bar{\alpha}}{\lambda}$ with c being the speed of sound in air and $\bar{\alpha}$ being the uniform room absorption coefficient. Throughout this dissertation, a bold variable denotes a vector quantity. Assuming a uniform sound energy density in the room, the acoustic diffusion equation reduces to the equation used for statistical acoustic analysis. The diffusion model and variations will be discussed in detail later in this dissertation.

The research discussed above has shown that the acoustic diffusion model is a promising tool that will provide accurate and more efficient solutions than its more commonly used counterparts

for room acoustics. However, there are several areas where diffusion model research is still needed. First, not many methods have been used to solve the acoustic diffusion equation and its variants for complex geometries. In the research mentioned, solutions to the equation have been limited to one-dimensional (1-D) analytical solutions or to the use of the FEM and FD techniques for three-dimensional (3-D) solutions. Second, other than fairly limited pieces of work, no research has been focused on coupling the transmission of sound through structural components to the indoor propagation of sound. Third, the diffusion model has only been applied to room acoustics, but diffuse fields exist in other areas of practical engineering importance. Thus, the diffusion model does have potential applications outside of room acoustics which have not been demonstrated. This dissertation addresses these current shortcomings in this research field.

1.2   Research Objectives and Original Contributions

The proposed research focuses on three of these new aspects: solving the acoustic diffusion equation, specifically using the BEM in conjunction with the Laplace transform, coupling the structural transmission of sound to the acoustic diffusion equation for room acoustics, and to demonstrate this new tool in problems of practical engineering importance. The objectives of the research are as follows:

- Develop a new efficient, accurate numerical solution to the acoustic diffusion model for interior acoustics using the BEM and techniques for the numerical computation of the inverse Laplace transform. This new solution method is referred to as the diffusion Boundary Element-Laplace Transform Solution (BE-LTS). Previously, the acoustic diffusion model has only been solved using 1-D analytical techniques, the FEM, and the FD technique. Also, the new method must be validated and the computational efficiency advantage investigated and demonstrated.

- Link indoor sound radiation to sound transmission through structural components for the prediction of the sound field in multiple acoustic volumes coupled by common structural components. Two methods are investigated using the new diffusion BE-LTS. First, simple coupling through a structural transmission coefficient (which has been examined using a FEM solution to the diffusion model) is implemented. Second, a more complex

4

coupling using a structural power flow model is implemented. This has never been considered in conjunction with the diffusion model.

- Demonstrate the robustness of the acoustic diffusion model to make accurate predictions in interior volumes other than rooms. As discussed previously, diffuse acoustic fields exist in other areas of practical engineering importance. The diffusion model and the BE-LTS are demonstrated to possess advantages at mid to high frequencies in the analysis of acoustic transmission through tube bundle heat exchangers and expansion chamber mufflers.

The acoustic diffusion model has the potential to become a powerful tool for interior acoustic predictions if a new, efficient, and accurate method of solution, such as the BE-LTS, is demonstrated to the research community. The BEM is a natural choice for many acoustic problems requiring numerical methods. Using this method, a discrete mesh of only the bounding surfaces of the acoustic volumes using two-dimensional (2-D) elements is required. This is advantageous in terms of computing requirements because most often, other numerical methods like the FEM or the FD method require extremely large discrete meshes of the entire acoustic media using 3-D elements. This advantage is demonstrated schematically in Figure 1.3.
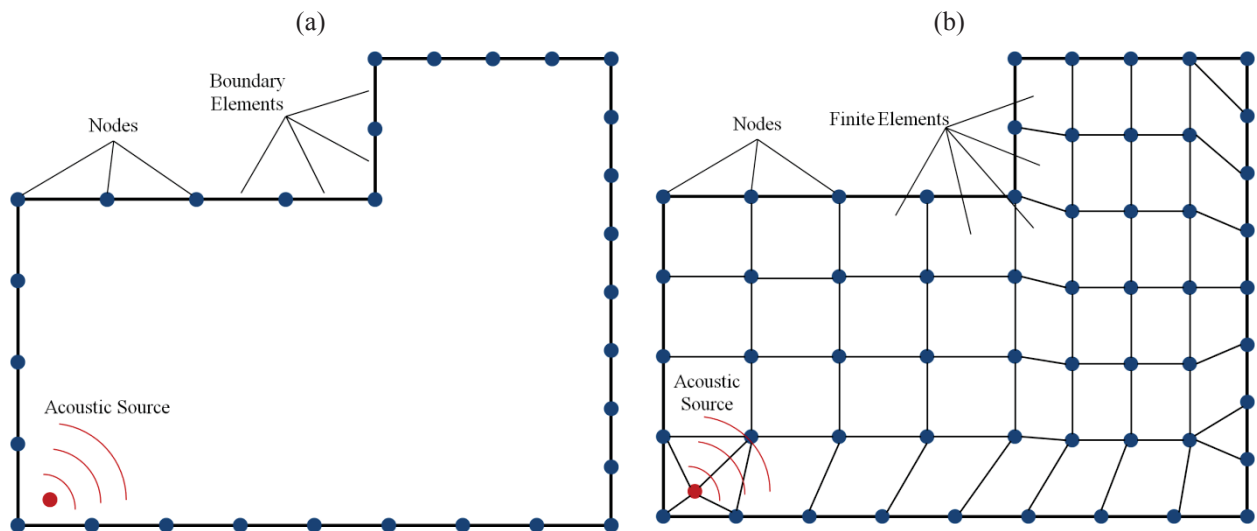
Figure 1.3: Large 2-D acoustic problem with example (a) boundary and (b) finite element meshes.

The coupling of the room acoustics of multiple rooms by common structural components is an aspect that is often ignored or primitively included in common methods of predicting the room acoustics. This new improvement is applied to the acoustic diffusion model. Previously, only simple coupling techniques have been used in conjunction with the acoustic diffusion model, i.e. through a known transmission coefficient which ignores the structural physics occurring in the coupling partition. Using a structural power flow model, the vibration can be analyzed as a system coupled with the acoustic volumes.

The method developed in this dissertation can be used in many other applications. A few are described here. Recently, NASA has expressed interest in the development of software which can predict the response inside commercial or residential structures exposed to incident sonic booms over a large frequency range. To this end, researchers at Virginia Tech have devised software capable of performing these predictions (Remillieux et al., 2009; Corcoran et al., 2012).

At low frequencies, coupled structural and acoustic modal models are used to compute the vibro-acoustic response (Remllieux et al., 2009). The structural modes are computed with the FEM, while the acoustic modes are computed analytically. Exterior pressure loading excites the structure into vibration which, in turn, excites the interior acoustic cavity. At low frequencies, it is important to include the forcing on the structure due to the interior acoustic modes which are also modeled. Due to computational restrictions, the low frequency model is typically effective only at frequencies below 200 to 300 Hz.

At high frequencies, analytical methods with simplifying assumptions are used to compute the transmission loss (TL) of building components. The transmitted acoustic waves are used as the input to a commercial ray tracing software package to compute the interior acoustic radiation (Corcoran et al., 2012). This high frequency model is expected to cover the frequency range from 300 Hz to 6000 Hz. The diffusion BE-LTS could be used as an alternative to ray tracing at these frequencies. In this application, the method offers a couple of noticeable advantages. First, the diffusion model has been shown to be significantly more computationally efficient than ray tracing (Valeau et al., 2006). Second, boundary sources (such as the acoustic radiation from the interior surfaces of a vibrating structure excited by a sonic boom) can be explicitly modeled in

the diffusion BE-LTS, whereas ray tracing requires point sources. To accurately represent a vibrating surface using ray tracing, a distribution of point sources is necessary which costs computational efficiency and/or accuracy. Ray tracing is a conventional method in room acoustics that has been validated in many different cases and will provide valuable comparisons to the BE-LTS of the acoustic diffusion equation.

Obviously, the BEM solution to the acoustic diffusion equation could be applied as a module of this software to predict the indoor radiation of the sonic boom noise. One of the methods to predict the indoor radiation which is currently under investigation is the use of commercial ray tracing software packages which will provide valuable comparisons to the BE-LTS of the acoustic diffusion equation.

As stated previously, it is expected that this model is capable of predictions in problems other than room acoustics. The acoustic field inside mufflers and silencers becomes diffuse quickly even at relatively low frequencies. The diffusion model is likely to be able to describe the acoustic field within and the transmission loss (TL) or insertion loss (IL) of these devices.

Many other applications for this research could be imagined as there are virtually no limits to the size, type, or location of the volume of interest. For example, the analysis of noise in and vibration of vehicle cabins is another potential application. This powerful, efficient numerical solution of the acoustic diffusion equation can replace or be used in conjunction with more common methods of room acoustics predictions such as room acoustics software packages or finite element packages.

1.3   Dissertation Organization

This dissertation is structured in the following manner as shown in Figure 1.4. First, a literature review is presented in Chapter 2. This includes a section on the discussion and derivation of the important acoustic quantities, energy density and intensity, and the relationship between them. Then, other existing acoustic energy models including Sabine theory, geometrical acoustics (image source method and ray tracing), and acoustic radiosity are reviewed. In the final section

of the chapter, the acoustic diffusion model, the foundation of this dissertation, is discussed in detail.

The new, acoustic diffusion BE-LTS is described in Chapter 3. The chapter begins with the Laplace transform method used to derive the integral equation. Then, the BEM is applied to obtain a matrix equation which can be solved for the energy density on the boundary. Finally, the energy at a point in the volume is computed using the energy density on the boundary.

Chapter 4 is concerned with methods of computing the numerical inverse Laplace transform. To convert the Laplace domain results at a point of interest into the physical time domain, a numerical inversion must be applied. Three methods are examined: exponential expansion, Legendre polynomial expansion, and trigonometric expansion. They are then compared and applied to complete the formulation of the BE-LTS to the diffusion model.

The diffusion BE-LTS developed in Chapters 3 and 4 is validated in Chapter 5. Validation is carried out through comparison of the BE-LTS with Sabine theory, ray tracing, and a FEM solution to the diffusion model. Three aspects are considered: convergence in the numerical technique, accuracy of the method, and computational efficiency.

Structural coupling included with the diffusion BE-LTS is discussed in Chapter 6. Two methods are investigated and validated in this chapter. In the first method, multiple acoustic volumes separated by a partition are coupled through a simple transmission coefficient. In the second method, a power flow model is used to model the vibration of the partition itself. Forcing and radiation of the partition is incorporated through the coupling boundary conditions.

Finally, Chapter 7 discusses practical applications of the diffusion BE-LTS. As the rest of the dissertation is mainly applied in room acoustics, this chapter presents other practical engineering examples which can be analyzed with the diffusion BE-LTS. The examples include the acoustic transmission through a tube-bundle heat exchanger and the transmission through an expansion chamber muffler.
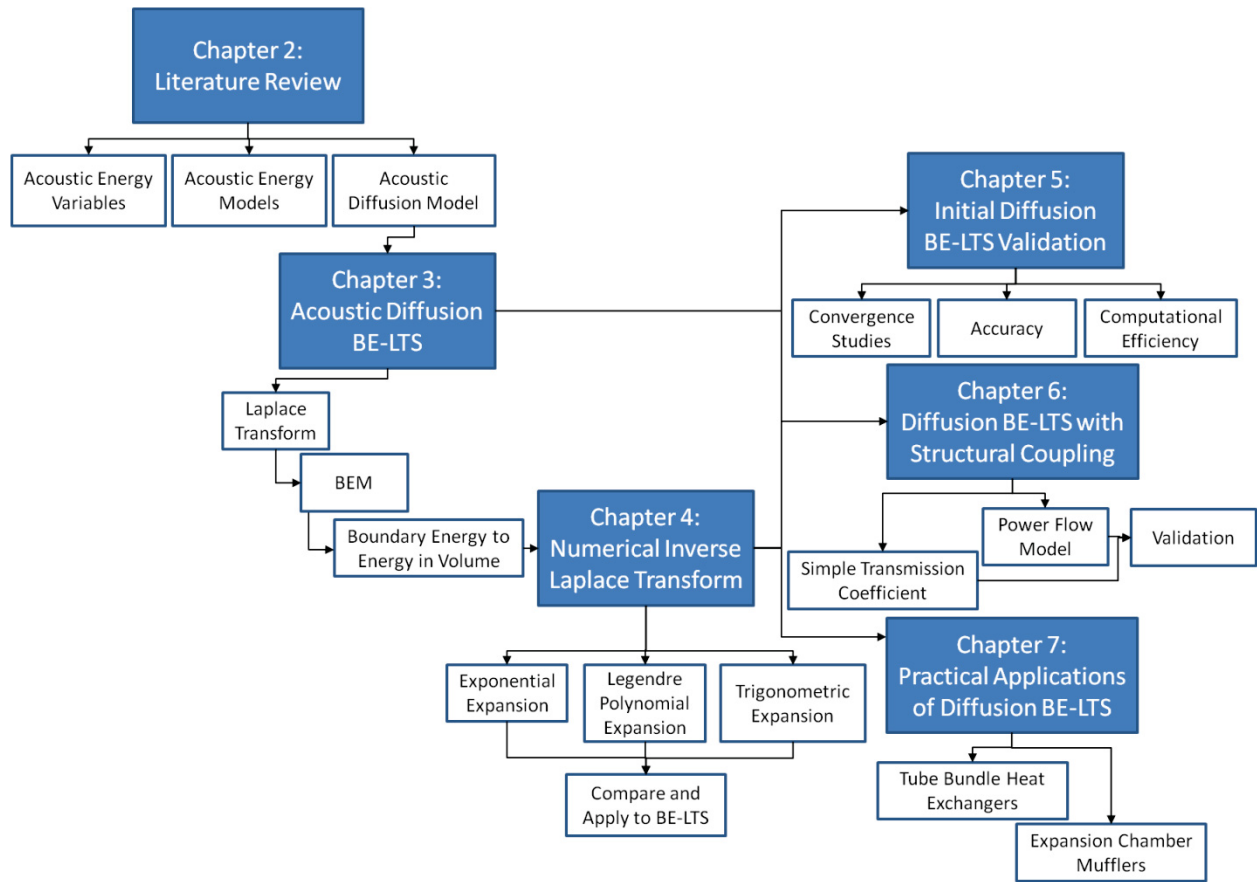
Figure 1.4: Flow chart of dissertation organization showing the main chapters and important sections..

Chapter 2: Literature Review of Energy Methods in Acoustics

Since the research topic is an energy method, a review of energy related methods used in acoustics is presented here. Acoustic intensity and energy density relations are derived with respect to common energy methods in the first section. The second section uses these relations to discuss the fundamental relations in the most common energy methods used in acoustics. Finally, the acoustic diffusion models and its variations and improvements are discussed in detail.

2.1   Basic Acoustic Energy Derivations

In this section, theoretical aspects of different energy models for acoustics, i.e. acoustic diffusion and radiosity, will be derived and discussed. First, important acoustic quantities related to energy is derived for spherical waves. Then, an energy balance is performed to derive 3-D acoustic energy models. Finally, different relationships between acoustic variables are considered resulting in popular forms of acoustic energy models.

It is important to understand where the acoustic energy quantities come from since they are the variables of interest in energy analysis methods. Specifically, acoustic energy density and intensity are presented and derived. Acoustic energy density is the field variable in the research on the diffusion model presented here. It is defined as the total amount of energy (kinetic and potential) carried by a sound wave per unit volume of fluid. Intensity is the primary variable of interest in another new, promising energy method, radiosity. Intensity is a vector which describes the rate of transmission of acoustic energy through a unit of surface area (normal to the vector). The relationship between intensity and energy density is key in the derivation of any energy method and it is also discussed in this section. The most important equations are boxed.

The fundamental physical model for the propagation of sound is the acoustic wave equation given by

$$\frac{\partial^2 p(\mathbf{r},t)}{\partial t^2} - c^2 \nabla^2 p(\mathbf{r},t) = 0$$

<div align="right">2.1</div>

where $p(\mathbf{r},t)$ is the acoustic pressure at position $\mathbf{r}$, and time t, c is the speed of sound. For spherical waves, as shown in Figure 2.1, the acoustic wave equation can be rewritten in spherical coordinates as

$$\frac{\partial^2 p(\mathbf{r},t)}{\partial t^2} - c^2 \left[\frac{\partial^2 p(\mathbf{r},t)}{\partial |\mathbf{r}|^2} + \frac{2}{|\mathbf{r}|} \frac{\partial p(\mathbf{r},t)}{\partial |\mathbf{r}|} \right] = 0 .$$

<div align="right">2.2</div>
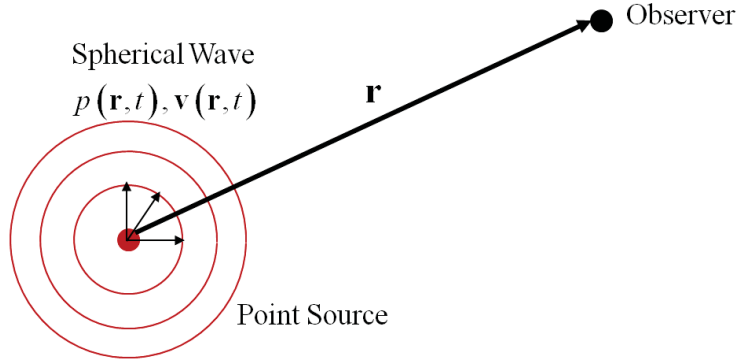
Figure 2.1: Spherical waves propagating from a point source in a 3-D free field.

The acoustic pressure takes the complex form of

$$p(\mathbf{r},t) = \frac{A}{|\mathbf{r}|} \exp\left(i\omega t - ik|\mathbf{r}| \right)$$

<div align="right">2.3</div>

where A is the unknown amplitude of the wave and k is the acoustic wavenumber. The particle velocity of the spherical wave is given by (Kinsler et al., 2000)

$$\mathbf{v}(\mathbf{r},t) = \left(1 - \frac{i}{k|\mathbf{r}|} \right) \frac{p(\mathbf{r},t)}{\rho c} \frac{\mathbf{r}}{|\mathbf{r}|} .$$

<div align="right">2.4</div>

where ρ is the density of the fluid medium. For periodic wave, the acoustic intensity, $\mathbf{I}(\mathbf{r})$, can be found using (Kinsler et al., 2000)

$$\mathbf{I}(\mathbf{r}) = \frac{1}{2} \text{Re}\left[p(\mathbf{r},t) \mathbf{v}^*(\mathbf{r},t) \right]$$

<div align="right">2.5</div>

where $\mathrm{Re}[\ ]$ denotes taking only the real part and * a complex conjugate. Substituting eq. 2.4 into eq. 2.5 gives

$$\mathbf{I}(\mathbf{r}) = \frac{1}{2\rho c} \mathrm{Re}\left[\left(1 + \frac{i}{k|\mathbf{r}|}\right)|p(\mathbf{r},t)|^2 \frac{\mathbf{r}}{|\mathbf{r}|}\right] \qquad 2.6$$

which reduces to

$$\mathbf{I}(\mathbf{r}) = \frac{1}{2\rho c}|p(\mathbf{r},t)|^2 \frac{\mathbf{r}}{|\mathbf{r}|}. \qquad 2.7$$

Substituting eq. 2.3 into 2.7 gives

$$\mathbf{I}(\mathbf{r}) = \frac{1}{2}\frac{|A|^2}{\rho c|\mathbf{r}|^2}\frac{\mathbf{r}}{|\mathbf{r}|}. \qquad 2.8$$

The acoustic energy density, $\psi(\mathbf{r})$, is defined by the sum of the kinetic and potential energy density and can be written (Kinsler et al., 2000)

$$\psi(\mathbf{r}) = \frac{1}{2}\rho\left\{|\mathbf{v}(\mathbf{r},t)|^2 + \frac{|p(\mathbf{r},t)|^2}{\rho^2 c^2}\right\} \qquad 2.9$$

Substituting eqs. 2.3 and 2.4 into eq. 2.9 gives

$$\psi(\mathbf{r}) = \frac{1}{2\rho c^2}\frac{|A|^2}{|\mathbf{r}|^2}\left\{\left|\left(1 - \frac{i}{k|\mathbf{r}|}\right)\right|^2 + 1\right\}. \qquad 2.10$$

Reducing the bracketed term yields

$$\psi(\mathbf{r}) = \frac{1}{2\rho c^2}\frac{|A|^2}{|\mathbf{r}|^2}\left\{2 + \frac{1}{k^2|\mathbf{r}|^2}\right\}. \qquad 2.11$$

Since the energy is dependent only on the distance from the source, the gradient of the energy density is given by

$$\nabla\psi(\mathbf{r}) = \frac{\partial\psi(\mathbf{r})}{\partial|\mathbf{r}|}\frac{\mathbf{r}}{|\mathbf{r}|}. \qquad 2.12$$

Substituting eq. 2.11 into eq. 2.12 gives

$$\nabla\psi(\mathbf{r}) = \frac{1}{2\rho c^2}\frac{\partial}{\partial|\mathbf{r}|}\left[\frac{|A|^2}{|\mathbf{r}|^2}\left(2 + \frac{1}{k^2|\mathbf{r}|^2}\right)\right]\frac{\mathbf{r}}{|\mathbf{r}|}. \qquad 2.13$$

12

Carrying out the differentiation gives the gradient of the energy density as

$$\nabla \psi(\mathbf{r}) = -\frac{2|A|^2}{\rho c^2 |\mathbf{r}|^3}\left(1 + \frac{1}{k^2 |\mathbf{r}|^2}\right)\frac{\mathbf{r}}{|\mathbf{r}|}.$$

2.14

Next, a spherical shell volume centered at the source of width $\Delta|\mathbf{r}|$ with total energy E is considered as shown in Figure 2.2.
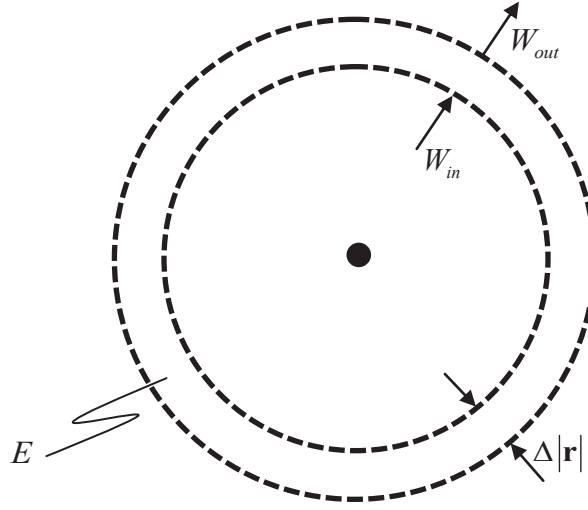
Figure 2.2: Energy balance on spherical shell volume centered at a point source drawn in 2-D for simplicity.

The total energy in this volume, E, is described by

$$\frac{\partial E(\mathbf{r},t)}{\partial t} = W_{in}(\mathbf{r},t) - W_{out}(\mathbf{r},t)$$

2.15

where W_{in} is the power flowing into the volume and W_{out} the power flowing out. Rewriting the power in terms of intensity gives

$$\frac{\partial E(\mathbf{r},t)}{\partial t} = |\mathbf{I}(\mathbf{r})|\left(4\pi|\mathbf{r}|^2\right) - \left[|\mathbf{I}(\mathbf{r})| + \frac{d|\mathbf{I}(\mathbf{r})|}{d|\mathbf{r}|}\Delta|\mathbf{r}|\right]\left[4\pi\left(|\mathbf{r}|+\Delta|\mathbf{r}|\right)^2\right].$$

2.16

Multiplying out all terms in brackets gives

13

$$\frac{\partial E(\mathbf{r},t)}{\partial t} = |\mathbf{I}(\mathbf{r})|\left(4\pi|\mathbf{r}|^2\right) - \left[|\mathbf{I}(\mathbf{r})|\left(4\pi|\mathbf{r}|^2\right) + \frac{d|\mathbf{I}(\mathbf{r})|}{d|\mathbf{r}|}\Delta|\mathbf{r}|\left(4\pi|\mathbf{r}|^2\right) + |\mathbf{I}(\mathbf{r})|\left(8\pi|\mathbf{r}|\Delta|\mathbf{r}|\right) + \right.$$

$$\left. \frac{d|\mathbf{I}(\mathbf{r})|}{d|\mathbf{r}|}\Delta|\mathbf{r}|\left(8\pi|\mathbf{r}|\Delta|\mathbf{r}|\right) + |\mathbf{I}(\mathbf{r})|\left(4\pi\Delta|\mathbf{r}|^2\right) + \frac{d|\mathbf{I}(\mathbf{r})|}{d|\mathbf{r}|}\Delta|\mathbf{r}|\left(4\pi\Delta|\mathbf{r}|^2\right)\right]$$

2.17

or

$$\frac{\partial E(\mathbf{r},t)}{\partial t} = |\mathbf{I}(\mathbf{r})|\left(4\pi|\mathbf{r}|^2\right) - \left[|\mathbf{I}(\mathbf{r})|\left(4\pi|\mathbf{r}|^2\right) + \frac{d|\mathbf{I}(\mathbf{r})|}{d|\mathbf{r}|}\Delta|\mathbf{r}|\left(4\pi|\mathbf{r}|^2\right) + \mathcal{O}\left(\Delta|\mathbf{r}|\right)\right]$$

2.18

where $\mathcal{O}\left(\Delta|\mathbf{r}|\right)$ represents all terms on the order of $\Delta|\mathbf{r}|$ or higher. Ignoring these higher order terms, eq. 2.18 becomes

$$\frac{\partial E(\mathbf{r},t)}{\partial t} = -4\pi|\mathbf{r}|^2\frac{d|\mathbf{I}(\mathbf{r})|}{d|\mathbf{r}|}\Delta|\mathbf{r}|.$$

2.19

Equation 2.19 can be converted to energy density using

$$\frac{\partial\psi(\mathbf{r},t)}{\partial t} = \lim_{V_{shell}\to0}\left(\frac{1}{V_{shell}}\frac{\partial E(\mathbf{r},t)}{\partial t}\right).$$

2.20

Substituting eq. 2.19 into eq. 2.20 gives

$$\frac{\partial\psi(\mathbf{r},t)}{\partial t} = \lim_{V_{shell}\to0}\left[-\frac{4\pi|\mathbf{r}|^2\Delta|\mathbf{r}|}{V_{shell}}\frac{d|\mathbf{I}(\mathbf{r})|}{d|\mathbf{r}|}\right]$$

2.21

where $V_{shell} = 4\pi|\mathbf{r}|^2\Delta|\mathbf{r}|$. Substituting the volume of the spherical shell gives

$$\frac{\partial\psi(\mathbf{r},t)}{\partial t} = -\frac{d|\mathbf{I}(\mathbf{r})|}{d|\mathbf{r}|}$$

2.22

or

$$\boxed{\frac{\partial\psi(\mathbf{r},t)}{\partial t} = -\nabla\cdot\mathbf{I}(\mathbf{r}).}$$

2.23

This is the basic acoustic energy balance equation from which all other acoustic energy models can be derived.

In this dissertation, results are typically presented as a sound pressure level (SPL), a more widely used quantity. The SPL, L_p, is computed from the acoustic energy density with

$$L_p = 10 \log_{10} \left(\frac{\rho c^2 \psi}{p_{ref}^2} \right). \qquad\qquad 2.24$$

2.2 Review of Acoustic Energy Models

Energy models are a common simplification in the study of acoustics when the wave equation is impractical to solve. This commonly occurs in complex 3-D geometry requiring numerical solutions and either the size of the problem is large (e.g. outdoors or in large volumes) or high frequency calculations are necessary. Considering the real, positive quantity of acoustic energy provides significant mathematical simplifications over the consideration of the coupled complex acoustic pressure and particle velocity.

2.2.1 Sabine Theory

The simplest of all acoustic energy methods relies on extreme assumptions to reduce complicated physics. Nevertheless, the theory is widely used as a first estimate before a more detailed analysis is attempted and is presented in this section. At sufficiently high frequencies when there is significant overlap from the individual modes that make up the overall acoustic response, the concept of a diffuse or reverberant acoustic field arises. A sound field in a volume is said to be diffuse when two conditions are met:

1. The sound waves at any point in the volume arrive from all directions with equal probability and intensity.
2. The intensity in the volume is the same at every position.

If these assumptions are met and the absorption is uniform everywhere in the volume, a simple balance of acoustic power can be written. The rate of change of acoustic energy in the volume, $\partial E(t) / \partial t$, is written in terms of energy density as in

$$\frac{\partial E(t)}{\partial t} = V_v \frac{\partial \psi(t)}{\partial t} \qquad\qquad 2.25$$

where V_v is the total volume of the volume. The rate at which energy is dissipated, W_a, is

$$W_a = \frac{S_v c \bar{\alpha}}{4} \psi(t). \qquad\qquad 2.26$$

Given a supply of acoustic power, W, the energy balance in the volume is

15

$$\frac{\partial E(t)}{\partial t} = W - W_a.$$

<div align="right">2.27</div>

Substituting eqs. 2.25 and 2.26 into eq. 2.27 gives a first order ordinary differential equation in terms of the energy density in the volume which is the basis for Sabine theory:

$$V_v \frac{\partial \psi(t)}{\partial t} = W - \frac{S_v c \bar{\alpha}}{4} \psi(t).$$

<div align="right">2.28</div>

The solution to eq. 2.28 is easily obtained as

$$\psi(t) = \frac{4W}{S_v c \bar{\alpha}} - \left[\frac{4W}{S_v c \bar{\alpha}} - \psi_0 \right] \exp\left(-\frac{t}{\tau_S} \right)$$

<div align="right">2.29</div>

where ψ_0 is the initial energy density in the volume and $\tau_S = \dfrac{4V_r}{S_r c \alpha}$ is the time constant.

Equation 2.29 is often solved for either a supplied acoustic power without initial energy giving

$$\psi(t) = \frac{4W}{S_v c \bar{\alpha}} \left[1 - \exp\left(-\frac{t}{\tau_S} \right) \right]$$

<div align="right">2.30</div>

or an initial energy density without a supply of acoustic power as in

$$\psi(t) = \psi_0 \exp\left(-\frac{t}{\tau_S} \right).$$

<div align="right">2.31</div>

The main limitations of Sabine theory are the restricting diffuse field assumptions made to simplify complex physics. These assumptions often inhibit the accuracy of the theory.

2.2.2   *Geometrical Acoustics*

Techniques in geometrical acoustics are some of the most commonly used in the field of room acoustics. The ray tracing method is used later for comparisons with the newer energy methods in room acoustic examples. Two related geometrical acoustics methods are presented in this section for completeness.

In the image source method, specular reflections from the surfaces of the volume are modeled by mirroring the source across the surfaces (Allen and Berkley, 1979). For a volume with six bounding surfaces, multiple orders of image sources can be created by mirroring image sources created across multiple surfaces consecutively. Higher order image sources represent reflections from multiple surfaces. The total response at a receiver is then calculated by summing

the response due to the direct radiated field of the source with the responses due to the fields generated by the image sources coherently. For a monopole source radiating sound at a frequency, ω, the pressure, $P(\omega)$, at a receiver in a rigid room is

$$P(\omega) = \sum_{n=1}^{\infty} \frac{\exp(ikr_n)}{4\pi r_n} \exp(-i\omega t) \qquad \qquad 2.32$$

where r_n is the distance from the receiver to the nth image source (Allen and Berkley, 1979). This can be easily extended for surfaces which absorb energy of incident waves (Allen and Berkley, 1979). The image source method becomes very computationally intensive very quickly if a large number of reflections contribute to the overall response. It is also difficult to include non-specularly reflecting surfaces and objects (Beranek and Vér, 1992).

Probably the most conventional technique used in room acoustics is ray tracing due to its ability to model any arbitrary acoustic volume. The method consists of emitting a large number of rays (lines) or other 3-D geometric shapes (cones or pyramids) from a point source (Beranek and Vér, 1992) as shown in Figure 2.3. The shapes and their associated energy are then tracked as they propagate around the room accounting for specular and diffusely reflecting surfaces. Often, the image source framework is incorporated into a ray tracing algorithm to account for specular reflections (Farina, 1995). In this manner, an impulse response from a point source to a receiver in the volume can be constructed (Farina, 1995).
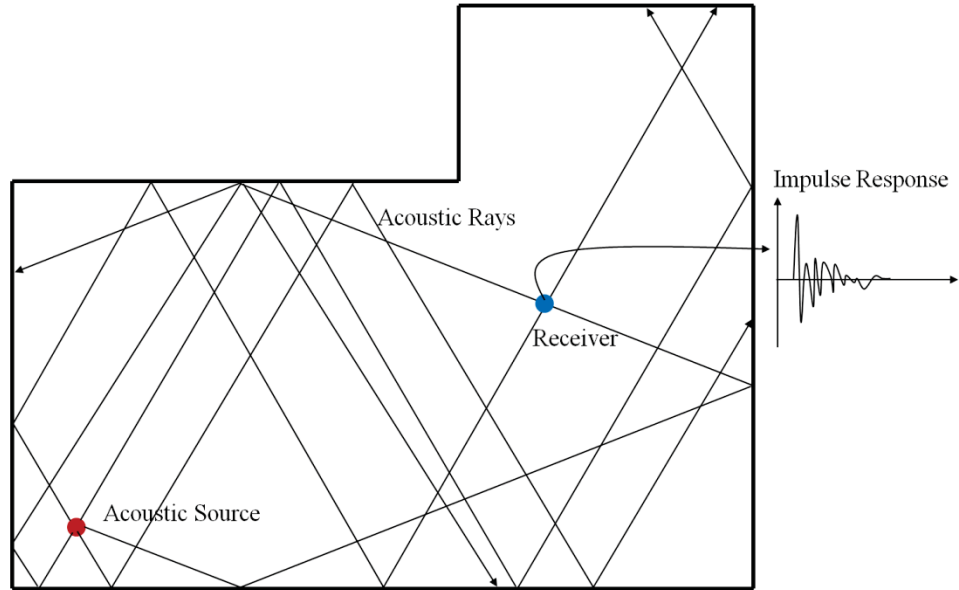
Figure 2.3: Schematic demonstrating basic idea behind the ray tracing method which tracks a large number of rays as they reflect around a room and are seen by a receiver to construct its impulse response.

Usually, a "brute force" approach is necessary to ensure accurate results using ray tracing, i.e. the use of more rays, accounting for more reflections, finer or more time steps. These types of model revisions often come at a great computational expense. Knowledge of surface absorption and especially scattering coefficients without any measurement can also result in a challenge to implement ray tracing for a particular problem.

2.2.3   Acoustic Radiosity

A more recently developed energy method that has been implemented for the study of room acoustics is known as radiosity (Le Bot, 1998). This is a relatively new energy-based technique which has shown promise in mid to high frequency vibro-acoustic analysis. Although both are based on acoustic energy variables, radiosity and diffusion have differences which are discussed in this section. The derivation and a description of the technique are presented in this section for the reader interested in this alternative acoustic energy method.

The basic idea behind this method is to represent a structural or acoustic energy field as the sum of sources (primary sources) and reverberant energy described by fictitious sources placed on the boundaries of the domain (secondary sources) as shown in Figure 2.4. The primary

sources are of known strength. The strengths of the secondary sources are determined by writing an energy balance at the location of each secondary source consecutively to create a system of integral equations which can be solved numerically.
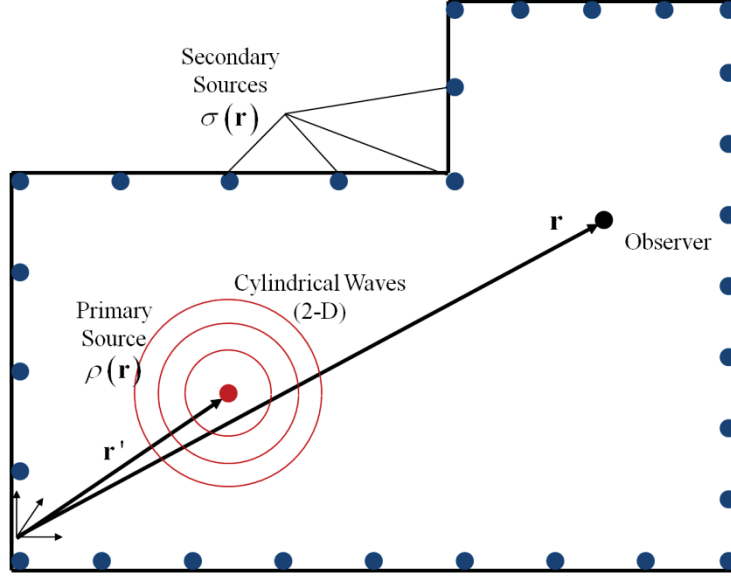
Figure 2.4: Schematic demonstrating basic idea behind the radiosity method which describes the energy field as the contribution of primary (real) sources and secondary (fictitious) sources.

The development begins with the steady state energy balance at a point, $\mathbf{r}$, in an arbitrary wave field, e.g. acoustic waves in a volume or bending waves in a plate, as in

$$\nabla \cdot \mathbf{I}(\mathbf{r}) + \psi_{diss}(\mathbf{r}) = \psi_{inj}(\mathbf{r}) \qquad 2.33$$

where $\psi_{diss}(\mathbf{r})$ is the energy density dissipated due to travel through the point and $\psi_{inj}(\mathbf{r})$ is the energy density injected at the point. The derivation is general enough to apply to 1-D, 2-D, or 3-D acoustic or structural wave fields. The energy dissipated is related to the energy density at the point through an attenuation coefficient, m, and the group velocity, c_g, of the medium:

$$\psi_{diss}(\mathbf{r}) = mc_g \psi(\mathbf{r}) \qquad 2.34$$

Assuming symmetric spreading from a point source located at $\mathbf{r}'$ in an isotropic media, the gradient of the intensity is

$$\nabla \cdot \mathbf{I}(\mathbf{r}|\mathbf{r}') = \frac{1}{|\mathbf{r}-\mathbf{r}'|^{n-1}} \frac{d}{d|\mathbf{r}-\mathbf{r}'|} \left[|\mathbf{r}-\mathbf{r}'|^{n-1} |\mathbf{I}(\mathbf{r}|\mathbf{r}')| \right] \qquad 2.35$$

where n is the dimension of the medium, i.e. 1-D, 2-D, or 3-D.

Dividing eq. 2.8 by eq. 2.11, it is shown that intensity can be written in terms of energy density in a free field as

$$\mathbf{I}(\mathbf{r}|\mathbf{r}') = c\left\{2 + \frac{1}{k^2|\mathbf{r}-\mathbf{r}'|^2}\right\}^{-1}\psi(\mathbf{r},t)\frac{\mathbf{r}-\mathbf{r}'}{|\mathbf{r}-\mathbf{r}'|}. \qquad 2.36$$

If $k|\mathbf{r}-\mathbf{r}'|$ is large, for example at high frequencies, eq. 2.36 can be approximated by

$$\mathbf{I}(\mathbf{r}|\mathbf{r}') \approx \frac{c}{2}\psi(\mathbf{r},t)\frac{\mathbf{r}-\mathbf{r}'}{|\mathbf{r}-\mathbf{r}'|}. \qquad 2.37$$

The downside to representing the intensity through eq. 2.37 is that it is accurate for the direct field of the source, as shown in Figure 2.5. After a wave encounters a reflection, the intensity vector calculated with eq. 2.37 is in the wrong direction compared to the actual intensity vector. Thus, the radiosity method relies on placing fictitious sources on the boundary to represent reflected or diffracted waves and calculating the correct strength of these sources based on real sources and room surface properties (Le Bot, 1998).
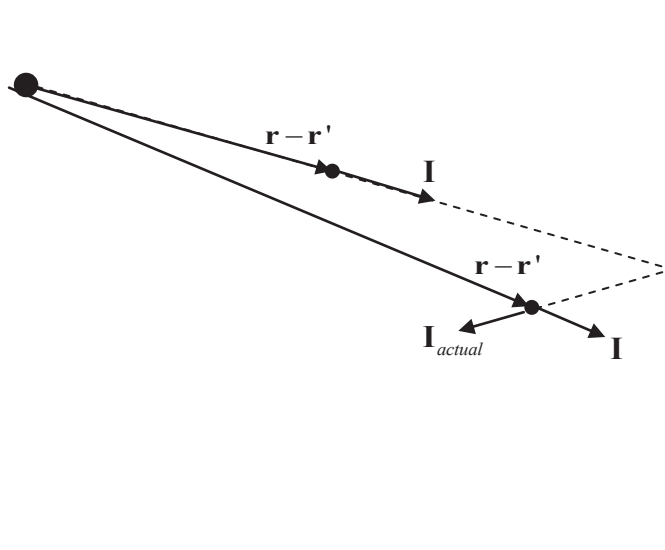
Figure 2.5: Schematic demonstrating the inability to represent the intensity vector as proportional to the energy density through eq. 2.37 outside of the direct field of the source.

At this point in the derivation of the radiosity method, it is assumed that the intensity vector is proportional to the energy density as in eq. 2.37:

$$I(r|r') = c_g \psi(r) \frac{r - r'}{|r - r'|}.$$

2.38

Thus, the energy balance at any point in the field (except at the point source) can be written by substituting eqs. 2.38 and 2.34 into eq. 2.33

$$\frac{1}{|r - r'|^{n-1}} \frac{d}{d|r - r'|} \left[|r - r'|^{n-1} \psi(r) \right] + m\psi(r) = 0.$$

2.39

The solution to this first order ordinary differential equation is

$$\psi(r) \propto G(r|r').$$

2.40

where

$$G(r|r') = \frac{\exp(-m|r - r'|)}{|r - r'|^{n-1}}.$$

2.41

Using eq. 2.38,

$$I(r) \propto H(r|r')$$

2.42

where

$$H(r|r') = c_g \frac{\exp(-m|r - r'|)}{|r - r'|^{n-1}} \frac{r - r'}{|r - r'|}.$$

2.43

Next, two principles are cited to continue the derivation of the radiosity method (Le Bot, 1998). First, a linear superposition principle is used to state that the total energy at a point due to several propagating waves is simply equal to the sum of the energy in each wave. Second, Huygens principle which states that a diffracted wave field can be recreated as the sum of point sources is cited. The result is that the energy density at any point in the field can be written as a sum of direct, primary sources and indirect, secondary sources that make up the diffracted field. Primary sources are actual sources in the wave field and the secondary sources are fictitious sources placed on the boundaries to create a diffracted field. The result is

$$\psi(r) = \int_V \rho(r') G(r|r') dV' + \int_S \sigma(r') f(r|r', n) G(r|r') dS'$$

2.44

where $\rho(\mathbf{r}')$ are the strengths of the primary sources, $\sigma(\mathbf{r}')$ are the strengths of the secondary sources, $\mathbf{n}$ is the unit normal to the bounding surface, $f(\mathbf{r}|\mathbf{r}',\mathbf{n})=1$ if the secondary sources are assumed to radiate sound in all directions (diffuse reflections), and $f(\mathbf{r}|\mathbf{r}',\mathbf{n})=\dfrac{\mathbf{r}-\mathbf{r}'}{|\mathbf{r}-\mathbf{r}'|}\cdot\mathbf{n}$ if the secondary sources reflect energy specularly. A similar equation can be written in terms of intensity as

$$\mathbf{I}(\mathbf{r})=\int_V \rho(\mathbf{r}')\mathbf{H}(\mathbf{r}|\mathbf{r}')dV'+\int_S \sigma(\mathbf{r}')f(\mathbf{r}|\mathbf{r}',\mathbf{n})\mathbf{H}(\mathbf{r}|\mathbf{r}')dS'. \qquad 2.45$$

Now, the strengths of the secondary sources, $\sigma(\mathbf{r}')$, located on the boundaries are solved using an energy balance technique. Considering an infinitesimally small hemispherical surface centered on one of the secondary sources, a power balance can be written as

$$W_{emit}(\mathbf{r})=\left[1-\alpha(\mathbf{r})\right]\left[W_{dir}(\mathbf{r})+W_{dif}(\mathbf{r})\right] \qquad 2.46$$

where $W_{emit}(\mathbf{r})$ is the power radiated by the secondary source, $W_{dir}(\mathbf{r})$ is the power radiated by the primary sources, and $W_{dif}(\mathbf{r})$ is the power radiated from all other secondary sources. The power emitted by the secondary source through a small angle of the hemispherical surface, $d\theta$, can be written

$$dW_{emit}(\mathbf{r})=c_g\sigma(\mathbf{r})f(\mathbf{r}|\mathbf{r}',\mathbf{n})d\theta. \qquad 2.47$$

Integrating over the entire hemispherical surface, S_θ, gives the total power radiated by the secondary source as

$$W_{emit}(\mathbf{r})=\int_{S_\theta} c_g\sigma(\mathbf{r}')f(\mathbf{r}|\mathbf{r}',\mathbf{n})d\theta'. \qquad 2.48$$

Carrying out the integration gives

$$W_{emit}(\mathbf{r})=\beta c_g\sigma(\mathbf{r}) \qquad 2.49$$

where β is a constant dependent on the dimension of the field and $f(\mathbf{r}|\mathbf{r}',\mathbf{n})$ (Le Bot, 1998).

The acoustic power radiated by the primary sources and entering the small hemispherical surface can be written as a volume integral as

$$W_{dir}(\mathbf{r}) = \int_V \rho(\mathbf{r}')\left[\mathbf{H}(\mathbf{r}|\mathbf{r}')\cdot\mathbf{n}\right]dV'. \tag{2.50}$$

Finally, the acoustic power radiated by all other secondary sources, entering the hemispherical surface can be written as a surface integral

$$W_{dif}(\mathbf{r}) = \int_S \sigma(\mathbf{r}')f(\mathbf{r}|\mathbf{r}',\mathbf{n})\left[\mathbf{H}(\mathbf{r}|\mathbf{r}')\cdot\mathbf{n}\right]dS'. \tag{2.51}$$

Substituting eqs. 2.49, 2.50, and 2.51 into 2.46 gives the integral equation forming the basis of the radiosity method in a single system:

$$c_g\beta\sigma(\mathbf{r}) = \left[1-\alpha(\mathbf{r})\right]\left\{\int_V \rho(\mathbf{r}')\left[\mathbf{H}(\mathbf{r}|\mathbf{r}')\cdot\mathbf{n}\right]dV' + \int_S \sigma(\mathbf{r}')f(\mathbf{r}|\mathbf{r}',\mathbf{n})\left[\mathbf{H}(\mathbf{r}|\mathbf{r}')\cdot\mathbf{n}\right]dS'\right\} \tag{2.52}$$

The surface integral can be evaluated essentially using the BEM, i.e. discretization of bounding surfaces into elements and consecutive collocation at each node of the boundary mesh. The volume integral is evaluated usually using analytical techniques. The derivation continues to encompass coupled structural acoustic systems (Le Bot, 1998), but that will be discussed in a later structural coupling section.

The difference between radiosity and the diffusion model is the following. Rather than imposing fictitious sources on volume boundaries, the acoustic diffusion model represents the intensity vector as being proportional to the energy density gradient. Dividing eq. 2.8 by eq. 2.14 demonstrates that intensity can instead be written in terms of the gradient of the energy density as

$$\mathbf{I}(\mathbf{r}|\mathbf{r}') = -\frac{c|\mathbf{r}-\mathbf{r}'|}{4}\left(1+\frac{1}{k^2|\mathbf{r}-\mathbf{r}'|^2}\right)^{-1}\nabla\psi(\mathbf{r},t) \tag{2.53}$$

Equation 2.53 can be approximated by

$$\mathbf{I}(\mathbf{r}|\mathbf{r}') \approx -\frac{c|\mathbf{r}-\mathbf{r}'|}{4}\nabla\psi(\mathbf{r},t) \tag{2.54}$$

if $k|\mathbf{r}-\mathbf{r}'|$ is large. Substituting eq. 2.54 into eq. 2.23 yields

$$\frac{\partial\psi(\mathbf{r},t)}{\partial t} = \nabla\cdot\left[\frac{c|\mathbf{r}|}{4}\nabla\psi(\mathbf{r},t)\right] \tag{2.55}$$

which states that the change in energy density over time is proportional to the Laplacian of the energy density. Considering a diffuse field in a volume with reflecting, absorptive boundaries and objects, eq. 2.55 can be transformed into the acoustic diffusion equation proposed by Picaut et al. (1997) which will be discussed in the next section.

2.3 Acoustic Diffusion Model

In this section, the acoustic diffusion model which forms the foundation for this research is discussed in detail. The acoustic diffusion model is a new energy method which describes a reverberant acoustic field as a flow (or diffusion) of acoustic energy. This concept is shown in Figure 2.6. At high frequencies, acoustic waves exhibit ray behavior; as shown in the figure, the buildup of many subsequent reflections of acoustic rays resembles concentrations of acoustic energy.

(a)

(b)
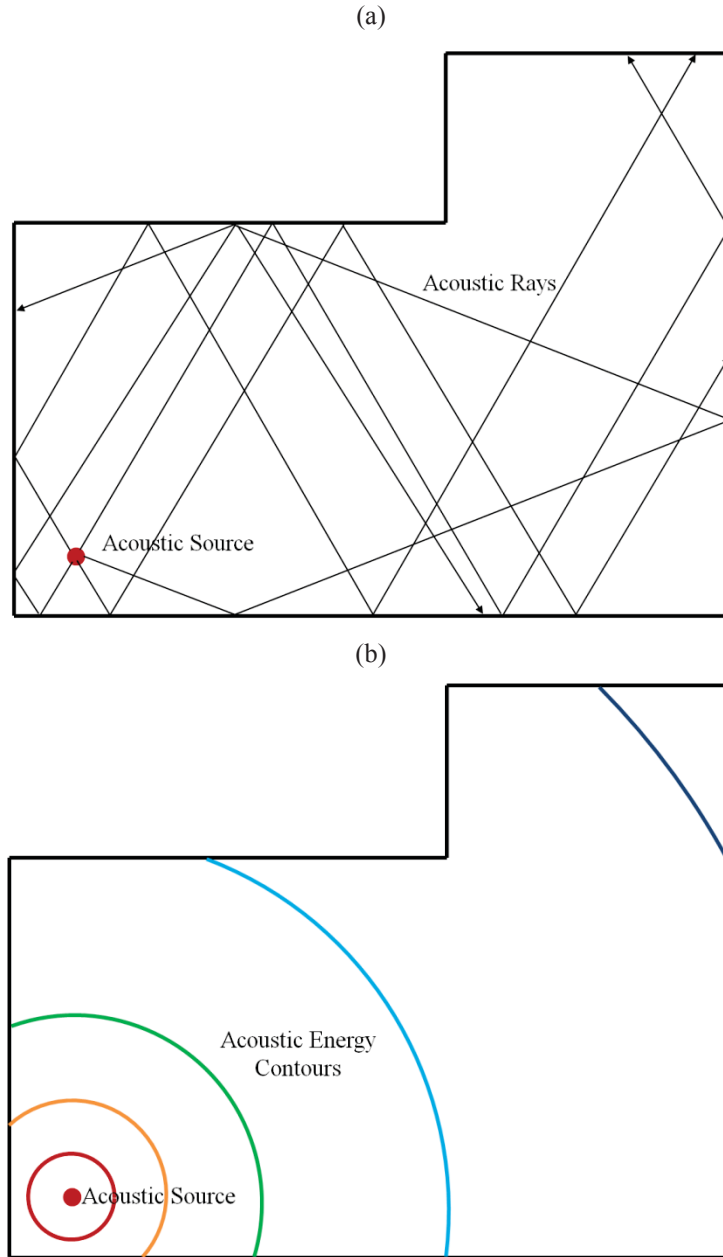
Figure 2.6: Schematic demonstrating basic idea behind the acoustic diffusion model which models (a) the buildup of many reflections of acoustic rays as (b) the diffusion of reverberant acoustic energy.

The discussion in this section is presented to convey the fundamentals of the method and the current state of the research surrounding the method. By describing the current state, the originality of the research presented later becomes clear.

2.3.1 Formal Derivation of the Acoustic Diffusion Model

In 1997, Picaut et al. proposed a new approach for modeling room acoustics based on diffusion theory, introducing an acoustic diffusion coefficient. The formal derivation of the model first presented by Picaut et al. (1997) is discussed here for the interested reader. However, the proposed numerical solution in this dissertation does not rely on this derivation, only on the final diffusion equation in eq. 2.72.

Picaut et al. (1997) first make the assumption that the scattering of particles of acoustic energy from the boundaries of a room is comparable to the motion of a particle in a gas colliding with other particles. For a basic review of diffusion theory, refer to Appendix A.

The distribution of acoustic particles in the volume, $f(\mathbf{r}, \mathbf{v}, t)$, is described as a function of position, $\mathbf{r}$, velocity, $\mathbf{v}$, and time, t. The energy density and flow, $\mathbf{J}(\mathbf{r}, t)$, at any point in the volume at a specific time can be written in terms of integrals over the velocity of this distribution as in

$$\psi(\mathbf{r}, t) = \iiint f(\mathbf{r}, \mathbf{v}, t) dV_{\mathbf{v}} \qquad 2.56$$

and

$$\mathbf{J}(\mathbf{r}, t) = \iiint \mathbf{v} f(\mathbf{r}, \mathbf{v}, t) dV_{\mathbf{v}} \qquad 2.57$$

where $V_{\mathbf{v}}$ is the 3-D velocity space. The acoustic particle distribution after a small time, dt, has passed can be rewritten as

$$f(\mathbf{r}, \mathbf{v}, t) = f(\mathbf{r} + \mathbf{v} dt, \mathbf{v}, t + dt). \qquad 2.58$$

Equation 2.58 can be expanded as a Taylor series. Retaining only the first order terms gives

$$\frac{\partial f(\mathbf{r}, \mathbf{v}, t)}{\partial t} \approx -\mathbf{v} \cdot \nabla f(\mathbf{r}, \mathbf{v}, t). \qquad 2.59$$

However, this equation neglects the acoustic particles scattered both into and out of the velocity space and the acoustic particles absorbed at the boundary. The scattering cross-section of the volume, S_s, is given by

$$S_s = (1 - \bar{\alpha}) S_r \qquad 2.60$$

and the absorbing cross-section, S_a, by

$$S_a = \overline{\alpha} S_r .$$

2.61

The total scattering area, S_t, is given by

$$S_t = S_s + S_a .$$

2.62

In the scattering of particles in a fluid, scattering objects are usually assumed to be spheres with a surface area equal to $S_f = 4\pi R^2$ and the cross-section is $S_f / 4$. Applying this analogy to the scattering of acoustic particles from the surfaces of a volume, the surface density per unit volume, $n_t S_f$, must be

$$n_t S_f = S_r / V_r .$$

2.63

Moving from total surface area to cross-sectional area, this becomes

$$n_t S_t = \frac{S_r}{4V_r} .$$

2.64

The mean free path between two collisions is then derived in this framework to give

$$\lambda = \frac{1}{n_t S_t} = \frac{4V_r}{S_r}$$

2.65

in agreement with classical reverberant theory (Bies and Hansen, 2003). Considering acoustic particles entering and leaving the velocity space through scattering and absorption, eq. 2.59 becomes

$$\frac{\partial f(\mathbf{r}, \mathbf{v}, t)}{\partial t} = -\mathbf{v} \cdot \nabla f(\mathbf{r}, \mathbf{v}, t) - n_t (S_s + S_a) |\mathbf{v}| f(\mathbf{r}, \mathbf{v}, t) + \frac{n_t S_s |\mathbf{v}|}{4\pi} \iiint f(\mathbf{r}, \mathbf{v}', t) dV_{v'} .$$

2.66

Now, the density function is expanded in powers of $\mathbf{v}$ assuming that the angle-dependence is small to give

$$f(\mathbf{r}, \mathbf{v}, t) \approx \frac{1}{4\pi} \psi(\mathbf{r}, t) + \frac{3}{4\pi |\mathbf{v}|^2} [\mathbf{v} \cdot \mathbf{I}(\mathbf{r}, t)]$$

2.67

in which only first order terms are retained. Substituting eq. 2.67 into eq. 2.66 results in an equation that can be separated by terms that change sign when the direction of $\mathbf{v}$ is reversed and those that do not. The terms that change sign give

$$\mathbf{I}(\mathbf{r}, t) = -\frac{|\mathbf{v}|}{3S_t n_t} \nabla \psi(\mathbf{r}, t).$$

2.68

27

Considering that the acoustic particles will move at the speed of sound, $|\mathbf{v}| = c$, and substituting eq. 2.65 gives

$$\mathbf{I}(\mathbf{r},t) = -\frac{\lambda c}{3} \nabla \psi(\mathbf{r},t).$$

2.69

The terms that do not change sign give

$$\frac{\partial \psi(\mathbf{r},t)}{\partial t} = -\frac{3}{|\mathbf{v}|^2} \mathbf{v} \cdot \nabla \big[|\mathbf{v}| \mathbf{I}(\mathbf{r},t) \big] - n_t S_a |\mathbf{v}| \psi(\mathbf{r},t).$$

2.70

Next, eq. 2.69 is substituted into eq. 2.70 and the result is averaged across all velocity directions in accordance with diffuse field theory. This gives

$$\frac{\partial \psi(\mathbf{r},t)}{\partial t} = \frac{\lambda c}{3} \nabla^2 \psi(\mathbf{r},t) - \frac{S_r c \overline{\alpha}}{4V_r} \psi(\mathbf{r},t).$$

2.71

Defining a diffusion coefficient, D, and the coefficient which accounts for absorption, σ, gives the diffusion model derived by Picaut et al. (1997)

$$\boxed{\frac{\partial \psi(\mathbf{r},t)}{\partial t} = D \nabla^2 \psi(\mathbf{r},t) - \sigma \psi(\mathbf{r},t)}$$

2.72

where

$$D = \frac{\lambda c}{3}$$

2.73

and

$$\sigma = \frac{c \overline{\alpha}}{\lambda}.$$

2.74

2.3.2 Analytical Solutions of the Acoustic Diffusion Model

The diffusion model in eq. 2.72 is amenable to closed form solutions for a 1-D problem (Picaut et al., 1997). For a 1-D volume without absorption, eq. 2.72 reduces to

$$\frac{\partial \psi(x,t)}{\partial t} = D \frac{\partial^2 \psi(x,t)}{\partial x^2}$$

2.75

Using separation of variables, the general solution to eq. 2.75 can be derived as

$$\psi(x,t) = \sum_{n=0}^{\infty} \big[A_n \sin(\gamma_n x) + B_n \cos(\gamma_n x) \big] e^{-\gamma_n D t}$$

2.76

28

where A_n, B_n, and γ_n, are constants to be determined from boundary and initial conditions. Consider an initial energy distribution, $\psi_0(x)$, described by

$$\psi_0(x) = \begin{cases} E_0, & 0 \le x \le h \\ 0, & x \ge h \end{cases}$$

2.77

where E_0 is a constant acoustic energy density. Taking into account rigid boundaries at $x = 0$ and $x = L$ and assuming the initial energy is concentrated in a very small space, $h \ll L$, eq. 2.76 becomes

$$\psi(x,t) \approx \frac{E_0 h}{L}\left[1 + 2\sum_{n=1}^{\infty} \cos\left(\frac{n\pi x}{L}\right)\exp\left(-\frac{n^2\pi^2 D}{L^2}t\right)\right].$$

2.78

If $Dt \gg L^2$, only the first term of the infinite sum is important and the solution reduces to

$$\psi(x,t) \approx \frac{E_0 h}{L}\left[1 + 2\cos\left(\frac{\pi x}{L}\right)\exp\left(-\frac{\pi^2 D}{L^2}t\right)\right].$$

2.79

More complex solutions are derived for the same volume with absorption and are expressed as an analytical steady state solution with an infinite sum and a decay solution in terms of the total energy integrated over the volume. For the case of an infinitely long 1-D volume, the diffusion model with absorption has an exact solution (Picaut et al., 1997).

In the diffusion model, the diffusion coefficient, D, is the controlling parameter. Thus, the validity of the proposed diffusion coefficient, D, in eq. 2.73 was evaluated (Picaut et al., 1997). To this end, many different volume configurations were then simulated using the diffusion model, eq. 2.72, and a diffuse-field integral formulation for room acoustics proposed by Kuttruff (1973). The 56 volumes simulated range from dimensions of 70 x 10 x 10 m^3 (with a mean free path of 9.33 m) to 40 x 4 x 4 m^3 (with a mean free path of 3.81 m). An average diffusion coefficient of each volume is estimated from the slope of the decay of sound calculated with Kuttruff's integral method using eq. 2.19 at several receiver positions. The coefficient is plotted against the mean free path of the volume along with the diffusion model coefficient, eq. 2.73, reproduced in Figure 2.7. The percent difference of the Kuttruff integral method diffusion coefficient compared to the average value in the 70 x 10 x 10 m^3 volume is also compared for several receiver locations in the paper and is reproduced in Figure 2.8. These figures show excellent agreement over the entire range of mean free path lengths studied in this paper for long,

skinny volumes. In this long, skinny volume, the diffusion coefficient does not deviate by more than 1 % from its mean value indicating that the constant coefficient derived in the diffusion model is appropriate.
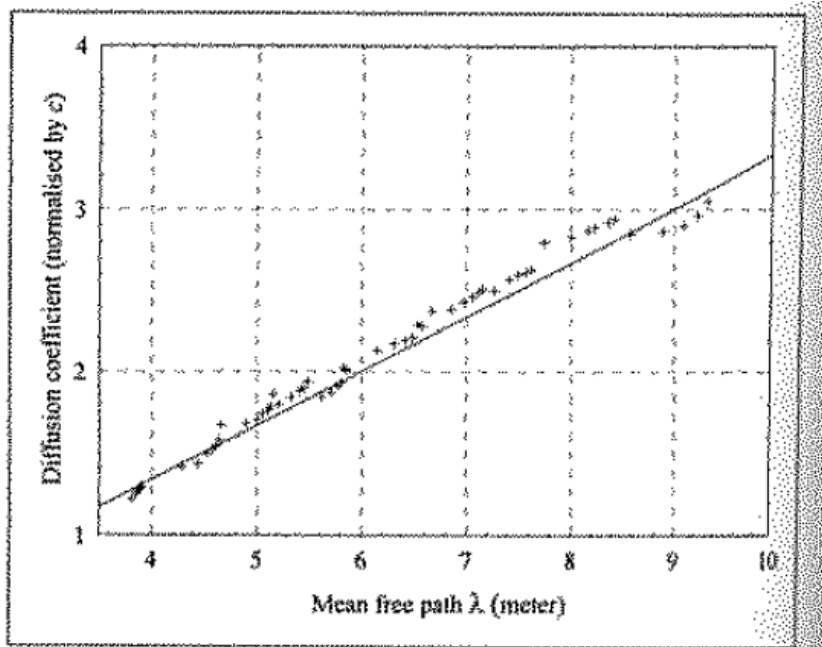
Figure 7. Diffusion coefficients D, normalised by the speed of sound c, versus mean free paths λ of the enclosure. '+', numerical estimation, '———', diffusion model (equation 16). See Table 1 for exact values of D and λ.

Figure 2.7: Average diffusion coefficients from many different volumes calculated with the use of Kuttruff's integral method for room acoustics and compared to the diffusion model's coefficient (Picaut et al., 1997) [fair use].

30
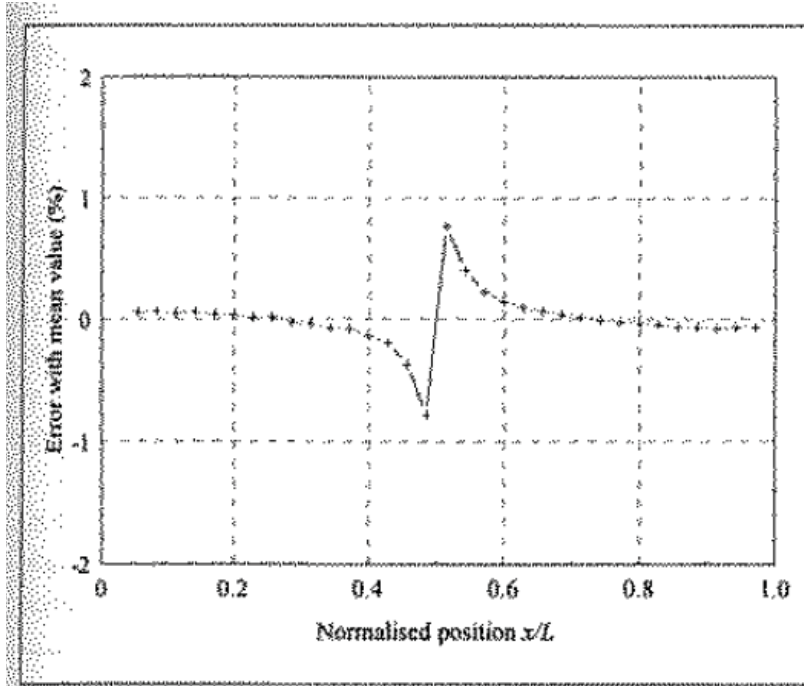
Figure 5. Difference between diffusion coefficients estimated at several locations along the middle line of a rectangular enclosure [70 : 10 : 10], and their mean values. '+', numerical simulation.

Figure 2.8: Variation in the diffusion coefficients from the mean value in the 70 x 10 x 10 m^3 volume calculated with the use of Kuttruff's integral method for room acoustics at several positions in the volume (Picaut et al., 1997) [fair use].

2.3.3 Reduction of the Diffusion Model to Sabine Theory

A brief exercise is presented in this section to show that the acoustic diffusion model has a relationship to the more conventional Sabine theory. Specifically, the acoustic diffusion model can be viewed as a more general form of Sabine theory which is reduced exactly to the Sabine equations using simplifying assumptions. The originally derived form of the diffusion model (Picaut et al., 1997), eq. 2.72, including a constant source of acoustic power, W, at every position in the volume is given by

$$\frac{\partial \psi(\mathbf{r},t)}{\partial t} = D\nabla^2 \psi(\mathbf{r},t) - \sigma\psi(\mathbf{r},t) + \frac{W}{V_v}.$$ 2.80

Using the definition of the attenuation coefficient, σ, and the mean free path, this can be rewritten as

31

$$\frac{\partial \psi(\mathbf{r},t)}{\partial t} = D\nabla^2 \psi(\mathbf{r},t) - \frac{cS_v\overline{\alpha}}{4V_v}\psi(\mathbf{r},t) + \frac{W}{V_v}.$$

<div align="right">2.81</div>

Next, consider the assumption that the acoustic intensity, thus energy density, at every position of the volume must be equal. This assumption eliminates any dependence on position in the volume and the term including the gradient of the energy density. Equation 2.81 becomes

$$\frac{\partial \psi(t)}{\partial t} = -\frac{cS_v\overline{\alpha}}{4V_v}\psi(t) + \frac{W}{V_v}.$$

<div align="right">2.82</div>

Simple algebraic manipulation yields the first order ordinary differential equation from which the Sabine equations are derived:

$$V_v\frac{\partial \psi(t)}{\partial t} = W - \frac{cS_v\overline{\alpha}}{4}\psi(t)$$

<div align="right">2.83</div>

2.3.4 Improvements to the Acoustic Diffusion Model

Subsequent research to improve the acoustic diffusion model and key results are presented in this section. This is presented to review the existing research and demonstrate the current state of the acoustic diffusion model.

One significant limitation of the original formal derivation is that the absorption must be uniform in the whole room. In a following paper, the same authors studied sound field prediction in long rooms including diffusely reflecting boundaries (Picaut et al., 1999b). In addition, they introduced a new parameter allowing the modeling of the distribution of absorption on the walls, the exchange coefficient, h. The exchange coefficient is frequently encountered in heat conduction to define the exchange of heat between the medium of propagation and the medium around. For applications in room acoustics, this coefficient characterizes the flow of energy at the boundaries. Thus, the normal intensity on the wall is expressed as (Picaut et al., 1999b)

$$\mathbf{I}(\mathbf{r},t)\cdot\mathbf{n} = h(\mathbf{r})\psi(\mathbf{r},t), \quad \mathbf{r}\in S.$$

<div align="right">2.84</div>

Using eq. 2.69, eq. 2.84 can be written as

$$-D\frac{\partial \psi(\mathbf{r},t)}{\partial \mathbf{n}} = h(\mathbf{r})\psi(\mathbf{r},t), \quad \mathbf{r}\in S$$

<div align="right">2.85</div>

which is then used as an absorbing boundary condition which can vary for each surface of the room.

The acoustic diffusion equation is then modified by removing the absorption term since the absorption is incorporated at the boundary and is given by (Picaut et al., 1999b)

$$\frac{\partial \psi(\mathbf{r},t)}{\partial t} - D\nabla^2 \psi(\mathbf{r},t) = 0 \qquad\qquad 2.86$$

with the boundary condition

$$D\frac{\partial \psi(\mathbf{r},t)}{\partial \mathbf{n}} + h(\mathbf{r})\psi(\mathbf{r},t) = 0, \quad \mathbf{r} \in S \qquad\qquad 2.87$$

if there is no energy flux in or out of the boundary other than that due to the absorption of the walls.

Next, the exchange coefficient is determined considering an infinitely long, thin 1-D rectangular volume with a $l_y \times l_z$ cross section. The 1-D diffusion equation is given by

$$\frac{\partial \psi(x,t)}{\partial t} - D\frac{\partial^2 \psi(x,t)}{\partial x^2} = 0 \ . \qquad\qquad 2.88$$

Now, the absorption of the walls is taken into account using the boundary condition which is

$$D\frac{\partial \psi(x,t)}{\partial \mathbf{n}} + h(x)\psi(x,t) = 0 \qquad\qquad 2.89$$

in 1-D. The loss of sound energy, dE, due to absorption of the side walls over a time dt in a small section of the volume with width Δx is

$$\frac{dE}{dt} = h(x)\psi(x,t)\Delta S_v = h(x)\psi(x,t)\left[2\left(l_y + l_z\right)\right]\Delta x \ . \qquad\qquad 2.90$$

where ΔS_v is the bounding area of the volume in the small width, Δx. Performing an energy balance in this small volume using the concept of diffusion gives

$$S_c\frac{\partial \psi(x,t)}{\partial t} = S_c D\frac{\partial^2 \psi(x,t)}{\partial x^2} - h(x)\frac{\Delta S_v}{\Delta x}\psi(x,t) \qquad\qquad 2.91$$

where S_c is the cross-sectional area of the volume. Substituting the known geometric parameters gives

$$\frac{\partial \psi(x,t)}{\partial t} = D\frac{\partial^2 \psi(x,t)}{\partial x^2} - h(x)\frac{2\left(l_y + l_z\right)}{l_y l_z}\psi(x,t) \qquad\qquad 2.92$$

Considering the original form of the diffusion model, eq. 2.72,

$$\sigma = h(x)\frac{2(l_y + l_z)}{l_y l_z}.$$

2.93

Substituting the definition of the attenuation coefficient, σ, gives

$$\frac{S_v c \bar{\alpha}(x)}{4V_v} = h(x)\frac{2(l_y + l_z)}{l_y l_z}.$$

2.94

If it is assumed that the room is very long, i.e. $l_x \ \Box \ l_y, l_z$, then $S_v / V_v \approx 2(l_y + l_z)/(l_y l_z)$ and the previous equation reduces to

$$h(x) \approx \frac{c\alpha(x)}{4}.$$

2.95

Several 1-D solutions were derived and compared to other theories and experimental data. For example, the analytical solution to a steady state problem in a 1-D finite long room is compared to experimental data measured in a 20.3 x 2.23 x 3.36 m^3 corridor excited at one end by a gun shot. Schroeder's method (1965) is employed to calculate steady state levels which are compared to the steady 1-D diffusion equation solution as reproduced in Figure 2.9 (Picaut et al., 1999). The reverberation times calculated from a transient 1-D analytical diffusion solution are also compared to measured data in Figure 2.9 (Picaut et al., 1999). Very good agreement is demonstrated in each case.

(a)
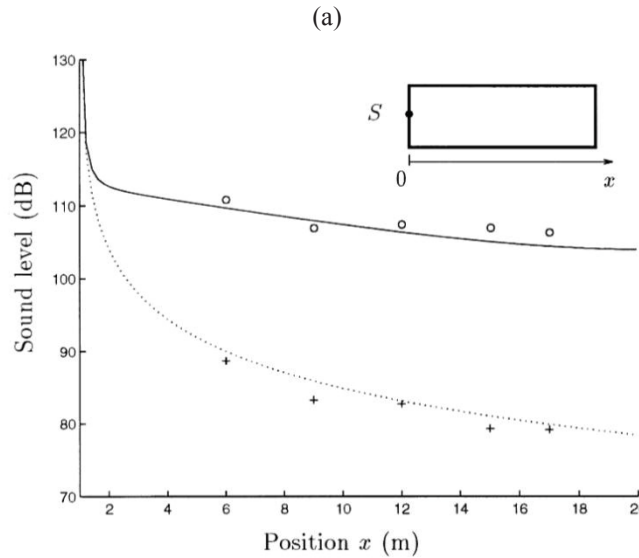
Fig. 12. Sound attenuation in a long room 20.3×2.23×3.36 m with a steady source at $x_0 = 1$ m:'o' measurements, '–' finite model by Eq. (35). Direct field: '+' measurements, '...' $1/r^2$ approximation.

(b)
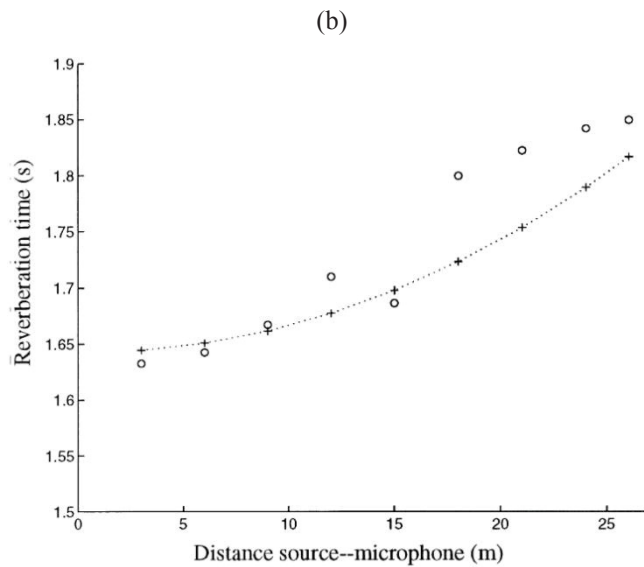
Fig. 15. Comparison between 'o' measured and '+' predicted reverberation times, at several locations along the corridor.

Figure 2.9: Experimental validation of the (a) steady and (b) transient response of a long corridor computed using the diffusion model (Picaut et al., 1999) [fair use].

Billon et al. (2008b) and Jing and Xiang (2007) noticed that because the diffusion model reduces to the Sabine equation when the appropriate assumptions are made, eq. 2.95 is only valid for low absorption coefficients. In highly absorbent rooms, the Sabine absorption coefficient, $\bar{\alpha}$,

is replaced by $\bar{\alpha} = \ln(1-\alpha)$ in what is known as Eyring theory (Bies and Hansen, 2003). Making this adjustment in eq. 2.95 gives an alternate exchange coefficient (Billon et al., 2008b; Jing and Xiang, 2007):

$$h(\mathbf{r}) = \frac{c \ln\left[1-\alpha(\mathbf{r})\right]}{4}$$ 2.96

which is shown to possess significantly more accuracy for rooms with absorption higher than about 0.1. Jing and Xiang (2008) proposed another modification which eliminates the singularity in the Eyring absorption coefficient which provides even greater accuracy

$$h(\mathbf{r}) = \frac{c}{4} \frac{\alpha(\mathbf{r})}{2\left[2-\alpha(\mathbf{r})\right]}.$$ 2.97

in the experiments they conducted in a small 1 x 1 x 0.2 m^3 box. The box had surface absorption varying from 0.05 (wood) on some surfaces to 0.96 (acoustic foam) on others. The steady state and transient results obtained using a commercial FEM solver are shown for the three different exchange coefficients in Figure 2.10 for the 2 kHz octave band (results scaled up by a factor of 8:1). The modified and the Eyring exchange coefficients tend to exhibit less error than the Sabine coefficient.
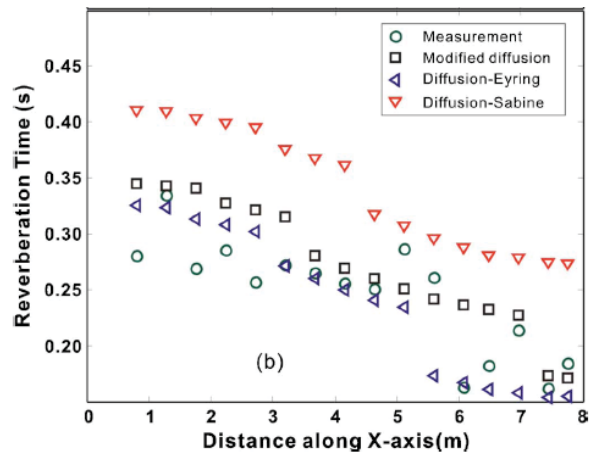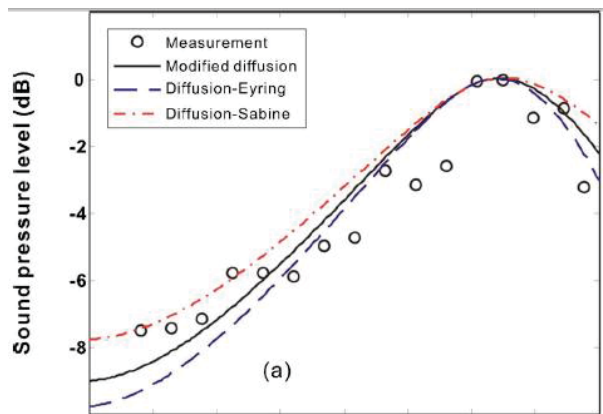
FIG. 9. (Color online). Comparison of three different diffusion models and experimental results in a scale-model flat room in the 2 kHz octave band along a line at y=0.64 m (full scale). (a) Sound pressure level distributions. (b) Reverberation times.

Figure 2.10: Experimental comparison of the three different exchange coefficients in the 2 kHz octave band (Jing and Xiang, 2008) [fair use].

Valeau et al. (2006) focused on the definition of the source term and boundary conditions in the acoustic diffusion equations. These equations are either

$$\frac{\partial \psi(\mathbf{r},t)}{\partial t} - D\nabla^2 \psi(\mathbf{r},t) + \sigma \psi(\mathbf{r},t) = f(\mathbf{r},t) \qquad \text{2.98}$$

for constant room absorption with source term, $f(\mathbf{r},t)$, or

$$\frac{\partial \psi(\mathbf{r},t)}{\partial t} - D\nabla^2 \psi(\mathbf{r},t) = f(\mathbf{r},t) \qquad \text{2.99}$$

for varying absorption in the room each with their corresponding boundary conditions discussed previously.

The source is defined in three ways, as a point source, a volume source, or a surface source. The volume source is defined on the assumption that a point source emitting some number of acoustic particles per second in the classical particle diffusion problem is comparable to an acoustic source of power, $W(t)$. Thus, the source term can be modeled as a point source with

$$f(\mathbf{r},t) = W(t)\delta(\mathbf{r} - \mathbf{r}_s) \qquad \text{2.100}$$

where $\mathbf{r}_s$ is the source position. If the source is defined in a sub-domain, V_s, of volume v, the source term becomes

$$f(\mathbf{r},t) = \begin{cases} \dfrac{W(t)}{v}, & \mathbf{r} \in V_s \\ 0, & \mathbf{r} \notin V_s \end{cases} . \qquad \text{2.101}$$

As for the surface source of power, $W(t)$, and surface area, s_s, it can be expressed by modifying the boundary condition, equation 2.85:

$$D\frac{\partial \psi(\mathbf{r},t)}{\partial \mathbf{n}} + h(\mathbf{r})\psi(\mathbf{r},t) = \begin{cases} \dfrac{W(t)}{s_s}, & \mathbf{r} \in S_s \\ 0, & \mathbf{r} \notin S_s \end{cases} . \qquad \text{2.102}$$

where S_s refers to the domain of the surface source.

To account for the direct field of a source in a steady state problem, Valeau et al. (2006) propose a simple correction as

$$L_p(\mathbf{r}) = 10\log\left\{\rho c\left[\frac{\bar{W}}{4\pi|\mathbf{r}-\mathbf{r}_s|^2} + c\bar{\psi}(\mathbf{r})\right]\Big/ p_{ref}^2\right\}$$
2.103

where $\bar{W}$ is the steady state power of the source and $\bar{\psi}(\mathbf{r})$ is the steady state energy density. The addition of the direct field radiated by a monopole source is included in all results presented in this dissertation.

An additional important point was introduced along with this study. The authors stated that the frequency dependence of the diffusion equation is accomplished through the absorption coefficient, α. Therefore, the diffusion equation with appropriate boundary conditions must be solved multiple times to obtain results for multiple frequency bands.

Some of the most recent developments in room acoustics concern the application of the diffusion theory to coupled rooms. In 2006, Billon et al. proposed a diffusion equation model to predict the sound field inside two rooms coupled through an aperture in steady and transient conditions. The model used was the diffusion equation discussed previously applied to three separate sub-volumes: V_s the source room subtracting the volume occupied by the physical source with bounding surface S_s, V_r the receiving room with bounding surface S_r, and V_{ss} the volume occupied by the acoustic source. The mean free path of each room, λ_s and λ_r, are calculated separately replacing the aperture with a surface. This physical interpretation of this approximation is that the aperture area is small with respect to the room surfaces for each room so that the mean free path is unaffected by the open aperture. The proposed coupled diffusion model is

$$\begin{aligned}
\frac{\partial\psi(\mathbf{r},t)}{\partial t} - D_s\nabla^2\psi(\mathbf{r},t) &= 0, \quad \mathbf{r}\in V_s \\
\frac{\partial\psi(\mathbf{r},t)}{\partial t} - D_s\nabla^2\psi(\mathbf{r},t) &= 0, \quad \mathbf{r}\in V_{ss} \\
\frac{\partial\psi(\mathbf{r},t)}{\partial t} - D_r\nabla^2\psi(\mathbf{r},t) &= 0, \quad \mathbf{r}\in V_r
\end{aligned}$$
2.104

with boundary conditions,

$$D_s \frac{\partial \psi(\mathbf{r},t)}{\partial \mathbf{n}} + h_s \psi(\mathbf{r},t) = 0, \quad \mathbf{r} \in S_s$$
$$D_r \frac{\partial \psi(\mathbf{r},t)}{\partial \mathbf{n}} + h_r \psi(\mathbf{r},t) = 0, \quad \mathbf{r} \in S_r$$

2.105

and initial conditions,

$$\psi(\mathbf{r},0) = 0, \quad \mathbf{r} \in V_s \cup V_r$$
$$\psi(\mathbf{r},0) = \psi_0, \quad \mathbf{r} \in V_{ss}$$

2.106

where D_s and D_r are the diffusion coefficients calculated with their respective mean free paths. The coupling is very primitive as the separate volumes are basically combined into one volume which still incorporates the absorption by the coupling surface, but energy is free to travel across it. Still, very reasonable results were obtained comparing the FEM solution to the diffusion model with experiments in two classrooms coupled through an open door which are reproduced for the 4 kHz octave band in Figure 2.11 (Billon et al., 2006).
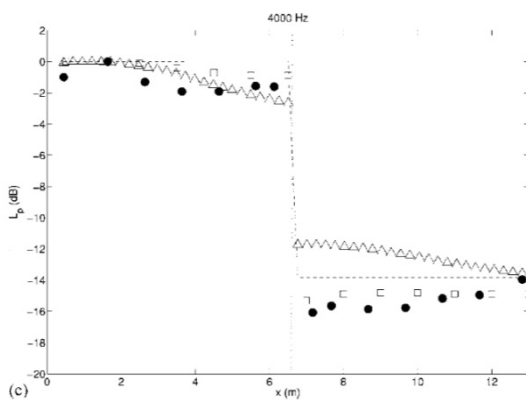
FIG. 8. Sound attenuation along the line C2 for configuration S2 (with direct field): (a) 250 Hz, (b) 1000 Hz; (c) 4000 Hz. (•) Experimental data; (△) diffusion model; (- - -) statistical theory; (□) ray-based model.
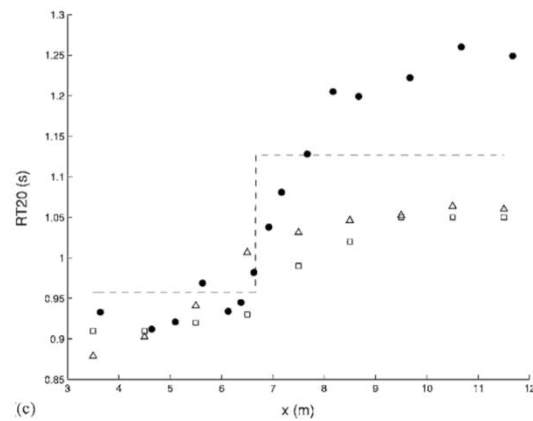
FIG. 11. Variation of the reverberation time (RT20) through the coupling aperture, for configuration S2 at (a) 250 Hz; (b) 1000 Hz; and (c) 4000 Hz. (•) Experimental data; (△) diffusion model; (□) ray-based model; (- - -) statistical theory.

Figure 2.11: Experimental validation of steady state and transient response of two classrooms coupled through an open door along a line passing through the coupling wall in the 4 kHz octave band (Billon et al., 2006) [fair use].

The same authors (Billon et al., 2008b) proposed a more sophisticated model for the steady diffusion in two rooms coupled through a partition wall. In this formulation, the geometry is defined by two room volumes, V_1 and V_2, their bounding surfaces without the partition surface, S_1 and S_2, and the partition surface, S_{12}, with the source being located in room 1. A steady state

diffusion model is proposed where the diffusion equations are solved for each room volume with mixed-type boundary conditions on the room surfaces and a separate boundary condition based on the transmission loss of the partition on each side of the partition surface. The steady state diffusion equations are

$$-D_1 \nabla^2 \bar{\psi}_1 (\mathbf{r}) = f(\mathbf{r}), \quad \mathbf{r} \in V_1$$
$$-D_2 \nabla^2 \bar{\psi}_2 (\mathbf{r}) = 0, \qquad \mathbf{r} \in V_2$$

2.107

where D_1 and D_2 are the diffusion coefficients of each room, and $\bar{\psi}_1$ and $\bar{\psi}_2$ are the energy densities in each room. The boundary conditions on the room bounding surfaces are

$$D_1 \frac{\partial \bar{\psi}_1 (\mathbf{r})}{\partial \mathbf{n}_1} + h_1 \bar{\psi}_1 (\mathbf{r}) = 0, \qquad \mathbf{r} \in S_1$$
$$D_2 \frac{\partial \bar{\psi}_2 (\mathbf{r})}{\partial \mathbf{n}_2} + h_2 \bar{\psi}_2 (\mathbf{r}) = 0, \qquad \mathbf{r} \in S_2$$

2.108

where h_1 and h_2 are the exchange coefficients of the room surfaces. The boundary condition on the room 1 side of the partition surface is

$$D_1 \frac{\partial \bar{\psi}_1 (\mathbf{r})}{\partial \mathbf{n}_1} + h_{12} \bar{\psi}_1 (\mathbf{r}) = \frac{\tau c}{4} \bar{\psi}_2 (\mathbf{r}), \quad \mathbf{r} \in S_{12}$$

2.109

and

$$D_2 \frac{\partial \bar{\psi}_2 (\mathbf{r})}{\partial \mathbf{n}_2} + h_{12} \bar{\psi}_2 (\mathbf{r}) = \frac{\tau c}{4} \bar{\psi}_1 (\mathbf{r}), \quad \mathbf{r} \in S_{12}$$

2.110

on the room 2 side where is the h_{12} exchange coefficient of the partition surface and τ is the transmission coefficient. In order to solve this model, the transmission coefficient of the coupling partition must be known. This model was shown to agree with experimental data taken in terms of the average SPL in two coupled classrooms in an average sense from 125 to 8000 Hz. Both of these diffusion equation models proposed by Billon et al. (2006; 2008b) can be easily generalized to complex geometry and systems of any number of coupled rooms.

A modification of the diffusion equation was proposed by Billon et al. (2008a) to account for atmospheric attenuation in very large rooms and/or at high frequencies. The modified diffusion equation is

$$\frac{\partial \psi(\mathbf{r},t)}{\partial t} - D'\nabla^2\psi(\mathbf{r},t) + mc\psi(\mathbf{r},t) = f(\mathbf{r},t) \qquad \text{2.111}$$

where m is the coefficient of atmospheric attenuation and the modified diffusion coefficient, D', is given by

$$D' = D\frac{1}{1+m\lambda}. \qquad \text{2.112}$$

Subsequently, a modification was proposed to account for scattering objects in a volume without explicitly modeling them (Billon et al., 2012). A mean free path, λ_o, defined by the average distance an acoustic ray must travel before encountering one of the scattering objects is given by

$$\lambda_o = \frac{1}{n_o S_o} \qquad \text{2.113}$$

where n_o is the number of scattering objects per unit volume and S_o is the average *cross-sectional* area, as opposed to surface area, of the scattering objects. The modified diffusion coefficient accounting for these objects, D_o, is given by

$$D_o = \frac{c\lambda\lambda_o}{3(\lambda+\lambda_o)} = \frac{DD_o}{D+D_o}. \qquad \text{2.114}$$

where the variables without subscripts refer to the parameters in the empty volume.

2.4　Summary

Several methods were reviewed including the newer methods, radiosity and the acoustic diffusion model, which attempt to overcome the deficiencies of the more conventional techniques. The key difference in the way radiosity relates intensity and energy density to how they are related in the diffusion model was noted. While the radiosity method is based on the direct proportionality of intensity and acoustic energy density, the acoustic diffusion model uses the proportionality of intensity to the gradient of energy density.

Significant detail behind the acoustic diffusion model, the foundation of this research, was presented including its formal derivation, relationship to Sabine theory, and the current state of acoustic diffusion research. The simple, 1-D analytical solutions and the 3-D solutions using

only the FEM and FD technique and limited investigation into structural coupling are noted deficiencies in the current state of diffusion research. The rest of this dissertation focuses on improving the solution technique and structural coupling of the acoustic diffusion model, new areas of research. The next chapter discusses a new BEM solution to the acoustic diffusion model using an efficient Laplace transform and inversion approach.

Chapter 3: Boundary Element-Laplace Transform Solution to the Acoustic Diffusion Model

In this chapter, a new efficient method to solve the acoustic diffusion model is developed. The solution is based on the BEM and makes use of the Laplace transform and an efficient numerical inversion method. The boundary element-Laplace transform solution method (BE-LTS) is described schematically in Figure 3.1.

3.1 Overview of the Proposed BE-LTS

First, the Laplace transform of the acoustic diffusion model is derived. This equation describes the diffusion of acoustic energy in a volume in the Laplace domain. Then, the BEM is applied to calculate the acoustic energy by solving a linear system of equations at the nodes on the boundary of the volume. The boundary energy at these nodes is then used to consecutively compute the acoustic energy at points of interest in the volume.

Both boundary energy and the energy in the volume are computed for the steady state case and at several discrete, real values of the Laplace variable. This is performed once per frequency band of interest as some of the parameters of the diffusion model can be considered functions of frequency. These include absorption coefficients, transmission coefficients, atmospheric attenuation coefficients, and possibly source and initial conditions.

Thus, (*Number of Frequency Bands)* x (1 *Steady State + Number of Discrete Laplace Variables*) full BE solutions are required to obtain the transient energy density. Therefore, the computational efficiency can be greatly improved by decreasing the number of Laplace variables necessary. This is further discussed in Chapter 4 which discusses the selection of a numerical inverse Laplace transform method to calculate the time domain response from the Laplace domain. If only the steady state response is of interest, one BE solution is necessary per frequency band and the procedures discussed in Chapter 4 are unnecessary.

Chapter 2: Acoustic Diffusion

Steady State Diffusion

$$-D\nabla^2\overline{\psi}(\mathbf{r})+mc\overline{\psi}(\mathbf{r})=\tilde{f}(\mathbf{r})$$

Transient Diffusion

$$\frac{\partial\psi(\mathbf{r},t)}{\partial t}-D\nabla^2\psi(\mathbf{r},t)+mc\psi(\mathbf{r},t)=f(\mathbf{r},t)$$

Path to steady state solution

Path to transient solution

Source

Receiver

Laplace Transform

$$(s+mc)\Psi(\mathbf{r},s)-\psi(\mathbf{r},0)-D\nabla^2\Psi(\mathbf{r},s)=F(\mathbf{r},s)$$

Chapter 3: Boundary Element/Laplace Transform Solution

Solve for Boundary Energy

Discrete Laplace Values

$$[\mathbf{A}]\overline{\psi}=\mathbf{B}$$

$$\left[\mathbf{A}(s_q)\right]\Psi(s_q)=\mathbf{B}(s_q)$$

Frequency Bands

$\Delta f_3:$ $\Delta f_2:$ $\Delta f_1:$

...

Solve for Energy in Volume

$$\overline{\psi}(\mathbf{r}')=B(\mathbf{r}')-\mathbf{C}(\mathbf{r}')^T\overline{\psi}$$

$$\Psi(\mathbf{r}',s_q)=B(\mathbf{r}',s_q)-\mathbf{C}(\mathbf{r}',s_q)^T\Psi(s_q)$$

Steady State Solution

...

Chapter 4: Numerical Inverse Laplace Transform

Transient Solution

$\Delta f_3:$

$\Delta f_2:$

$\Delta f_1:$ $\psi(\mathbf{r}',t)$

$\overline{\psi}(\mathbf{r}')$

t

Figure 3.1: Schematic of the boundary element-Laplace transform solution (BE-LTS) of the acoustic diffusion model.

44

3.2 Boundary Integral Equation Derivation

The development of the boundary integral equation begins with the room acoustic diffusion equation including atmospheric attenuation (Billon et al., 2008a),

$$\frac{\partial \psi(\mathbf{r},t)}{\partial t} - D\nabla^2 \psi(\mathbf{r},t) + mc\psi(\mathbf{r},t) = f(\mathbf{r},t), \qquad 3.1$$

where $\psi(\mathbf{r},t)$ is the energy density at any point, $\mathbf{r}$, in the room at time, t; D is the acoustic diffusion coefficient given by $D = \frac{\lambda c}{3} \frac{1}{1+m\lambda}$ with $\lambda = \frac{4V_v}{S_v}$ being the mean free path length of the room of volume, V_v, and total surface area, S_v; c is the speed of sound in air; ∇^2 is the Laplacian operator; m is the atmospheric attenuation coefficient; $f(\mathbf{r},t)$ is the acoustic source power per unit volume that the source occupies (Valeau et al., 2007).

The boundary condition at the bounding surfaces of the volume, S, is given by

$$D\frac{\partial \psi(\mathbf{r},t)}{\partial \mathbf{n}} + h(\mathbf{r})\psi(\mathbf{r},t) = 0, \quad \mathbf{r} \in S \qquad 3.2$$

where $h(\mathbf{r}) = \frac{c}{4}\frac{\alpha(\mathbf{r})}{2[2-\alpha(\mathbf{r})]}$ is the exchange coefficient on the bounding surface (Jing and Xiang, 2008), $\alpha(\mathbf{r})$ is the acoustic absorption coefficient of the surface, and $\mathbf{n}$ is the unit normal vector to the surface S which is defined to be positive outward to V. The arbitrary initial acoustic energy density distribution at time zero is denoted with $\psi(\mathbf{r},0)$. A schematic showing the room volume features with the notation used is given in Figure 3.2. Note that the schematic has been drawn with rectangular geometry for clarity, but the geometry in the theoretical formulation is arbitrary.
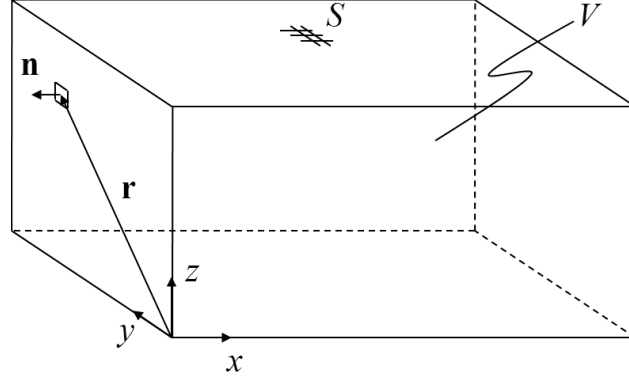
Figure 3.2: Schematic showing room volume features using the notation in the theoretical formulation.

The next step towards developing a solution to the partial differential equation is taking the Laplace transform of eq. 3.1. Other methods exist to solve this problem such as direct numerical integration techniques, for example modeling using finite elements or finite differences. In both cases, the complete domain must be discretized and the problem must be integrated multiple times since the system parameters are a function of frequency. However, the Laplace transform method used in this paper will be seen to be a very efficient technique for solving the energy density distribution in the room rather than direct integration in the time domain. The Laplace transform of eq. 3.1 is

$$(s+mc)\Psi(\mathbf{r},s)-\psi(\mathbf{r},0)-D\nabla^{2}\Psi(\mathbf{r},s)=F(\mathbf{r},s) \tag{3.3}$$

where s is the complex Laplace domain variable, $\Psi(\mathbf{r},s)=\mathcal{L}[\psi(\mathbf{r},t)]$ is the Laplace domain acoustic energy density, and $F(\mathbf{r},s)=\mathcal{L}[f(\mathbf{r},t)]$ is the supplied acoustic power per unit volume of the source in the Laplace domain, and $\mathcal{L}[\ ]$ denotes the Laplace transform. Rearranging, eq. 3.3 becomes

$$\nabla^{2}\Psi(\mathbf{r},s)=\frac{1}{D}\Big[(s+mc)\Psi(\mathbf{r},s)-\psi(\mathbf{r},0)-F(\mathbf{r},s)\Big]. \tag{3.4}$$

Similarly, the Laplace transform of the boundary condition, eq. 3.2, is

$$\frac{\partial\Psi(\mathbf{r},s)}{\partial\mathbf{n}}=-\frac{h(\mathbf{r})}{D}\Psi(\mathbf{r},s),\quad \mathbf{r}\in S. \tag{3.5}$$

To formulate the boundary integral equation, the acoustic diffusion equation must be formulated in terms of its Green's function, $G(\mathbf{r}|\mathbf{r}',s)$, which must be found for an infinite

spatial domain or free field. The Green's function of the acoustic diffusion equation is the solution to the differential equation obtained by setting the supplied acoustic power density to a Dirac delta function, δ. This differential equation in the time domain is given by

$$\frac{1}{D}\frac{\partial g(\mathbf{r}|\mathbf{r}',t)}{\partial t} - \nabla^2 g(\mathbf{r}|\mathbf{r}',t) + \frac{mc}{D} g(\mathbf{r}|\mathbf{r}',t) = \delta(\mathbf{r}-\mathbf{r}')\delta(t) \qquad 3.6$$

where $g(\mathbf{r}|\mathbf{r}',t)$ is the time domain Green's function with the initial condition for eq. 3.6 as $g(\mathbf{r}|\mathbf{r}',0) = 0$.

Taking the Laplace transform of eq. 3.6 and using the initial condition gives

$$\frac{s+mc}{D} G(\mathbf{r}|\mathbf{r}',s) - \nabla^2 G(\mathbf{r}|\mathbf{r}',s) = \delta(\mathbf{r}-\mathbf{r}'). \qquad 3.7$$

Rearranging eq. 3.7 yields

$$\nabla^2 G(\mathbf{r}|\mathbf{r}',s) = \frac{s+mc}{D} G(\mathbf{r}|\mathbf{r}',s) - \delta(\mathbf{r}-\mathbf{r}'). \qquad 3.8$$

The 3-D Green's Function which satisfies eq. 3.8 is given by (Butkovskiy, 1982)

$$G(\mathbf{r}|\mathbf{r}',s) = \frac{1}{4\pi|\mathbf{r}-\mathbf{r}'|} e^{-\sqrt{\frac{s+mc}{D}}|\mathbf{r}-\mathbf{r}'|}. \qquad 3.9$$

Note that the atmospheric attenuation constant, m, is thus accounted for automatically in the Green's function of the model. This is another advantage of the current method over other direct numerical solutions. In the FEM or FD technique, an extra term, $mc\psi(\mathbf{r},t)$, is added to the differential equation which must be evaluated, eq. 3.1, increasing computation time. This disadvantage is compounded by the fact that the constant is typically a function of frequency. In the BE-LTS of the diffusion model, the attenuation is simply inherent in the Green's function without any extra integration required.

Starting with the chain rule for differentiation, the Green's function normal derivative can be written as

$$\frac{\partial G(\mathbf{r}|\mathbf{r}',s)}{\partial \mathbf{n}} = \frac{\partial G(\mathbf{r}|\mathbf{r}',s)}{\partial(\mathbf{r}-\mathbf{r}')}\frac{\partial(\mathbf{r}-\mathbf{r}')}{\partial \mathbf{n}}. \qquad 3.10$$

Carrying out the derivative of the Green's function with respect to the position vector gives

$$\frac{\partial G(\mathbf{r}\,|\,\mathbf{r}',s)}{\partial(\mathbf{r}-\mathbf{r}')} = -\frac{1}{4\pi|\mathbf{r}-\mathbf{r}'|}e^{-\sqrt{\frac{s+mc}{D}}|\mathbf{r}-\mathbf{r}'|}\left[\sqrt{\frac{s+mc}{D}}+\frac{1}{|\mathbf{r}-\mathbf{r}'|}\right].$$

3.11

The directional derivative of the position vector in the normal direction is then found to be

$$\frac{\partial(\mathbf{r}-\mathbf{r}')}{\partial\mathbf{n}} = \frac{(\mathbf{r}-\mathbf{r}')\cdot\mathbf{n}}{|\mathbf{r}-\mathbf{r}'|}.$$

3.12

Substituting eqs. 3.11 and 3.12 into eq. 3.10 gives the Green's function derivative sought as

$$\frac{\partial G(\mathbf{r}\,|\,\mathbf{r}',s)}{\partial\mathbf{n}} = -\frac{1}{4\pi|\mathbf{r}-\mathbf{r}'|}e^{-\sqrt{\frac{s+mc}{D}}|\mathbf{r}-\mathbf{r}'|}\left[\sqrt{\frac{s+mc}{D}}+\frac{1}{|\mathbf{r}-\mathbf{r}'|}\right]\frac{(\mathbf{r}-\mathbf{r}')\cdot\mathbf{n}}{|\mathbf{r}-\mathbf{r}'|}$$

3.13

which is required later in the formulation.

Next, applying the Green's Second Identity to the functions $\Psi(\mathbf{r},s)$ and $G(\mathbf{r}\,|\,\mathbf{r}',s)$ gives (Stewart, 2003)

$$\int_{V'}\left[G(\mathbf{r}\,|\,\mathbf{r}',s)\nabla^2\Psi(\mathbf{r},s)-\Psi(\mathbf{r},s)\nabla^2 G(\mathbf{r}\,|\,\mathbf{r}',s)\right]dV =$$
$$\int_{S'}\left[G(\mathbf{r}\,|\,\mathbf{r}',s)\frac{\partial\Psi(\mathbf{r},s)}{\partial\mathbf{n}}-\Psi(\mathbf{r},s)\frac{\partial G(\mathbf{r}\,|\,\mathbf{r}',s)}{\partial\mathbf{n}}\right]dS$$

3.14

where $\int_{V'}[\ ]dV$ and $\int_{S'}[\ ]dS$ represent integration over the room volume, V, and the bounding surface, S, respectively, with respect to the unprimed spatial variable, $\mathbf{r}$. Substitution of eqs. 3.4 and 3.8 into eq. 3.14 gives

$$\frac{1}{D}\int_{V'}\left[D\Psi(\mathbf{r},s)\delta(\mathbf{r}-\mathbf{r}')-G(\mathbf{r}\,|\,\mathbf{r}',s)\psi(\mathbf{r},0)-G(\mathbf{r}\,|\,\mathbf{r}',s)F(\mathbf{r},s)\right]dV =$$
$$\int_{S'}\left[G(\mathbf{r}\,|\,\mathbf{r}',s)\frac{\partial\Psi(\mathbf{r},s)}{\partial\mathbf{n}}-\Psi(\mathbf{r},s)\frac{\partial G(\mathbf{r}\,|\,\mathbf{r}',s)}{\partial\mathbf{n}}\right]dS$$

3.15

Carrying out the volume integration of the term with the delta function and rearranging gives

$$\beta\Psi(\mathbf{r}',s) = \frac{1}{D}\int_{V'}G(\mathbf{r}\,|\,\mathbf{r}',s)\psi(\mathbf{r},0)dV + \frac{1}{D}\int_{V'}G(\mathbf{r}\,|\,\mathbf{r}',s)F(\mathbf{r},s)dV +$$
$$\int_{S'}\left[G(\mathbf{r}\,|\,\mathbf{r}',s)\frac{\partial\Psi(\mathbf{r},s)}{\partial\mathbf{n}}-\Psi(\mathbf{r},s)\frac{\partial G(\mathbf{r}\,|\,\mathbf{r}',s)}{\partial\mathbf{n}}\right]dS$$

3.16

where β is computed using the property of the Dirac delta function (Lighthill, 1958),

$$\int_V \Psi(\mathbf{r},s)\delta(\mathbf{r}-\mathbf{r}')dV = \begin{cases} \Psi(\mathbf{r}',s), & \mathbf{r}' \in V \\ \Psi(\mathbf{r}',s)/2, & \mathbf{r}' \in S \\ 0, & \mathbf{r}' \notin V, S \end{cases}. \tag{3.17}$$

Substituting the boundary condition, eq. 3.5, into eq. 3.16 gives

$$\beta\Psi(\mathbf{r}',s) = \frac{1}{D}\int_{V'} G(\mathbf{r}|\mathbf{r}',s)\psi(\mathbf{r},0)dV + \frac{1}{D}\int_{V'} G(\mathbf{r}|\mathbf{r}',s)F(\mathbf{r},s)dV -$$
$$\int_{S'}\Psi(\mathbf{r},s)\left[\frac{h(\mathbf{r})}{D}G(\mathbf{r}|\mathbf{r}',s) + \frac{\partial G(\mathbf{r}|\mathbf{r}',s)}{\partial \mathbf{n}}\right]dS . \tag{3.18}$$

Equation 3.18 is the most general integral equation form of the acoustic diffusion equation in the Laplace domain with the boundary condition given by eq. 3.5. Examining this equation, it can be seen that the acoustic energy density at any point in the domain, which includes the volume and its bounding surface, is equal to a sum of three integrals. The first volume integral accounts for the effect of the initial energy distribution in the domain. A practical case in which this information would be known is when the acoustic source is allowed to input power into the room until the steady state energy density distribution is reached. Then the source is turned off and the energy in the room is allowed to decay as would be the case of measurement of room reverberation time, T_{60} (Bies and Hansen, 2003).

The second volume integral represents the acoustic energy density due to the arbitrary supplied acoustic power per volume of the source. Although it is integrated over the volume, the source will rarely encompass the entire room volume. Most often the bounds of this integral will reduce to a sub volume, V_s, such as a point, a surface, or a smaller volume. The last integral represents the diffusion of the acoustic energy density accounting for the shape of the volume which is obtained by integrating only over the bounding surface of the domain.

To determine the steady state form of the boundary integral equation, the Final Value Theorem (FVT) is used. To this end, eq. 3.18 is multiplied by s and the limit is taken as $s \to 0$ giving

$$\lim_{s\to 0}\left[\beta s\Psi(\mathbf{r}',s)\right]=\lim_{s\to 0}\left[\frac{s}{D}\int_{V'}G(\mathbf{r}\,|\,\mathbf{r}',s)\psi(\mathbf{r},0)dV\right]+\lim_{s\to 0}\left[\frac{s}{D}\int_{V_s'}G(\mathbf{r}\,|\,\mathbf{r}',s)F(\mathbf{r},s)dV_s\right]$$
$$-\lim_{s\to 0}\left\{\int_{S'}s\Psi(\mathbf{r},s)\left[\frac{h(\mathbf{r})}{D}G(\mathbf{r}\,|\,\mathbf{r}',s)+\frac{\partial G(\mathbf{r}\,|\,\mathbf{r}',s)}{\partial \mathbf{n}}\right]dS\right\}$$

3.19

The FVT states that

$$\lim_{t\to\infty}u(t)=\lim_{s\to 0}\left[sU(s)\right]$$

3.20

where $u(t)$ is any function of time and $U(s)$ is its Laplace transform as long as both limits exist. Rearranging terms and using some properties of limits in eq. 3.19 gives

$$\beta\lim_{s\to 0}\left[s\Psi(\mathbf{r}',s)\right]=\frac{1}{D}\lim_{s\to 0}\left[s\int_{V'}G(\mathbf{r}\,|\,\mathbf{r}',s)\psi(\mathbf{r},0)dV\right]+\frac{1}{D}\int_{V_s'}\lim_{s\to 0}G(\mathbf{r}\,|\,\mathbf{r}',s)\lim_{s\to 0}\left[sF(\mathbf{r},s)\right]dV_s$$
$$-\int_{S'}\lim_{s\to 0}\left[s\Psi(\mathbf{r},s)\right]\left[\frac{c\alpha(\mathbf{r})}{4D}\lim_{s\to 0}G(\mathbf{r}\,|\,\mathbf{r}',s)+\lim_{s\to 0}\frac{\partial G(\mathbf{r}\,|\,\mathbf{r}',s)}{\partial \mathbf{n}}\right]dS.$$

3.21

Now, let

$$\bar{\psi}(\mathbf{r})=\lim_{t\to\infty}\psi(\mathbf{r},t)=\lim_{s\to 0}\left[s\Psi(\mathbf{r},s)\right]$$

3.22

and

$$\bar{f}(\mathbf{r})=\lim_{t\to\infty}f(\mathbf{r},t)=\lim_{s\to 0}\left[sF(\mathbf{r},s)\right]$$

3.23

where the overbar denotes a steady state quantity. Substituting eqs. 3.22 and 3.23 into eq. 3.21 yields

$$\beta\bar{\psi}(\mathbf{r}')=\frac{1}{D}\lim_{s\to 0}\left[s\int_{V'}G(\mathbf{r}\,|\,\mathbf{r}',s)\psi(\mathbf{r},0)dV\right]+\frac{1}{D}\int_{V_s'}\lim_{s\to 0}\left[G(\mathbf{r}\,|\,\mathbf{r}',s)\right]\bar{f}(\mathbf{r})dV_s$$
$$-\int_{S'}\bar{\psi}(\mathbf{r})\left[\frac{h(\mathbf{r})}{D}\lim_{s\to 0}G(\mathbf{r}\,|\,\mathbf{r}',s)+\lim_{s\to 0}\frac{\partial G(\mathbf{r}\,|\,\mathbf{r}',s)}{\partial \mathbf{n}}\right]dS.$$

3.24

Now, the steady state integral equation is obtained through simple evaluation of the remaining limits as

$$\beta\bar{\psi}(\mathbf{r}')=\frac{1}{D}\int_{V_s'}G(\mathbf{r}\,|\,\mathbf{r}',0)\bar{f}(\mathbf{r})dV_s-\int_{S'}\bar{\psi}(\mathbf{r})\left[\frac{h(\mathbf{r})}{D}G(\mathbf{r}\,|\,\mathbf{r}',0)+\frac{\partial G(\mathbf{r}\,|\,\mathbf{r}',0)}{\partial \mathbf{n}}\right]dS.$$

3.25

Comparing the steady state integral equation, eq. 3.25, to the Laplace domain integral equation, eq. 3.18, it can be seen that the application of the FVT causes several differences. First, the integration of the initial energy density distribution over the volume disappears, which makes physical sense as the steady state solution will not be affected by the initial state in the room. Second, the Green's functions are all evaluated at $s = 0$ due to the limits taken. Finally, only the steady state portion of the forcing function plays a role in the steady state energy density.

Like all integral formulations, finding the energy density $\Psi(\mathbf{r}',s)$ or $\bar{\psi}(\mathbf{r}')$ at a point $\mathbf{r}'$, either in the domain or on the boundary, in eq. 3.18 requires knowledge of the solution on the boundary (needed in the last integral), the boundary properties (absorption), the source power, and the initial condition for the energy density distribution. Thus, eq. 3.18 must be solved first by selecting $\mathbf{r}'$ on the boundary.

3.3   Numerical Formulation of the Matrix Equations

The surface integral in the integral equation can be solved numerically using the boundary element method. The transformation of the surface integral into an algebraic sum of nodal values using Gaussian quadrature is shown schematically in Figure 3.3. For the mathematical details behind the discretization of the boundary into isoparametric elements and element transformations, refer to Appendix B. This appendix provides every equation in detail necessary for the actual implementation of the BE-LTS and is presented there for the reader interested in using the method.

$$I_S = \int_S C\psi dS$$

$$\psi \approx \psi_1 N_1 + \psi_2 N_2$$

$$\int_S CN_1 dS \approx w_1 CN_1 + w_2 CN_1$$

$$C\psi$$

$$I_S \approx \psi_1 \left(w_1 CN_1 + w_2 CN_1 \right) + \psi_2 \left(w_1 CN_2 + w_2 CN_2 \right)$$
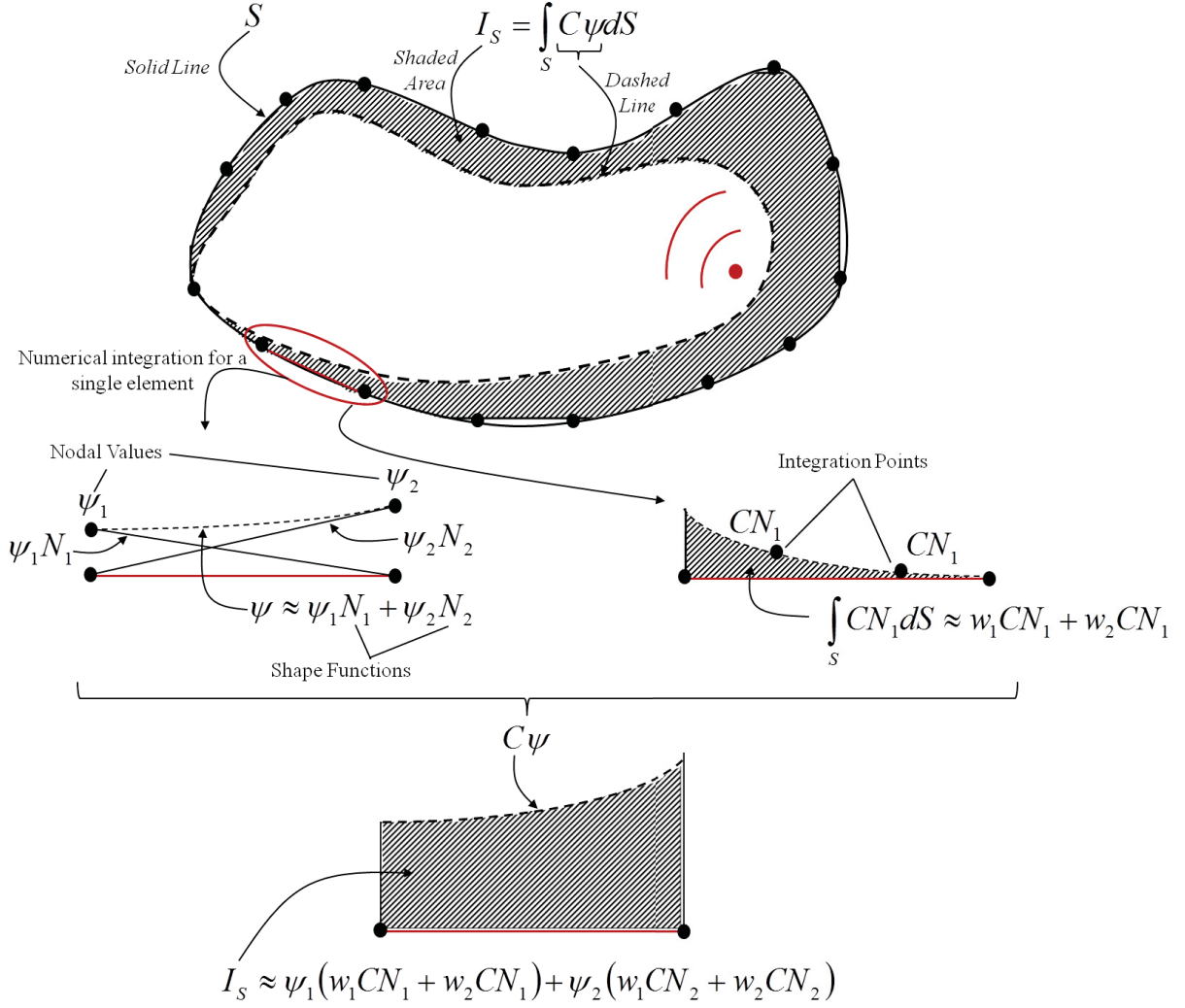
Figure 3.3: Numerical integration of the bounding surface in terms of a sum of nodal values of the energy density.

Using some numerical integration technique for each node of each element of a BE mesh, eq. 3.18 becomes

$$\beta\Psi\left(\mathbf{r}',s\right) = \frac{1}{D}\int_{V'} G\left(\mathbf{r}\,|\,\mathbf{r}',s\right)\psi\left(\mathbf{r},0\right)dV + \frac{1}{D}\int_{V_s'} G\left(\mathbf{r}\,|\,\mathbf{r}',s\right)F\left(\mathbf{r},s\right)dV_s - \\ \sum_{j=1}^{J}\sum_{i=1}^{I}\Psi_{ij}\left(s\right)C_{ij}\left(\mathbf{r}',s\right)$$

3.26

where $\Psi_{ij}(s)$ is the energy density and $C_{ij}(\mathbf{r}',s)$ is dependent on the Green's function and its normal derivative (given specifically in Appendix B) at the ith node of the jth element. This

equation is now evaluated for $\mathbf{r}' = \mathbf{r}'_l$ at the position of the lth node where the mesh has a total of L unique nodes. After some rearranging, eq. 3.26 becomes

$$\beta\Psi_l(s) + \sum_{j=1}^{J}\sum_{i=1}^{I}\Psi_{ij}(s)C_{l,ij}(s) = \frac{1}{D}\int_{V'}G(\mathbf{r}\,|\,\mathbf{r}_l',s)\psi(\mathbf{r},0)dV + \frac{1}{D}\int_{V_s'}G(\mathbf{r}\,|\,\mathbf{r}_l',s)F(\mathbf{r},s)dV_s \qquad 3.27$$

where $C_{l,ij}(s) = C_{ij}(\mathbf{r}_l',s)$ and $\beta = 1/2$ as required by eq. 3.17.

Now examining only the volume integrals evaluated at $\mathbf{r}' = \mathbf{r}_l'$ on the right hand side of eq. 3.26, let

$$B_l(s) = \frac{1}{D}\int_{V'}G(\mathbf{r}\,|\,\mathbf{r}_l',s)\psi(\mathbf{r},0)dV + \frac{1}{D}\int_{V_s'}G(\mathbf{r}\,|\,\mathbf{r}_l',s)F(\mathbf{r},s)dV_s\,. \qquad 3.28$$

The initial energy density distribution and supplied acoustic power are known for any given acoustic problem of interest. Since the Green's function is also known, these volume integrals can be approximated fairly easily or solved accurately using some other numerical integration procedure. Without loss of generality, specific cases in which these integrals can be determined or approximated will be examined.

3.3.1   Case 1: Uniform Distribution of Initial Energy Density

In room acoustics, the reverberation time, T_{60}, of a room is important to characterize its acoustics. This parameter is measured or computed from the decay of sound in a room. This can be described using a known initial acoustic energy without a source and eqn. 3.28 becomes

$$B_l(s) = \frac{1}{D}\int_{V'}G(\mathbf{r}\,|\,\mathbf{r}_l',s)\psi(\mathbf{r},0)dV\,. \qquad 3.29$$

Since only the boundary can be integrated using a sophisticated numerical technique when applying the BEM, the value of this volume integral will be calculated in a simplistic way. Specifically, the total volume will be divided into discrete sub-volumes, ΔV_v, assigned a uniform initial energy density, $\psi_v(\mathbf{r}_v,0)$, which gives

$$B_l(s) = \frac{1}{D}\sum_{v=1}^{N_v}G(\mathbf{r}_v\,|\,\mathbf{r}_l',s)\psi_v(\mathbf{r}_v,0)\Delta V_v \qquad 3.30$$

where the vth sub-volume is centered at $\mathbf{r}_v$. A special case when the sub-volumes are all of equal volume, ΔV, and the volume has a uniform initial energy, ψ_0, will be considered. In this case, eqn. 3.30 becomes

$$B_l(s) = \frac{1}{D} \psi_0 \Delta V \sum_{v=1}^{N_v} G(\mathbf{r}_v \mid \mathbf{r}_l', s)$$

3.31

which can be easily implemented numerically.

3.3.2 Case 2: Omnidirectional Point Sound Source

If the initial acoustic energy density is zero everywhere in the volume, only the volume integral containing the source must then be evaluated. Equation 3.28 reduces to

$$B_l(s) = \frac{1}{D} \int_{V_s'} G(\mathbf{r} \mid \mathbf{r}_l', s) F(\mathbf{r}, s) dV_s .$$

3.32

If the acoustic source is assumed to be an omnidirectional single point at $\mathbf{r}_s$, such as a speaker at low frequencies, the source term can be written as

$$f(\mathbf{r}, t) = w(t) \delta(\mathbf{r} - \mathbf{r}_s)$$

3.33

where $w(t)$ is an arbitrary acoustic power as a function of time. Taking the Laplace transform and carrying out the volume integration of the source integral gives

$$B_l(s) = \frac{1}{D} G(\mathbf{r}_s \mid \mathbf{r}_l', s) W(s)$$

3.34

where $W(s) = \mathcal{L}[w(t)]$. If the point source is modeled as a step function at time $t = \tau$ with constant acoustic power, W, eq. 3.34 becomes

$$B_l(s) = \frac{We^{-\tau s}}{sD} G(\mathbf{r}_s \mid \mathbf{r}_l', s).$$

3.35

3.3.3 Case 3: Radiating Boundary

An acoustic source located on the bounding surface of the domain or a portion of the bounding surface, S_s, can be accounted for by modifying the boundary condition in eq. 3.5 to

$$\frac{\partial \Psi(\mathbf{r},s)}{\partial \mathbf{n}} = \frac{F(\mathbf{r},s)}{D} - \frac{h(\mathbf{r})}{D}\Psi(\mathbf{r},s), \quad \mathbf{r} \in S_s$$

$$\frac{\partial \Psi(\mathbf{r},s)}{\partial \mathbf{n}} = -\frac{h(\mathbf{r})}{D}\Psi(\mathbf{r},s), \qquad \mathbf{r} \in S - S_s$$

3.36

where $F(\mathbf{r},s)$ is now a distribution of acoustic power per unit area. The modified boundary condition can be used to describe either (a) a boundary excited into vibration causing acoustic radiation or (b) an external sound source transmitted through the boundary as shown in Figure 3.4.
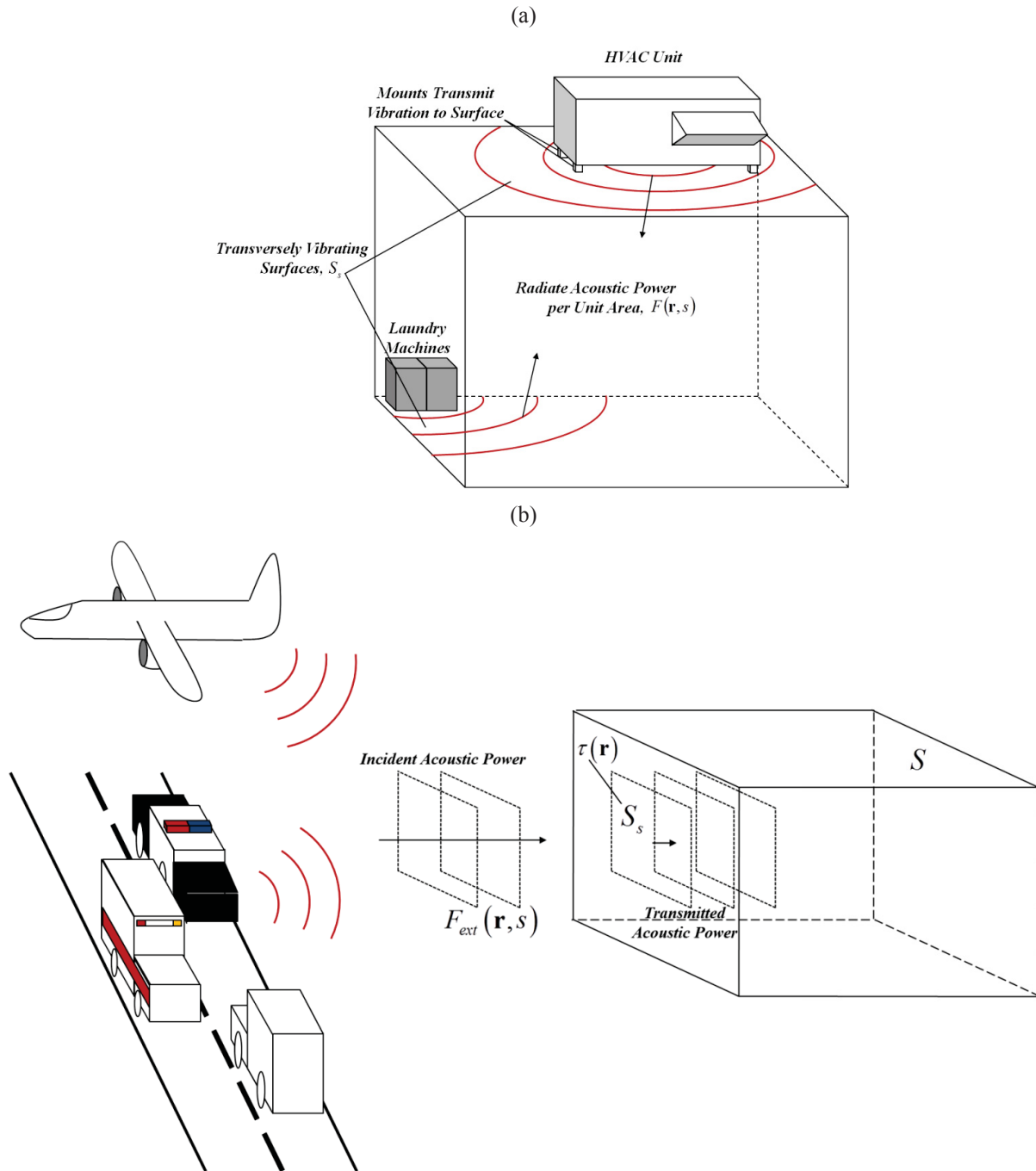
Figure 3.4: Schematic of acoustic radiation from part of the bounding surface of a room due to (a) a vibrating boundary or (b) an external sound source transmitting through the surface.

For the case of a vibrating boundary, time or frequency domain structural analysis of the structural partition excited by some known force, e.g. a rotating machine, can provide the partition's velocity response. From the velocity response and acoustic radiation properties of the

interior surface, the flow of energy, $F(\mathbf{r},s)$, from the structural vibration to the acoustic volume can be computed.

An acoustic power per unit area loading, $F_{ext}(\mathbf{r},s)$, on the exterior side of the bounding surface or a portion of it as shown in Figure 3.4(b), can be represented with

$$F(\mathbf{r},s)=\tau(\mathbf{r})F_{ext}(\mathbf{r},s) \qquad 3.37$$

where $\tau(\mathbf{r})$ is the known transmission coefficient of the partition. The transmission coefficient is the ratio of the transmitted to incident acoustic intensity. It can be a function of the direction of the exterior loading if it is known and can vary with position if the exterior loading covers multiple types of partitions. Substituting eq. 3.36 into eq. 3.16, the boundary integral equation becomes

$$\beta\Psi(\mathbf{r}',s)=\frac{1}{D}\int_{V'}G(\mathbf{r}\,|\,\mathbf{r}',s)\psi(\mathbf{r},0)dV+\frac{1}{D}\int_{S_s'}G(\mathbf{r}\,|\,\mathbf{r}',s)F(\mathbf{r},s)dS_s-$$
$$\int_{S'}\Psi(\mathbf{r},s)\left[\frac{h(\mathbf{r})}{D}G(\mathbf{r}\,|\,\mathbf{r}',s)+\frac{\partial G(\mathbf{r}\,|\,\mathbf{r}',s)}{\partial\mathbf{n}}\right]dS \qquad 3.38$$

For zero initial acoustic energy density eq. 3.28 becomes

$$B_l(s)=\frac{1}{D}\int_{S_s'}G(\mathbf{r}\,|\,\mathbf{r}',s)F(\mathbf{r},s)dS_s \; . \qquad 3.39$$

If the surface source is uniformly distributed over the surface, eq. 3.39 reduces to

$$B_l(s)=\frac{F(s)}{D}\int_{S_s'}G(\mathbf{r}\,|\,\mathbf{r}',s)dS_s \qquad 3.40$$

where $F(s)$ is the uniform power per area of the surface source.

Equations 3.39 and 3.40 are convenient forms of the source integral because they can be numerically integrated using the existing boundary mesh and the same numerical integration procedure even for complex spatially distributed surface sources.

3.3.4 Boundary and Volume Energy Density Computation

Now, the matrix form of the boundary integral equation is developed. Solving the matrix equation allows for the computation of the energy density on the boundary of the volume as shown in the second line in Figure 3.1. Then, the equation necessary to compute the energy density at points inside the volume using the boundary energy density is developed as shown in the third line of figures in Figure 3.1.

Using eqs. 3.28, 3.32, 3.34, 3.35, 3.39, or 3.40 to evaluate $B_l(s)$, eq. 3.26 becomes

$$\beta \Psi_l(s) + \sum_{j=1}^{J} \sum_{i=1}^{I} \Psi_{ij}(s) C_{l,ij}(s) = B_l(s). \qquad 3.41$$

Next, the energy density and the values of $B_l(s)$ at each node are arranged into vectors such that $\Psi(s)_{L\times1} = \{\Psi_1(s) \quad \Psi_2(s) \quad \cdots \quad \Psi_L(s)\}^T$ and $\mathbf{B}(s)_{L\times1} = \{B_1(s) \quad B_2(s) \quad \cdots \quad B_L(s)\}^T$. Thus, eq. 3.41 becomes a set of L linear, algebraic equations in $\Psi_l(s)$ given by

$$[\mathbf{A}(s)]_{L\times L} \Psi(s)_{L\times1} = \mathbf{B}(s)_{L\times1}. \qquad 3.42$$

The solution of this matrix equation provides the energy density at each node of the boundary mesh and can be used with shape functions to compute the energy density at any point on the boundary surface. The $L \times L$ matrix of coefficients, $[\mathbf{A}(s)]$, is given by

$$[\mathbf{A}(s)]_{L\times L} = \frac{1}{2}[\mathbf{I}] + [\mathbf{C}(s)] = \frac{1}{2}\begin{bmatrix} 1 & 0 & \cdots & 0 \\ 0 & 1 & \ddots & 0 \\ \vdots & \ddots & \ddots & 0 \\ 0 & 0 & 0 & 1 \end{bmatrix}_{L\times L} +$$

$$\begin{bmatrix} \sum_{j=1}^{J_{e1}} C_{1,ij}(s) & \sum_{j=1}^{J_{e2}} C_{1,ij}(s) & \cdots & \sum_{j=1}^{J_{eL}} C_{1,ij}(s) \\ \sum_{j=1}^{J_{e1}} C_{2,ij}(s) & \sum_{j=1}^{J_{e2}} C_{2,ij}(s) & \ddots & \vdots \\ \vdots & & \ddots & \ddots & \vdots \\ \sum_{j=1}^{J_{e1}} C_{L,ij}(s) & \cdots & \cdots & \sum_{j=1}^{J_{eL}} C_{L,ij}(s) \end{bmatrix}_{L\times L} \qquad 3.43$$

where J_{el} is the number of elements the lth node belongs to in volume v; the index, i, takes on only one value for each of these elements as each unique node will correspond to a single node of the jth element.

Note that the matrix and vectors of eq. 3.42 are all functions of the Laplace variable. Therefore, the linear system of equations can only be solved for discrete values of the Laplace variable, s_q. Evaluating the matrix $[\mathbf{A}(s)]$ and the vector $\mathbf{B}(s)$ at $s = s_q$ and solving eq. 3.42 gives the energy density in the Laplace domain at the nodes of the mesh that bounds the volume for this value of the Laplace variable. Additionally, the exchange coefficient, $h(\mathbf{r})$, which depends on the absorption coefficients of the room surfaces, $\alpha(\mathbf{r})$, or the transmission coefficient, $\tau(\mathbf{r})$, if an acoustic source is being transmitted from the outside are typically functions of frequency. Thus, eq. 3.42 on the boundary and eq. 3.26 in the volume must be solved a number of times for separate frequency bands with the appropriate absorption and transmission coefficients.

After solving the matrix equation, eq. 3.42, for the energy density at each node on the boundary, $\mathbf{\Psi}(s_q)_{L\times 1}$, eq. 3.26 can be subsequently solved for any point inside the domain in which it becomes

$$\Psi(\mathbf{r}', s_q) = \frac{1}{D}\int_{V'} G(\mathbf{r}\mid \mathbf{r}')\psi(\mathbf{r},0)dV + \frac{1}{D}\int_{V_s'} G(\mathbf{r}\mid \mathbf{r}')F(\mathbf{r}, s_q)dV -$$
$$\sum_{j=1}^{J}\sum_{i=1}^{I}\Psi_{ij}(s_q)C_{ij}(\mathbf{r}', s_q) \qquad , \qquad 3.44$$

is repeated here for convenience where $\mathbf{r}' \in V$, $C_{ij}(\mathbf{r}', s_q)$ is computed from numerical integration of the boundary mesh provided and $\Psi_{ij}(s_q)$ is the energy density at the nodes of the boundary mesh. The energy density at any point, $\mathbf{r}' \in V$, in the volume can be rewritten in matrix form with

$$\Psi(\mathbf{r}', s_q) = B(\mathbf{r}', s_q) - [\mathbf{C}(\mathbf{r}', s_q)]_{L\times L}\mathbf{\Psi}(s_q)_{L\times 1}. \qquad 3.45$$

Thus, the energy in the volume is obtained basically through simple, efficient matrix multiplication as opposed to the boundary energy which requires the inversion of the large matrix, $[\mathbf{A}(s_q)]$. Equation 3.45 can be solved consecutively for many points of interest in the volume.

To obtain useful results in the time domain, the inverse Laplace transform of the energy density must be computed. However, the Laplace domain energy is known only at discrete values of the Laplace variable, so a numerical inverse Laplace transform must be used. Several candidate methods are investigated in this research and described in the next chapter.

Chapter 4:   Numerical Inverse Laplace Transform

This chapter is concerned with the computation of the inverse Laplace transform of the BE-LTS for the acoustic diffusion model. To obtain more useful results from the BE-LTS, the energy density in the Laplace domain, $\Psi(\mathbf{r}, s)$, e.g. the solutions to eqs. 3.42 and/or 3.45, must be transformed to the time domain using

$$\psi(\mathbf{r}, t) = \mathcal{L}^{-1}\left[\Psi(\mathbf{r}, s)\right] \tag{4.1}$$

where $\mathcal{L}^{-1}[\ ]$ denotes an inverse Laplace transform. Since $\Psi(\mathbf{r}, s)$ is only known at discrete values of $s = s_q$, an analytical inverse transform does not exist. Many methods for computing the numerical inverse Laplace transform have been developed and studied (Davies and Martin, 1979) and a few are discussed here with application to acoustic problems. These methods have been used for solving a variety of simple equations, e.g. a single ordinary differential equation. The application of these numerical inverse Laplace transforms to a partial differential equation solved with the BEM is unique to this research.

The main goal of using the Laplace domain approach is to minimize the number of times that the matrix, $\left[\mathbf{A}(s_q)\right]$, is calculated and inverted as this is the most computationally expensive procedure in the BE-LTS. Each of the methods discussed assumes that the time domain function can be expanded as

$$\psi(\mathbf{r}, t) = \sum_{q=1}^{Q} a_q p_q\left(s_q, t\right) \tag{4.2}$$

where a_q is a coefficient computed from the Laplace domain function and $p_q\left(s_q, t\right)$ is a function of both the Laplace variable value and time. The form of $p_q\left(s_q, t\right)$ is dependent on the particular method. The Laplace transform of eq. 4.2 is

$$\Psi(\mathbf{r}, s) = \sum_{q=1}^{Q} a_q P_q\left(s_q, s\right) \tag{4.3}$$

where $P_q\left(s_q,s\right)=\mathcal{L}\left[p_q\left(s_q,t\right)\right]$. Evaluating $s=s_{q'}$ where $q'=1,2,...,Q$ allows for the calculation of a_q. It is shown later that the computation of these coefficients in many cases requires a linear system of Q equations to be solved for each point in the domain.

The general process is shown in Figure 4.1 for the case of a buildup of energy and the decay of energy. For the buildup, functions of energy increasing at varying rates are subtracted from a large steady state energy. In the decay problem, decaying functions of energy with varying decay rates are simply added to compute an energy decay curve.
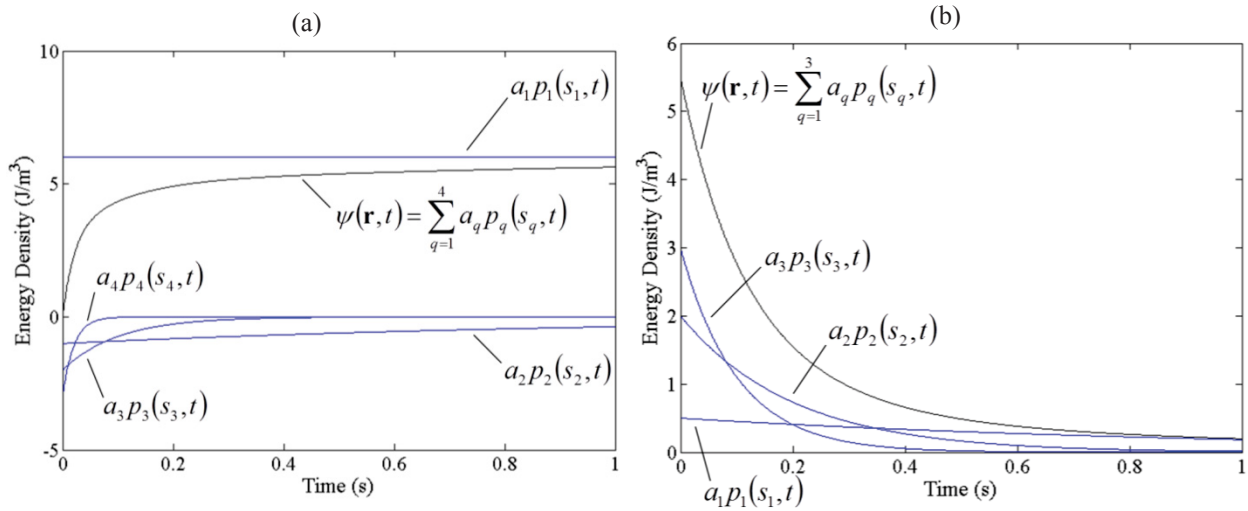
Figure 4.1: Schematic demonstrating the numerical inverse Laplace transform using expansion methods for (a) the buildup and (b) the decay of energy density.

In the following subsections, three numerical inverse Laplace transform methods are briefly described. Then, they are applied to the Sabine buildup and decay of acoustic energy density, which have known analytical solutions, eqs. 2.30 and 2.31. The Sabine theory solution for the buildup of acoustic energy in an initially undisturbed volume, eq. 2.30, and for the decay of acoustic energy from an initial uniform distribution, eq. 2.31, are repeated here:

$$\psi(t) = \frac{4W}{S_v c\bar{\alpha}}\left[1 - \exp\left(-\frac{t}{\tau_S}\right)\right] \qquad 4.4$$

and

$$\psi(t) = \psi_0 \exp\left(-\frac{t}{\tau_S}\right). \qquad 4.5$$

The exponential expansion procedure is examined for the case of a 10 x 10 x 10 m³ volume with an absorption coefficient of 0.1. For the buildup problem, the source emits a power of 0.01 W. For the decay problem, the energy in the volume is initially 1.9 x 10⁻⁶ J/m³. This uniform cubic volume configuration is studied in greater detail in a subsequent section using the diffusion model.

The Laplace transforms of eqs. 4.4 and 4.5 are

$$\Psi(s) = \frac{4W}{S_v c \bar{\alpha}} \left(\frac{1}{s} - \frac{1}{s + \tau_S}\right) \qquad 4.6$$

and

$$\Psi(s) = \frac{\psi_0}{1 + \tau_S}, \qquad 4.7$$

respectively.

The inversion methods' ability to reproduce the analytical solutions accurately using as few discrete values of the Laplace variable as possible is used to determine which to apply to the BEM solution to the acoustic diffusion model. It is very desirable to use as few discrete Laplace variable values for significant improvement in computational efficiency. This is because the full BEM procedure, i.e. setting up and solving eqs. 3.42 and/or 3.45, must be repeated once per frequency band for each additional discrete value required to compute the inverse Laplace transform.

4.1   Exponential Expansion Method

Based on the comparison of these methods by Davies and Martin (1979), the procedure proposed by Liggett and Liu (1983) will be discussed first. In this approach, it is assumed that the solution, $\psi(\mathbf{r},t)$, can be expanded in a series as

$$\psi(\mathbf{r},t) = \bar{\psi}(\mathbf{r}) + \sum_{q=1}^{Q} a_q e^{-b_q t} \qquad 4.8$$

63

where $\bar{\psi}(\mathbf{r})$ is the steady state value, Q is the number of Laplace variable values, and a_q and b_q are arbitrary constants to be determined.

The assumed form of the solution is valid for any combination of initial energy and energy added to the system from some source. For the extreme case in which no energy is added to the system, $\bar{\psi}(\mathbf{r})=0$, which decays from an initial energy, the coefficients, a_q, are mostly positive and the time domain function is formed from the sum of decaying exponentials. The opposite extreme case is one in which there is no initial energy and a source of energy provides a steady state value, $\bar{\psi}(\mathbf{r})\neq 0$. In this case, the coefficients, a_q, are mostly negative and the time domain function is computed by subtracting decaying exponentials from the steady state value. In a problem with both an initial energy and a source of energy, a_q are both positive and negative which forms a more complex time domain solution.

The next step is to compute the coefficients a_q and b_q in the series of eq. 4.8. Taking the Laplace Transform of eq. 4.8 results in

$$\Psi(\mathbf{r},s)=\frac{\bar{\psi}(\mathbf{r})}{s}+\sum_{q=1}^{Q}\frac{a_q}{b_q+s}. \qquad\qquad 4.9$$

Next, Q discrete values of b_q are chosen so that

$$b_q = s_q, \qquad q=1,2,...,Q \qquad\qquad 4.10$$

are the values of the Laplace variable for which the energy density has been computed. These values can be chosen for an efficient numerical inverse Laplace transform using knowledge of the physical problem. It is shown later that one value of critical importance to the accurate, efficient calculation of the inverse Laplace transform can be estimated using the mean free path length of the volume.

Substituting eq. 4.10 into eqs. 4.8 and 4.9 gives

$$\psi(\mathbf{r},t)=\bar{\psi}(\mathbf{r})+\sum_{q=1}^{Q}a_q e^{-s_q t} \qquad\qquad 4.11$$

and

$$\Psi(\mathbf{r},s) = \frac{\bar{\bar{\psi}}(\mathbf{r})}{s} + \sum_{q=1}^{Q}\frac{a_q}{s_q + s}, \qquad\qquad 4.12$$

respectively. Notice that eqs. 4.4 and 4.5 are already in the form of eq. 4.11 and eqs. 4.6 and 4.7 in the form of eq. 4.12 with $s_q = 1/\tau_S$ and $Q = 1$.

Equation 4.12 represents a set of Q algebraic equations which can be solved simultaneously for the values of a_q. These equations can be written in matrix form as

$$[\mathbf{S}]_{Q\times Q}\,\mathbf{a}_{Q\times 1} = \left\{\Psi(\mathbf{r},\mathbf{s}) - \frac{\bar{\bar{\psi}}(\mathbf{r})}{\mathbf{s}}\right\}_{Q\times 1} \qquad\qquad 4.13$$

where $\mathbf{a}_{Q\times 1} = [a_1, a_2, ..., a_Q]^T$, $\mathbf{s}_{Q\times 1} = [s_1, s_2, ..., s_Q]^T$,

$$[\mathbf{S}]_{Q\times Q} = \begin{bmatrix} (s_1 + s_1)^{-1} & (s_1 + s_2)^{-1} & \cdots & (s_1 + s_Q)^{-1} \\ (s_2 + s_1)^{-1} & (s_2 + s_2)^{-1} & \ddots & \vdots \\ \vdots & & \ddots & \ddots & \vdots \\ (s_Q + s_1)^{-1} & \cdots & \cdots & (s_Q + s_Q)^{-1} \end{bmatrix}, \qquad 4.14$$

and

$$\left\{\Psi(\mathbf{r},\mathbf{s}) - \frac{\bar{\bar{\psi}}(\mathbf{r})}{\mathbf{s}}\right\}_{Q\times 1} = \left\{ \begin{array}{c} \Psi(\mathbf{r},s_1) - \dfrac{\bar{\bar{\psi}}(\mathbf{r},0)}{s_1} \\[2mm] \Psi(\mathbf{r},s_2) - \dfrac{\bar{\bar{\psi}}(\mathbf{r},0)}{s_2} \\[2mm] \vdots \\[2mm] \Psi(\mathbf{r},s_Q) - \dfrac{\bar{\bar{\psi}}(\mathbf{r},0)}{s_Q} \end{array} \right\}. \qquad 4.15$$

Once eq. 4.13 is solved for the values of a_q, eq. 4.11 is used to determine the acoustic energy density for any point in space as a function of time, $\psi(\mathbf{r},t)$. Liggett and Liu (1983) recommend to use $5 \le Q \le 12$ and that s_q are chosen as a geometric series as in

$$s_q = d^{q-1}s_1 \qquad\qquad 4.16$$

where d is a constant real number. It is possible and shown later that less than five values can create an accurate time domain solution; this greatly improves the computational efficiency of the BE-LTS as discussed previously. The constant, d, is chosen based on the range of Laplace

variable values which are important to the time domain solution which are usually close to the critical value discussed previously, i.e. within a factor of two.

4.2   Legendre Polynomial Expansion Method

Papoulis (1956) proposed to expand the time domain function as a sum of Legendre polynomials in $\exp(-rt)$ as in

$$\psi(t) = \sum_{q=0}^{Q-1} a_q P_{2q}\left(e^{-rt}\right) \qquad 4.17$$

where a_q are unknown coefficients, P_{2q} are the $2q^{\text{th}}$ degree Legendre polynomials, r is a constant parameter of the numerical inversion used to define the discrete values of the Laplace variable, s_k, as

$$s_k = (2k+1)r, \quad k = 0,1,...,Q-1. \qquad 4.18$$

Taking the Laplace transform of eq. 4.17 and substituting eq. 4.18 gives

$$r\Psi(s_k) = \sum_{q=0}^{k} \frac{\prod_{m=0}^{q}(k-q+m+1)}{2\prod_{m=0}^{q+1}(k+m+1/2)} a_q . \qquad 4.19$$

This equation represents a linear system of Q equations with a_q as the unknowns. Interestingly, eq. 4.19 does not have to be solved simultaneously for all a_q, but can be solved recursively. That is, setting $k=0$ results in one equation with one unknown, a_0. Consecutively increasing k results in only one additional unknown coefficient at a time. Thus, this method is more computationally efficient than the exponential expansion method presented in the previous section which requires creating a matrix of Laplace values and simultaneously solving a linear system of equations for the coefficients, a_q. However, the number of Laplace values is generally a small number, i.e. less than ten, so this is not a major detriment to the exponential expansion method.

4.3   Trigonometric Expansion Method

Papoulis (1956) also proposed to expand the time domain function as a sum of trigonometric functions as in

$$\psi(t) = \sum_{q=0}^{Q-1} a_q \sin\left[(2q+1)e^{-rt}\right]$$ 4.20

where a_q are unknown coefficients, r is a constant parameter of the numerical inversion used to define the discrete values of the Laplace variable, s_k, as

$$s_k = (2k+1)r, \quad k = 0, 1, ..., Q-1$$ 4.21

Taking the Laplace transform of eq. 5.1 and substituting eq. 5.3 gives

$$r\Psi(s_k) = \pi 2^{-2(k+1)} \sum_{q=0}^{k} \left[\binom{2k}{k-q} - \binom{2k}{k-q-1} \right] a_q .$$ 4.22

This equation represents a linear system of Q equations with a_q as the unknowns. As with the Legendre polynomial expansion method, eq. 4.22 does not have to be solved simultaneously for all a_q, but can be solved recursively, one coefficient at a time.

4.4   Application to Sabine Theory Solution

In this section, the inverse Laplace transform of the Sabine theory solutions are computed numerically using the expansion methods discussed and discrete values of the exact solution. Initially, s_q are chosen assuming knowledge only of the order of magnitude of the single required exponential, $s_q = 1/\tau_S$. When the numerical inversion method chosen is used with the BEM solution to the diffusion model, it is expected that only an order of magnitude estimate of the required exponential or exponentials is known. For the exponential inversion method, the first and last values are chosen such that $s_1 = 2$ and $s_Q = 8$ and the rest are chosen according to eq. 4.16. For the Legendre polynomial and trigonometric expansion, r is chosen as 0.3. The number of values is varied from $Q = 1$ to $Q = 30$.

The numerically calculated time domain solutions to the energy decay are shown for a subset of these values in Figure 4.2 to show the evolution of the solution as Q is increased. For a single value of the Laplace variable, the exponential expansion procedure produces a curve based on a single exponential decay rate. In this case, the inverted solution is incorrect because the decay rate does not match the correct rate. Using only one value of the Laplace variable with the other

methods results in a horizontal line and is not plotted. Two values of the Laplace variable give the horizontal line slight curvature, but not enough to reproduce the decay in the Sabine solution.

(a)

(b)   (c)
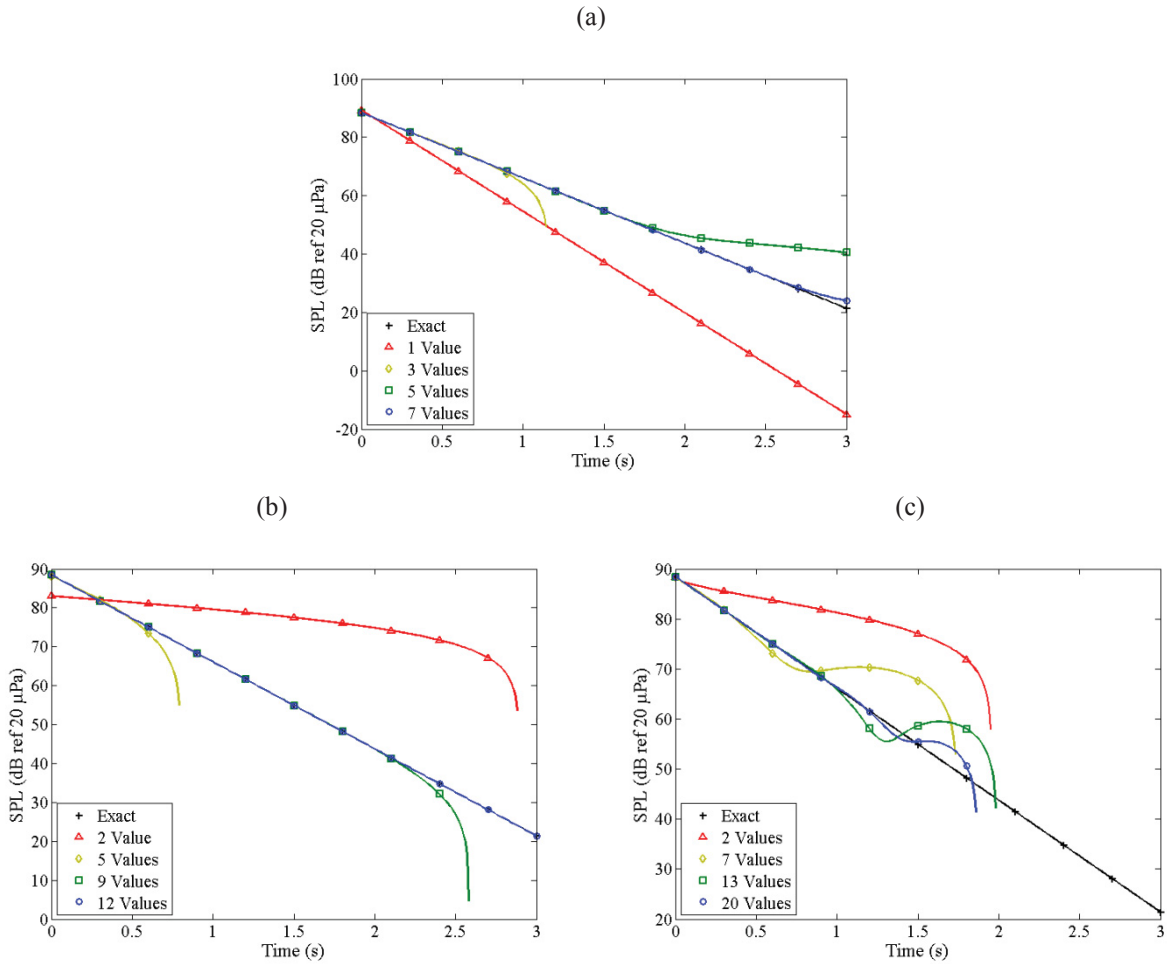
Figure 4.2: Decay of SPL over three seconds from known Sabine theory solution using the (a) exponential expansion, (b) Legendre polynomial expansion, and (c) trigonometric expansion methods for increasing numbers of the Laplace variable.

In general, more Laplace values increases the length of time for which the decay curve is accurate. Using exponential expansion, three values produces an accurate curve for one second, five values for two seconds, and seven values for almost three seconds nearly overlapping the exact solution. Expansion in Legendre polynomials gives an accurate curve to about half of a second using five values. Nine values produce an accurate curve to about two seconds and twelve values produces a curve accurate for three seconds. Seven Laplace values give an accurate solution to half of a second using trigonometric expansion. Thirteen and twenty values

produce accurate decay to about one and one and a half seconds. Trigonometric expansion, however, is unable to accurately reproduce the exact solution for the full three seconds.

Each expansion method is now used to compute a three second long discrete time history of the energy density in the room consisting of 301 time steps. The energy density at each time step is compared to the exact solution to compute a percent error. This error is averaged for all time steps. The average percent error is plotted in Figure 4.3 for both the buildup and decay solutions using a logarithmic y-axis for increasing numbers of Laplace variable values.
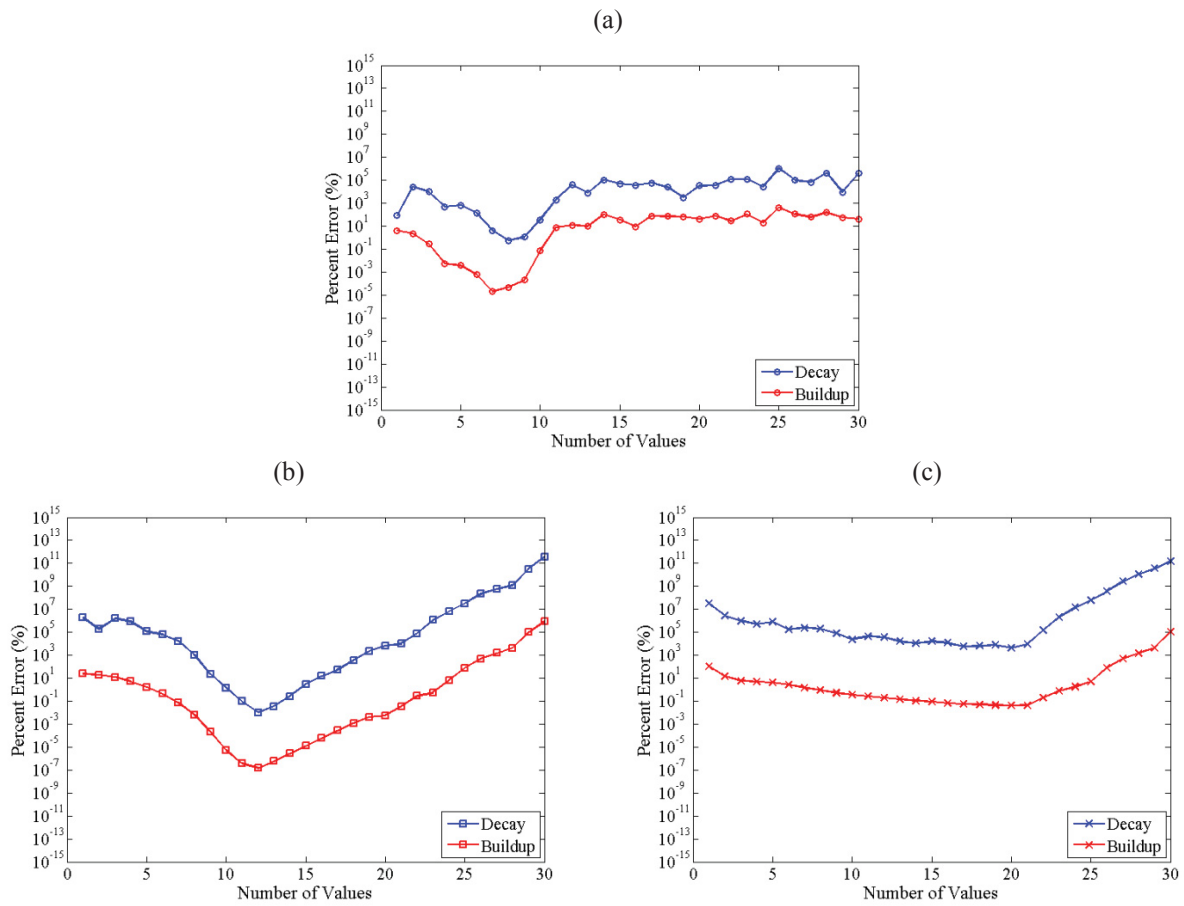
Figure 4.3: Average percent error in energy density over three seconds from known Sabine theory solution using the exponential expansion numerical inversion method and order of magnitude knowledge of correct Laplace value.

In general, the average error begins fairly low for $Q=1$ and decreases to some minimum error as Q is increased. Further increase of Q causes numerical instabilities in the methods which render inaccuracies. In the exponential expansion method, this error increases quickly and

levels off to some large amount on the order of 100 % for the buildup problem and 10000 % for the decay problem which is caused by the matrix, $[S]$, in eqs. 4.13 and 4.14 becoming effectively singular. For the energy buildup, the minimum error occurs using 7 values of the Laplace variable, but anywhere from 1 to 11 values gives an average error of less than 10 %. In the case of energy decay, 7 to 9 values gives less than 10 % error with the minimum at 8 values.

Using the Legendre polynomial expansion, one Laplace value causes very large error, especially for the decay solution. The average error decreases to a minimum when 12 values are used. Then, the error increases at a constant rate as the method becomes unstable.

For the energy buildup, the trigonometric expansion method is able to reproduce the exact time-domain solution to within 5 % average error using as few as three values of the Laplace variable. This error decreases very slowly to a minimum of 0.04 % average error using 20 values. This method is unable to accurately reproduce the decay curve with a minimum of over 4000 % average error using 20 values of the Laplace variable.

When using less than about ten values of the Laplace variable, the exponential expansion provides the most accurate solution. When more than ten are used, the Legendre polynomial expansion is the most accurate. All three methods are capable of computing the inverse Laplace transform of the Sabine buildup solution accurately with only a few values of the Laplace variable. The trigonometric expansion method is unable to compute the inverse Laplace transform of the decay solution, but the other methods can do so accurately.

The SPL's computed with the numerical computation of the inverse Laplace transform are compared to the exact solutions in Figure 4.4. As expected, the numerical curves overlap the exact solution almost perfectly, except in the decay computed with the trigonometric expansion method.

70
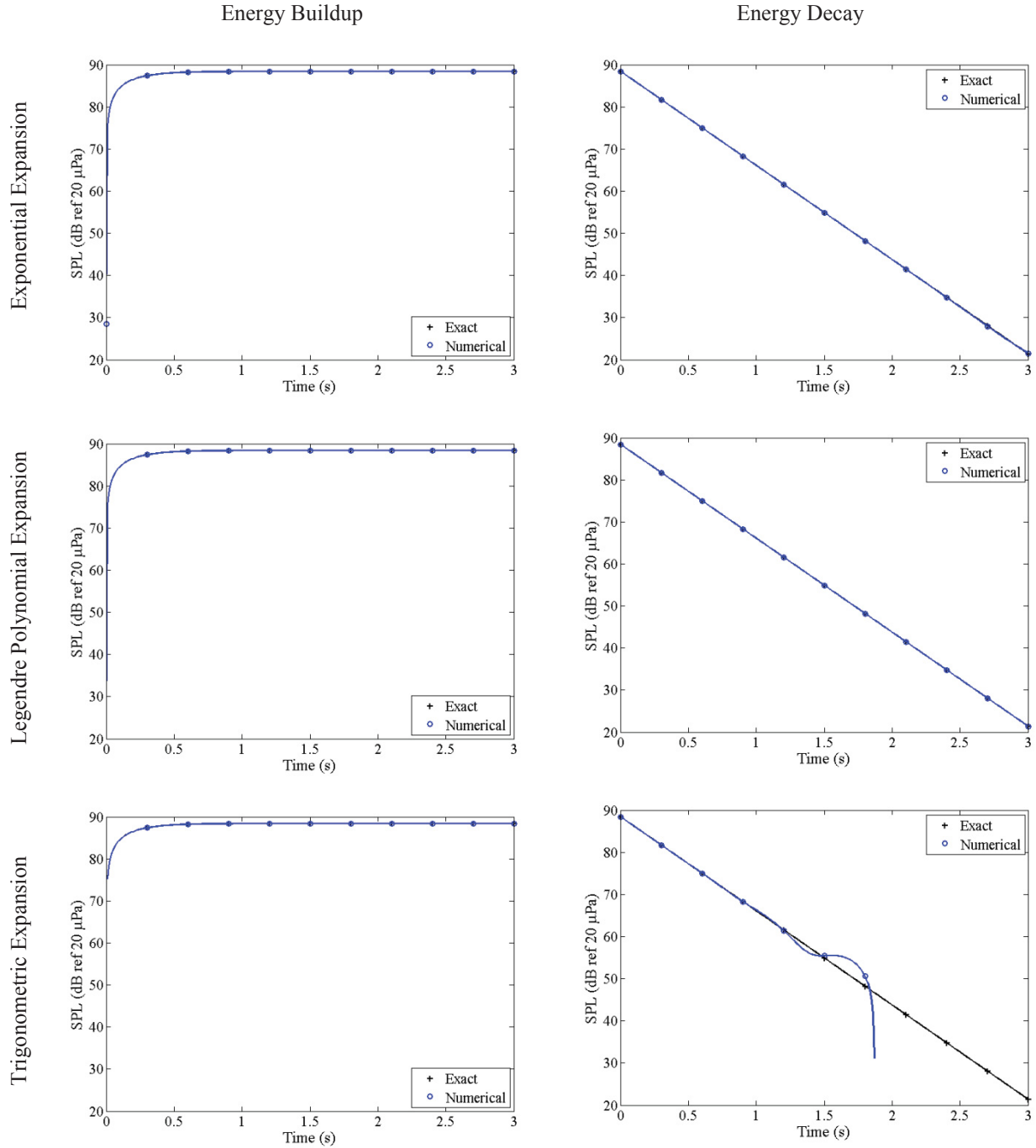
Figure 4.4: (a) Buildup and (b) decay of SPL using the exponential expansion numerical inversion method and (a) seven and (b) eight values of the Laplace variable spaced with order of magnitude knowledge of correct value.

Now, the discrete values, s_q, are chosen using the knowledge that only $s_q = 1/\tau_S$ is needed to recreate the solution exactly. To this end, the first and last values are chosen such that $s_1 = 1/(2\tau_S)$ and $s_Q = 2/\tau_S$ and the rest are chosen according to eq. 4.16 for the exponential

expansion method. Thus, there will be one value where $s_q = 1/\tau_S$ whenever Q is an odd greater than one. For the Legendre polynomial expansion, r is selected to be one tenth of $s_q = 1/\tau_S$. With the trigonometric expansion method, r is selected to be one third of $s_q = 1/\tau_S$. The average error of each method using these values is plotted in Figure 4.5.
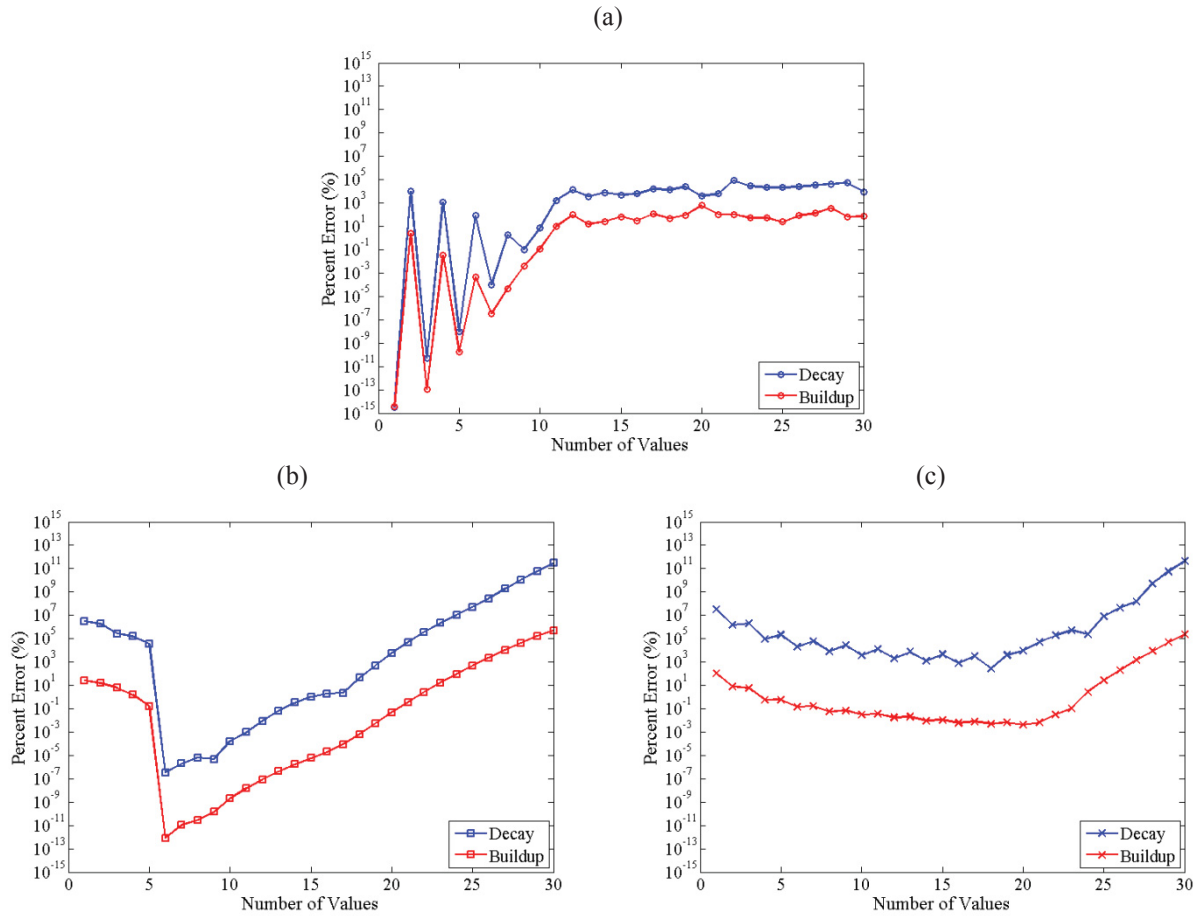
Figure 4.5: Average percent error in energy density over three seconds from known Sabine theory solution using the exponential expansion numerical inversion method and exact knowledge of correct Laplace value.

Using the exponential expansion, the average error is minimized in each solution using only the exact value of the Laplace variable necessary to create the solution. Extra, unnecessary exponentials simply introduce more error into the inverted solution. The error increases for even values of Q when the exact exponential is no longer present; the error in these cases follows the same trend as Figure 4.3.

When less than six Laplace variable values are used with the Legendre polynomial expansion method, the error is essentially the same as the previous case with $r = 0.3$. However, as soon as $Q > 5$ and $s_Q > 1/\tau_S$, the error drops drastically to its minimum, 3 x 10^{-7} % in the decay and 8 x 10^{-13} % in the buildup, which is almost an exact reproduction of the known solution. Subsequent increase in Q simply introduces more error. Interestingly, $r = 1/(10\tau_S)$ is the only value which produces this effect in the inversion procedure. Any other value, even $r = 1/\tau_S$, produces a smooth error curve similar to Figure 4.3.

Knowledge of the correct Laplace value gives an order of magnitude drop in average error when using more than three Laplace variable values with the trigonometric expansion method. At least four values are required to obtain this improvement because the exact Laplace variable value is not present in the inversion until this point. The minimum error is still obtained when 20 values are used, so knowledge of the exact value does not improve the method in this aspect.

The improvement in average error is about one order of magnitude for the calculation of the decay solution with trigonometric expansion. Using an even number of values offers even more improvement, in some cases, more than two orders of magnitude. Also, the minimum error is now obtained using only 18 values of the Laplace variable, fewer than are needed without knowing the exact Laplace variable value. However, the average error is still over 250 % indicating that the method is inadequate for reproducing the energy decay curve accurately.

The number of values needed to obtain less than 10 % average error and less than 1 % average error is given in Table 4.1. The exponential expansion inversion is the best in the energy buildup case requiring fewer values than either of the other methods. With order of magnitude knowledge of the correct Laplace value, the trigonometric expansion requires fewer values to produce a solution within 10 % average error than the Legendre polynomial expansion, but needs more to be within 1 % average error. With exact knowledge of the correct value, the trigonometric expansion requires less Laplace variable values than the Legendre polynomial expansion.

In the case of energy decay, the exponential expansion method still requires fewer values of the Laplace variable than other methods, seven or eight with order of magnitude knowledge of the correct value and only one with exact knowledge. The Legendre polynomial expansion is able to produce accurate decay solutions using 10 or 11 values of the Laplace variable and only six with exact knowledge of the correct value.

Table 4.1: Number of Laplace variable values needed to numerically invert the Sabine theory solutions to within 10 % and 1 % error using order of magnitude or exact knowledge of the correct value.

Expansion Method	*Buildup (Order of Magnitude)*		*Buildup (Exact)*		*Decay (Order of Magnitude)*		*Decay (Exact)*	
	10 %	**1 %**	**10 %**	**1 %**	**10 %**	**1 %**	**10 %**	**1 %**
Exponential	1	3	1	1	7	8	1	1
Legendre Polynomial	4	6	3	5	10	11	6	6
Trigonometric	3	8	2	4	---	---	---	---

Based on this comparison, the exponential expansion method is chosen to numerically invert the Laplace domain BEM solution to the acoustic diffusion model. Again, it is important for the efficiency of the method to require as few Laplace values as possible because a full BEM solution must be set up and solved for each discrete value in each frequency band. The exponential expansion method gives accurate solutions using very few values of the Laplace variable. In the next section, a method of selecting the discrete Laplace values in order to minimize the number required is discussed.

4.5   Application to BE-LTS of the Diffusion Model

Since the diffusion model is not a simple first order differential equation like Sabine theory discussed in the previous section, multiple values of the Laplace variable may be required to compute the numerical inverse Laplace transform. However, there is one critical Laplace variable which minimizes the number of values required. This section discusses the calculation and selection of that value for the uniform cubic volume used in the previous section.

Assuming uniform energy density in the volume and uniform absorption of the bounding surfaces, the Sabine model describes the decay of acoustic energy with eq. 2.31 repeated here for convenience:

$$\psi(t)=\psi_0 \exp\left(-\frac{t}{\tau_S}\right) \tag{4.23}$$

where $\tau_S = \dfrac{4V_r}{S_r c \alpha}$ is the volume time constant. Taking the Laplace transform of eq. 4.23 gives

$$\Psi(s)=\frac{\psi_0}{s+1/\tau_S}. \tag{4.24}$$

The energy density in the Laplace domain computed with the BEM and averaged across about 700 positions in the volume is plotted with the Sabine model in Figure 4.6.
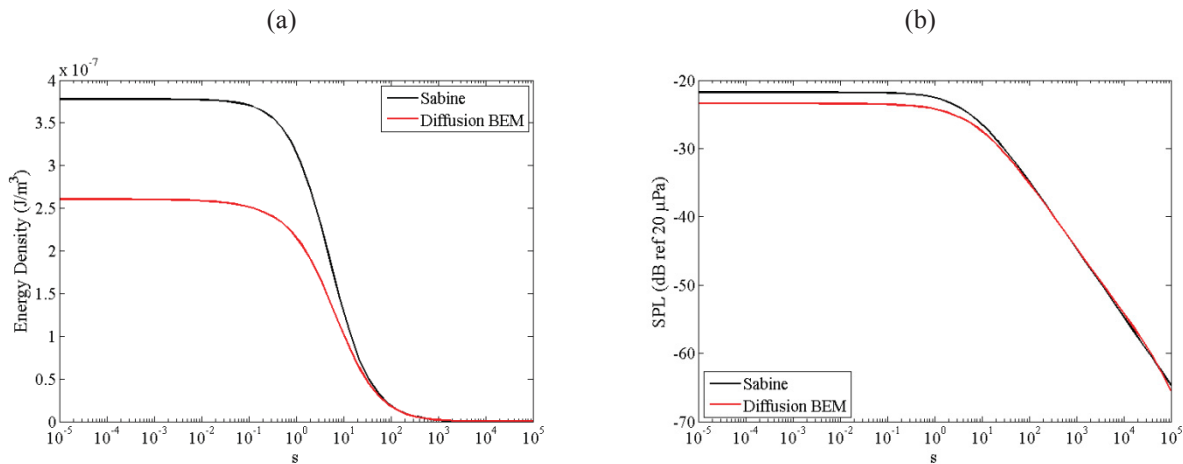
Figure 4.6: Laplace domain (a) energy density and (b) SPL using the Sabine analytical model and the acoustic diffusion model using increasingly refined grids for the integration of the initial condition in the cubic volume.

In the Laplace domain, the energy density exhibits a backwards S-shaped curve. At low values of the Laplace variable, this curve levels off at a particular value as demonstrated by taking the limit of eq. 4.24 which gives

$$\lim_{s\to 0}\Psi(s)=\psi_0 \tau_S. \tag{4.25}$$

The difference between the BEM solution and the Sabine model appears significant in energy density at these low values, but is less than 2 dB in terms of SPL. The different models come into closer agreement at mid to high values of the Laplace variable as the energy density decreases to

zero. This is also where the primary difference in numerical integration of the initial condition integral manifests as shown in the SPL. At high values of the Laplace variable, the use of less sub-volumes grants under-prediction of the energy density in the volume.

Physically, low values of the Laplace variable represent the steady state energy which is shown by the fact that $\lim_{s \to 0} \exp(-st) = 1$. Any exponentials that decay with low values of the Laplace variable are essentially a flat line when compared with exponentials that decay with a higher value of the Laplace variable. On the other hand, high values of the Laplace variable represent the initial energy. Exponentials that decay with an infinite rate (a very high Laplace variable value) are basically vertical lines at zero time representing the initial energy. Further evidence of this is provided by examining the effect of refining the initial condition integral in which the energy converges to the Sabine prediction at these high values.

Examining the Sabine model more closely, it is clear that only one value of the Laplace variable is used to describe the rate of exponential decay. That is, if eq. 4.23 is rewritten as

$$\psi(t) = \psi_0 \exp(-s_1 t),$$

4.26

then $s_1 = 1/\tau_S$. Interestingly, substituting this value into eq. 4.24 gives

$$\Psi(1/\tau_S) = 0.5\psi_0 \tau_S$$

4.27

which is exactly half the energy as the Laplace variable goes to zero. This information is the key for the determination of the Laplace variable values necessary to accurately invert the Laplace domain solution.

For the uniform cubic volume, the average Laplace variable at which the energy density is half of the energy density at very low values of the Laplace variable is 6.36. The value computed from eq. 4.27 is 5.15. Given that the domain of the transient region of the S-shaped curve is many orders of magnitude wide, eq. 4.27 provides a very close estimate of the correct value.

Also, the minimum value computed from the BE-LTS is 6.21 and the maximum is of 6.45. Thus, the variation of this value between receivers in the volume is very small with a standard deviation of 0.04 (less than 1 % of the mean value). The value computed from eq. 4.27 is 5.15.

Therefore, most of the Laplace variable values are chosen around this value and in the range from 1 to 10. The validation of this method is given in the next chapter.

Chapter 5: Initial Validation of the BE-LTS for Acoustic Diffusion

In this chapter, acoustic diffusion examples are considered to further examine the new BE-LTS method developed. Detailed comparisons are made with Sabine theory, ray tracing, and a FEM solution to the diffusion model for validation of the BE-LTS for acoustic diffusion. The ray tracing solutions and FEM solutions are computed with commercially available codes (Farina, 1995; COMSOL, 2007). Three volumes of increasing complexity are considered: 1) a uniform cubic volume, 2) a realistic rectangular volume, and 3) an L-shaped volume.

First, the volume configurations are described in terms of geometry, acoustic absorption, sources, and receivers. Three issues are then studied and discussed using the volume configurations: convergence of the numerical solution, accuracy of the numerical methods, and computational efficiency.

5.1 Volume Configuration Descriptions

In this section, the three volumes studied to provide the initial validation of the BE-LTS of the diffusion model are described. The three volumes, referred to as the uniform cubic volume, the realistic rectangular volume, and the L-shaped volume, are shown in Figure 5.1. The uniform cubic volume is selected because it accurately models the assumptions of Sabine theory which is then used as a baseline method of comparison. The realistic rectangular volume and L-shaped volume are used to demonstrate the capability of the diffusion model to adapt to more complex, realistic configurations for which analytical solutions do not exist.

Each volume contains a monopole source, a receiver grid (for average results in the volume), and lines of receivers (to examine distributions of acoustic parameters). The grid of 728 receivers is shown explicitly in the uniform cubic volume (spaced every 1 m). The realistic rectangular and L-shaped volumes contain grids of 896 (spaced 0.3 m apart) and 1099 (spaced every 0.35 m) receivers, respectively.
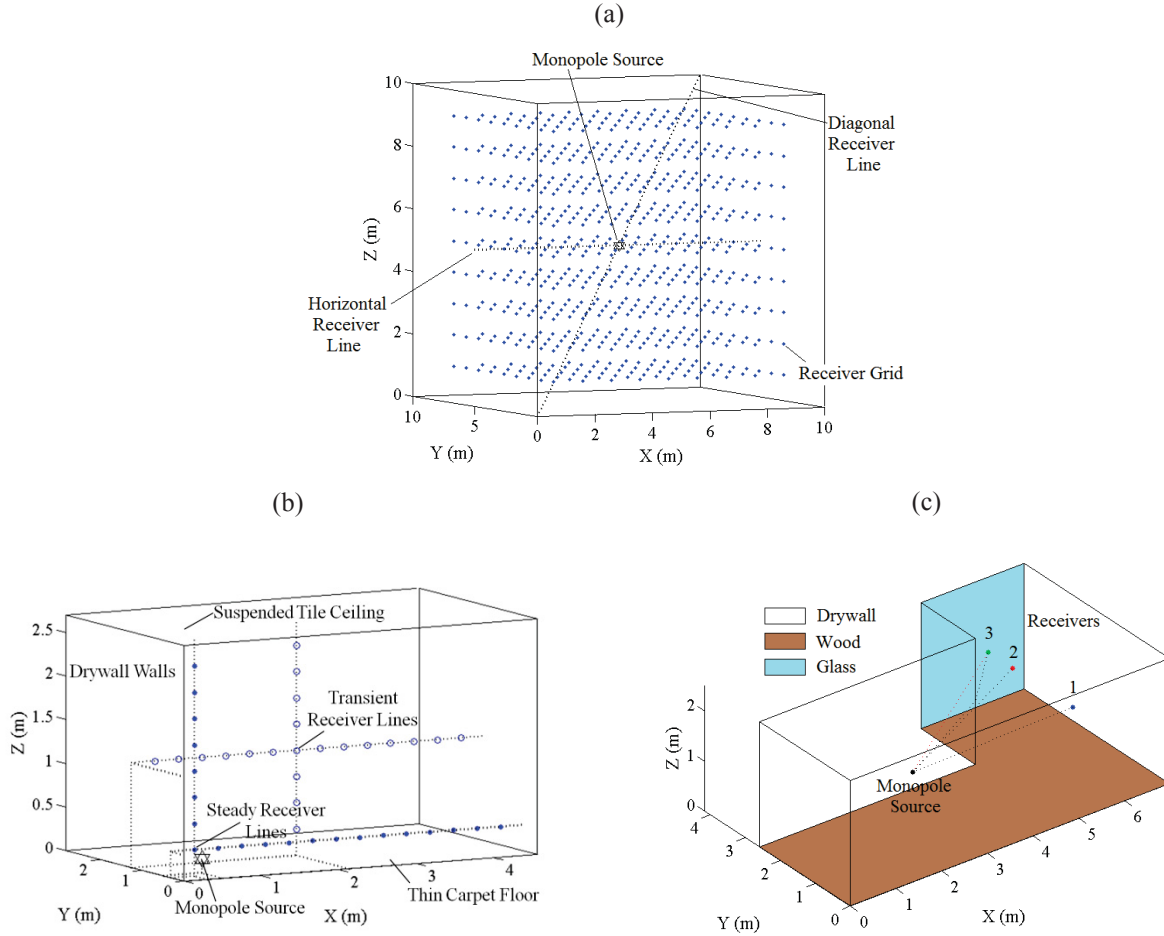
Figure 5.1: Example problem schematics for the (a) uniform cubic volume, (b) realistic rectangular volume, and (c) L-shaped volume used for initial validation of the BEM solution to the acoustic diffusion equation showing geometry, surface type, and source location.

The surface absorption coefficients for the volumes are plotted in Figure 5.2. Also, the ray tracing software used in this paper, Ramsete (Farina, 1995), automatically assumes an atmospheric absorption coefficient calculated by

$$m(f) = 1.7 \times 10^{-8} \frac{f^2}{\varphi\%} \qquad 5.1$$

where f is the frequency (in Hz) and $\varphi\%$ is the percent relative humidity. The relative humidity in the volume is selected to be 100 % to decrease the importance of the atmospheric attenuation, but it is included in all numerical calculations for valid comparisons.

(a)

(b)

(c)
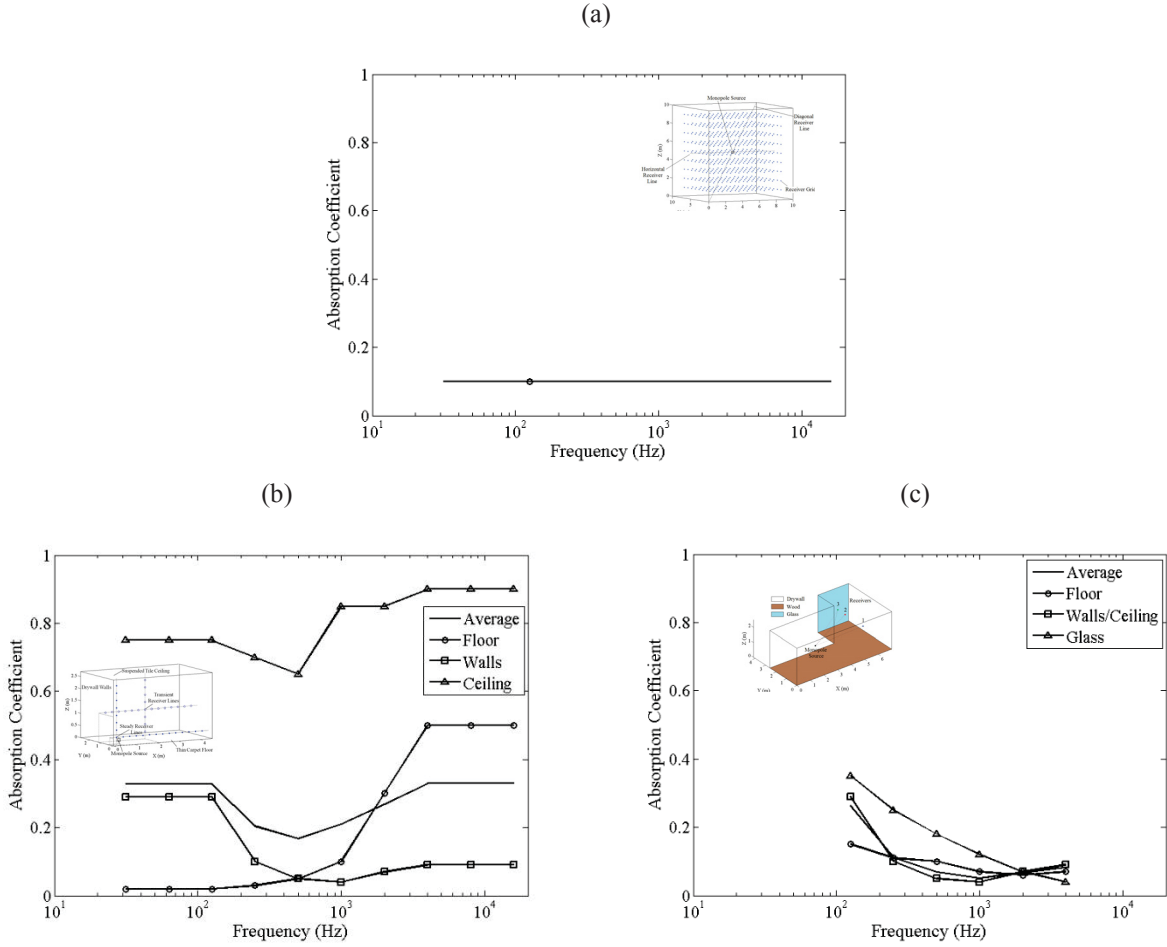
Figure 5.2: Surface absorption coefficients (Bies and Hansen, 2003) in octave bands of the (a) uniform cubic volume, (b) realistic rectangular volume, and (c) L-shaped volume.

The frequency bands (shown using symbols in Figure 5.2) under consideration vary for each case. Due to its uniform nature, the uniform cubic volume is only examined at a single frequency. This is sufficient in this case because the only frequency dependent parameter, the atmospheric attenuation, is set to be negligible at all frequencies. Frequency dependent results are examined for the other two configurations.

In the steady state problems, the SPL in the volume due to a constant point source radiating acoustic power (sound power levels of 100 dB in the uniform cubic and L-shaped volumes, and 96 dB in the realistic rectangular volume) is examined. Two different transient cases are considered using the three configurations: the decay from uniform acoustic energy in the uniform

cubic and realistic rectangular volumes and the buildup of acoustic energy in the L-shaped volume. The initial energies in the decay cases are computed with

$$\psi_0 = 4W / \left(S_r c \bar{\alpha} \right) \qquad\qquad 5.2$$

where W is the source power of the steady problem and $\bar{\alpha}$ is the area-weighted average absorption coefficient; this is the Sabine theory solution to the reverberant field of the steady problem.

5.2   Convergence Studies of Numerical Solutions

With any numerical method, convergence must be studied and obtained before the results of the method are meaningful. Numerical convergence is studied in detail for the uniform cubic volume and the realistic rectangular volume. The mesh refinement strategy used with the BE-LTS of the diffusion model is summarized in Figure 5.3 which shows the actual meshes of linear elements used to compute the solutions. Ellipses represent omitted meshes which continue in the same pattern as the previous.

(a)

(b)
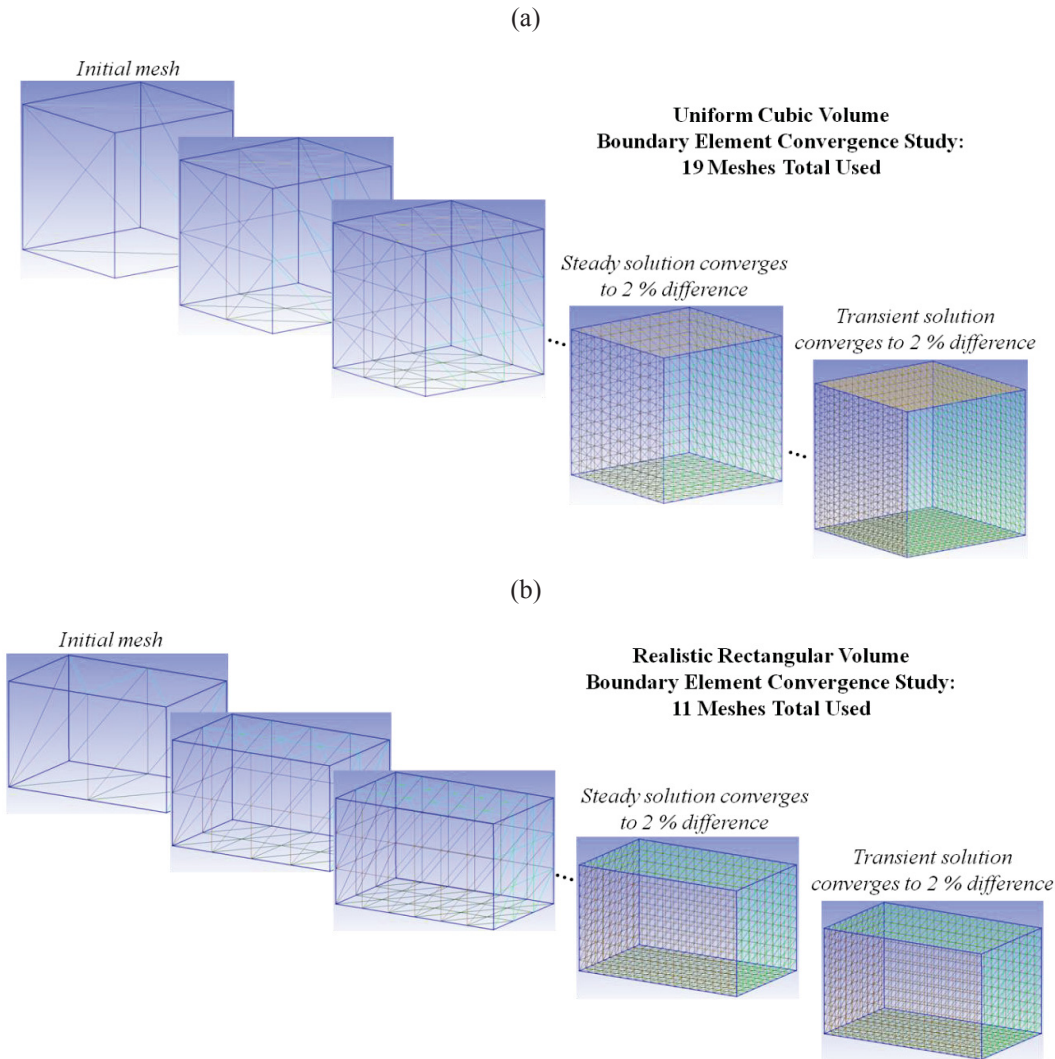
Figure 5.3: Boundary element mesh refinement used in the convergence study of (a) the uniform cubic volume and (b) the realistic rectangular volume.

As mentioned previously, a FEM solution to the acoustic diffusion model is also calculated using the commercial software (COMSOL, 2007) for comparison with the BEM solution which is the only other numerical tool that has been researched with the acoustic diffusion model. This is valuable as the comparison is between different methods of solving the same model. For the steady state problem, the monopole source is modeled as a small spherical volume, 0.003 % of the total volume (Valeau et al., 2006). The acoustic diffusion model is given by (Valeau et al., 2006)

$$\begin{cases} -D\nabla^2\psi(\mathbf{r},t) + mc\psi(\mathbf{r},t) = 0, & \mathbf{r} \in V - V_s \\ -D\nabla^2\psi(\mathbf{r},t) + mc\psi(\mathbf{r},t) = \dfrac{W}{v_s}, & \mathbf{r} \in V_s \end{cases} \qquad 5.3$$

with the same boundary conditions used previously given by eqn. 3.2. The FE meshes of the 3-D volume concentrate linear, Lagrange-type, tetrahedral elements in the small source volume that get larger as the position is moved towards the outer boundaries. The 3-D mesh and refinement strategy used in the convergence study of the steady state and transient problems are shown in Figure 5.4.

(a)

(b)
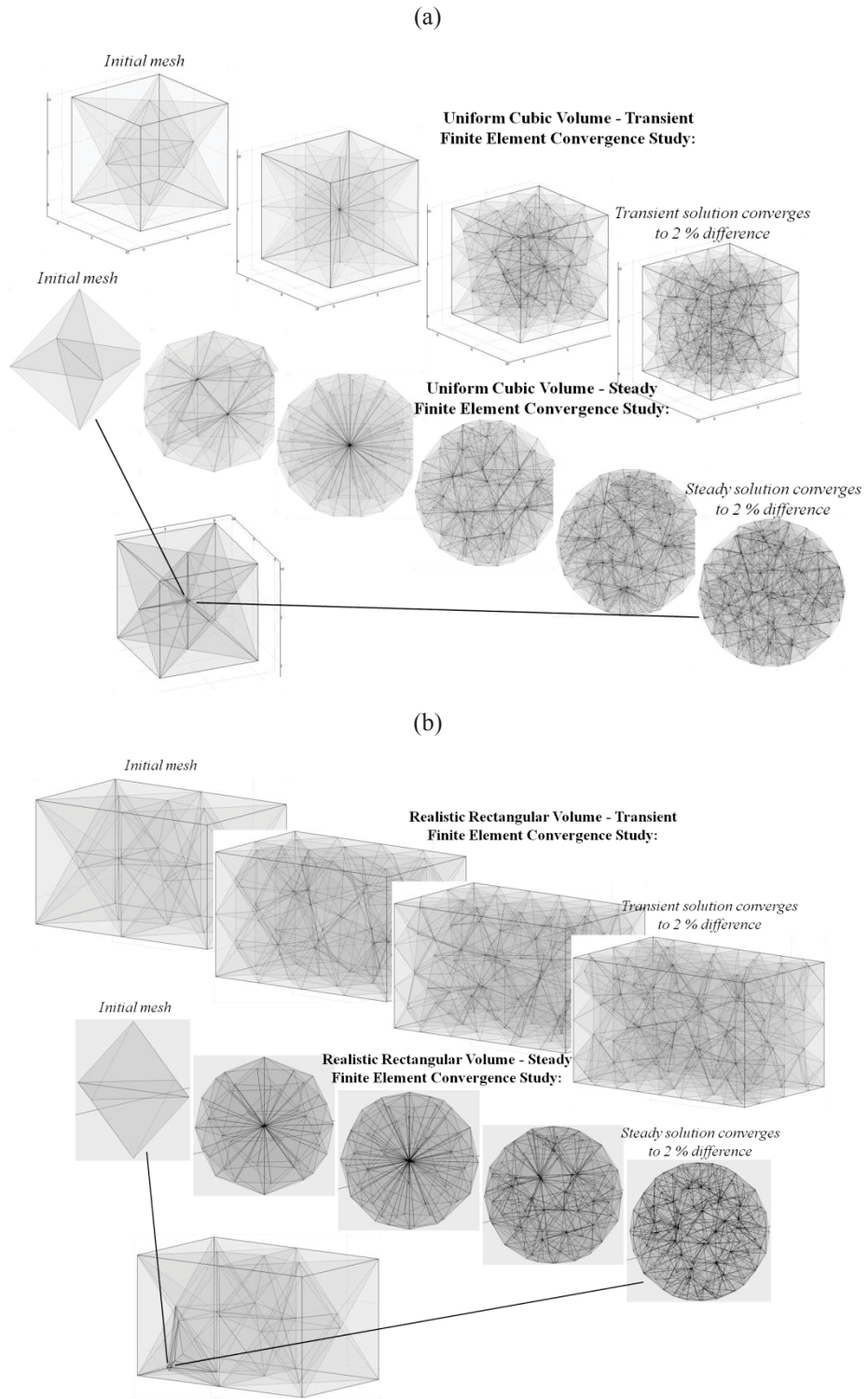
Figure 5.4: Finite element mesh refinement used in the convergence study of (a) the uniform cubic volume and (b) the realistic rectangular volume.

To provide validation of the BEM solution to the diffusion model through comparison with a completely different numerical method commonly used in room acoustics, this problem is also solved using the commercial software, Ramsete (Farina, 1995). Ramsete uses a technique in which 3-D pyramids carrying acoustic energy are emitted from a small spherical source and tracked as a function of time through the volume, i.e. ray tracing.

In Ramsete, the source is divided into 8×2^n pyramids where n is a positive integer. To obtain a valid comparison to the diffusion model, all surfaces are considered purely diffusely reflecting. Since ray tracing is an inherently transient technique, the steady state is taken to be the solution after 3 seconds have passed. Refinement in the ray tracing solution requires division of the source into more rays. To study convergence, the division level is simply increased. To simulate the transient decay using ray tracing, a source is placed at the center of the volume. The resulting impulse response is backwards integrated to calculate the Schroeder decay curve (Schroeder, 1965) which is used for comparison with the energy diffusion models and Sabine theory.

Convergence in the different numerical solutions is characterized as follows. The average energy density in the volume is compared to the previous discretization calculating a percent difference. For the steady state solution, the average steady state energy density is compared. The average energy density at the Sabine reverberation time is used to compare convergence in the transient solution.

The results of the convergence study in the uniform cubic volume are plotted in Figure 5.5. First, the average steady state SPL is plotted against the number of degrees of freedom (DOF) of the numerical solution (this is the number of rays for the ray tracing solution) in Figure 5.5(a). The percent difference in average steady state energy density is plotted against the number of DOF in Figure 5.5(b). Convergence to within 2 % difference is obtained extremely quickly in the FEM solution with less than 500 DOF. The BE-LTS requires more refinements than the FEM to obtain a convergent solution but still converges quickly to within 2 % difference with only 2000 DOF in the transient solution and about 1200 DOF in the steady solution. Ray tracing requires significantly more DOF to converge. Convergence to within 2 % difference is computed using

about 65000 pyramids in the steady state solution while only 10 % difference is obtained using 2097152 rays in the transient solution.

(a)   (b)
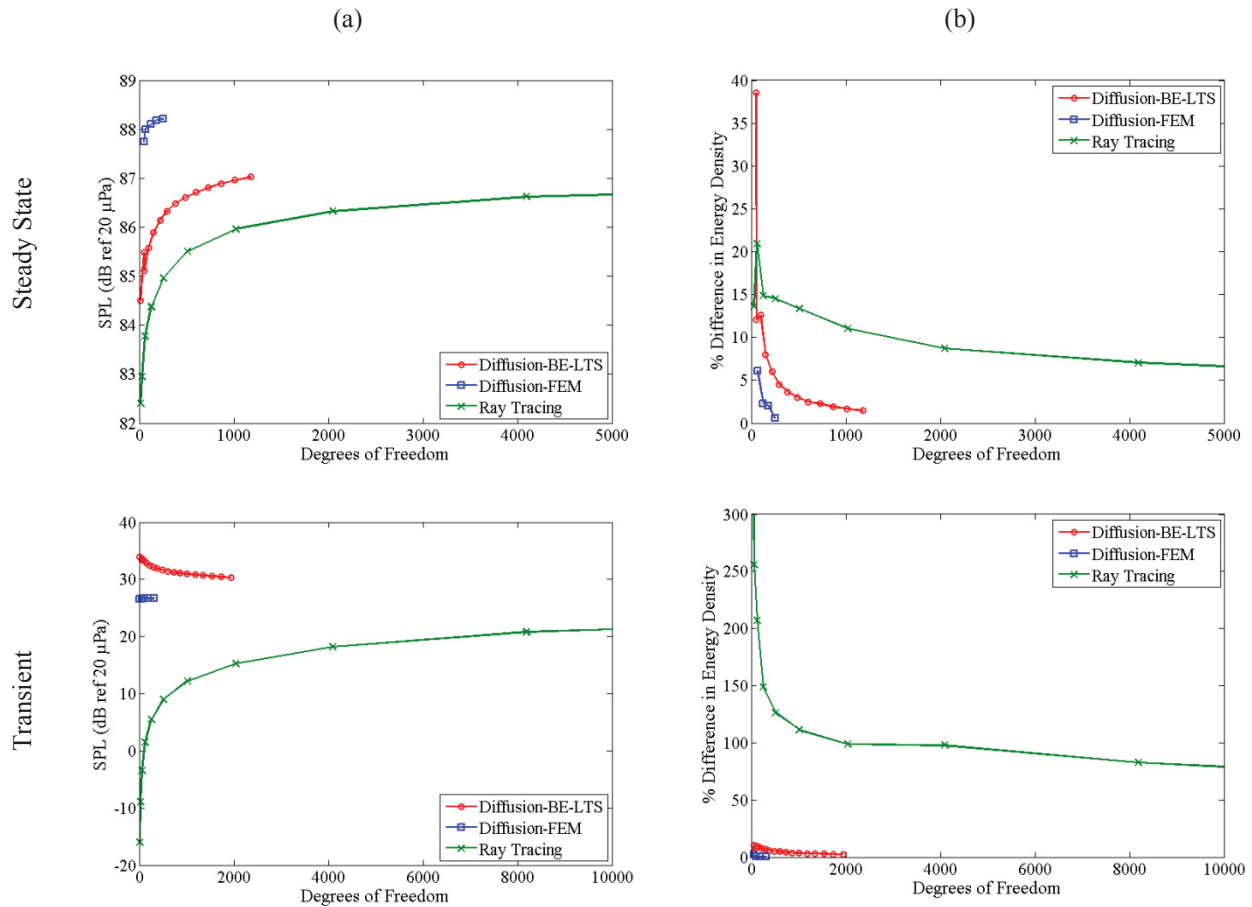
Figure 5.5: (a) Average SPL and (b) percent difference in average energy density in the uniform cubic volume for increasingly refined numerical solutions plotted against the number of degrees of freedom of the solution.

For the BE-LTS and FEM, the average steady state SPL is plotted against the number of elements per MFPL in Figure 5.6. This is done because the MFPL is the most relevant length scale in the acoustic diffusion model and provides a general guideline which can be applied to other problems. The transient BE-LTS converges to within 2 % difference using nine elements per MFPL, but needs less than seven for 2 % convergence in the steady solution. The transient FEM solution converges to within 2 % difference using about three elements per MFPL, while the steady FEM solution requires four.
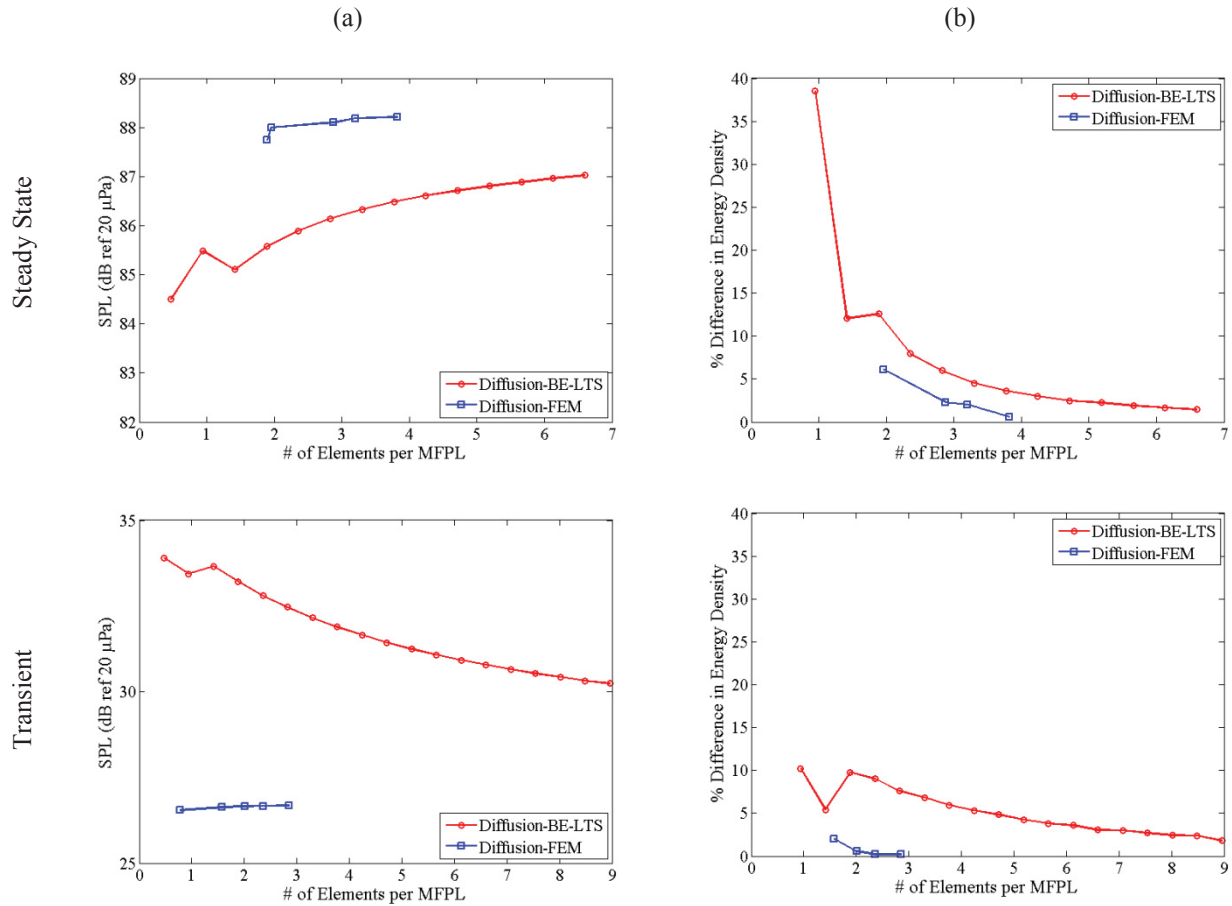
Figure 5.6: Average (a) SPL and (b) energy density percent difference in the uniform cubic volume for increasingly refined meshes plotted against plotted against the number of elements per mean free path length.

The results of a similar study in the realistic rectangular volume are summarized in Figure 5.7. The number of elements per MFPL required for convergence to within 2, 5, or 10 % difference is plotted in Figure 5.7 for the steady state and transient solutions in the uniform cubic and realistic rectangular volumes.

In the steady problems, the BEM consistently needs at least 2.5 elements per MFPL for 10 % convergence, 3 elements per MFPL for 5 % convergence, and 5 per MFPL for 2 % convergence which appears to demonstrate an exponentially increasing trend with lower convergence levels. The FEM, on the other hand, shows a linear trend but requires about one more element per MFPL for the smaller non-uniform rectangular volume than the larger uniform cubic volume which must be due to either the size of the volume or the varying absorption.

In the transient problem, the BEM demonstrates an exponentially increasing trend with level of convergence. However, the rate of increase is different depending on the volume. The FEM solution converges very quickly in this case requiring only about two elements per mean free path length for convergence to 2 % difference. The faster convergence in the transient compared to the steady problem in the FEM solution is likely due to the absence of the very small source volume which requires a significant number of elements to model.

(a)   (b)
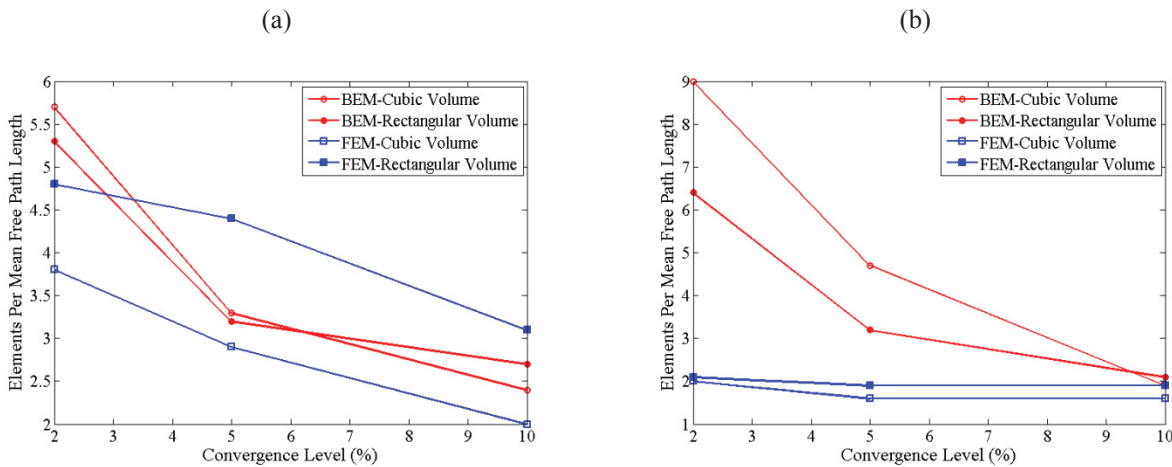
Figure 5.7: Number of elements per MFPL required for convergence of the numerical solutions to the diffusion model in (a) steady and (b) transient cases of the uniform cubic and non-uniform rectangular volumes.

5.3 Accuracy of the Diffusion BE-LTS
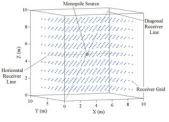
In this section, the accuracy of the BE-LTS is validated through comparison with other analysis methods. In the uniform cubic volume, the analytical Sabine solution is expected to be the most accurate because the configuration is designed to accurately model Sabine theory assumptions. No analytical solution exists for the more realistic volumes. However, Sabine theory is still used for comparisons with diffusion and ray tracing. Ray tracing is used exclusively for the comparisons in the L-shaped volume. First, the steady state SPL due to a source of acoustic power is examined in the three volume configurations. Then, the transient problems are examined.

5.3.1 Steady State Comparisons

The average SPL in the uniform cubic volume is given in Table 5.1 and in the realistic rectangular volume in Figure 5.8. Note that the divisions of the y-axis in Figure 5.8 are only 1 dB

to show the trend more clearly. In general, all three methods are in very close agreement. In the uniform cubic volume, the average SPL in the volume differs from Sabine theory by less than 1 dB using the BE-LTS, less than 0.5 dB using the FEM, and only 1.2 dB using ray tracing. In the realistic rectangular volume, all methods agree mostly within 2 dB with the largest discrepancy between diffusion and ray tracing at low frequencies. The decrease in the last three octave bands which is not captured with Sabine theory is due to the air absorption (absent from Sabine theory) becoming significant.

Table 5.1: Comparison in average acoustic energy density and SPL in the uniform cubic volume using different methods and Sabine theory as a reference.

Method	Average SPL (dB ref 20 x 10⁻⁶ Pa)	Absolute Difference (dB)
Sabine Theory	88.4	0 (reference)
Diffusion BE-LTS	87.6	0.8
Diffusion FEM	88.7	0.3
Ray Tracing	87.2	1.2
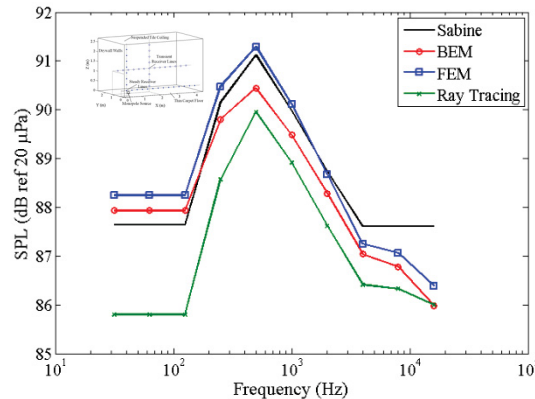
Figure 5.8: Steady state SPL averaged across all receivers in the realistic rectangular volume.

The SPL along lines of receivers running through the center of the uniform cubic volume is plotted in Figure 5.9. Again, note the very small scales (1 dB/div and 0.5 dB/div). Both solutions to the diffusion model capture the trend of Sabine theory with high levels close to the source which monotonically decrease with distance from the source. However, this decrease is more

drastic for both solutions along both lines with exception of the FEM solution along the horizontal line which captures a nearly identical decrease. The ray tracing solution decreases with distance from the source to a point, then begins to increase as acoustic energy builds up close to the boundaries of the volume. This is a unique trend which is not captured by any other method used. The SPL computed with the ray tracing method is always below the Sabine SPL.

(a)   (b)
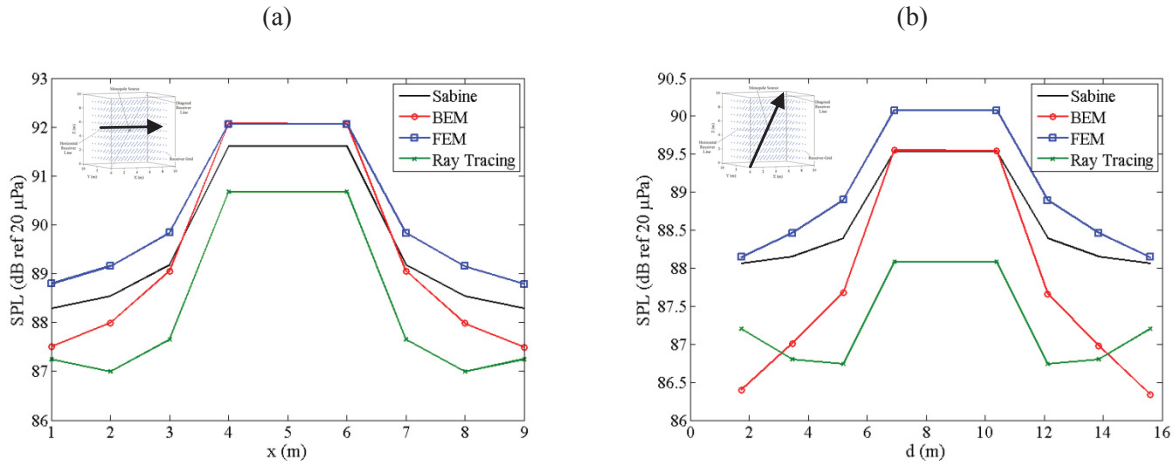
Figure 5.9: Steady state SPL in the uniform cubic volume with a source at the center of the volume at several points along (a) a horizontal line and (b) a diagonal line through the center of the volume.

The steady state SPL along the steady receiver lines in the realistic rectangular volume is plotted for two octave bands, with the lowest and highest absorption (500 Hz and 16 kHz, respectively), in Figure 5.10. Overall, the results are very similar to those of the uniform cubic volume. Closer agreement with Sabine theory is obtained in the 500 Hz band with light absorption, which is one of the assumptions of Sabine theory. The two diffusion model solutions agree very closely in the 16 kHz band with heavy absorption and compare quite favorably to ray tracing as well. Larger discrepancies are demonstrated in this octave band when compared to Sabine theory. In each case, the slope of the SPL is steeper with the numerical methods than with Sabine theory, with the exception of the leveling off and subsequent increase demonstrated with ray tracing in the horizontal receiver line.

Along the vertical lines, the slope is closer to linear with the numerical methods due to the distribution of absorption in the volume. The ray tracing no longer shows the buildup of energy

close to the highly absorbent ceiling. Sabine theory does not capture the effect of the varying absorption. All three numerical methods demonstrate very close agreement in each case.

(a)   (b)

Figure 5.10: Steady state SPL in the non-uniform rectangular volume at several points along the (a) horizontal and (b) vertical steady receiver lines for the 500 Hz and 16 kHz bands.

The steady state SPL distribution in the L-shaped room calculated using the diffusion BE-LTS and ray tracing is plotted for comparison in Figure 5.11 for three octave bands. The difference in steady state SPL between the two methods obtained by subtracting the ray tracing SPL from the diffusion BEM is plotted in Figure 5.12 for the same octave bands. In the 125 Hz octave band, the overall level in the room is higher when using diffusion BE-LTS compared to ray tracing. The maximum difference (3.1 dB) occurs in the region hidden from line of sight of the source with the diffusion BEM predicting levels higher than ray tracing by 2.5 to 3 dB. The diffusion BEM predicts higher levels in this region even though edge diffraction is included in

the ray tracing calculation. Another region of discrepancy between the two methods is in a sphere surrounding the source of about a 1 m radius.

The two methods match to within a 1.5 dB difference everywhere in the room in the 250 Hz octave band. In this case, the largest discrepancies occur in the corners of the room furthest from the source. The overall level in the room calculated by the BEM is lower than that computed by ray tracing in the 1 kHz octave band, the band with the lowest absorption. Again, the largest discrepancies occur in the corners of the room furthest from the source where the diffusion BEM predicts levels lower than ray tracing by about 2 dB. In summary, when the absorption in the room is low, the diffusion BEM predicts lower levels than the ray tracing method. When the absorption in the room is high, the diffusion BEM predicts higher levels than ray tracing. Overall, however, the steady state SPL results demonstrate very good agreement between the two methods.
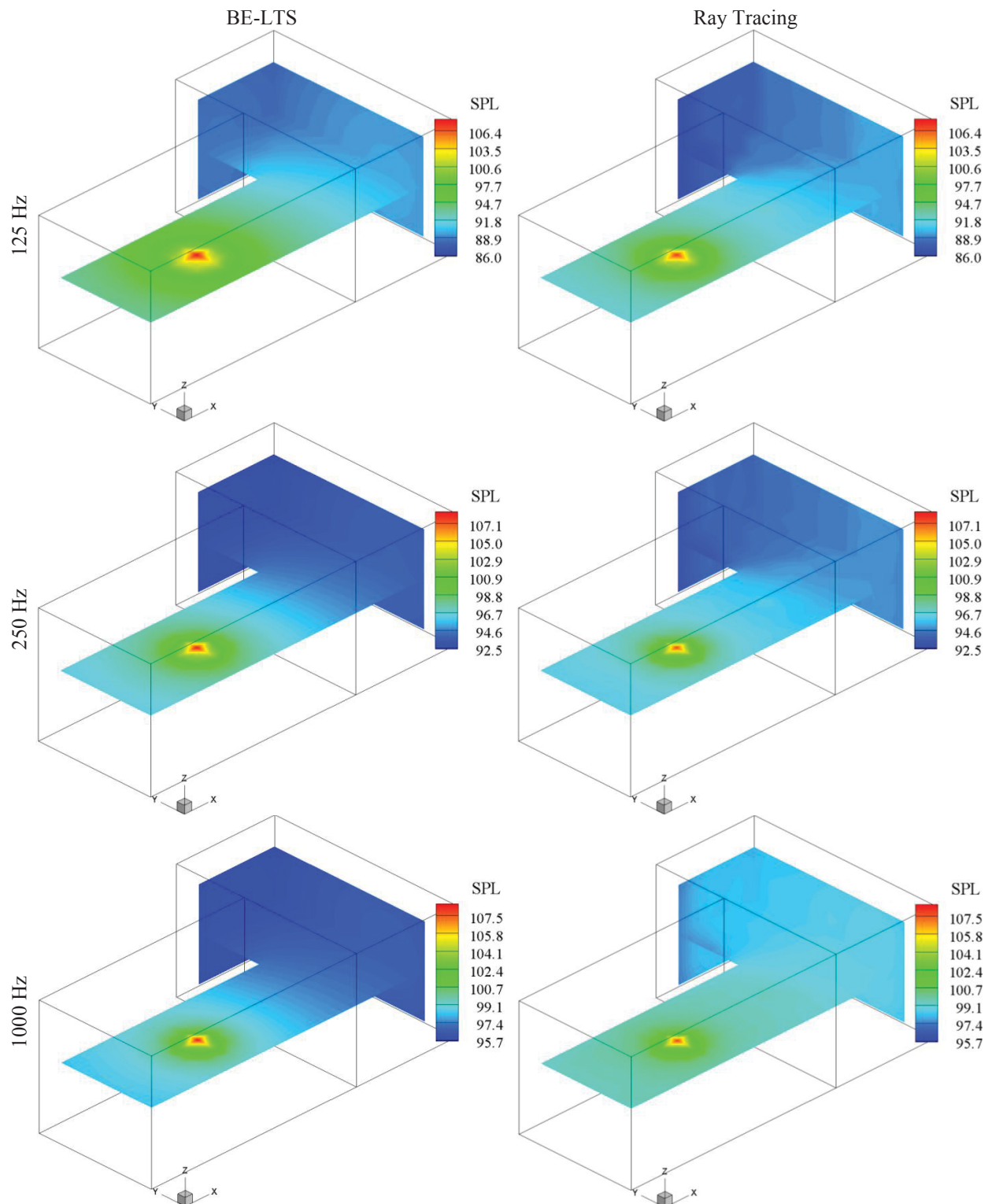
Figure 5.11: Steady SPL throughout the horizontal mid-plane and two vertical surfaces of the L-shaped volume computed with the diffusion BE-LTS and ray tracing for the 125 Hz, 250 Hz, and 1 kHz octave bands.
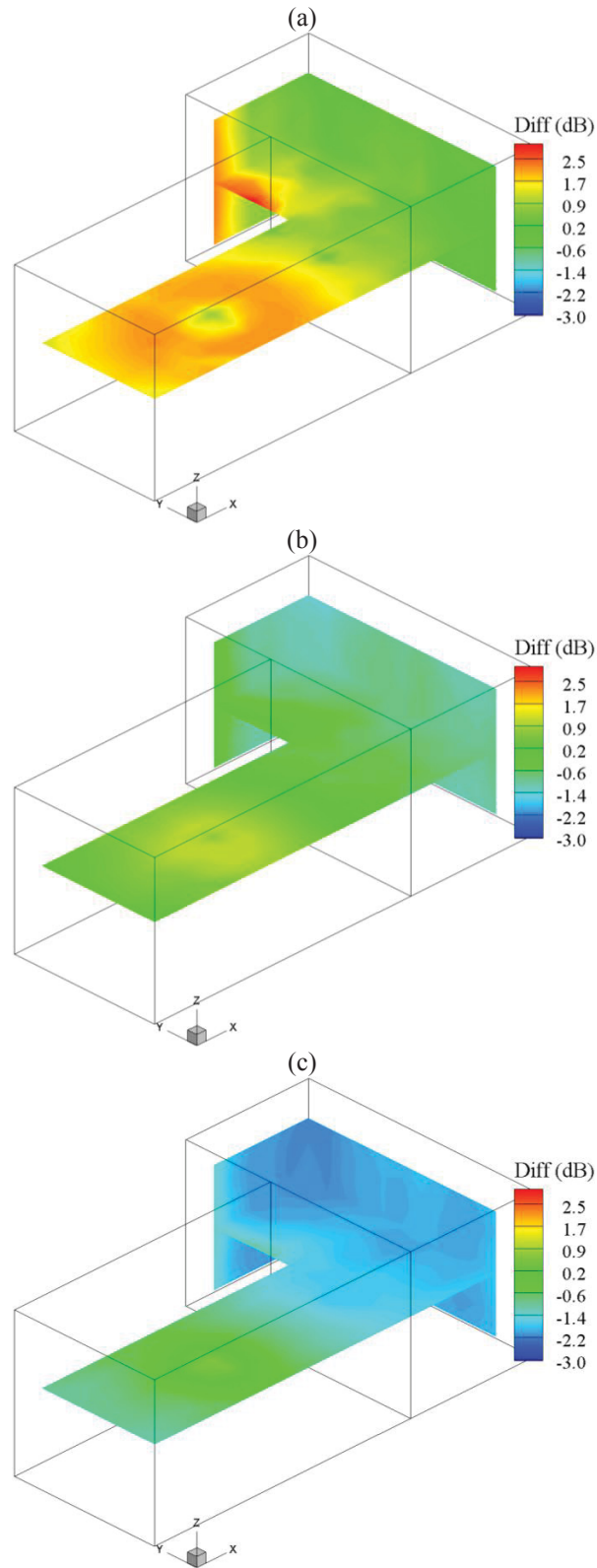
Figure 5.12: Steady SPL difference (diffusion BE-LTS SPL minus ray tracing SPL) throughout the horizontal mid-plane and two vertical surfaces for the (a) 125 Hz, (b) 250 Hz, and (c) 1 kHz octave bands.

5.3.2 Transient Comparisons

The SPL decay averaged across all receivers in the uniform cubic volume and realistic rectangular volume at each time step is plotted in Figure 5.13. Using the method to estimate the critical Laplace value, the numerical inverse Laplace transform is computed using three values of the Laplace variable. In the uniform cubic volume, these are the average value discussed in the previous chapter, 6.36, one value 25% below the average value and one value 25 % above the average. The BE-LTS solution demonstrates more curvature in the uniform cubic volume than the linear Sabine theory with a steep drop from 0 to 1 s. The FEM solution stays fairly linear but with a steeper slope than Sabine theory. The ray tracing solution agrees closely at the beginning, but develops a flatter slope than Sabine theory after 1.5 s.

In the realistic rectangular volume, there is a significant discrepancy between ray tracing and the diffusion model with the diffusion model predicting a significantly steeper decay slope. Sabine theory, a model independent of either ray tracing or the diffusion model, agrees more closely with the diffusion model in both cases. The BEM solution gives a steeper decay slope than the FEM. It is unclear which method provides the most accurate solution, but the agreement between the diffusion model and Sabine theory gives evidence that they may be closer to reality.
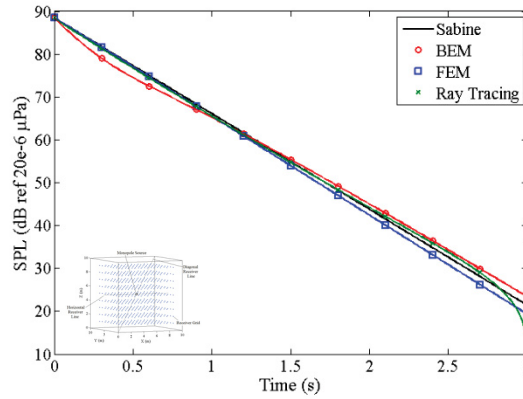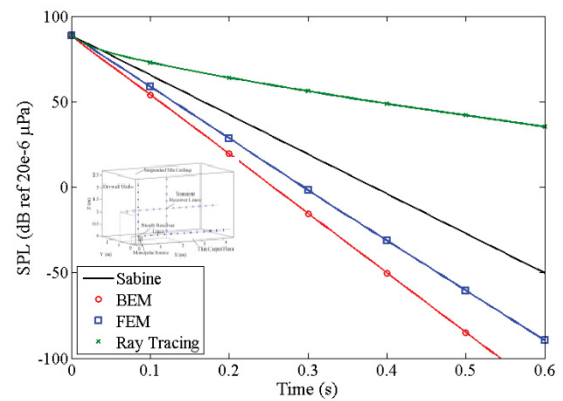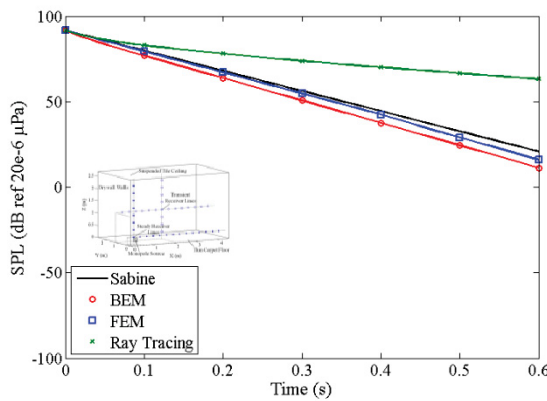
Figure 5.13: Decay of SPL from a uniform initial acoustic energy distribution averaged across all receivers in the uniform cubic volume and realistic rectangular volume in the 500 Hz and 16 kHz bands.

Next, the reverberation times in the uniform cubic and realistic rectangular volumes are calculated by the time taken for the SPL at each receiver to decay from the initial value by 60 dB. An overall reverberation time averaged across all receivers is calculated for each method and is given in Table 5.2 for the uniform cubic volume and in Figure 5.14 for the realistic rectangular volume. In the uniform cubic volume, all three methods provide a very accurate reverberation time to within 100 ms. In the realistic rectangular volume, the reverberation times calculated with the diffusion model and Sabine theory agree quite closely, while ray tracing gives significantly higher values (especially for octave bands with low absorption). Most likely, the issue is related to the method used to model reverberant energy in the ray tracing software which does not create realistic decay for this type of energy (Farina, 2000). As with steady state SPL, the drop in reverberation time captured by the diffusion model and ray tracing at high frequencies does not appear in Sabine theory due to the lack of modeling air absorption.

Table 5.2: Comparison in average reverberation time in the uniform cubic volume using different methods and Sabine theory as a reference.

Method	Average Reverberation Time (s)	Percent Difference (%)
Sabine Theory	2.68	0
Diffusion BEM	2.75	2.59
Diffusion FEM	2.61	2.65
Ray Tracing	2.73	1.76
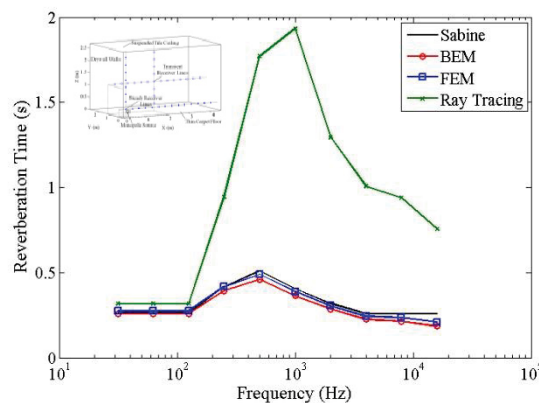
Figure 5.14: Reverberation time averaged across all receivers in the non-uniform rectangular volume.

The reverberation time is plotted in Figure 5.15 for receivers along the same lines through the volume as in Figure 5.9. Note the y-axis scales of these plots are very small with 50 ms divisions to show the details of the distribution. The BE-LTS demonstrate significantly more variability in reverberation time than any other method. It varies along the horizontal receiver line, but appears to have an average value very close to the FEM solution. The BEM is relatively inaccurate at several positions on the diagonal line (as much as 0.3 s), but extremely accurate near the corners and center of the room (within 50 ms). This is due to inherent instability in the numerical Laplace inversion procedure.

The FEM solution displays a very uniform trend (in agreement with Sabine theory), but consistently under-predicts the reverberation time by about 70 ms. Ray tracing predicts a fairly uniform reverberation time but decreases slightly towards the edges of the volume due to the build-up of energy demonstrated in the steady state problem. Nevertheless, it is very accurate

with less than 70 ms error in the worst cases towards the center of the volume and only about 35 ms error towards the edges of the volume.

(a)   (b)
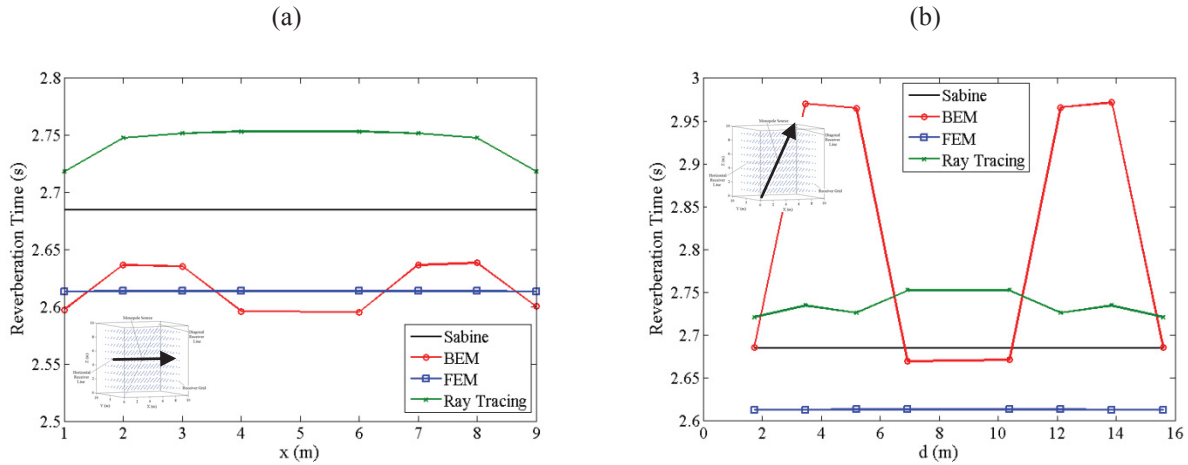
Figure 5.15: Reverberation time in the uniform cubic volume at several points along (a) a horizontal line and (b) a diagonal line through the center of the volume.

The reverberation times in the realistic rectangular volume for the 500 Hz and 16 kHz bands are plotted along the transient receiver lines in Figure 5.16. The diffusion models and Sabine theory demonstrate essentially uniform trends. Ray tracing appears to capture a more varying trend along either line.

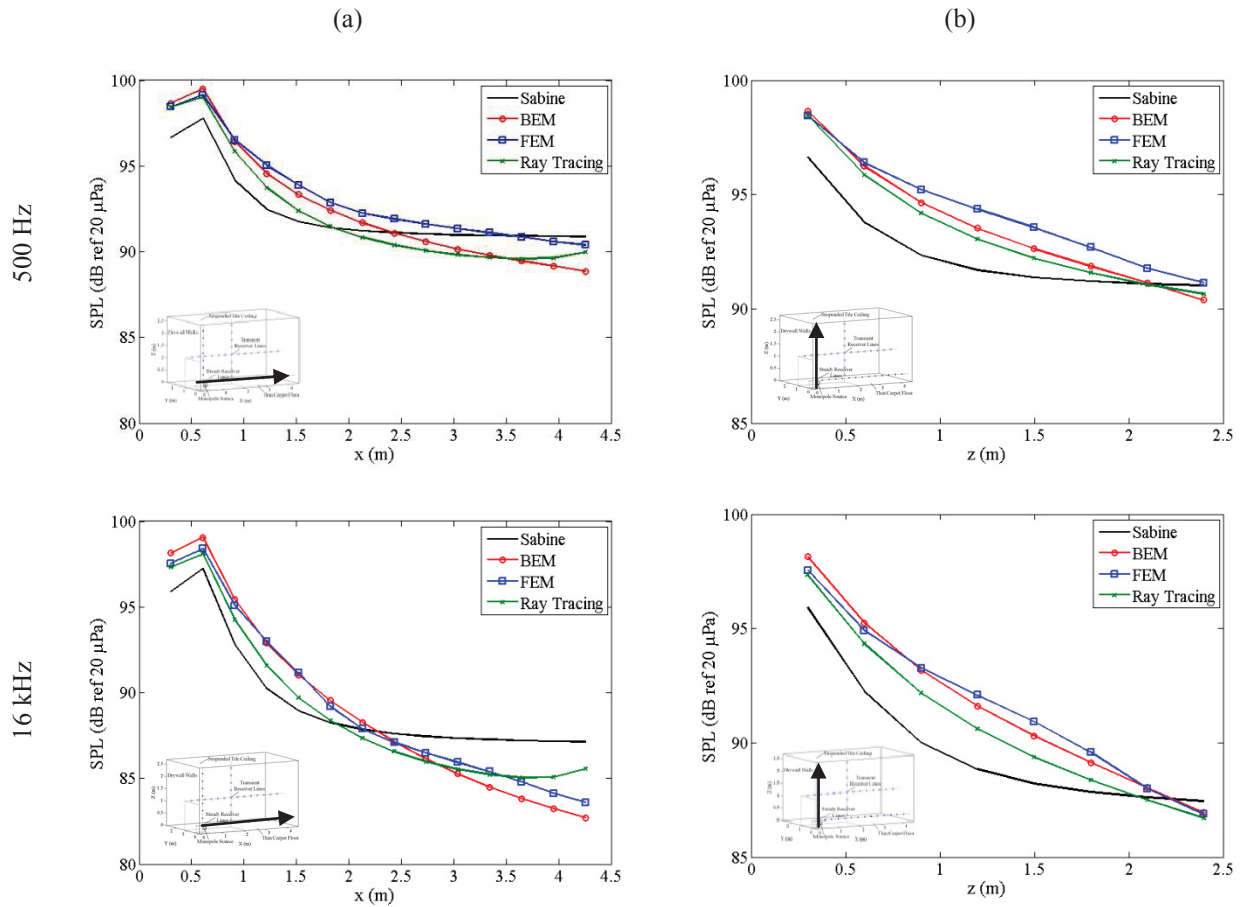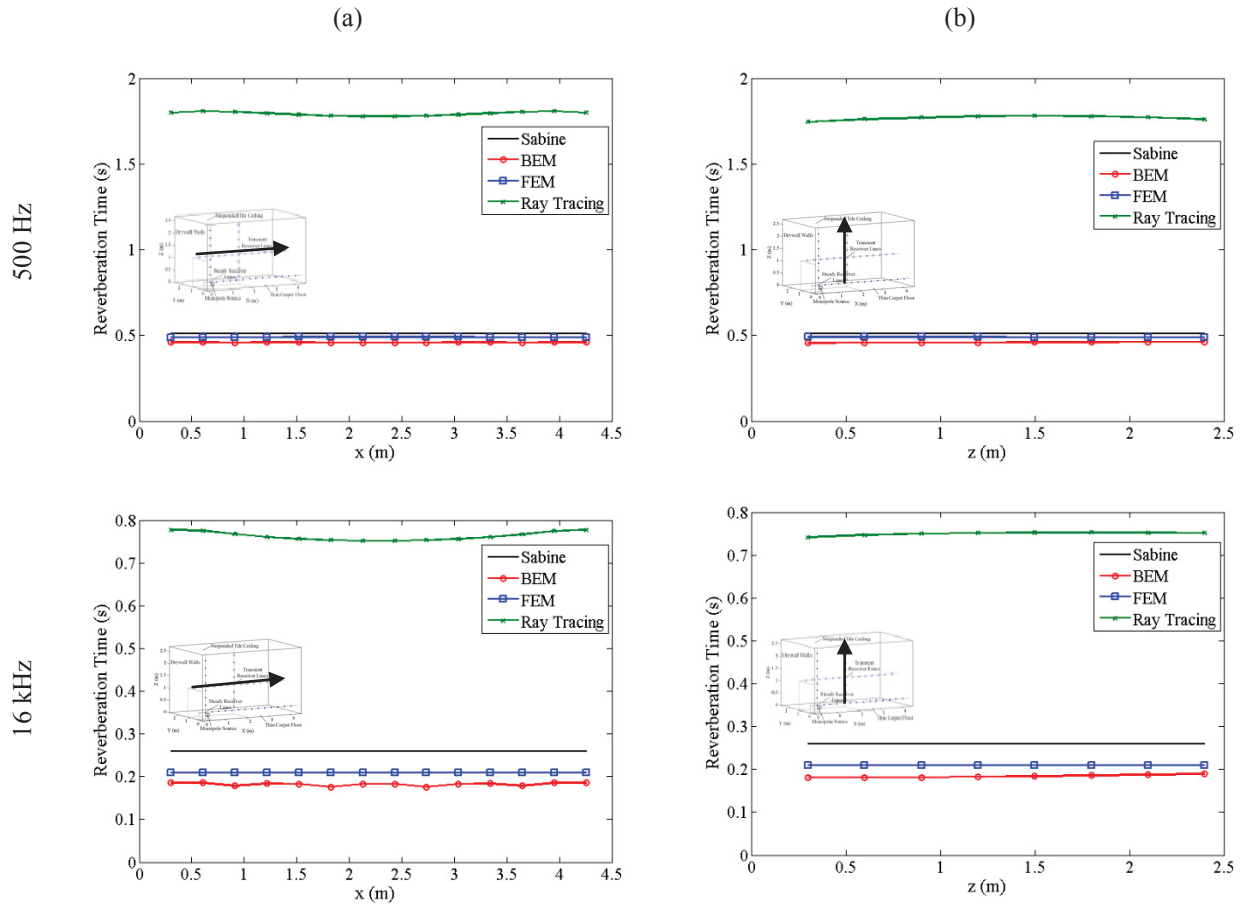**Figure 5.16:** Reverberation time in the non-uniform rectangular volume at several points along the (a) horizontal and (b) vertical transient receiver line for the 500 Hz and 16 kHz bands.

The transient SPL in the L-shaped volume is plotted in Figure 5.17 for Receivers 1, 2, and 3 for the 125 Hz and 1 kHz octave bands. In each case, the exponential increase is nearly identical between the BE-LTS and ray tracing methods with both sets of results reaching their respective steady state levels at about the same time. The role the absorption plays is evident as the three receivers reach steady state levels much quicker in the high absorption case in the 125 Hz octave band than in the low absorption case in the 1 kHz band. Each receiver reaches its steady state value at about the same time whether it is in direct line of sight with the source or not.
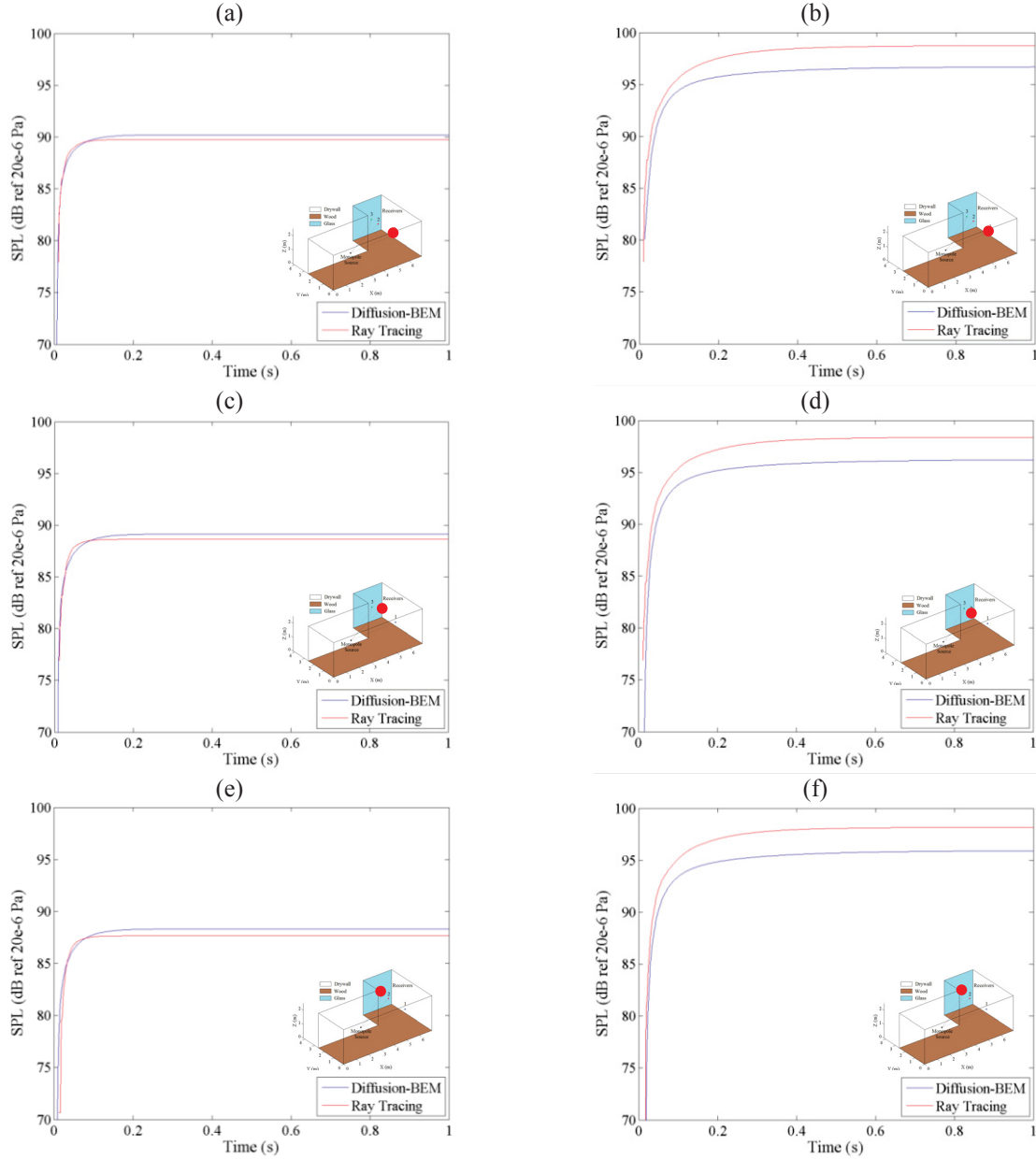
Figure 5.17: Transient sound pressure level in the L-shaped room calculated using the diffusion BE-LTS and ray tracing for the (a,c,e) 125 Hz and (b,d,f) 1 kHz at the position of (a,b) Receiver 1, (c,d) Receiver 2, and (e,f) Receiver 3.

5.4   Computational Efficiency of Numerical Methods

The total computation time for each solution method is timed using a desktop personal computer with an Intel Core i5 3 GHz quad-core processor and 8 GB of RAM. The BE-LTS to the diffusion model is written in the Fortran programming language. Thus, the computational comparisons are assumed to be valid because consistent programming languages, i.e. codes

compiled into an executable file and run, are used, e.g. Fortan and C++. Care is taken to ensure similar memory and processor states for each method through complete shutdown and boot up of the computer before each run. The computation times required to calculate the steady state solution in the uniform cubic volume are tabulated for each convergence level in Table 5.3. The number of DOF and error compared to the Sabine solution is also tabulated for comparison.

The two different methods of solving the diffusion model, i.e. BE-LTS and FEM, have comparable computation times. The BE-LTS gives quicker solutions to lower levels of convergence while the FEM is faster when calculating the most convergent solution. While both diffusion solutions take only a fraction of a second to obtain a solution, ray tracing takes minutes or more. Clearly, the diffusion model is superior to ray tracing in terms of computational efficiency for this problem.

Comparing numerical solutions with similar numbers of DOF (highlighted in green), a BE-LTS with 2168 DOF takes almost five seconds to compute while a ray tracing solution with 2048 DOF still takes over two minutes to compute (146 s). Examining solutions with similar error (highlighted in blue), the 5 % convergent steady BE-LTS and 10 % convergent steady ray tracing solution both exhibit 2.1 dB error compared to the Sabine solution. In this case, the BE-LTS takes 78 ms while the ray tracing solution requires 146 s to compute a solution. For steady solutions which both have about 1.5 dB error, the BE-LTS requires 0.36 s and ray tracing 1098 s.

Table 5.3: Comparison of computation times, number of degrees of freedom, and error for solutions in the uniform cubic volume to three different levels of convergence.

	Parameter	Steady Convergence Level			Transient Convergence Level		
		10%	5%	2%	10%	5%	2%
Diffusion BE-LTS	DOF (#)	152	296	866	56	602	2168
	Error (dB)	2.5	2.1	1.5	5.0	3.0	1.8
	Computation Time (s)	0.032	0.078	0.359	0.078	0.608	4.991
Diffusion FEM	DOF (#)	67	125	250	55	55	103
	Error (dB)	0.4	0.3	0.2	1.8	1.8	1.7
	Computation Time (s)	0.109	0.109	0.125	0.218	0.218	0.234
Ray Tracing	DOF (#)	2048	16384	65536	2097152	---	---
	Error (dB)	2.1	1.4	1.2	1.3	---	---
	Computation Time (s)	146	1098	4088	126861	---	---

The computation times and number of DOF required to obtain solutions to the three different convergence levels for ten octave bands in the realistic rectangular volume are tabulated in Table 5.4 for each numerical method. In this volume, it is clear that the FEM is more efficient than the BE-LTS in almost every case due to the relatively small size, while they are both still comparable. Also, the BE-LTS has a greater computational efficiency expense for increased levels of convergence than the FEM. An obvious explanation for the superior efficiency of the FEM is unclear due to the black-box nature of the commercial FE software. The most likely explanation is that the FE software is a parallelized code capable of running computations on multiple processor cores while the BE-LTS code is not written in parallel and utilizes only one core of the quad-core processor used.

The BE-LTS gains some computational efficiency advantage over the FEM in the significantly larger uniform cubic volume at lower levels of convergence as the FEM solution generally converges very quickly. Thus, the expected trend of greater computational efficiency from the BE-LTS as the size of the volume increases is demonstrated.

Comparing the diffusion BE-LTS to ray tracing, the computation time of the BE-LTS is on the order of seconds compared to ray tracing which is on the order of minutes for lower levels of convergence and hours for the highest convergence level. Even for a similar number of DOF

(highlighted in green), the steady BE-LTS takes only 5 % of the computation time compared to ray tracing. However, considering transient solutions, a BE-LTS with 1442 DOF takes 30 s and ray tracing with 1024 DOF takes 113 s. Thus, the efficiency advantage of the BE-LTS in transient problems is slightly reduced. Still, the BE-LTS demonstrates significant computational efficiency advantage over ray tracing.

Table 5.4: Comparison of computation times and number of degrees of freedom for solutions in the realistic rectangular volume to three different levels of convergence.

	Parameter	Steady Convergence Level			Transient Convergence Level		
		10%	5%	2%	10%	5%	2%
Diffusion	DOF (#)	252	362	1002	162	362	1442
BE-LTS	Computation Time (s)	1.87	2.66	5.78	1.71	4.06	30.09
Diffusion	DOF (#)	131	211	272	100	100	128
FEM	Computation Time (s)	1.09	1.24	1.41	2.34	2.34	2.50
Ray	DOF (#)	1024	8192	65536	1048576	---	---
Tracing	Computation Time (s)	113	880	7703	126861	---	---

Chapter 6: Acoustic Diffusion with Structural Coupling

In this chapter, an investigation of acoustic volumes coupled to vibrating structural components (structural acoustics) using the BE-LTS method developed is presented. First, a review of common energy methods used in structural acoustic analysis is presented. Then, the BE-LTS to the acoustic diffusion model with structural coupling is presented for two cases: implemented through 1) a simple transmission coefficient and 2) a more sophisticated coupling using a structural power flow model. Finally, the two formulations are validated for the case of acoustic transmission from a uniform cubic volume to a similar uniform cubic volume through a partition. The validation is undertaken through comparison of the diffusion BE-LTS to the diffusion FEM solution, statistical energy analysis (SEA), ray tracing, and experimental data.

6.1 Review of Current Structural-Acoustic Energy Models

In this section, common energy models used in structural acoustic analysis are discussed. They are SEA, radiosity, and power flow models which form the basis of the energy finite element method (EFEM). Statistical energy analysis is used for validation of the BE-LTS to the diffusion model later in this chapter. The power flow models of vibrating structures are implemented in the BE-LTS of the diffusion model for acoustic volumes coupled to a structure. Radiosity and the EFEM are new methods for acoustic analysis which can be considered alternatives to the diffusion BE-LTS and are presented briefly to discuss their differences.

6.1.1 Statistical Energy Analysis

Perhaps the most common high frequency analysis method for problems which include both acoustic and structural systems is SEA. The method allows for the analysis of energy flow between coupled resonant structures and acoustic cavities and is described briefly in this section.

Consider a subsystem (acoustic or structural) of resonant modes, all with equal energy, over a frequency band. Next, consider a similar subsystem coupled to the first forming a system as shown in Figure 6.1.
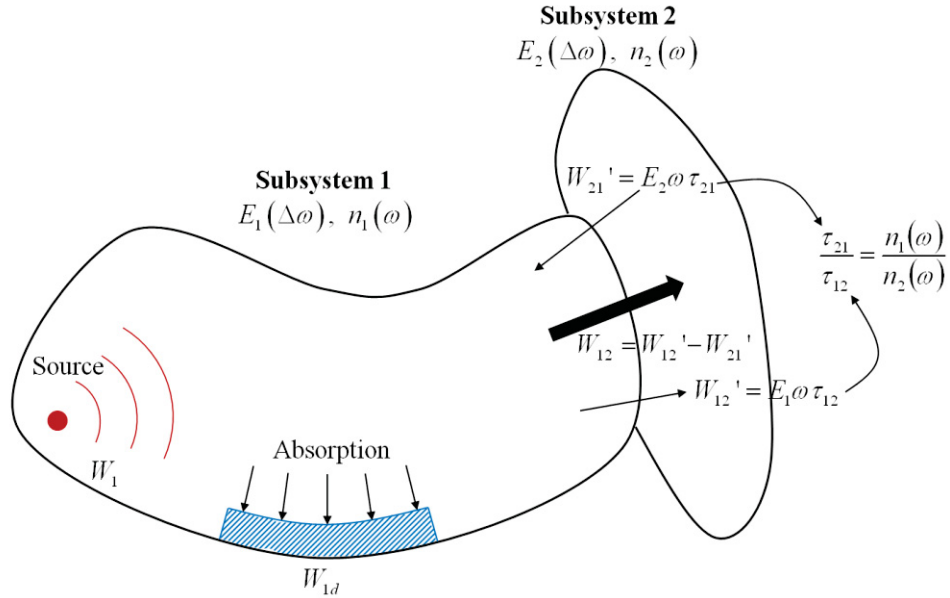
Figure 6.1: Schematic demonstrating statistical energy analysis.

An expression for the power transmitted is derived assuming all the resonating modes in the frequency band transfer energy from one subsystem to the other similarly and that the modes between subsystems are uncorrelated. The analytical expression is based on the modal density of resonating modes and coupling loss factors which describe the transfer of power from dissimilar subsystems.

Steady state power balances of the total energy in each subsystem are derived considering supplied, absorbed, and transmitted power. Then, an algebraic system of equations is formed from the power balance for each subsystem. The total energy in each subsystem is solved for giving a uniform value for each component subsystem. For a more detailed review and the derivation of the solution to two coupled volumes separated by a plate using SEA, refer to Appendix C.

6.1.2   Radiosity

The radiosity method (Le Bot, 1998) discussed previously is derived generally enough to be applied to any reverberant system, structural or acoustic of any dimension. For two coupled systems as shown in Figure 6.2, a power balance similar to that undertaken to determine the secondary source strength is written at a position on the common interface in terms of transmission and reflection coefficients which are assumed to be known.
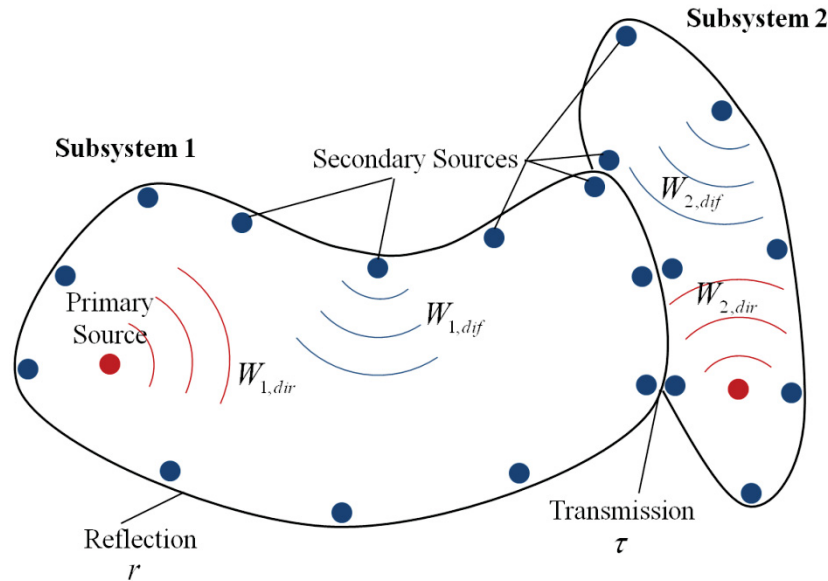
Figure 6.2: Schematic demonstrating the radiosity method for coupled subsystems.

Using the power balance over the small hemispherical volume as was done previously, the power of the secondary sources can be expressed in terms of an integral equation. For the coupled systems, this integral equation depends on the transmission and reflection coefficients which must be calculated analytically before the integral equation can be solved.

There are two main differences between radiosity and the diffusion BE-LTS. First, radiosity is a purely steady state method whereas the diffusion BE-LTS uses the Laplace transform and numerical inverse to compute a transient solution. Second, the diffusion BE-LTS is formulated in terms of energy on the boundaries and the radiosity method in terms of fictitious source strengths. Therefore, the diffusion BE-LTS only transfers energy to the coupled system from elements on the coupling surface. In radiosity, the secondary sources at every point on the boundary of the system transmit energy to the coupled system, not only the sources on the coupling surface as shown in Figure 6.3.
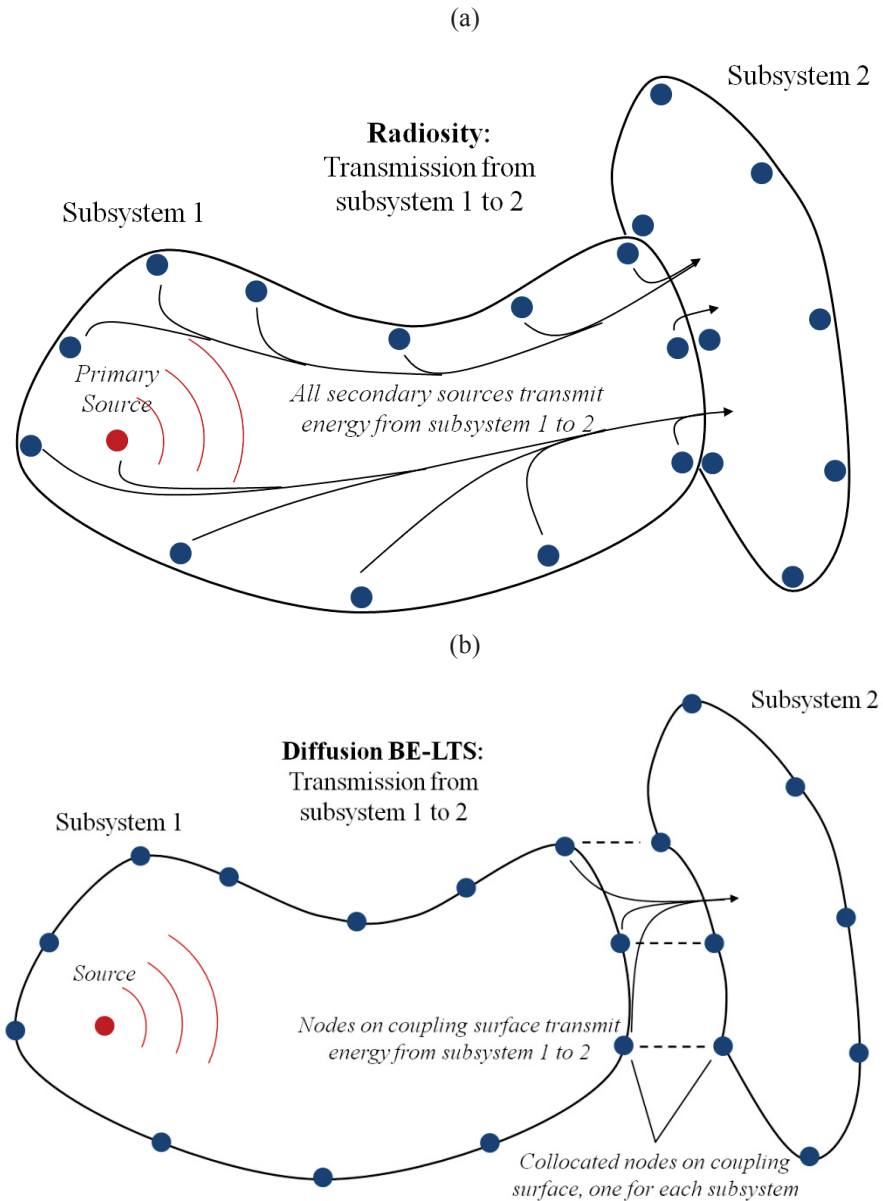
Figure 6.3: The difference in transmission between coupled subsystems using (a) radiosity and (b) the diffusion BE-LTS drawn schematically.

6.1.3   *Power Flow Models/Energy Finite Element Method*

A power flow model for structural analysis was proposed by Nefske and Sung (1989). In the paper, they consider a small control volume inside of a structural system, e.g. a vibrating plate. Applying a power balance on this volume and using relationships between energy density and intensity results in the governing differential equation for the power flow model as

$$\frac{\partial \varphi(\mathbf{r},t)}{\partial t} = \frac{c_g^{\,2}}{\omega \eta} \nabla^2 \varphi(\mathbf{r},t) - \omega \eta \varphi(\mathbf{r},t).$$

<div align="right">6.1</div>

where $\varphi(\mathbf{r},t)$ is the energy density in the volume, c_g is the group velocity of waves propagating in the structure, ω is the angular frequency, and η is the loss factor. Using essentially the same method, the power flow model of the acoustic system is given by

$$\frac{\partial \psi(\mathbf{r},t)}{\partial t} = \frac{c^2}{\omega \eta} \nabla^2 \psi(\mathbf{r},t) - \omega \eta \psi(\mathbf{r},t).$$

<div align="right">6.2</div>

Equations 6.1 and 6.2 are of exactly the same form as the acoustic diffusion model. However, they differ in terms of both the diffusion and attenuation coefficients.

The differing diffusion coefficients pose significant changes to the fundamental physics of the model as shown in Figure 6.4. As discussed in its derivation, the diffusion of acoustic energy in the acoustic diffusion model is driven by the probability that acoustic energy particles are scattered from the bounding surfaces of the volume. The result is a diffusion coefficient that depends only on the speed of sound and geometry of the volume. The diffusion of acoustic energy in the power flow model is driven simply by the gradient of energy across a differential volume due to the atmospheric attenuation.
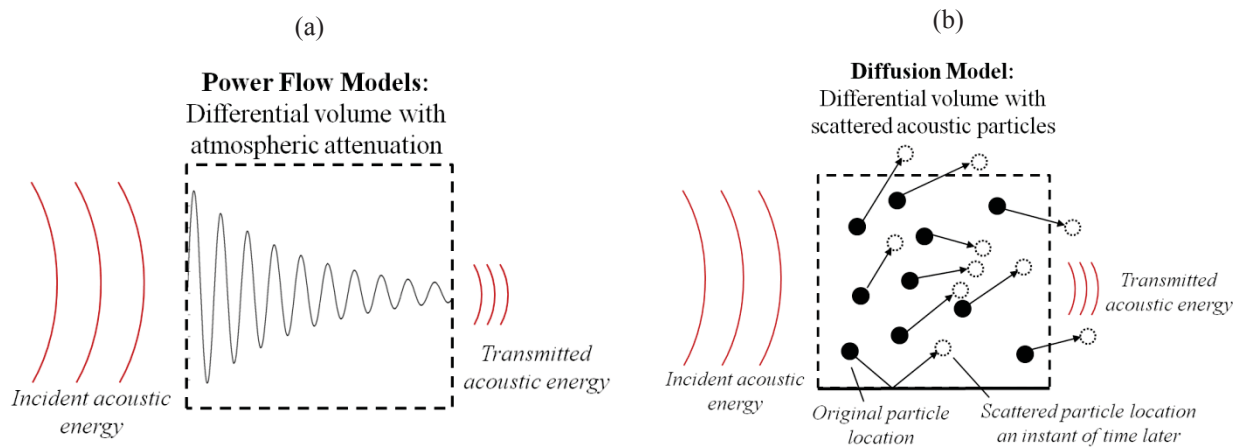
Figure 6.4: The difference between the diffusion of acoustic energy in a small differential volume using (a) the power flow model and (b) the acoustic diffusion model shown schematically.

These equations form the basis of the energy finite element method (EFEM) formulated by Bitsie (1997). The EFEM mainly concerns the extension to coupled systems where it provides

significant advantages over other techniques in the analysis of complex built-up structures. The basis for the EFEM is shown in Figure 6.5.

$$\frac{\partial \psi(\mathbf{r},t)}{\partial t} = \frac{c^2}{\omega \eta} \nabla^2 \psi(\mathbf{r},t) - \omega \eta \psi(\mathbf{r},t) \qquad \frac{\partial \varphi(\mathbf{r},t)}{\partial t} = \frac{c_g^2}{\omega \eta} \nabla^2 \varphi(\mathbf{r},t) - \omega \eta \varphi(\mathbf{r},t)$$
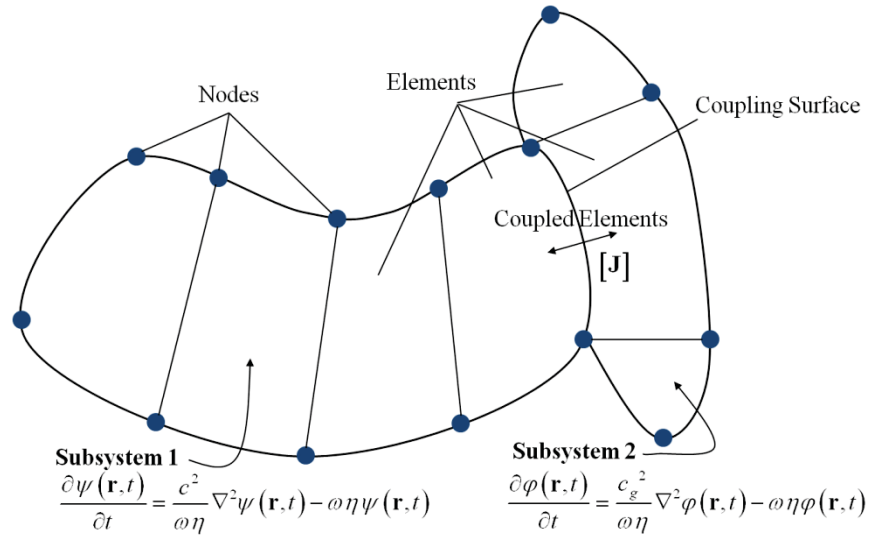
Figure 6.5: Schematic demonstrating the energy finite element method for coupled subsystems.

For two coupled systems, the power flow from one system to the next over the coupling surface must be conserved. Performing a balance of intensity, a coupling boundary condition can be derived which relates the gradient of the acoustic energy on each side of the coupling surface to the energy on the other side through a joint matrix of transmission coefficients. The total system is then solved numerically with the FEM to complete the formulation of the EFEM. For a more detailed review of this method, refer to Appendix D.

6.2   Diffusion BE-LTS for Structural-Acoustic Problems

Two formulations of the diffusion BE-LTS applied to coupled structural-acoustic problems are presented in this section. The first is a simple formulation which couples acoustic volumes through a partition with a known transmission coefficient. Then, a more complex formulation which uses a power flow model of the vibrating structure is presented.

6.2.1   BE-LTS with Simple Structural Coupling

In this section, the BE-LTS to the acoustic diffusion model for multiple acoustic volumes coupled through a known transmission coefficient is summarized. For the full derivation of the

solution, refer to Appendix E. Using the same procedure to derive the single volume BE-LTS gives the integral equation in the vth volume as

$$\beta \Psi_v(\mathbf{r}',s) = \frac{1}{D_v} \int_{V_v'} G_v(\mathbf{r}|\mathbf{r}',s)\psi_v(\mathbf{r},0)dV + \frac{1}{D_v} \int_{V_v'} G_v(\mathbf{r}|\mathbf{r}',s)F_v(\mathbf{r},s)dV -$$

$$\int_{S_v'+S_{cv}'} \Psi_v(\mathbf{r},s)\left[\frac{h_{\alpha v}(\mathbf{r})+h_{\tau v}(\mathbf{r})}{D_v}G_v(\mathbf{r}|\mathbf{r}',s)+\frac{\partial G_v(\mathbf{r}|\mathbf{r}',s)}{\partial \mathbf{n}_v}\right]dS +$$

$$\boxed{\frac{1}{D_v} \int_{S_{cv}'} h_{\tau u}(\mathbf{r})\Psi_u(\mathbf{r},s)G_v(\mathbf{r}|\mathbf{r}',s)dS,} \qquad \mathbf{r}' \in V_v \cup S_v \cup S_{cv} \qquad 6.3$$

where the subscript, u, denotes the coupled volume. Note that the integral equation is nearly the same as in the single volume case with the addition of one more integral of the energy density transmitted from the coupled volume over the coupling surface boxed in red.

Discretizing the bounding surfaces forms a matrix equation which can be solved for the energy on the bounding surfaces (using the methods described previously) given by

$$\frac{1}{2}[\mathbf{I}]_{K_v \times K_v}\{\Psi_v(s)\}_{K_v \times 1} + [\mathbf{C}_{vv}(s)]_{K_v \times K_v}\{\Psi_v(s)\}_{K_v \times 1} +$$

$$\boxed{[\mathbf{C}_{vu}(s)]_{K_v \times K_u}\{\Psi_u(s)\}_{K_u \times 1}} = \{\mathbf{B}_v(s)\}_{K_v \times 1} \qquad 6.4$$

Again, this equation is identical to the matrix equation derived for the BE-LTS previously with the addition of one term boxed in red representing the energy transmitted from the coupled volume. Individually, eq. 6.4 represents an underdetermined linear system of equations with K_v in $K = K_v + K_u$ unknowns. However, writing one for each volume, $v = 1, 2, ..., N_V$, gives

$$\frac{1}{2}[\mathbf{I}]_{K \times K} \begin{Bmatrix} \{\Psi_1(s)\} \\ \{\Psi_2(s)\} \\ \vdots \\ \{\Psi_{N_V}(s)\} \end{Bmatrix}_{K \times 1} + \begin{bmatrix} [\mathbf{C}_{11}(s)] & [\mathbf{C}_{12}(s)] & \cdots & [\mathbf{C}_{1N_V}(s)] \\ [\mathbf{C}_{21}(s)] & [\mathbf{C}_{22}(s)] & & \\ \vdots & & \ddots & \\ [\mathbf{C}_{N_V1}(s)] & & & [\mathbf{C}_{N_VN_V}(s)] \end{bmatrix}_{K \times K} \begin{Bmatrix} \{\Psi_1(s)\} \\ \{\Psi_2(s)\} \\ \vdots \\ \{\Psi_{N_V}(s)\} \end{Bmatrix}_{K \times 1} = \begin{Bmatrix} \{\mathbf{B}_1(s)\} \\ \{\mathbf{B}_2(s)\} \\ \vdots \\ \{\mathbf{B}_{N_V}(s)\} \end{Bmatrix}_{K \times 1} \qquad 6.5$$

More compactly,

$$[\mathbf{A}(s)]_{K \times K}\{\Psi(s)\}_{K \times 1} = \{\mathbf{B}(s)\}_{K \times 1}. \qquad 6.6$$

The structure of the transmission matrix, $[\mathbf{C}_{12}(s)]$, in the complete system of equations of eq. 6.4 is shown for two coupled volumes in Figure 6.6. The off-diagonal matrices, $[\mathbf{C}_{vu}(s)]$

represent the flow of energy transmitted into the vth volume from the uth volume. Thus, these matrices have full columns of values multiplying the energy at nodes on the coupling surfaces; all other columns multiplying energy at nodes not on the coupling surfaces are zero. The matrices $\left[\mathbf{C}_{vv}(s)\right]$ are fully populated and identical to the coefficient matrix for the BE-LTS in a single volume.

$$\left[\mathbf{C}_{12}(s)\right] = \begin{bmatrix} C_{12,11}(s) & C_{12,12}(s) & C_{12,13}(s) & 0 & 0 & 0 & 0 & 0 \\ C_{12,21}(s) & C_{12,22}(s) & C_{12,23}(s) & 0 & 0 & 0 & 0 & 0 \\ C_{12,31}(s) & C_{12,32}(s) & C_{12,33}(s) & 0 & 0 & 0 & 0 & 0 \\ C_{12,41}(s) & C_{12,42}(s) & C_{12,43}(s) & 0 & 0 & 0 & 0 & 0 \end{bmatrix}$$
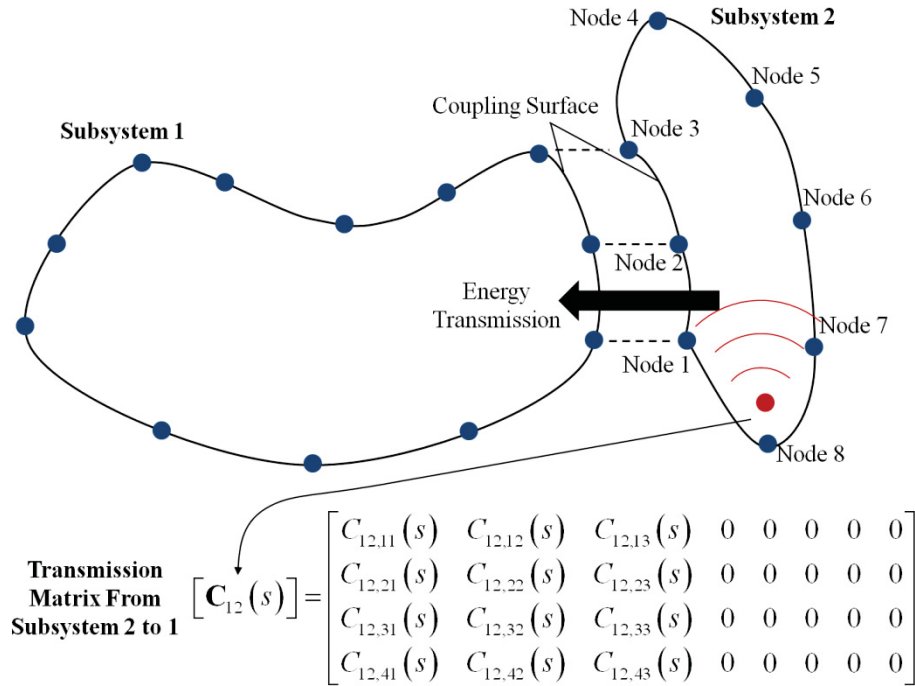
Figure 6.6: Structure of the BE-LTS matrix for two coupled acoustic volumes.

A discussion of typical transmission coefficients of building components and the derivation of the transmission coefficient for a layer with a known acoustic impedance for which this formulation is particularly useful is given in Appendix F.

6.2.2 BE-LTS with Power Flow Model Structural Coupling

In this section, a diffusion model for a multiple volumes, V_v, with absorbing boundaries, S_v, and coupled through vibrating structural boundaries, S_P, is developed. The geometry for this case is shown in Figure 6.7 where the vibrating boundary is considered to be a transversely vibrating thin plate with thickness, h, bounded by the contour, ∂S_P, which has a unit normal vector, $\mathbf{n}_P$, pointing away from contour and parallel to the plate.
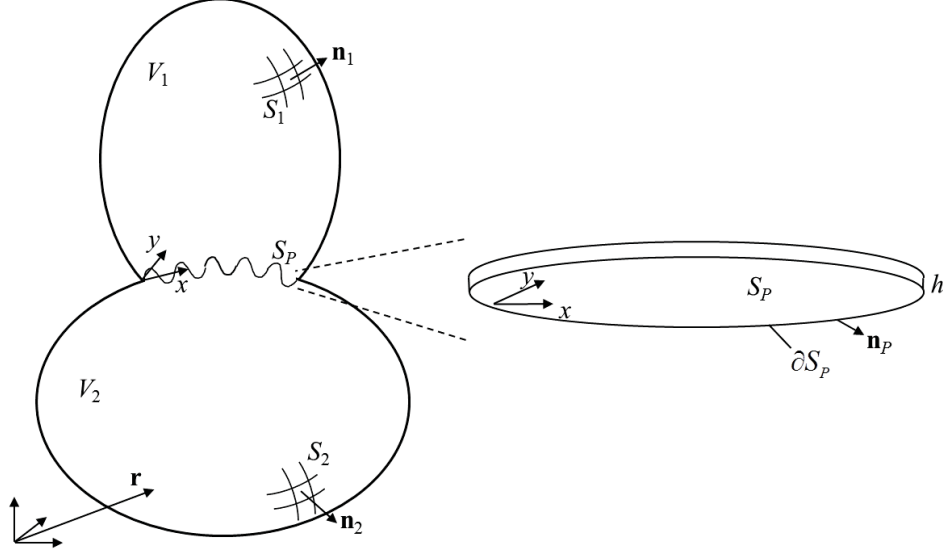
Figure 6.7: Schematic demonstrating the geometry for a single acoustic volume with both absorbing and vibrating boundaries.

Again, the energy equation which governs points in either volume is the acoustic diffusion equation given by

$$\frac{\partial \psi_v(\mathbf{r},t)}{\partial t} - D_v \nabla^2 \psi_v(\mathbf{r},t) + m_v c_v \psi_v(\mathbf{r},t) = f_v(\mathbf{r},t), \quad \mathbf{r} \in V_v \qquad 6.7$$

To develop the boundary condition, the transfer of energy from an acoustic system to a mechanically vibrating system is considered using methods in SEA. The difference is that, now, the energy density can vary within the subsystem. Generalizing SEA coupling with spatially varying, transient energy density gives

$$\int_{S_P} \mathbf{I}_{\psi v}(\mathbf{r},t) \cdot \mathbf{n} dS = \int_{V_v} \psi_v(\mathbf{r},t) \omega \tau_\psi dV - \int_{S_P} \varphi(\mathbf{r},t) \omega \tau_\varphi h dS \qquad 6.8$$

assuming that the structural energy density, $\varphi(\mathbf{r},t)$, does not vary through the thickness of the thin plate. In this equation, $\mathbf{I}_{\psi v}(\mathbf{r},t)$ is the acoustic intensity, ω is the angular frequency, τ_ψ is the structural transmission coefficient (the ratio of transmitted structural power to incident acoustic power), and τ_φ is the acoustic transmission coefficient (the ratio of transmitted acoustic power to incident structural power). Analytical expressions have been derived for the transmission coefficients for use with SEA and are discussed in Appendix C.

The acoustic intensity normal to the plate can be rewritten using the acoustic diffusion coefficient as

$$-D\int_{S_P}\frac{\partial\psi_v(\mathbf{r},t)}{\partial\mathbf{n}}dS = \int_{V_v}\psi_v(\mathbf{r},t)\omega\tau_\psi dV - \int_{S_P}\varphi(\mathbf{r},t)\omega\tau_\varphi hdS. \qquad 6.9$$

Now, it is assumed that the acoustic energy density does not very much in the direction normal to the plate. Equation 6.9 can then be approximated by

$$-D\int_{S_P}\frac{\partial\psi_v(\mathbf{r},t)}{\partial\mathbf{n}}dS \approx \omega\tau_\psi\int_{S_P}\psi_v(\mathbf{r},t)LdS - \omega\tau_\varphi\int_{S_P}\varphi(\mathbf{r},t)hdS. \qquad 6.10$$

where $L = V_v/S_P$ is the average length of the volume relative to the plate area. Equation 6.10 holds true if

$$D\frac{\partial\psi_v(\mathbf{r},t)}{\partial\mathbf{n}} - \omega\tau_\psi L\psi_v(\mathbf{r},t) = \omega\tau_\varphi h\varphi(\mathbf{r},t), \quad \mathbf{r}\in S_P \qquad 6.11$$

is satisfied at every point on the coupling plate.

The structural energy density at points on the vibrating plate are governed by (Bouthier and Bernhard, 1995)

$$\frac{\partial\varphi(\mathbf{r},t)}{\partial t} - D_P\nabla_P^2\varphi(\mathbf{r},t) + \omega(\eta + N_v\tau_\varphi)\varphi(\mathbf{r},t) = f_P(\mathbf{r},t) + \sum_{v=1}^{N_v}\omega\tau_\psi\psi_v(\mathbf{r},t), \quad \mathbf{r}\in S_P \qquad 6.12$$

where D_P is the plate diffusion coefficient given by

$$D_P = \frac{4}{\eta}\sqrt{\frac{K_P}{\rho_P h}}, \qquad 6.13$$

$\nabla_P^2 = \frac{\partial^2}{\partial x^2} + \frac{\partial^2}{\partial y^2}$ is a two-dimensional Laplacian in the plate coordinate system, $K_P = Eh^3/12/(1-v^2)$ is the plate rigidity, E is the elastic modulus of the plate, η is the structural loss factor, v is the Poisson's ratio of the plate, ρ_P is the density of the plate, ω is the angular frequency, N_v is the number of acoustic volumes coupled to the plate, and $f_P(\mathbf{r},t)$ is power supplied directly to the plate. Note that the plate diffusion coefficient depends primarily on mechanical properties of the plate, the mass, stiffness, and damping, unlike the acoustic diffusion coefficient which depends only on the volume geometry and speed of sound.

At the connection between the plate boundaries and absorbing surface boundaries, ∂S_P, the structural intensity associated with transverse vibrations, $\mathbf{I}_\varphi(\mathbf{r},t)$, must be zero, i.e. the plate is fastened to the adjoining, rigid surface, or

$$\mathbf{I}_\varphi(\mathbf{r},t)\cdot\mathbf{n}_P = 0, \qquad \mathbf{r}\in\partial S_P. \tag{6.14}$$

In terms of energy density, eq. 6.14 is

$$\frac{\partial\varphi(\mathbf{r},t)}{\partial\mathbf{n}_P} = 0, \quad \mathbf{r}\in\partial S_P. \tag{6.15}$$

Together with known initial energy densities, the N_v governing differential equations for the acoustic energies in the volumes, eq. 6.7, the governing equation for the structural energy of the plate, eq. 6.12, and the boundary conditions, eq. 6.11 and an absorptive condition for the non-coupling surface and eq. 6.15 for the plate boundaries, form a well-posed problem.

There are four key differences between the BE-LTS with power flow model structural coupling and the EFEM which are summarized in Figure 6.8. First, only the boundaries of acoustic volumes are meshed using the BE-LTS where the entire domain must be discretized using EFEM. Second, the energy flow between coupled subsystems is derived as an integral over the coupling surface in the EFEM, so only the total transmitted energy in a global sense is transferred to the coupled subsystem. In the diffusion BE-LTS with power flow structural coupling, the energy transmission is performed locally on a point by point basis. Third, the energy models for acoustic volumes are controlled by the atmospheric attenuation in the EFEM as discussed in Figure 6.4, whereas the diffusion BE-LTS uses a statistical scattering formulation based only on the room geometry. Finally, the EFEM is derived purely as a steady state method, but the diffusion BE-LTS can compute transient solutions.

(a)

(b)
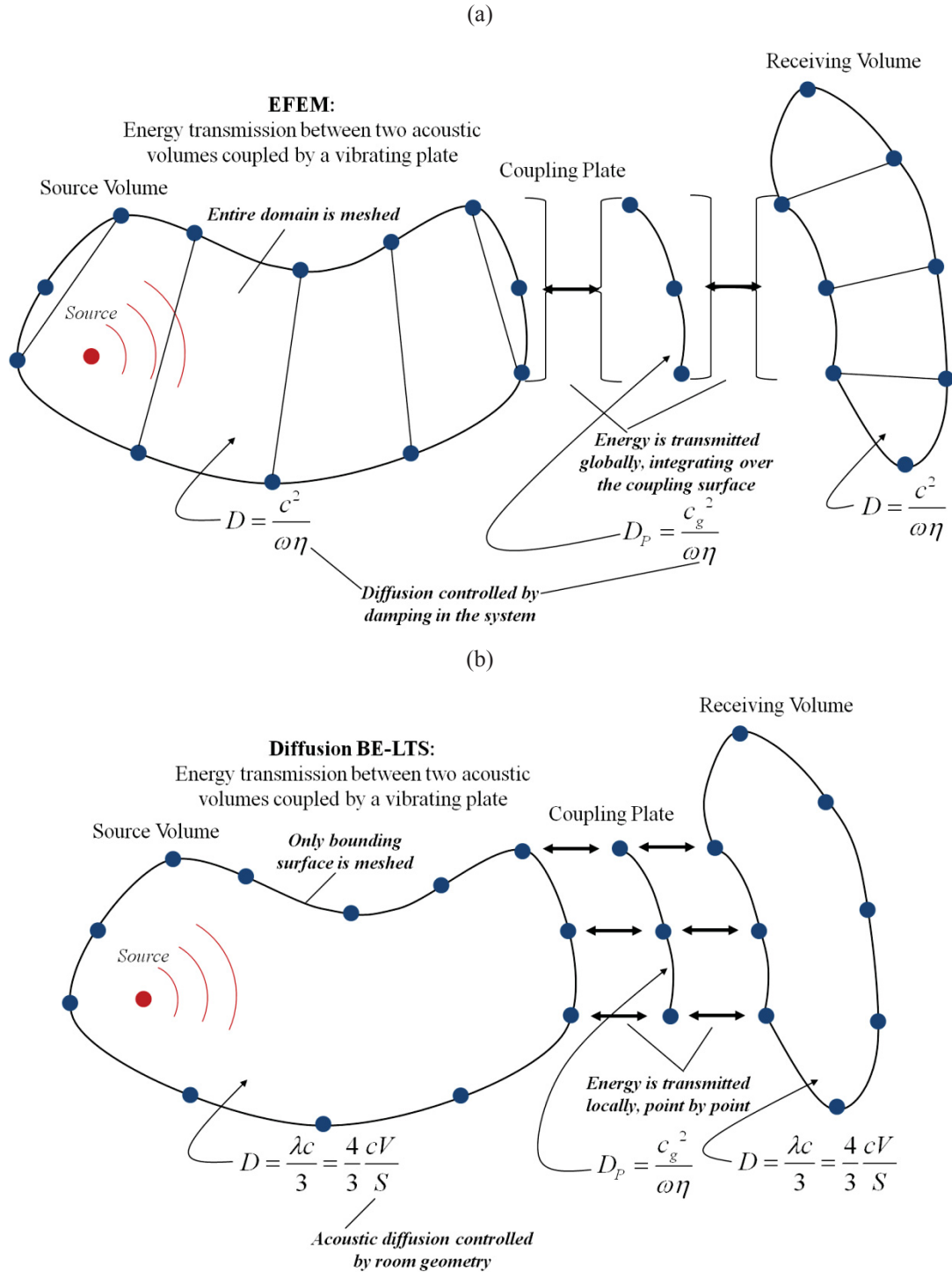
Figure 6.8: Schematic demonstrating the key differences between (a) EFEM and (b) the diffusion BE-LTS with power flow structural coupling.

6.3   Numerical Validation

To examine the BE-LTS solution to the acoustic diffusion model for volumes coupled by a partition, a simple room configuration first presented by Billon et al. (2008a) is simulated. The geometry, shown in Figure 6.9, consists of two, cubic, 5 x 5 x 5 m volumes with a 25 m^2 coupling partition. A monopole source is placed in the corner of one of the volumes, the source volume, 2 m away from each surface which radiates a power of 100 dB (ref 10^{-12} W). The volume without the source is referred to as the receiving volume. A 3-D grid of 125 receivers is placed in each volume with a uniform spacing of 1 m, skipping the source position and not placing receivers on the boundaries. The boundaries of each volume, excluding the coupling surface, have a uniform acoustic absorption coefficient of 0.1.
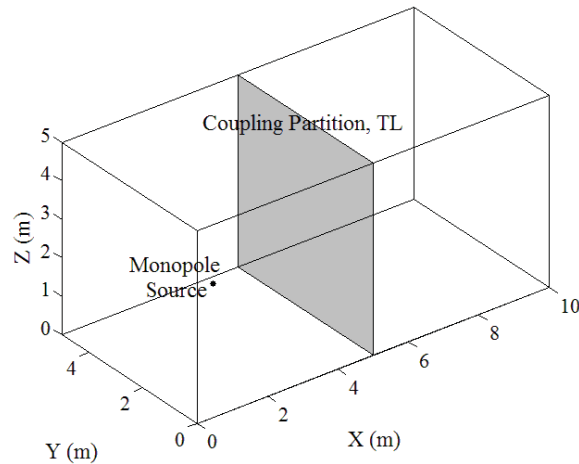
Figure 6.9: Example problem schematic used for initial validation of the BEM solution to the coupled acoustic diffusion equation showing geometry and source location.

Both steady and transient responses are computed using both BE-LTS formulations presented previously. These are compared to an approximate solution based on Sabine theory, a FEM solution, ray tracing, and SEA to provide numerical validation of the formulations. First, the simple structural coupling diffusion BE-LTS to the coupled uniform cubic volumes is presented. Then, the power flow model structural coupling diffusion model is computed for the same coupled volume configuration.

6.3.1 *Simple Structural Coupling*

First, the steady state solution is analyzed using several different computation methods. Then, the transient buildup of energy from initially undisturbed volumes is examined. The diffusion BE-LTS is compared to statistical theory, a FEM solution to the coupled diffusion model, and ray tracing. The statistical theory formulation based on Sabine theory used to solve the simple coupled example is presented in Appendix G.

6.3.1.1 Steady State Solution

A detailed study of the convergence of the numerical solutions is given in Appendix H. The meshes shown in Figure 6.10 and 16384 rays are used in all results presented in this section to provide convergence in the average steady state energy density to within 5 % difference.
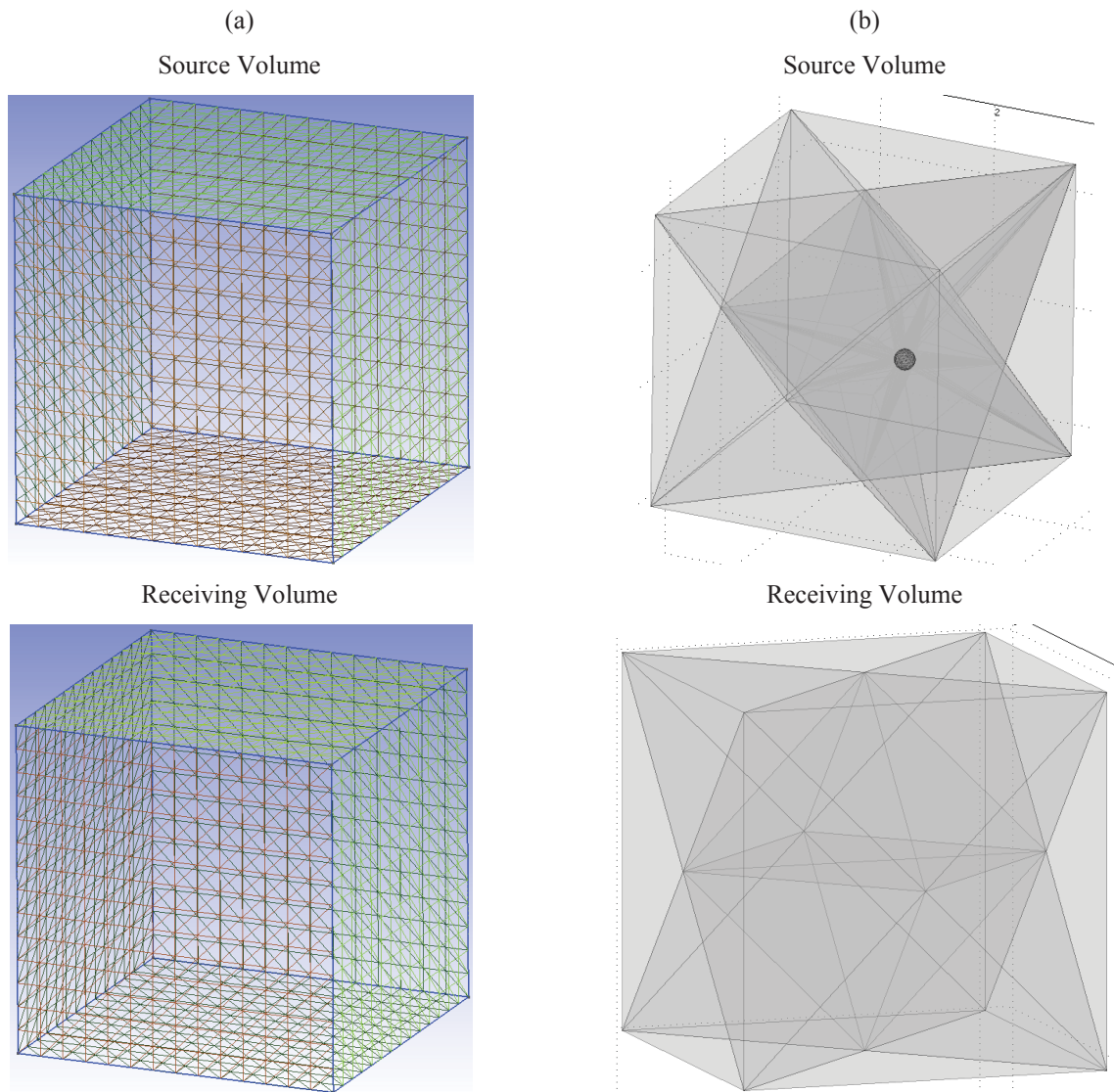
Figure 6.10: Meshes used to compute the (a) BE-LTS and (b) FEM solution to the acoustic diffusion model with simple structural coupling.

The average steady state SPL in each volume computed using the three numerical methods and statistical theory is plotted against the coupling partition TL in Figure 6.11. As with the uniform cubic volume, this configuration accurately models the assumptions made in the statistical theory which is thus used as a baseline method of comparison.

For low values of the coupling partition TL, a significant amount of energy is transmitted into the receiving volume yielding relatively low energy levels in the source volume. As the partition TL increases, more energy becomes trapped in the source volume. However, at a certain

point, the absorption of the non-transmitting surfaces dominates the energy dissipation and the energy in the source volume becomes independent of the partition TL. Ray tracing does not capture this effect. However, all three numerical methods agree closely with the statistical theory to within 2 dB with the FEM solution of the diffusion model demonstrating the greatest accuracy.

In the receiving volume, the average SPL decreases slowly for low values of the TL. The slope increases from about 0 to 10 dB TL corresponding to the increase in SPL in the source volume. After a TL of 10 dB, the decrease in average SPL in the receiving volume becomes linear demonstrating a decrease in average SPL of exactly 1 dB per 1 dB increase in TL. Again, both the statistical theory and diffusion models capture this trend, but ray tracing captures only the linear decrease. The diffusion FEM solution demonstrates the most accurate results in the receiving volume mostly to within 0.5 dB accuracy. The diffusion BE-LTS computes levels about 5 dB lower than statistical theory and ray tracing about 11 dB lower.

(a)   (b)
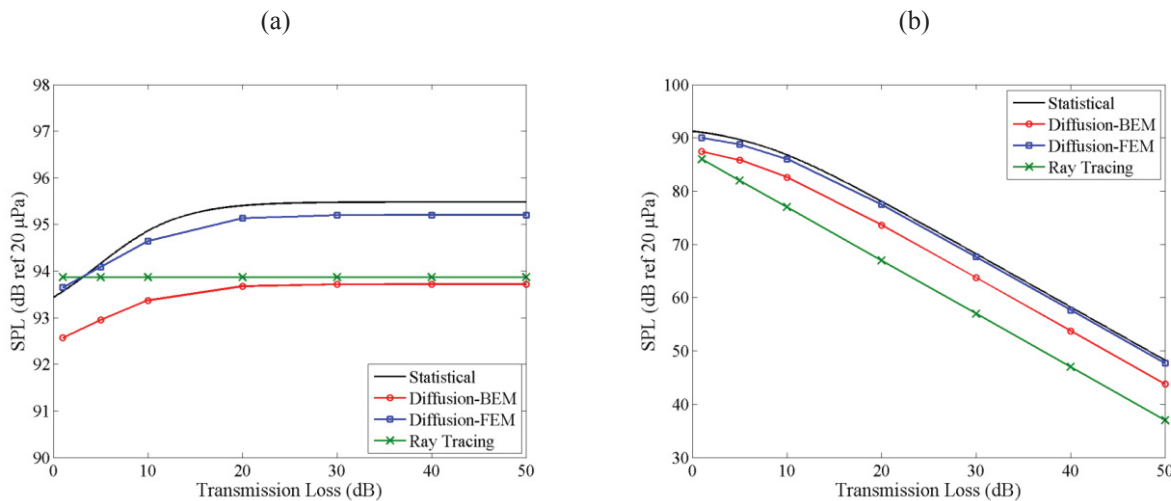
Figure 6.11: Average SPL in the (a) source and (b) receiving volume calculated using statistical theory, the diffusion BEM, and ray tracing for different partition TL's.

The steady state SPL along a line of receivers perpendicular to the coupling surface through the center of each volume is plotted in Figure 6.12. Levels in the source volume are plotted as solid lines while the SPL's computed in the receiving volume are plotted as dashed lines. The first observation to note is that the SPL distribution in either volume is independent of the TL of

the coupling partition. In the source volume, statistical theory and the diffusion models compute a maximum SPL at the location closest to the source with minima close to the back surface and coupling partition. The SPL distribution exhibited by statistical theory exists solely due to the direct field radiated by the source as the reverberant energy is assumed to be constant throughout the volume.

In the receiving volume, statistical theory computes only one constant energy level for each TL due to only the reverberant energy, assumed constant, being transmitted through the partition. The diffusion models compute an SPL which decays as the receivers move further from the coupling partition. However, the decay is very slow, nearly the uniform trend of statistical theory, dropping by less than 2 dB. Ray tracing computes a stronger decay as the receivers move further from the coupling partition dropping by about 6 dB from the partition to the back surface.

(a)

(b)   (c)
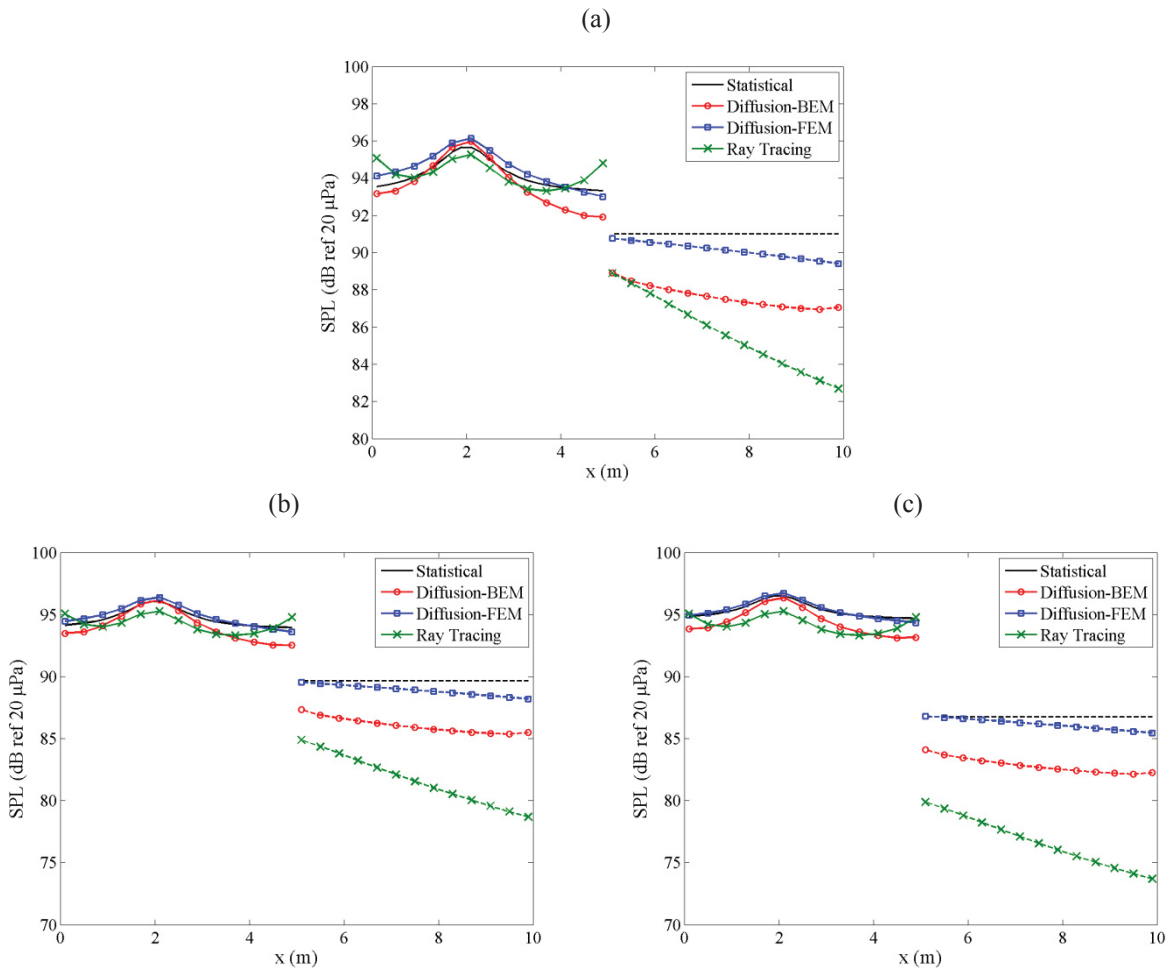
Figure 6.12: Steady state SPL calculated using different methods for (a) 1 dB, (b) 5 dB, (c) 10 dB, (d) 20 dB, (e) 30 dB, (f) 40 dB, and (g) 50 dB TL plotted against a coordinate perpendicular to the coupling surface.

120
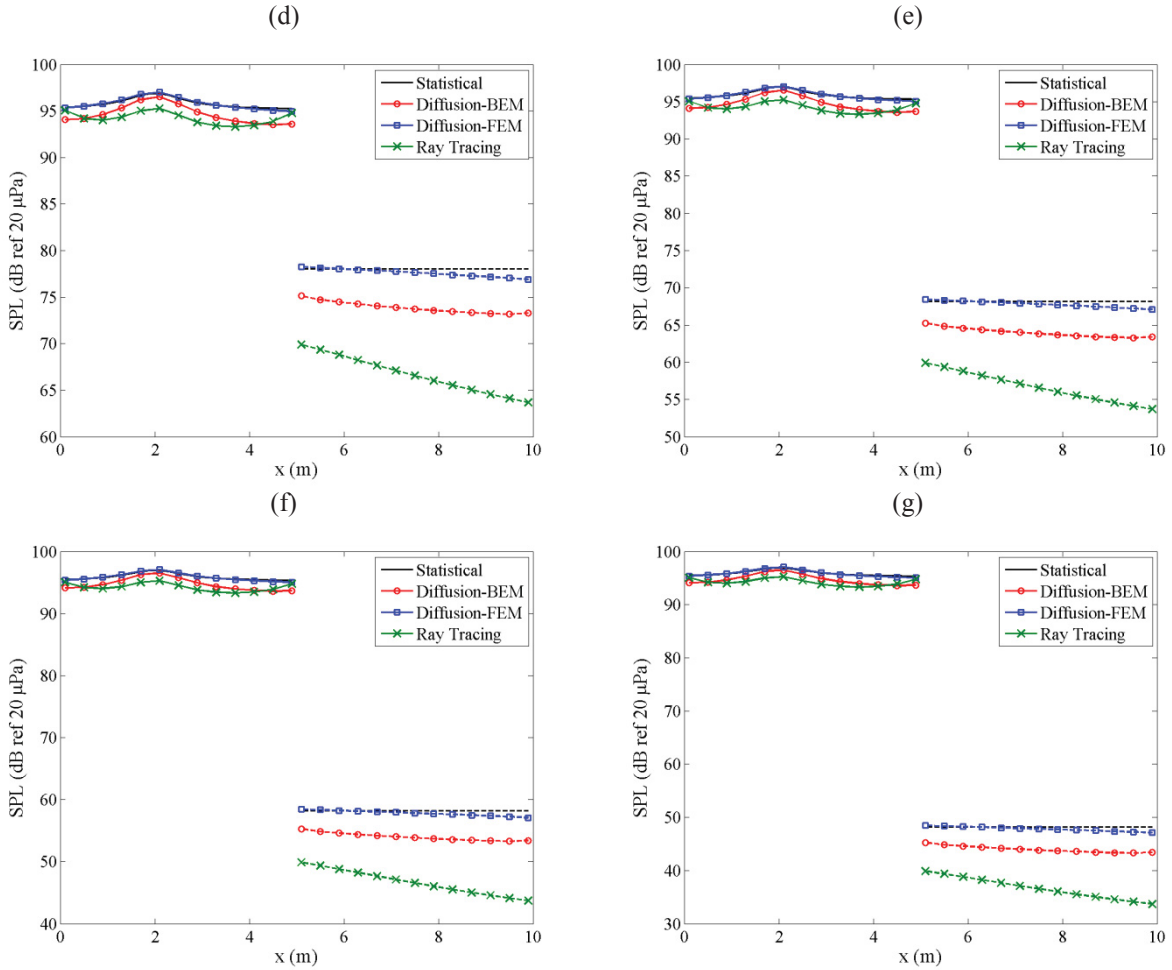
Figure 6.12, cont.: Steady state SPL calculated using different methods for (a) 1 dB, (b) 5 dB, (c) 10 dB, (d) 20 dB, (e) 30 dB, (f) 40 dB, and (g) 50 dB TL plotted against a coordinate perpendicular to the coupling surface.

6.3.1.2 Transient Buildup Solution

The buildup of energy from initially undisturbed source and receiving volumes is also computed using the same methods. A detailed convergence study of the numerical solutions to the transient buildup is also presented in Appendix H. All results shown are calculated with the same meshes shown in Figure 6.10 and 32768 rays which provide convergence in the transient average energy density to within 5 % difference.

The transient BEM solution is computed using two values of the Laplace variable. The values used are the midpoints of the S-shaped curve produced by computing an average $s\Psi(s)$ in each volume. The average SPL in each volume is computed as a function of time and plotted

in Figure 6.13 for different TL's of the coupling partition. In the source volume, the steady state level is reached quickly. The steady state level takes longer to reach in the receiving volume using statistical theory and the diffusion models, but is still reached very quickly using ray tracing.
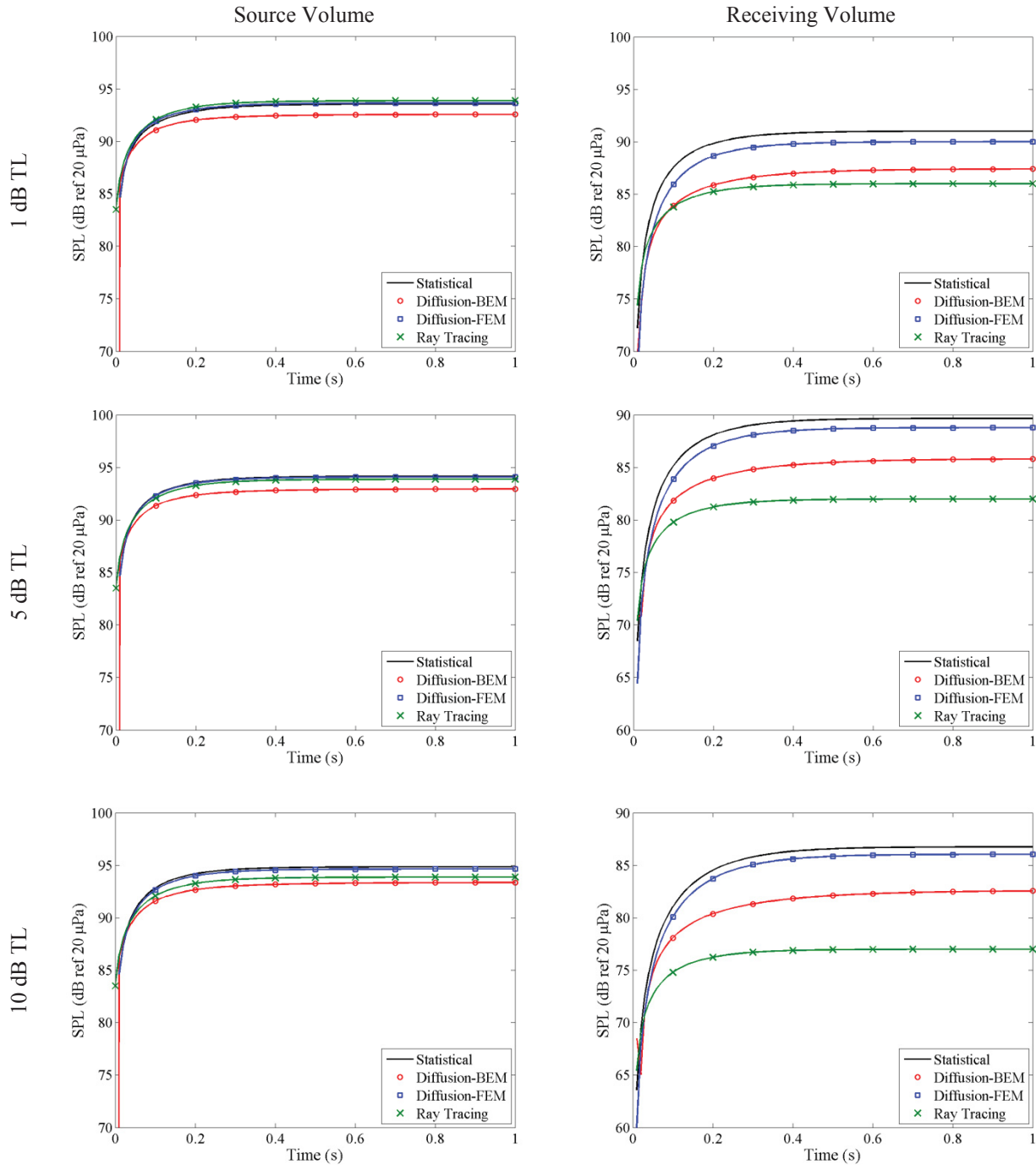
Figure 6.13: Average SPL in the source and receiving volumes as a function of time compared using different analysis methods for varying TL of the coupling partition.
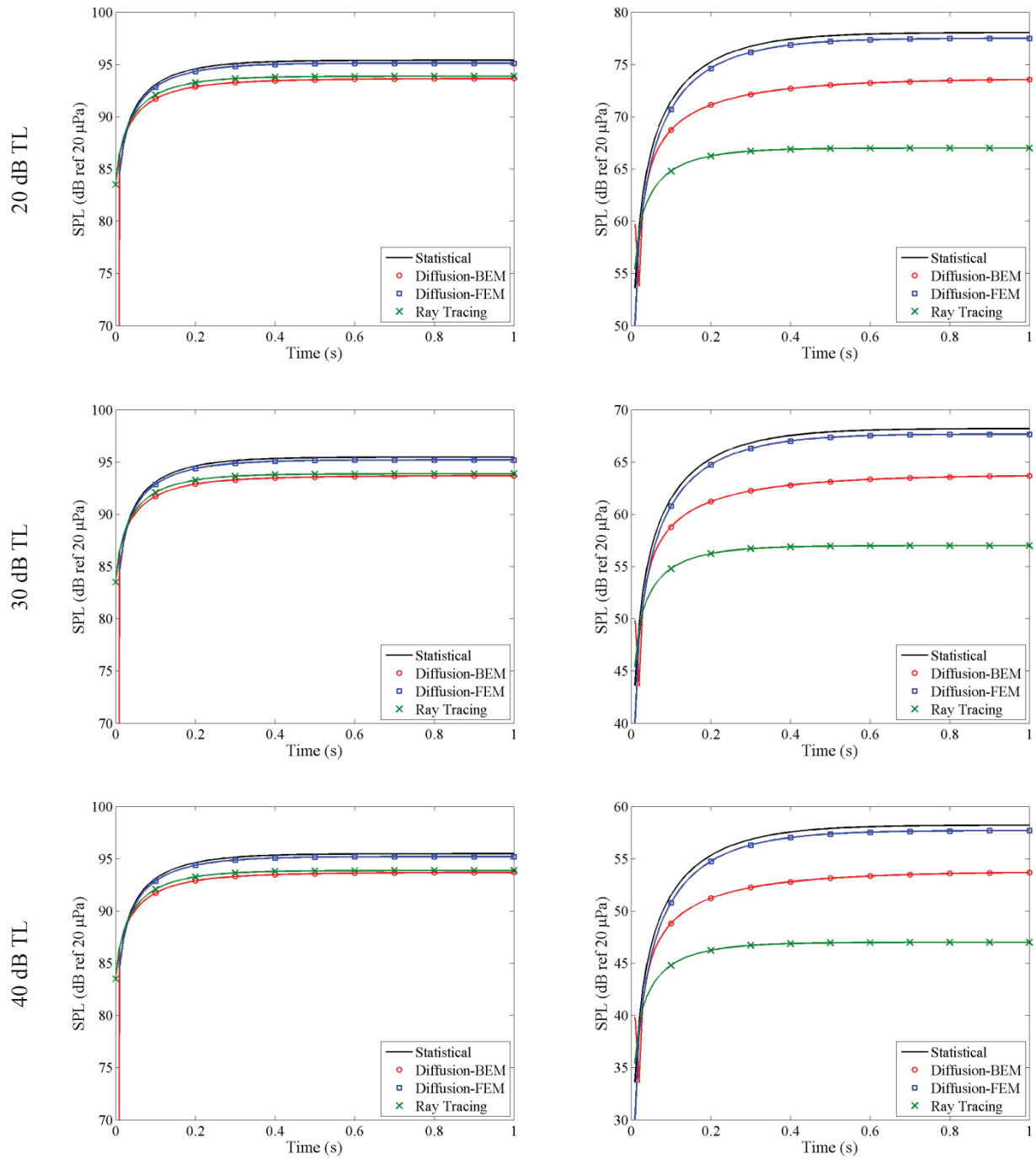
Figure 6.13, cont.: Average SPL in the source and receiving volumes as a function of time compared using different analysis methods for varying TL of the coupling partition.
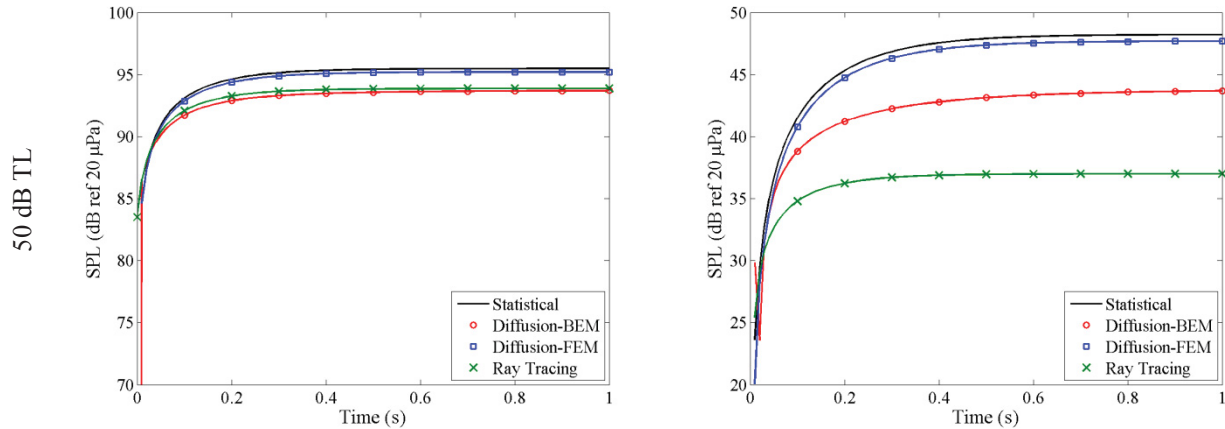
Figure 6.13, cont.: Average SPL in the source and receiving volumes as a function of time compared using different analysis methods for varying TL of the coupling partition.

To better understand these buildup times, the metric is quantified as the length of time taken to reach 95 % of the steady state energy density. The average buildup time in each volume is plotted against partition TL in Figure 6.14. In the source volume, statistical theory and the diffusion FEM produce low buildup times for very low TL's that decrease to a minimum between 5 and 10 dB TL. The buildup time then increases to a constant value about 0.35 s above 20 dB. The diffusion BE-LTS captures the increase from low buildup times in the source volume for low partition TL's to higher buildup times above 20 dB. However, the buildup time is longer than statistical theory or the diffusion FEM rendering it the least accurate method. The buildup time is not affected by the partition TL using ray tracing in either volume; it is more accurate for low partition TL's, but is fairly accurate for any TL in the source volume.

In the receiving volume, the buildup time increases from a low value for low partition TL's below 20 dB to a higher value above 20 dB TL. This trend is captured by statistical theory and both diffusion models, though the buildup time is significantly longer using the diffusion BEM. Again, the buildup time computed with ray tracing is more accurate for low partition TL's and becomes less accurate for higher TL's due to its inability to capture the increase in buildup time from a higher TL.

(a)   (b)
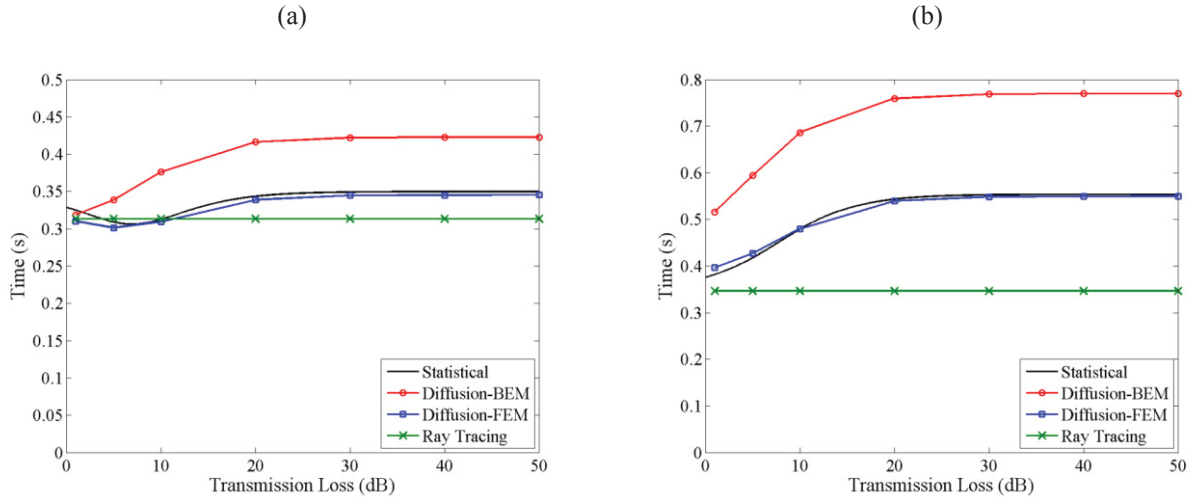
Figure 6.14: Average time taken to reach 95 % of the steady state energy density in the (a) source and (b) receiving volume calculated using different methods for different partition TL's.

The buildup times along a line of receivers perpendicular to the coupling surface through the center of each volume is plotted in Figure 6.15. Buildup times in the source volume are plotted as solid lines while the SPL's computed in the receiving volume are plotted as dashed lines. The buildup time computed using statistical theory is constant in each volume due to the uniform energy density assumption. In the source room, the diffusion FEM computes a fairly constant buildup time in the source room which increases slightly closer to the coupling partition. The diffusion BE-LTS gives a buildup time which varies significantly reaching a minimum close to the source and a maximum close to the coupling partition. Ray tracing also produces a minimum buildup time close to the source. However, local minima are also produced close to the back surface and coupling partition due to the buildup of energy close to these surfaces that was observed in the steady state problem.

In the receiving volume, the numerical methods compute buildup times which increase further from the coupling partition. The increase is fairly linear in the FEM and ray tracing solutions, but demonstrates small curvature in the BEM solution. All of these trends are independent of coupling partition TL.

(a)

(b)   (c)

(d)   (e)
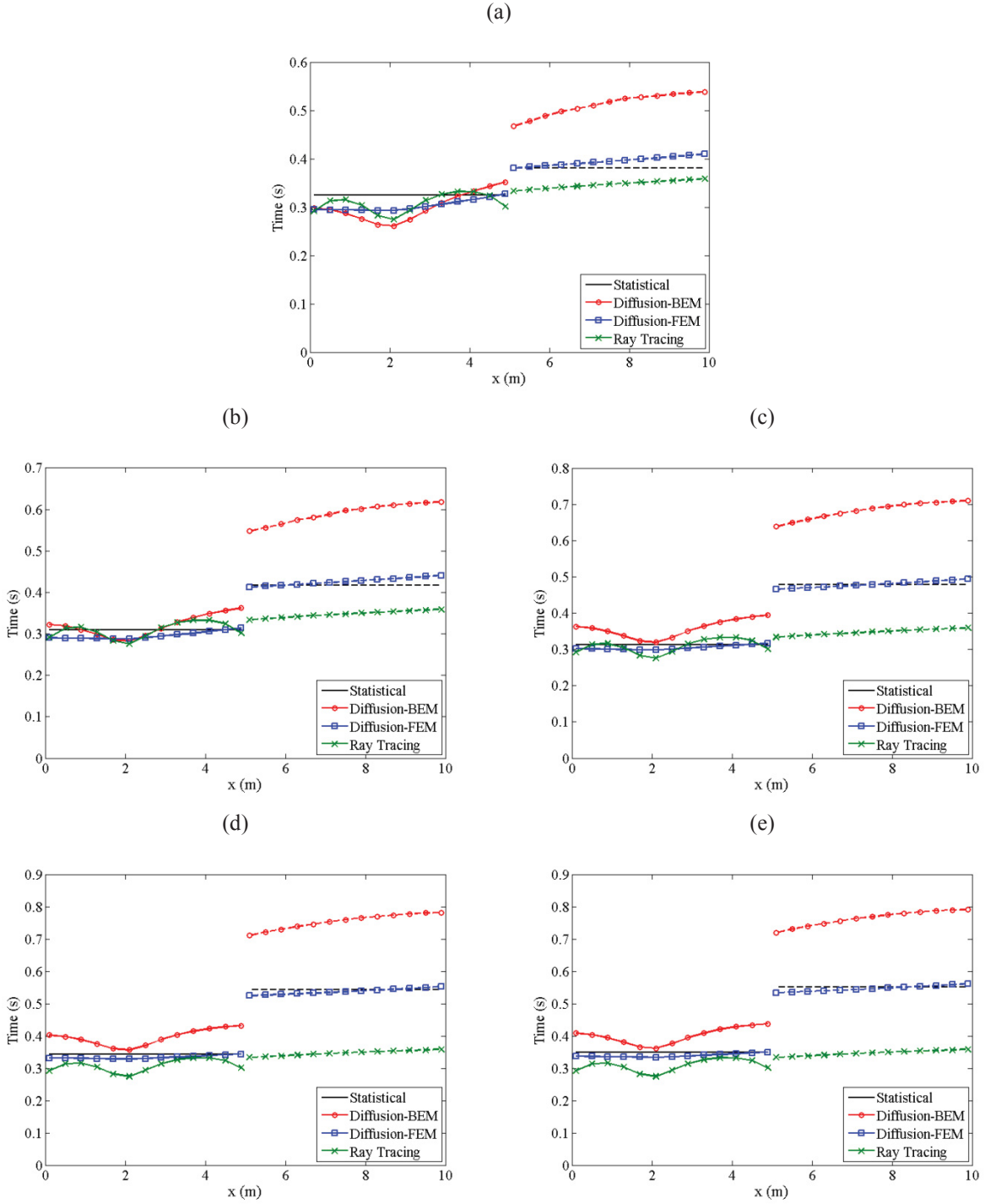
Figure 6.15: Time taken to reach 95 % of the steady state energy calculated using different methods for (a) 1, (b) 5, (c) 10, (d) 20, (e) 30, (f) 40, and (g) 50 dB TL plotted against a coordinate perpendicular to the coupling surface.

126

(f)   (g)
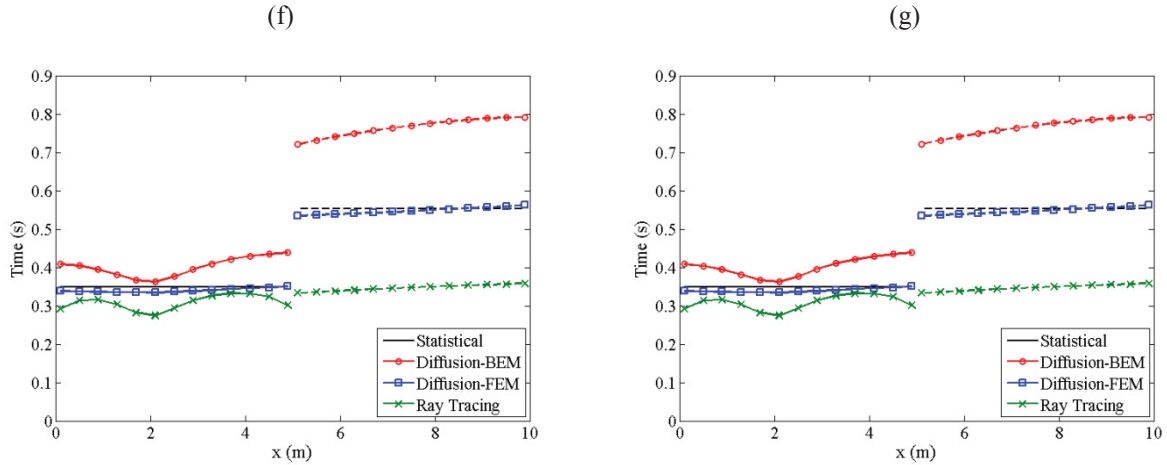
Figure 6.15, cont.: Time taken to reach 95 % of the steady state energy calculated using different methods for (a) 1, (b) 5, (c) 10, (d) 20, (e) 30, (f) 40, and (g) 50 dB TL plotted against a coordinate perpendicular to the coupling surface.

Overall, the FEM solution to the diffusion model produces the most accurate results in this simple transmission example for both steady state and transient buildup cases. The diffusion BE-LTS solution is fairly accurate in the steady state case, but encounters small difficulties in predicting the amount of time it takes for the energy to build up in the volumes. However, computational efficiency considerations may promote the use of the Laplace domain technique. In general, ray tracing produces the least accurate results.

6.3.2   *Power Flow Model Structural Coupling*

In this section, the uniform volumes of the previous section are coupled through different vibrating plates. The TL is computed from the results and compared to experimental data as well as a SEA of the system. For the TL calculation, four plates of varying material and thickness are considered:

    a) A thin aluminum sheet 0.9 mm thick

    b) A steel plate 6 mm thick

    c) A glass plate 6 mm thick

    d) A plywood sheet 12 mm thick

The mechanical properties of these materials are given in Table 6.1.

Table 6.1: Mechanical properties of the vibrating plates coupling the uniform acoustic volumes.

Material	Elastic Modulus (GPa)	Density (kg/m^3)	Poisson's Ratio	Loss Factor
Aluminum	71.6	2700	0.34	0.001
Steel	207	7800	0.29	0.001
Glass	67.6	2400	0.24	0.02
Plywood	8.7	600	0.26	0.015

Rather than program the BE-LTS with power flow structural coupling, an initial study is performed using a full FEM solution in a commercial software, COMSOL (COMSOL, 2007). The discrete mesh used to compute the FEM solution is shown in Figure 6.16.
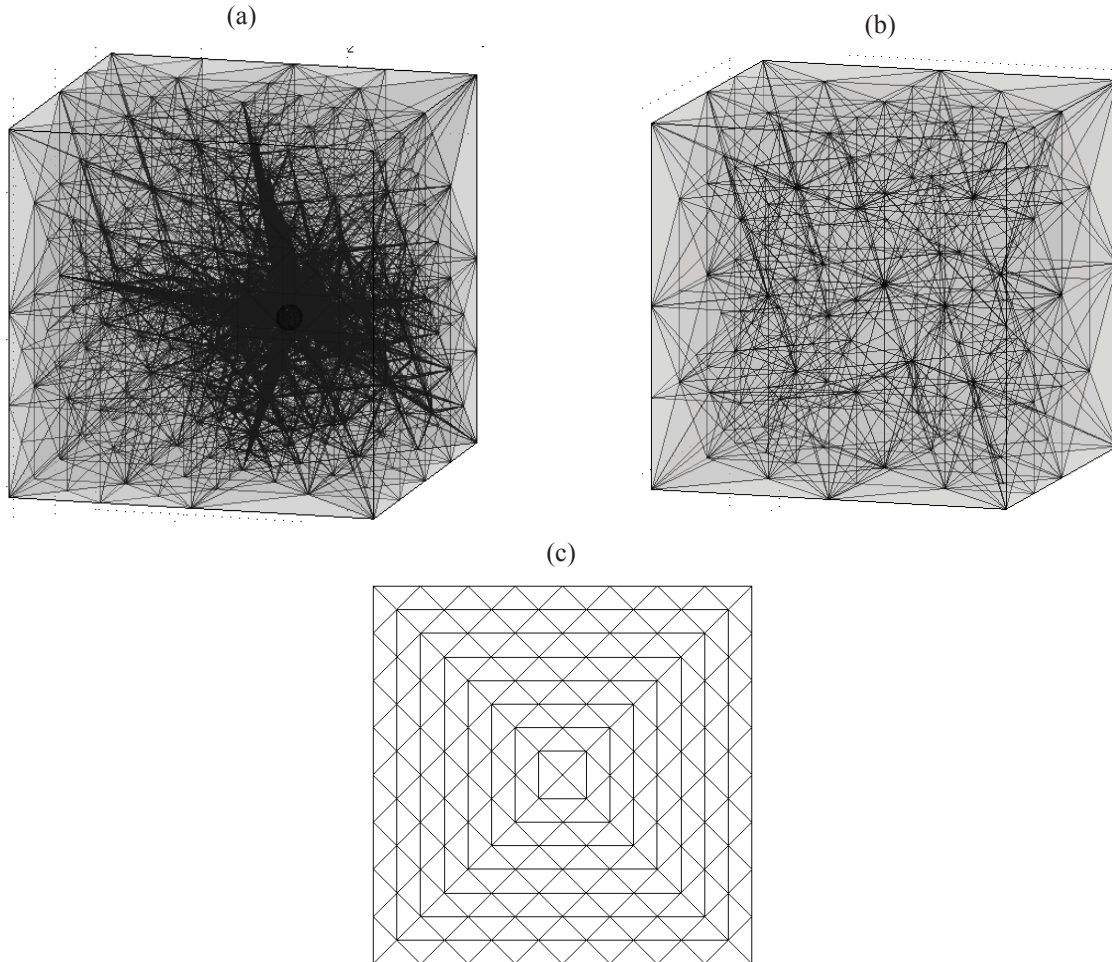
Figure 6.16: Meshes of (a) the source volume, (b) the receiving volume, and (c) the coupling plate used to compute the power flow model structural coupling solution to the acoustic diffusion model.

6.3.2.1 Steady State Solution

The average steady state SPL in the source volume computed with both the full structural acoustic diffusion model and SEA is plotted in Figure 6.17 for each partition type. In general, the results in the source volume are in good agreement. The sharp drop is caused by coincidence, when the acoustic wavelength matches the wavelength of flexural waves in the plate. Coincidence causes significant transmission of acoustic energy from the source volume to the plate, subsequently radiated into the receiving volume. This effect is captured by both methods at the same frequency. The only disagreement between the two methods is at very low frequencies below 200 Hz in most partitions. This disagreement is magnified in the light, flexible aluminum partition up to 700 Hz. As these methods are not strictly valid at such low frequencies, these disagreements are not relevant.
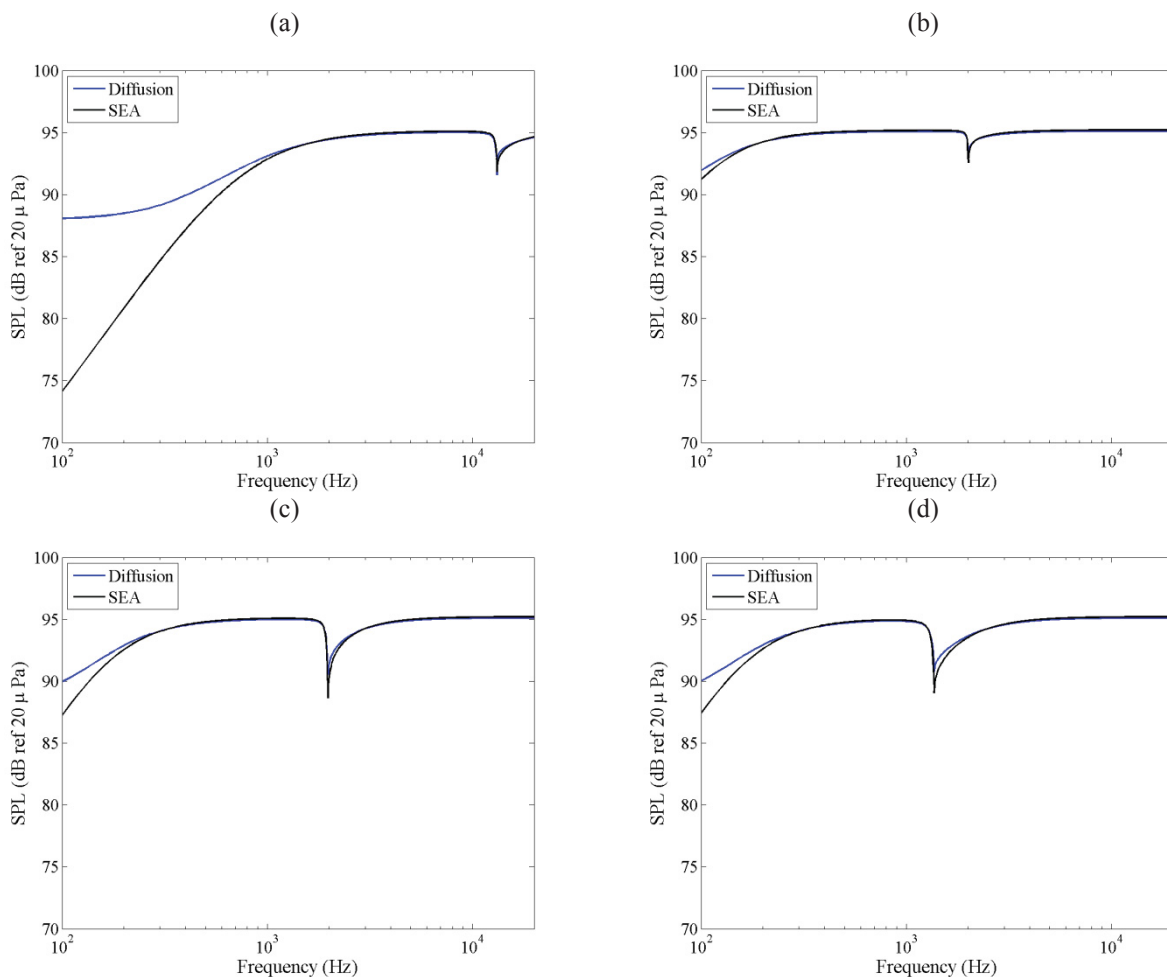
Figure 6.17: Average steady state SPL in the source volume calculated using the fully coupled diffusion model and statistical energy analysis for coupling partitions made of (a) aluminum, (b) steel, (c) glass, and (d) plywood.

The average steady state vibration energy level in the coupling partition is plotted in Figure 6.18. The diffusion model and SEA agree almost exactly; the disagreement noted at low frequencies in the source volume does not affect the vibration of the plate significantly. In the plate vibration, coincidence causes a peak at the critical frequency in an otherwise decreasing energy curve. Next, the radiation from the plate into the receiving volume is examined.
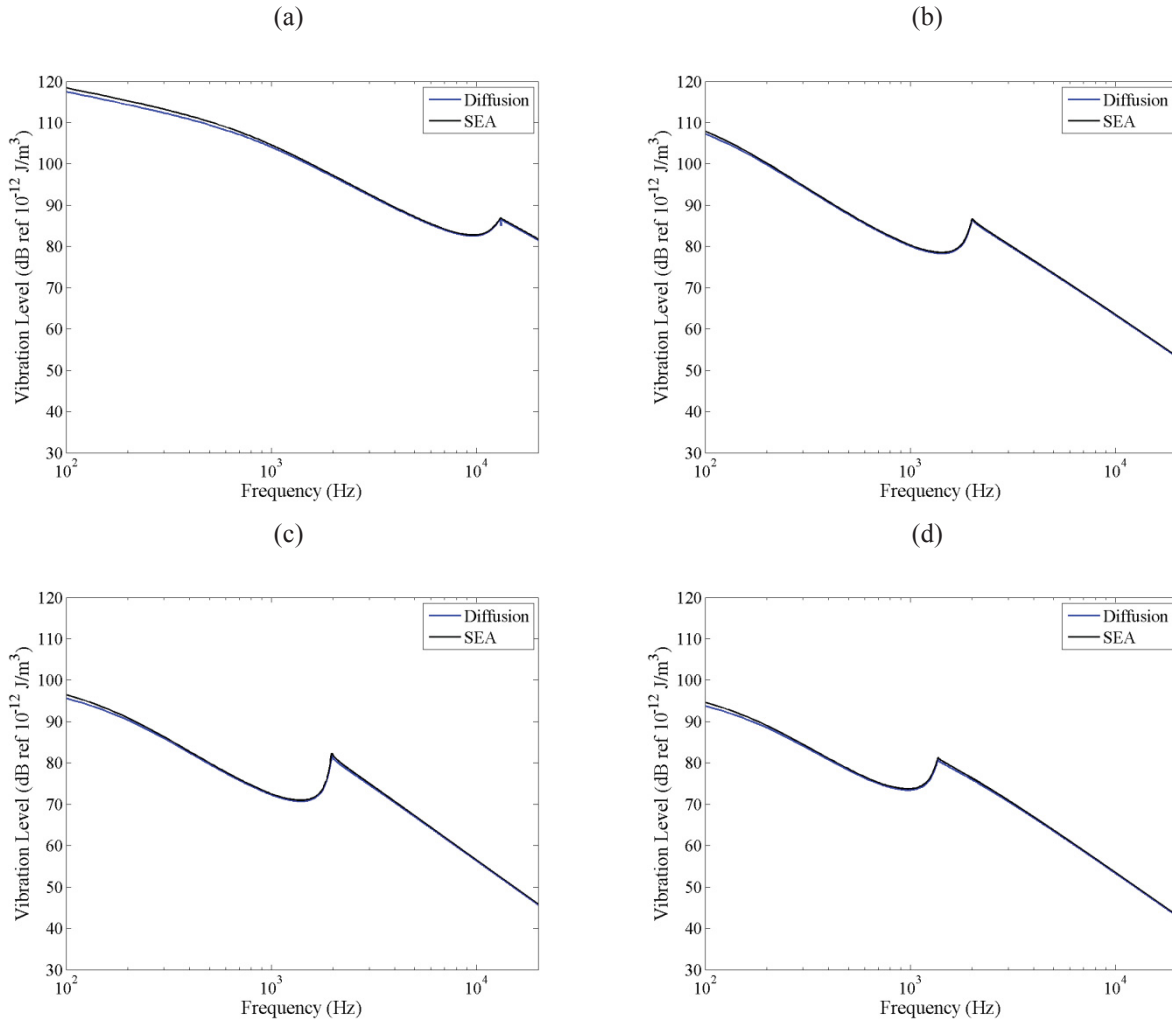
Figure 6.18: Average steady vibration energy level of the plate calculated using the fully coupled diffusion model and statistical energy analysis for coupling partitions made of (a) aluminum, (b) steel, (c) glass, and (d) plywood.

The average steady state SPL in the receiving volume is plotted in Figure 6.19. Again, there is excellent agreement between the diffusion model and SEA in general. The disagreement at low frequencies is very slight in the receiving volume. Coincidence causes a significant peak in acoustic energy transmitted into the receiving volume, to the point where the acoustic energy is

basically balanced between the two volumes. That is, the coupling partition is acoustically invisible at this critical frequency.

(a) (b)

(c) (d)
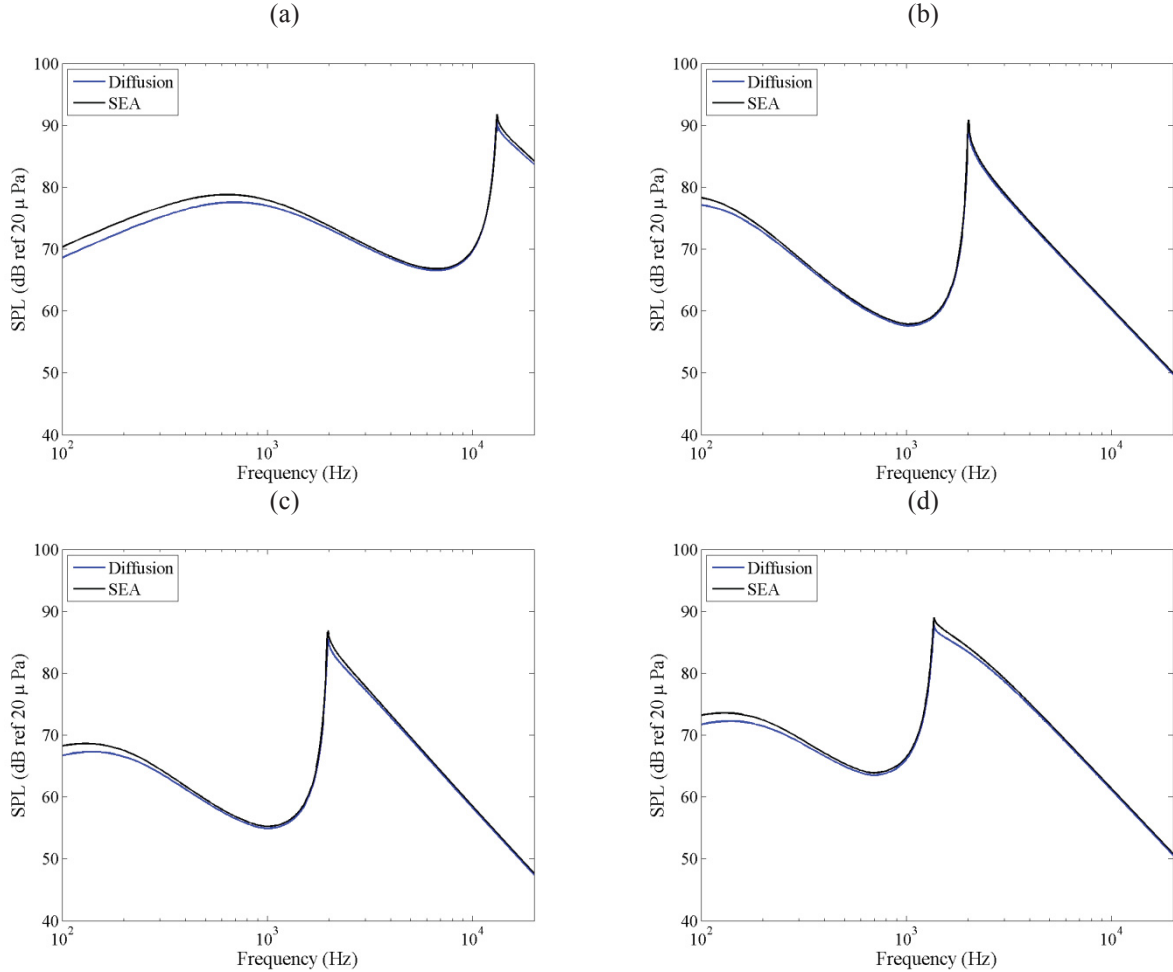
Figure 6.19: Average steady state SPL in the receiving volume calculated using the fully coupled diffusion model and statistical energy analysis for coupling partitions made of (a) aluminum, (b) steel, (c) glass, and (d) plywood.

The TL's of the four coupling partitions can be computed as is commonly performed in experimental measurements in a reverberant chamber using (Beranek and Vér, 1992)

$$TL = 10\log_{10}\left(\frac{\bar{\psi}_{1,ave}S_P}{\bar{\psi}_{2,ave}\alpha S_{a2}}\right)$$

6.16

where $\bar{\psi}_{1,ave}$ and $\bar{\psi}_{2,ave}$ are the average steady state energy densities in the source and receiving volumes, respectively, S_P is the area of the coupling partition, α is the acoustic absorption in the receiving volume, and S_{a2} is the total absorbing area in the receiving volume. The TL of

each partition computed with the diffusion model and SEA is plotted in Figure 6.20. The TL curves agree closely except at low frequencies of the aluminum partition.

(a) (b)

(c) (d)
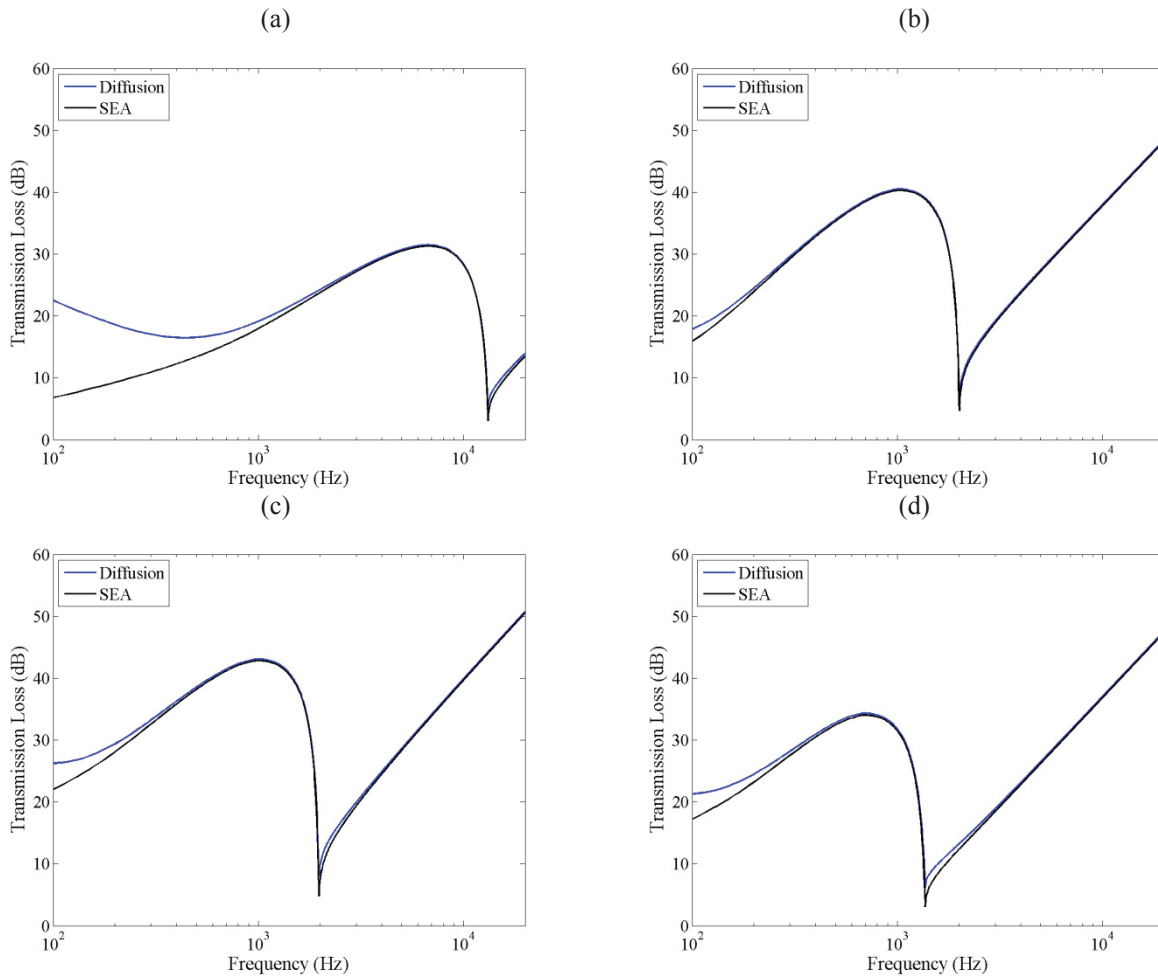
Figure 6.20: Transmission loss of coupling partitions made of (a) aluminum, (b) steel, (c) glass, and (d) plywood calculated using the fully coupled diffusion model and statistical energy analysis.

The TL is now averaged in octave bands for the aluminum, steel, and plywood partitions and one third octave bands for the glass partition for comparison with published data. The aluminum, steel, and plywood TL data comes from Bies and Hansen (2003) and the glass TL data from Quirt (1982). The experimental comparisons are plotted in Figure 6.21.
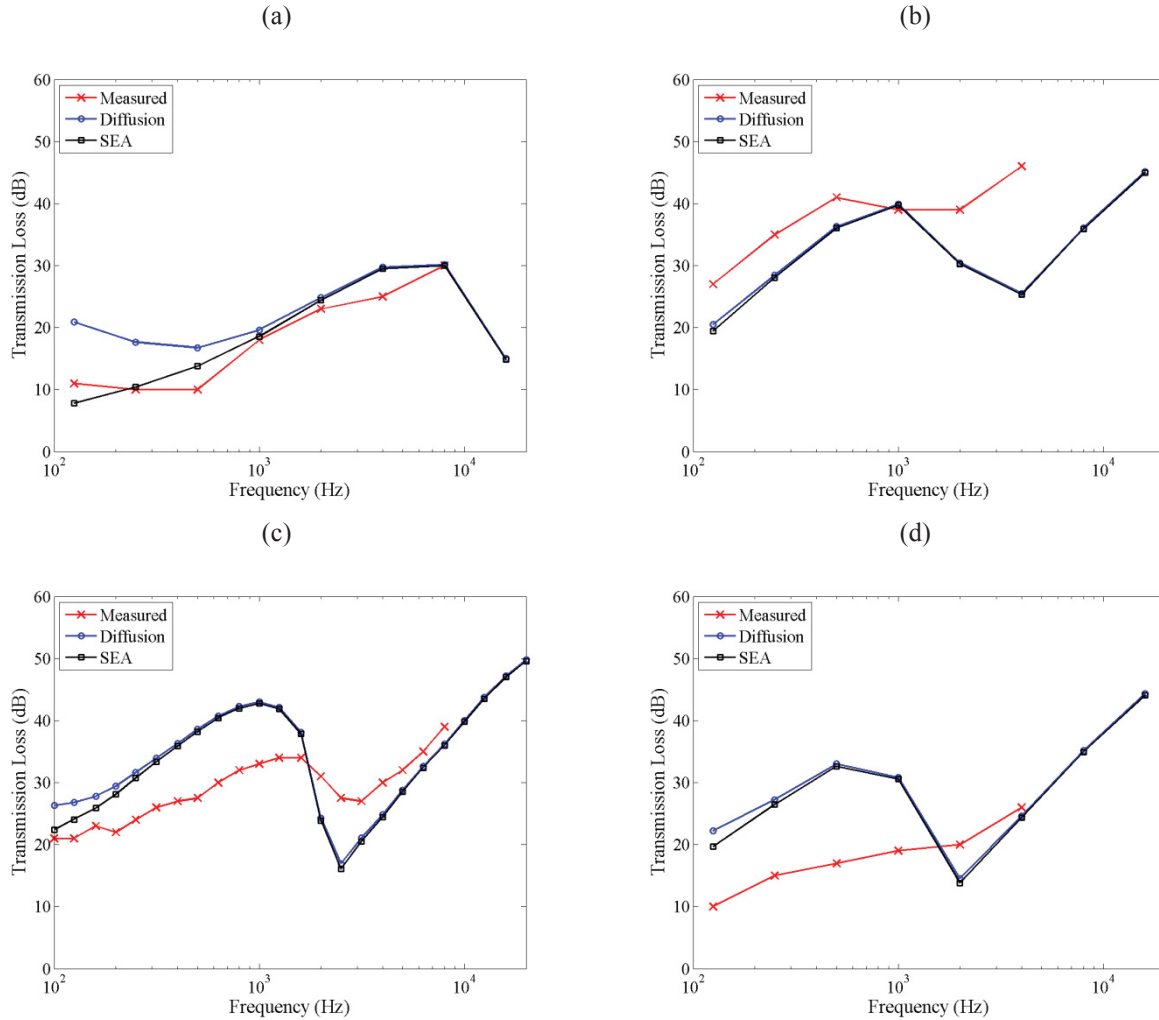
Figure 6.21: Transmission loss in (a,b,d) octave bands and (c) one third octave bands of coupling partitions made of (a) aluminum, (b) steel, (c) glass, and (d) plywood calculated using the fully coupled diffusion model and statistical energy analysis compared to measured data.

For the aluminum partition, SEA agrees with the experimental data to within 5 dB over the entire frequency range. The diffusion model exhibits greater than 10 dB error at very low frequencies, but demonstrates good agreement to within 5 dB in the frequency bands of 1000 Hz and higher. The TL of the steel partition is not well-predicted except in the 1000 Hz band. All other frequency bands exhibit at least 5 dB error. In the system coupled with a glass plate, the TL is significantly over-predicted at low frequencies until the region of coincidence is reached. Above 2000 Hz, the predicted TL is in good agreement with the measured data in general. Also, the slope of the damping controlled region (at high frequencies past coincidence) of the TL is very well predicted. The prediction of the TL of the plywood plate is similar to that of the glass

plate with significant over-prediction at low frequencies. At frequencies past coincidence, the predicted TL comes into close agreement with the measured data. Next, the system with the glass partition is examined more detail.

First, the distribution of steady state acoustic and structural energy density computed using the diffusion model throughout the coupled system is examined. The SEA solution is also plotted although it is assumed in the method that the energy density is constant in each subsystem. The SPL along a line of receivers perpendicular to the coupling partition running through the center of each volume is plotted in Figure 6.22 for several frequency bands.

As expected, a peak in SPL is computed close to the source in the source volume and the SPL decreases further from the source. The SPL decays fairly linearly in the receiving volume as the receivers are positioned further from the coupling partition. The SPL is fairly uniform in each volume for each frequency band with the highest variation in the frequency band near coincidence at 2000 Hz. Still, the range of SPL is much less than 5 dB in this case.
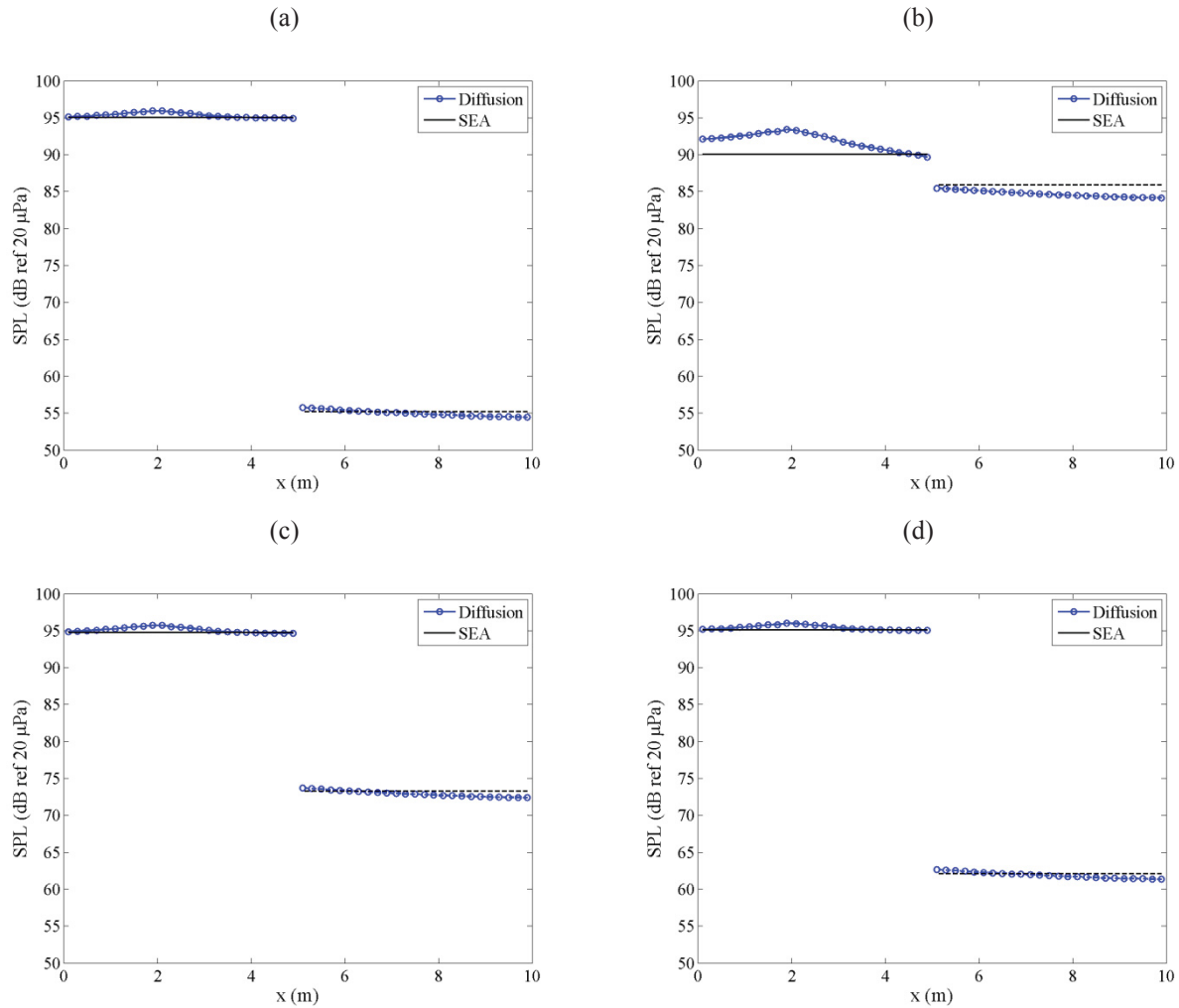
Figure 6.22: Steady state SPL in the volumes coupled by a glass partition at (a) 1000 Hz, (b) 2000 Hz , (c) 4000 Hz, and (d) 8000 Hz plotted against a coordinate perpendicular to the coupling surface with the source volume plotted as a straight line and receiving volume a dashed line.

The structural vibration energy level is plotted along a diagonal line of receivers running from corner to corner of the coupling partition through the projection of the source onto the plate. The vibration of the plate is very uniform in each frequency band. Slight variation is exhibited with a maximum close to the projection of the source but the range of energy levels is less than 1 dB in each case. The uniformity in acoustic and structural energy density is expected as the configuration is selected to be very uniform. However, the advantage of the diffusion model over SEA is demonstrated as the prediction of energy variation throughout a subsystem is possible with the former, not so with the latter.
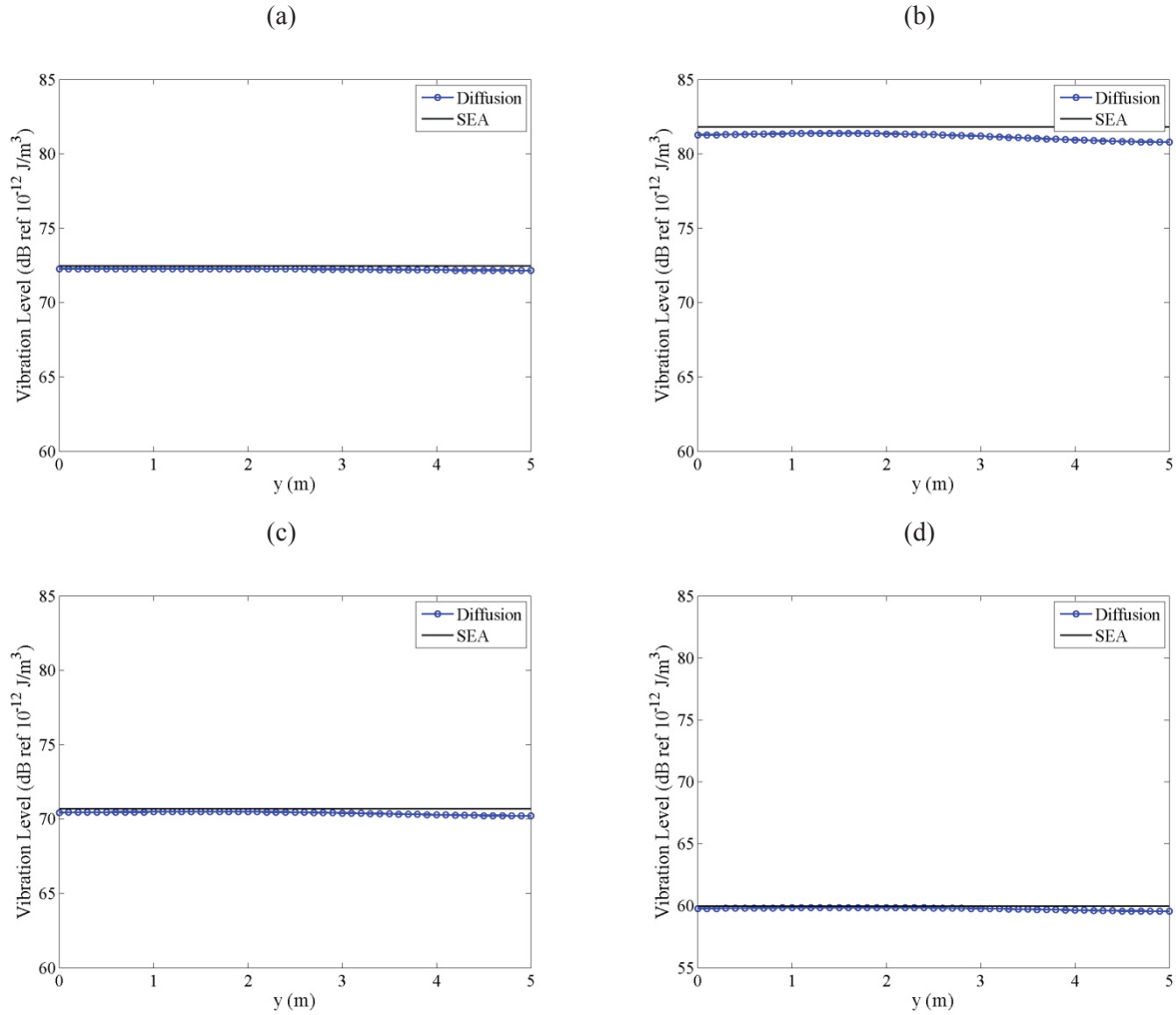
Figure 6.23: Steady state vibration energy level in the glass partition at (a) 1000 Hz, (b) 2000 Hz, (c) 4000 Hz, and (d) 8000 Hz plotted against a diagonal line from corner to corner through the projection of the source.

6.3.2.2 Transient Buildup Solution

Another advantage of the diffusion model is the ability to compute transient buildup or decay of energy density, which is now examined for the uniform cubic volumes coupled with the glass plate. The average buildup of SPL in the source and receiving volumes is plotted in Figure 6.24 for the 1000, 2000, 4000, and 8000 Hz octave bands. The SPL builds to its steady state level faster in the source volume than the receiving volume, as expected. However, the buildup at 2000 Hz (near coincidence) occurs quickly for both volumes. The buildup of average vibration energy level in the coupling plate is plotted in Figure 6.25. The buildup of structural vibration energy at these frequency bands occurs at a similar rate to the source volume. To examine the

136

buildup in each subsystem in more detail, the buildup time (time required for the energy density to build up to 95 % of its steady state value) is computed.
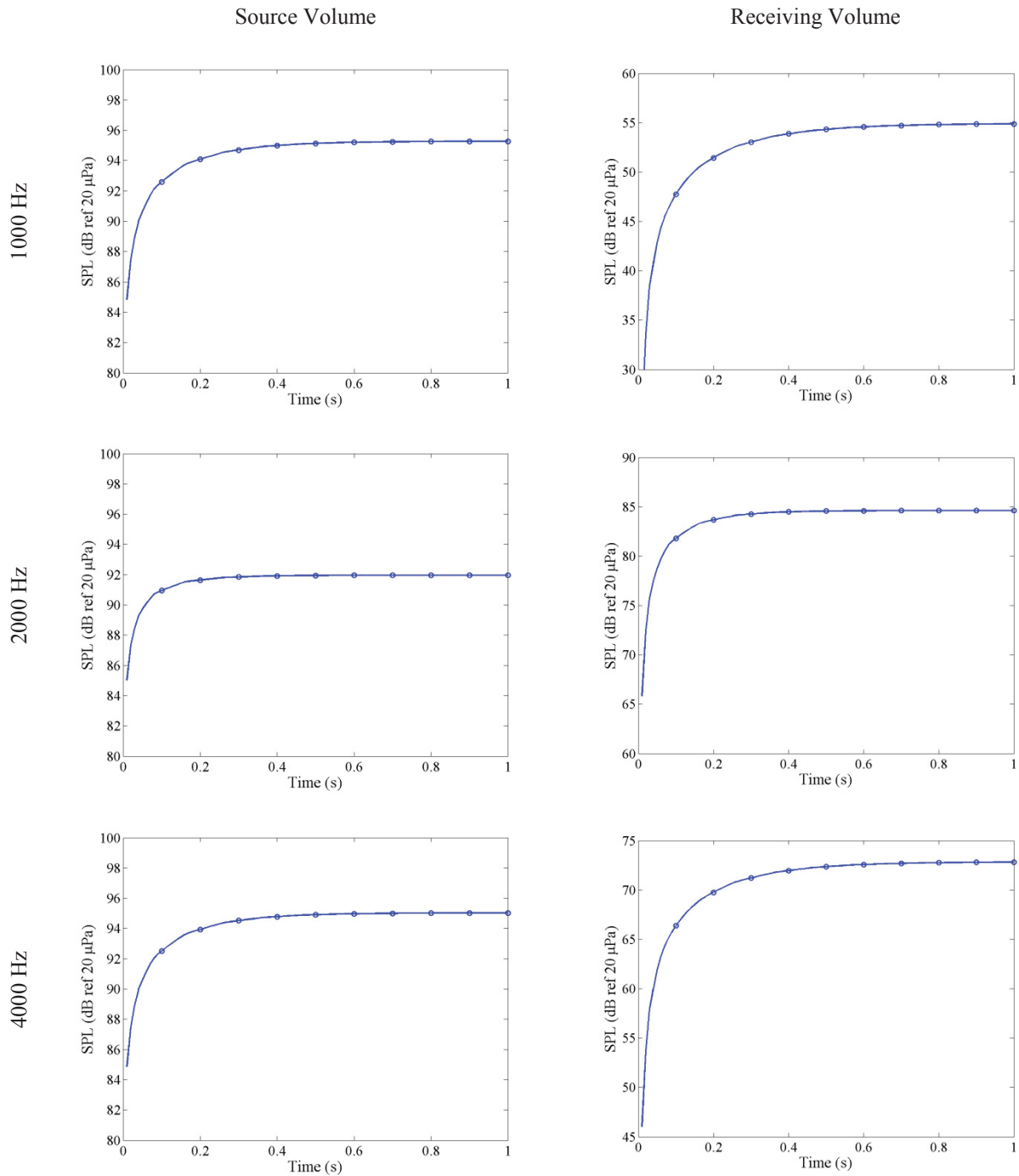
Figure 6.24: Buildup of the average SPL in the source and receiving volume coupled by a glass partition at 1000 Hz, 2000 Hz , 4000 Hz, and 8000 Hz.

8000 Hz

(a)

(b)
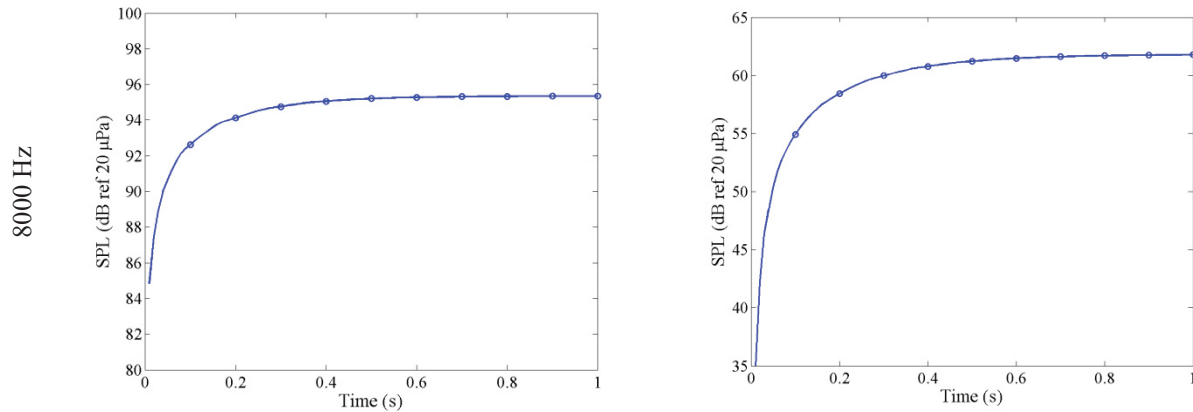
Figure 6.24, cont.: Buildup of the average SPL in the source and receiving volume coupled by a glass partition at 1000 Hz, 2000 Hz , 4000 Hz, and 8000 Hz.

(c)

(d)
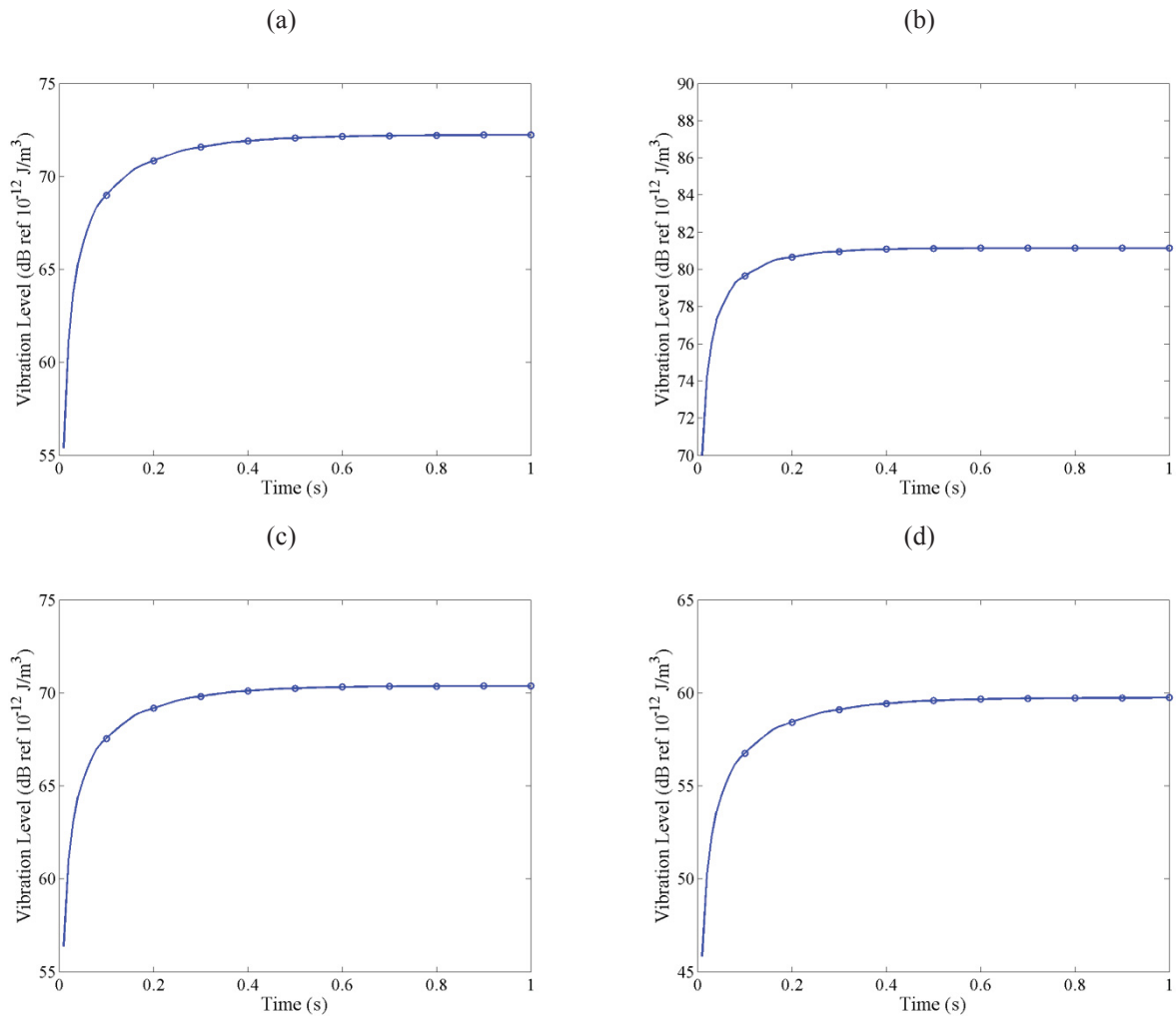
Figure 6.25: Buildup of the average vibration energy level in the glass coupling partition at (a) 1000 Hz, (b) 2000 Hz , (c) 4000 Hz, and (d) 8000 Hz.

The buildup time averaged across the receiver grids in each subsystem is plotted in Figure 6.26 in 1/3rd octave bands. The buildup time in the source volume is generally about 200-250 ms faster than the receiving volume. At coincidence, this difference narrows to only about 100 ms. The buildup time for the coupling plate is only slightly longer than the source volume, except at low frequencies where the buildup time for the coupling plate can take up to about 230 ms longer.
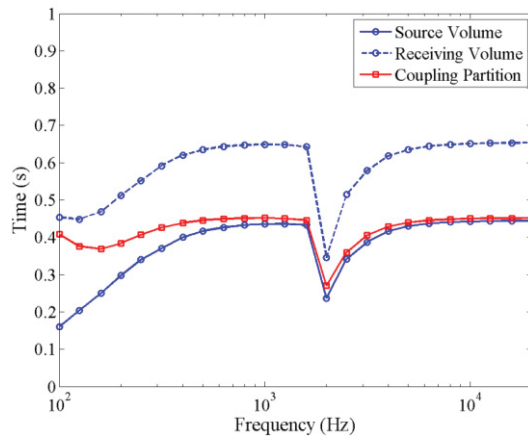
Figure 6.26: Average buildup time in the source and receiving volumes and the coupling partition.

Now, the distribution of buildup time is examined. The buildup time along a line of receivers perpendicular to the coupling plate through the center of the acoustic volumes is plotted in Figure 6.27. As with the steady state SPL, the buildup time is very uniform in each volume. It is slightly shorter very close to the source in the source volume and slightly longer as the receivers are positioned further from the coupling partition in the receiving volume. The buildup time along a diagonal line of receivers from corner to corner of the coupling plate through the projection of the source onto the plate is plotted in Figure 6.28. The buildup of vibration energy across the plate is essentially uniform.
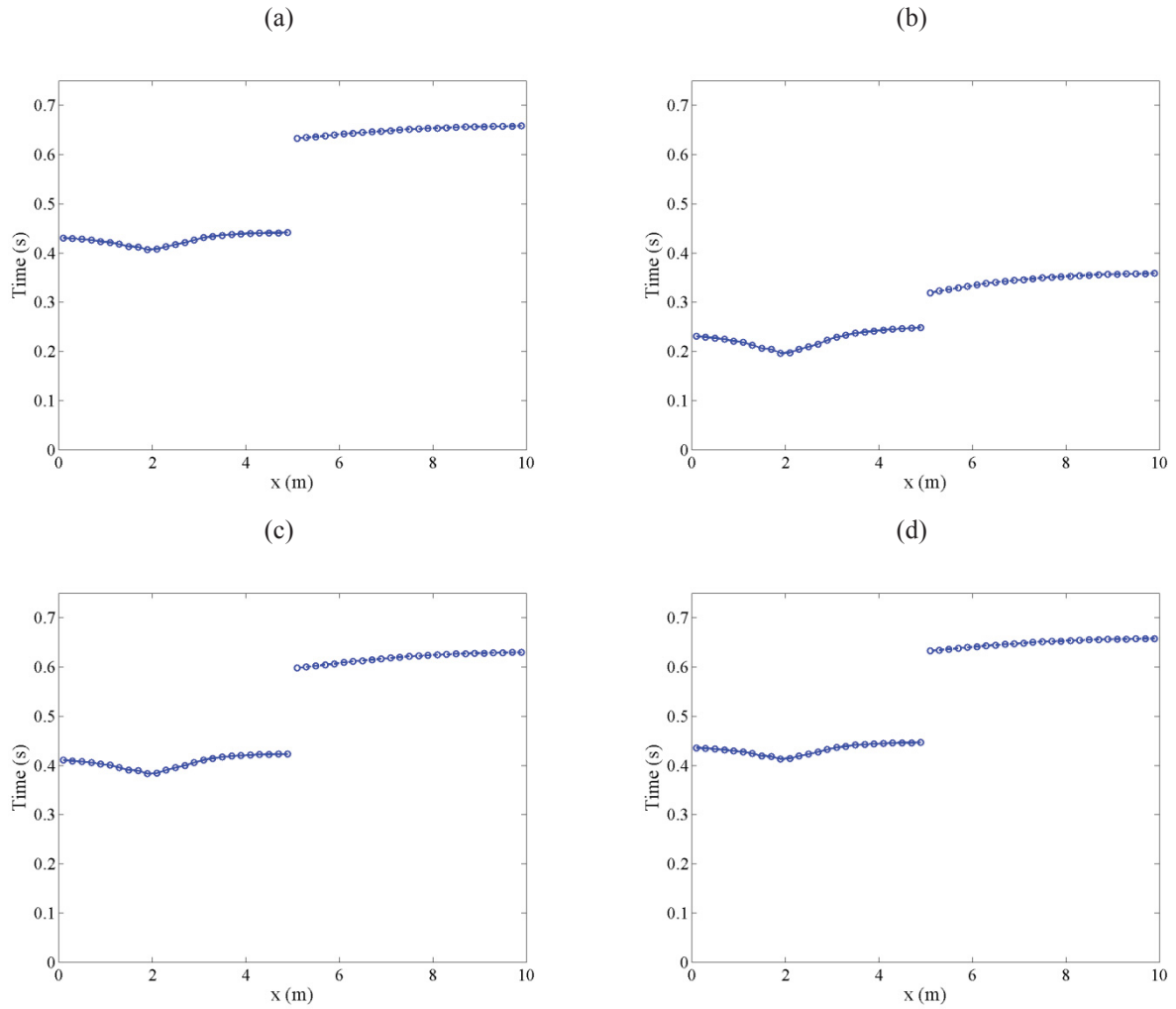
Figure 6.27: Buildup time in the volumes coupled by a glass partition at (a) 1000 Hz, (b) 2000 Hz, (c) 4000 Hz, and (d) 8000 Hz plotted against a coordinate perpendicular to the coupling surface with the source volume plotted as a straight line and receiving volume a dashed line.
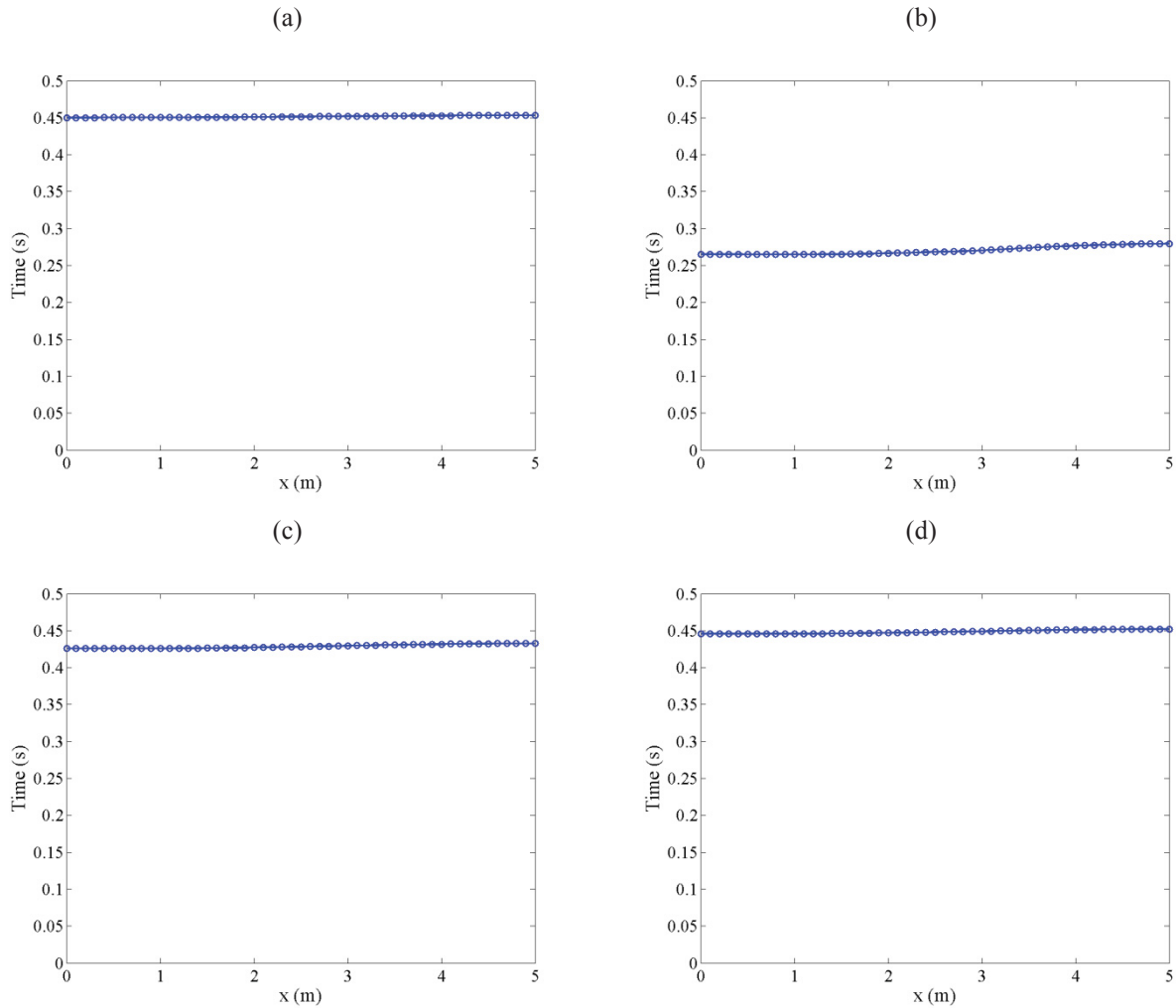
Figure 6.28: Buildup time in the glass partition at (a) 1000 Hz, (b) 2000 Hz, (c) 4000 Hz, and (d) 8000 Hz plotted against a diagonal line from corner to corner through the projection of the source.

Now that the new proposed models and solutions have been validated for these simple test cases, their use is examined in acoustic problems other than room acoustics. In the next chapter, the diffusion model and the BE-LTS is used to compute acoustic transmission through different engineering devices.

Chapter 7: Practical Applications of the Acoustic Diffusion BE-LTS

This chapter presents practical engineering applications of the newly developed BE-LTS to the acoustic diffusion model. The applications in this chapter are not exhaustive but are presented to show the potential of the method. The main goal is to show that the BE-LTS provides accurate results and can be used in real applications.

7.1   Noise Reduction of Tube Bundle Heat Exchangers

Tube bundle heat exchangers are often employed to transfer heat from one fluid to another. In the device, one fluid runs through a bundle of tubes and the other flows across the tubes. They are commonly employed in industrial applications, e.g. steam generators, evaporators, and microturbine generators (Heckl, 1995). The acoustic propagation through these dense bundles of tubes is important in many situations, e.g. in aerospace applications, in factories where hearing damage is a risk, and when ultrasound is used to detect damage in the heat exchanger (Heckl, 1995). Tube bundle heat exchangers have been shown both to increase noise due to acoustic resonances excited by vortex shedding from the flow (Cumpsty and Whitehead, 1971) and to reduce the amount of transmitted acoustic energy by providing a reflection of acoustic waves (Heckl, 1995). In this section, the acoustic transmission loss of a small tube bundle heat exchanger is studied using the BE-LTS to the acoustic diffusion model with simple coupling of acoustic volumes.

A series of experiments were performed to determine the transmission loss of a small heat exchanger. The heat exchanger consists of two dense bundles of small aluminum tubes. There are 6000 1.1 mm diameter tubes total. The two rectangular bundles are about 7 x 13 x 15 cm spaced about 4 cm apart. In this section, these measurements are simulated using the diffusion BE-LTS. The experiments were in a long box constructed with MDF with dimensions 1.5 x 0.15 x 0.18 m^3; an anechoic termination was fitted to one end of the box to absorb all acoustic energy. A speaker was placed about one inch from the rigid end of the box. Six microphones were used to measure the average SPL over a cross-section of the duct 1.2 m from the rigid end.

Measurements were made in an empty box, a box with the heat exchanger, and a box with a block of reticulated vitreous carbon (RVC) foam (Ultramet, 2013).

First, a diffusion model of the empty duct problem, shown schematically in Figure 7.1, is created and solved with the diffusion BE-LTS. A monopole source is assumed to be located at the center of the cross section at the axial location of the speaker and a single receiver also at the cross section center is placed on the measurement plane. All walls are assumed perfectly rigid and the anechoic termination is assumed perfectly absorptive. Two cases are run assuming negligible atmospheric attenuation and atmospheric attenuation included using eq. 5.1 for an environment with 40% relative humidity. The mesh used for the calculations of this configuration which gives at least ten elements per mean free path is shown in Figure 7.2.
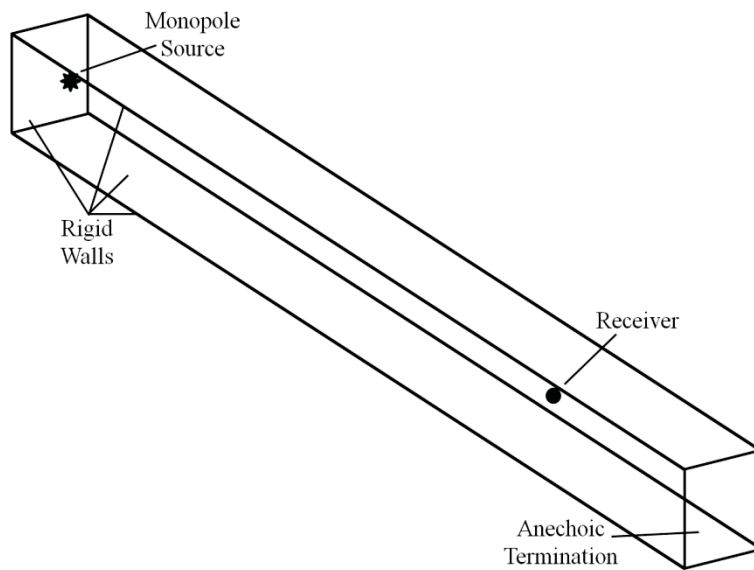
Figure 7.1: Schematic of the empty box problem used to calibrate the source power of the diffusion model of the heat exchanger TL experiments.
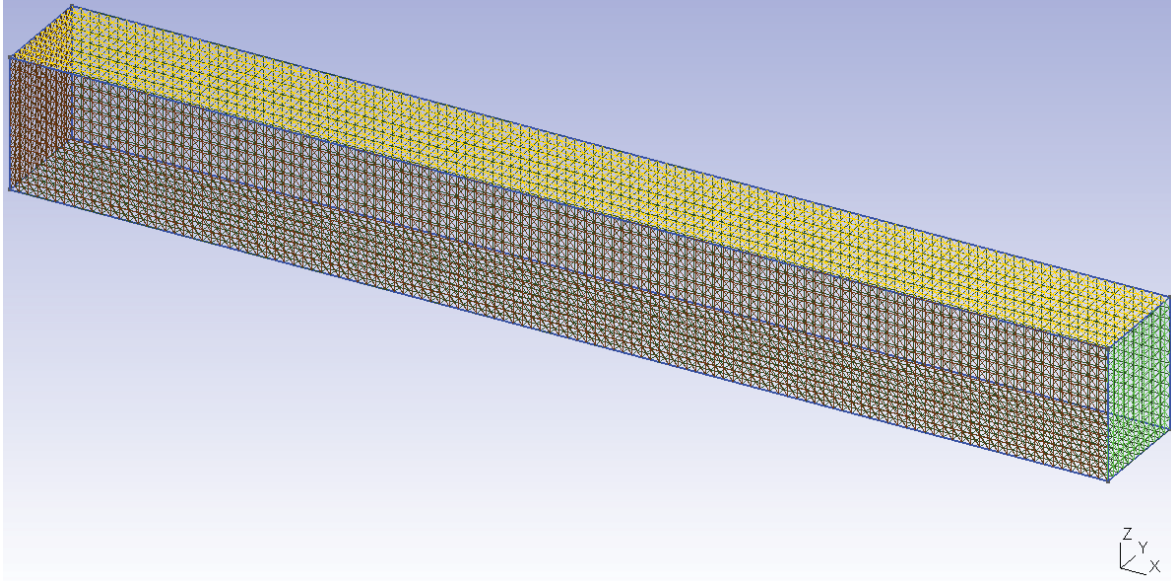
Figure 7.2: Diffusion BEM mesh of the empty box used to calibrate the source power of the diffusion model of the heat exchanger TL experiments.

Because the input power is unknown in the experiments, the empty duct configuration is used to calibrate it. For each 1/3rd octave band from 200 Hz to 20 kHz, the input power in the diffusion model is adjusted so that the SPL calculated matches the average SPL on the measurement plane. Note that the BE-LTS is not strictly valid at low frequencies where the diffuse field assumption is not satisfied. In this problem, it is estimated that a diffuse field exists at in the 1000 Hz one-third octave band and above, where the modal density in the empty duct is greater than 3. Results for the full frequency range are presented to examine the transition region.

Now, using the calibrated source power, a diffusion model of the box with the heat exchanger is created. Three volumes are coupled using the simple coupling diffusion BEM. As shown in Figure 7.3, the first volume on the left is made of five rigid walls with the calibrated monopole source at the same position as in the empty duct and filled with air. The second volume consists of the two tube bundles. Acoustically, the tube bundle domain is modeled as a modification with a diffusion coefficient which is a function of the tube bundle geometry as discussed by Billon et al. (2012). The diffusion coefficient in the tube bundle is smaller compared to other sections of the duct due to the large increase in surface area provided by the tubes (Billon et al., 2012). The third volume contains the receiver (at the same position as in the empty duct) and the anechoic termination. All boundaries coupling volumes are assumed to have

144

no absorption and perfect transmission (transmission coefficient of one). The meshes of each volume are shown in Figure 7.4 in which an attempt is made to preserve the approximate element size of the empty duct.
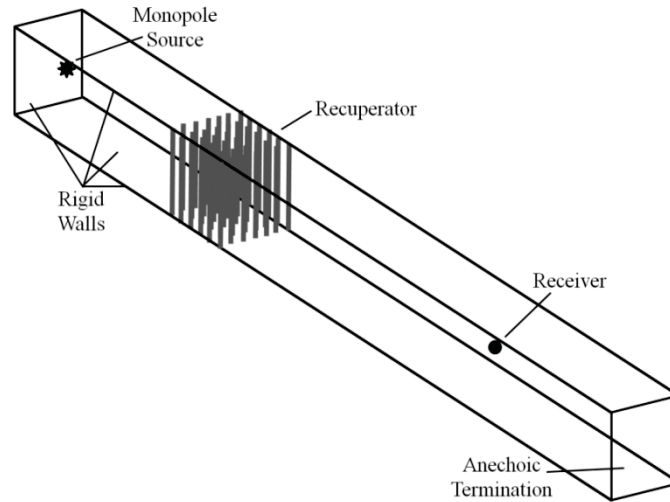
Figure 7.3: Schematic of the problem setup used to determine the TL of the tube bundle heat exchanger.
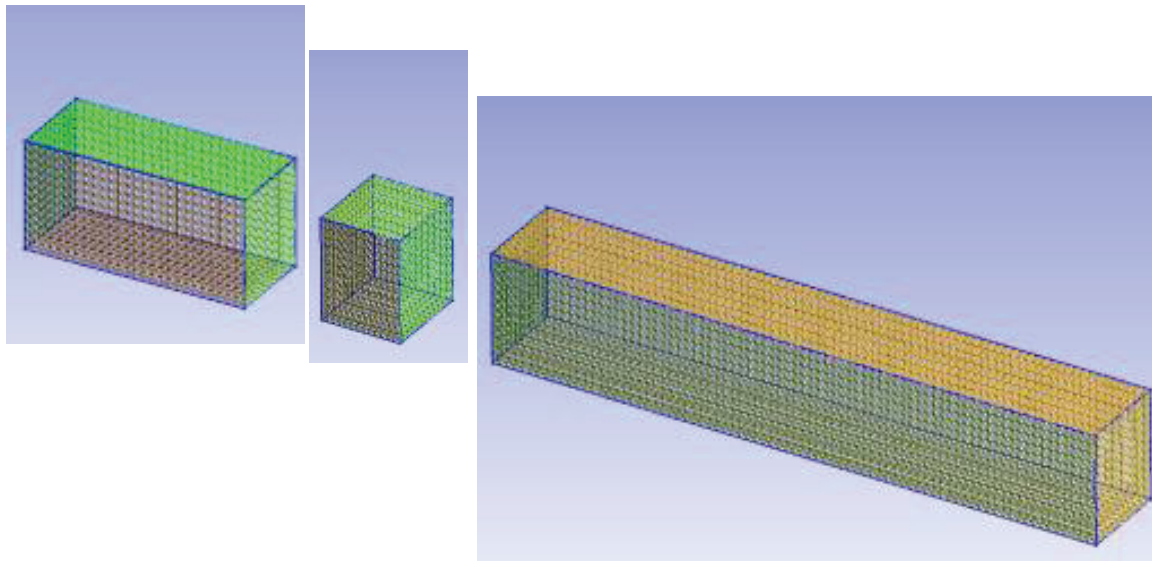
Figure 7.4: Diffusion BEM meshes of the box split into three volumes filled with air, a dense tube bundle, and air, respectively.

Assuming plane waves propagating along the longest axis of the box, the TL of the tube bundle heat exchanger is determined by subtracting the sound power measured with the device in the duct from the sound power measured in the empty duct. The measured average SPL and TL

145

are compared to the SPL and TL calculated from the diffusion model in 1/3rd octave bands in Figure 7.5 with and without atmospheric attenuation. Without any absorption, there are no frequency dependent parameters in the model. Thus, the TL is a constant value. The diffusion model is accurate exhibiting less than 2 dB error in both SPL and TL in the mid-frequency bands, 3150 Hz to 8000 Hz. Large errors of at least 5 dB are observed in the frequency bands below 3150 Hz as high as 10 dB, however. Also, the octave bands of 10 kHz and above exhibit error close to 3 dB or higher.

Including atmospheric attenuation greatly improves the accuracy of the diffusion model. The very high frequency bands above 3000 Hz demonstrate very good agreement with less than 2 dB error in each band. The significant improvement in the 1/3rd octave bands of 8000 Hz and above demonstrates that atmospheric attenuation is a factor in this range. The range of bands from 200 to 2500 Hz have the largest error ranging from 2.8 to 10 dB and show similar results to those excluding atmospheric attenuation as it is not as important at low frequencies.
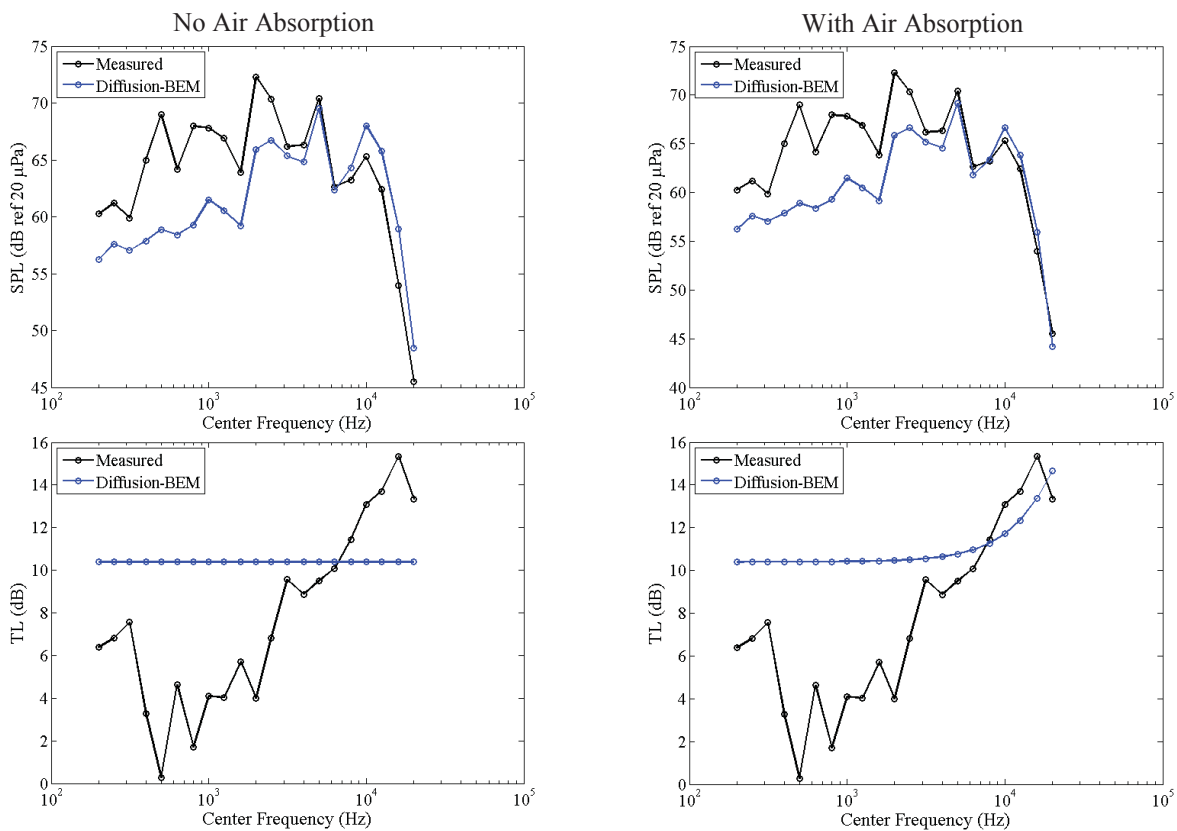
Figure 7.5: Comparison of the average measured (a,b) SPL and (c,d) TL and the SPL and TL computed from the diffusion model for the case (a,c) with no absorption and (b,d) including atmospheric attenuation.

It can be concluded that two mechanisms are acting in concert to provide the attenuation of the tube bundle heat exchanger. First, the very low diffusion coefficient in the equivalent tube bundle medium causes the medium to provide a very low flow of acoustic energy. Therefore, a significant amount of acoustic energy is stored in this medium as evidenced by the TL of Figure 7.5. Second, the energy that very slowly travels through this medium loses a much greater amount of energy from atmospheric attenuation than the energy that propagates very quickly through air.

Next, a block of reticulated vitreous carbon (RVC) foam is placed in the long box as shown in the schematic in Figure 7.6. The configuration is measured experimentally and simulated using a diffusion model. This study is performed only to determine an empirical model for the attenuation coefficient of the RVC foam block which will be used in subsequent studies. Similar to the heat exchanger configuration, the diffusion model consists of three volumes: one filled with air and a monopole source, the second filled with an absorptive acoustic material characterized by its own attenuation coefficient, and the third volume is filled with air, the receiver, and an anechoic termination. The RVC foam volume is modeled with the diffusion coefficient that would be used if the volume were filled with air. All exterior surfaces are perfectly reflecting except the anechoic termination which is perfectly absorptive. The interior surfaces are perfectly transmitting.
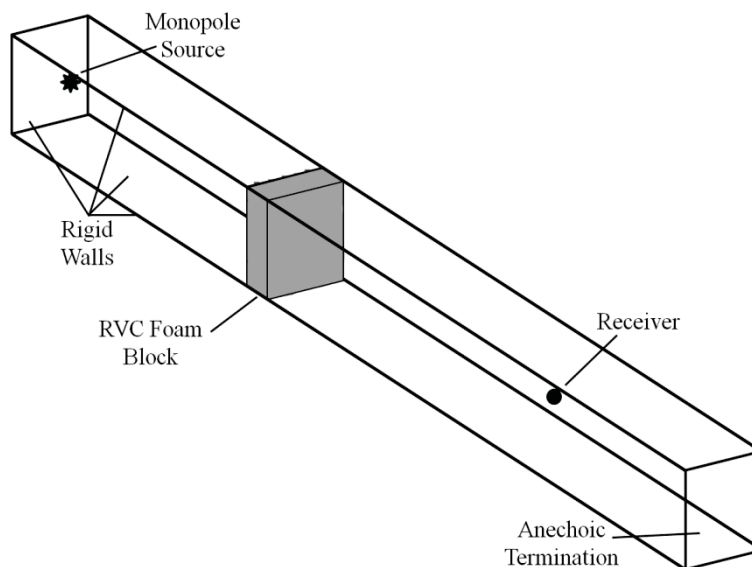
Figure 7.6: Schematic of the problem setup used to calculate an empirical model for the attenuation coefficient of an RVC foam block.

In the diffusion model, the absorptive medium is modeled by an atmospheric attenuation constant, m_m; the speed of sound through the material is assumed to be that of air. RVC foam is a relatively new material capable of withstanding high temperatures; acoustic energy models have not yet been developed. In this initial simulation, an empirical model is determined for the calculation of the attenuation constant.

The empirical model for the RVC foam attenuation coefficient is of the form

$$m_f(f) = b_f e^{\beta_f \ln f}$$ 7.1

where b_f and β_f are the empirical coefficients. The coefficients are determined by performing the diffusion simulation for the 1/3rd octave bands from 2500 Hz to 20000 Hz using different values until the difference between the SPL simulated and measured is less than 0.03 dB. Then, the coefficients are calculated through a curve that fits the attenuation coefficients in a least-squares sense. The coefficients are

$$b_f = 1.2108 \times 10^{-5}$$
$$\beta_f = 1.6294$$ 7.2

The SPL and TL from the calibrated diffusion model are compared to experiments in Figure 7.7. Not surprisingly, the results match well in the frequency range which was used to calculate the empirical model for the RVC foam exhibiting less than 1 dB error except in the 20 kHz octave band which is less than 2 dB error. At low frequencies below the 2500 Hz band, the empirical model still agrees with experimental data to within 2 dB except in the 250, 315, 630 Hz bands.
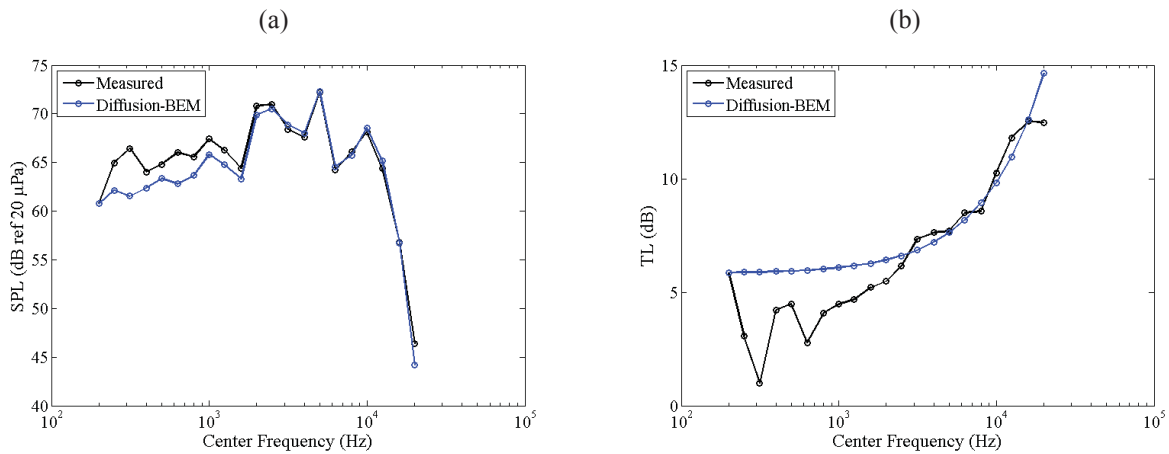
Figure 7.7: Comparison of measured and predicted (a) SPL and (b) TL of the block of foam using the empirical model of the foam.

7.2   Expansion Chamber Mufflers with Foam

Expansion chamber mufflers are employed in engines to reduce the noise produced by the combustion process. An expansion chamber is a reactive muffler which reflects acoustic waves back towards the source by presenting a mismatch of acoustic impedance through varying cross sectional areas. Acoustic foam can be added to expansion chambers to provide a dissipative mechanism for loss of acoustic energy. At low frequencies, expansion chambers can be modeled analytically assuming plane waves, but other methods must be used at higher frequencies where the plane wave assumption is invalid. Often, a FEM solution to the acoustic wave equation is used. Since the BE-LTS to the acoustic diffusion model offers a significant computational efficiency advantage over a traditional FEM solution, its use to compute the TL of these mufflers is now examined.

In this section, the diffusion model and the BE-LTS is used to compute the acoustic transmission through three different expansion chamber mufflers with RVC foam. These simulations serve two purposes: 1) to validate the diffusion model and the BE-LTS in high frequency muffler acoustics and 2) to validate the empirical model for the propagation of acoustic energy through RVC foam proposed in the previous section.

Three cylindrical expansion chambers were constructed, one of which is shown in Figure 7.8, and tested with a single speaker and microphone as a part of previous research (Sesler, 2003).

Figure 7.8: Silencer with 13 inch long expansion chamber with RVC foam lining and an airflow channel with bends (Sesler, 2003) [fair use].

The cross-sections of the three cylindrical expansion chambers are shown in Figure 7.9 (Sesler, 2003). The different mufflers are referred to as the chevron, 13" bend flow, and 6" bend flow based on the shape of the airflow channels through the RVC foam.

(a)

(b)

(c)
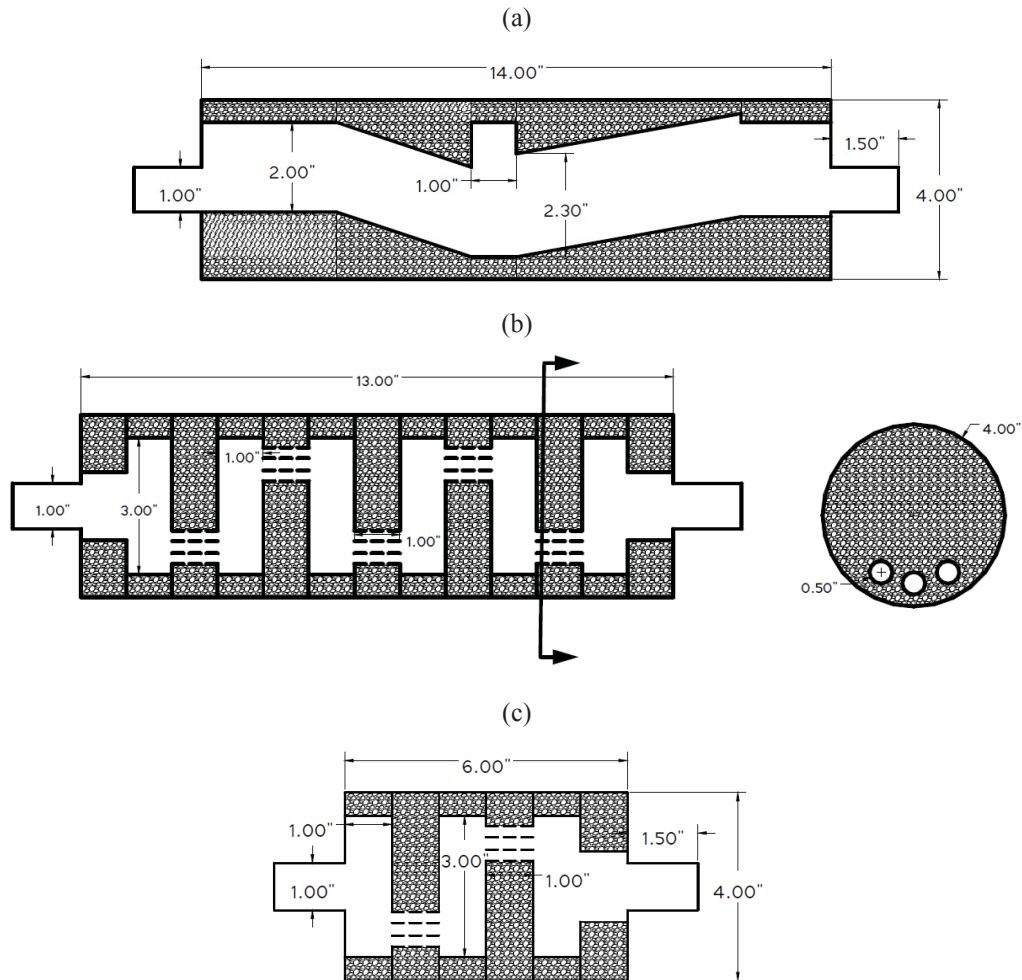
Figure 7.9: Drawings of the cross-section of the (a) chevron, (b) 13" bend flow, and (c) 6" bend flow expansion chamber mufflers with RVC foam linings (Sesler, 2003) [fair use].

For simplicity, each expansion chamber is modeled as a single 3-D volume as shown in Figure 7.10. Acoustic power (1 W) supplied as a surface source on one of the one inch diameter circular ends in each case models the sound propagating through the engine to which the muffler is connected. The opposite one inch diameter circular end is given an absorption coefficient of one to simulate the acoustic energy transmitted through the muffler and radiated from the exhaust. The other surfaces are given absorption coefficients of zero. The attenuation coefficient

is computed using a volume-weighted average of RVC foam, using the empirical model, and air which is assumed to have negligible attenuation compared to the foam. The TL's of the devices are computed by integrating the energy density over the perfectly absorbing surface and dividing the result by the input power.
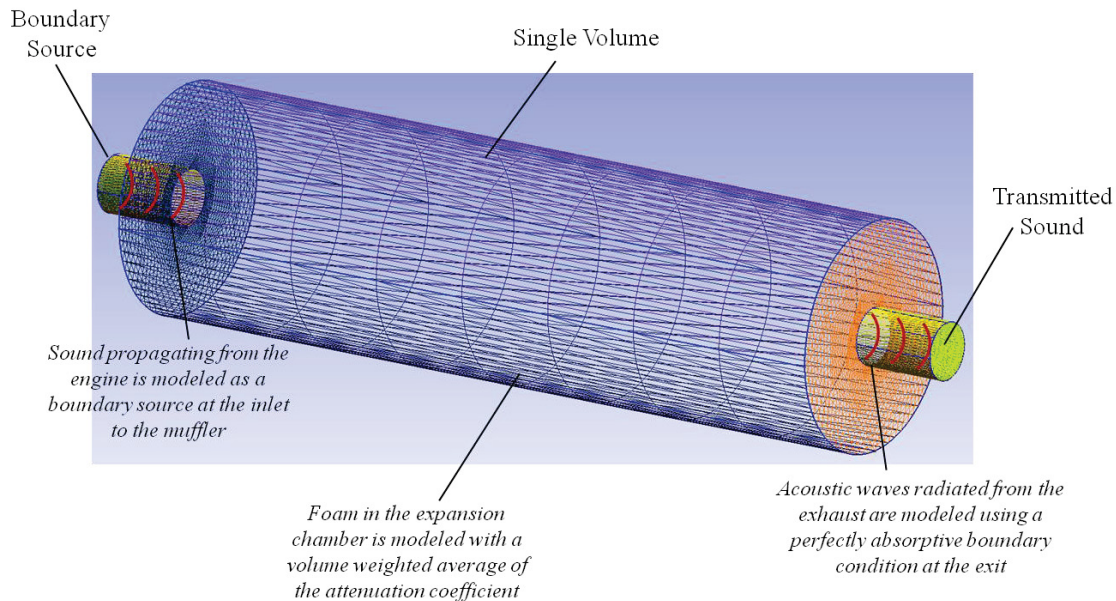
Figure 7.10: Schematic of the model used to represent an expansion chamber with acoustic diffusion and BE-LTS.

The TL's of the three different expansion chambers computed with the diffusion BE-LTS with the RVC foam are plotted in Figure 7.11 and overlaid on scanned images from the measurements made by Sesler (2003). Note that the measured data is plotted in narrowband and the diffusion BE-LTS is computed in one-third octave bands. Thus, the more accurate comparison is to average the narrowband data in each one-third octave band and compare to the diffusion BE-LTS. Due to the unavailability of the measured data, this computation is not possible and is left up to the interpretation of the reader. Imagine a curve of best fit running through the narrowband data.

It is demonstrated that the TL predicted by the diffusion BE-LTS demonstrates very good agreement with the average measured TL for each expansion chamber with RVC foam. In the chevron and 13 inch bend flow mufflers, the TL appears to be in good agreement from the 630 Hz band throughout the entire frequency range to the 5 kHz band with measured data scattered about equally above and below the predicted curves. The TL of the six inch bend flow muffler

151

with RVC foam appears to be slightly over-predicted as the measured data rarely exceeds the diffusion BE-LTS curve.

(a)

(b)   (c)
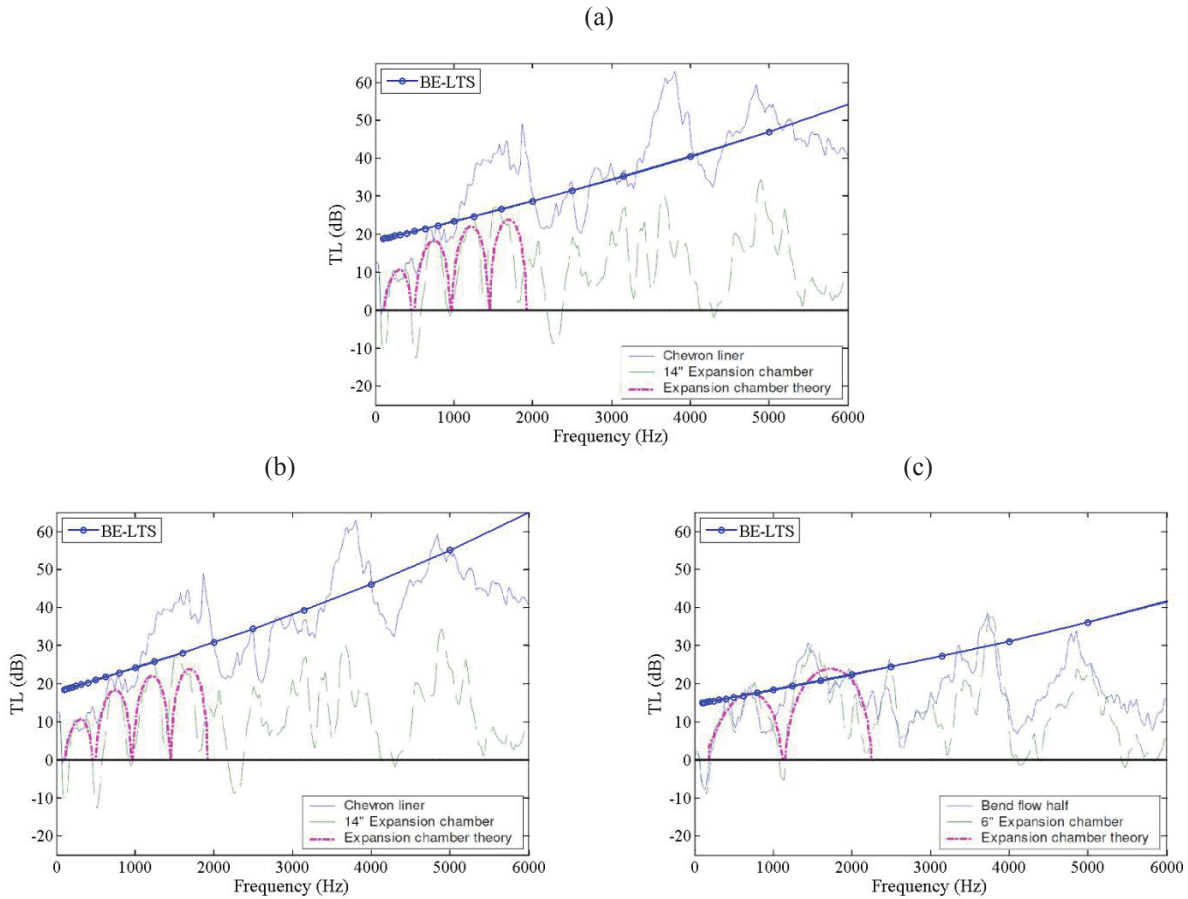
Figure 7.11: Transmission loss of the (a) chevron, (b) 13 inch bend flow, and (c) six inch bend flow expansion chambers computed using the BE-LTS to the diffusion model compared to measured data (Sesler, 2003) [fair use].

Overall, the diffusion model and the BE-LTS performs very well in the prediction of the TL of these different types of expansion chamber mufflers. This provides validation of the empirical model developed to predict the loss of acoustic energy of the RVC foam as well as the diffusion BE-LTS in yet another practical engineering application.

Chapter 8: Conclusions and Future Work

In this dissertation, a new, computationally efficient method of solution to the acoustic diffusion model was derived. A unique Laplace domain BEM solution and numerical inverse Laplace transform technique, the BE-LTS, was used to compute the time domain buildup and decay of acoustic energy in a volume. Previously, only a straight FEM solution to the diffusion model had been developed. The computational efficiency of the BE-LTS is greatly improved by minimizing the number of Laplace variable values necessary to accurately compute the numerical inverse Laplace transform. It was shown that one critical value of the Laplace variable can be estimated using the volume geometry and surface absorption.

The new acoustic diffusion BE-LTS was then validated through comparisons in three different rooms with statistical theory, ray tracing, and a FEM solution to the diffusion model. Both steady and transient solutions computed with the Laplace transform technique were compared in all volumes. Significant advantages in numerical convergence and computational efficiency of the diffusion BE-LTS over ray tracing were demonstrated.

Structural coupling of the BE-LTS to the diffusion model was investigated for acoustic volumes coupled by vibrating structural partitions. Two methods were investigated. The first used a simple transmission coefficient to compute the diffusion BE-LTS in coupled volumes. The second used a more complex power flow modeling of the structural partition which has never before been coupled to the diffusion model. The simple structural coupling method was validated through comparisons with statistical theory, ray tracing, and a FEM diffusion model solution. The power flow model coupling was validated through comparisons with SEA and by computing the TL for different structural partitions and comparing to experimental data.

Finally, the BE-LTS to the diffusion model was used in two problems of practical engineering importance other than room acoustics which is the diffusion model's only reported application. The method was used to compute the acoustic transmission loss through a tube bundle heat exchanger. Comparisons with experimental data demonstrated that the combination of slowly diffusing acoustic energy and air absorption work in concert to provide transmission

loss. Excellent agreement between the diffusion BE-LTS and the experimental data is observed. The TL of three expansion chamber mufflers with the same RVC foam was then computed using the diffusion BE-LTS and compared to experimental data. Excellent agreement provided further validation of the BE-LTS.

Although the research presented in this dissertation is comprehensive, a few details remain uninvestigated. First, more coupled structural-acoustic problems should be investigated to determine how accurate the method is for much more complex systems. Second, it is recommended that the lower frequency limits to this method is explored for varying problems and compared to other energy methods for acoustics. Finally, impulsive sources involving both energy buildup and decay can be explored to determine the model's effectiveness in more transient scenarios.

References

Allen, J.B. and D.A. Berkley. 1979. "Image method for efficiently simulating small-room acoustics." *Journal of Acoustical Society of America.* **65** (4): 943-950.

Beranek, L.L. and I.L. Ver. 1992. *Noise and Vibration Control Engineering: Principles and Applications*. New York: John Wiley & Sons, Inc.

Berendt, R.D., Winzer, G.E. and C.B. Burroughs. 1967. "A guide to airborne, impact, and structure borne noise: control in multifamily dwellings." U.S. Department of Housing and Urban Development, Washington, D.C.

Bies, D.A. and C.H. Hansen. 2003. *Engineering Noise Control: Theory and Practice*. 3rd ed. London and New York: Spon Press.

Billon, A., Valeau, V., Sakout, A., and J. Picaut. 2006. "On the use of a diffusion model for acoustically coupled rooms." *Journal of Acoustical Society of America.* **120** (4): 2043-2054.

Billon, A., Foy, C., Picaut, J., Valeau, V., and A. Sakout. 2008a. "Modeling the sound transmission between rooms coupled through partition walls by using a diffusion model." *Journal of Acoustical Society of America.* **123** (6): 4261-4271.

Billon, A., Picaut, J., Foy, C., Valeau, V., and A. Sakout. 2008b. "Introducing atmospheric attenuation within a diffusion model for room-acoustic predictions." *Journal of Acoustical Society of America.* **123** (6): 4040-4043.

Billon, A., Picaut, J., and A. Sakout. 2008c. "Prediction of the reverberation time in high absorbent room using a modified-diffusion model." *Applied Acoustics.* **69** (1): 68-74.

Billon, A., Picaut, J., Valeau, V., and A. Sakout. 2009. "Numerical simulations of the sound propagation in non rectilinear streets." *Euronoise 2009.* Edinburgh, Scotland, October 26-28.

Billon, A., Picaut, J., Valeau, V., and A. Sakout. 2012. "Acoustic predictions in industrial spaces using a diffusion model." Advances in Acoustics and Vibrations. **2012**: 1-9.

Bitsie, F. 1996. *The Structural-Acoustic Energy Finite Element Method and Energy Boundary Element Method*. Ph.D. Thesis. Purdue University: U.S.

Bouthier, O.M. and R.J. Bernhard. 1995. "Simple models of the energetics of transversely vibrating plates." *Journal of Sound and Vibration*. **182** (1): 149-166.

Butkovskiy, A.G. 1982. *Green's Functions and Transfer Functions Handbook*. Chichester, West Sussex, UK: Ellis Horwood Limited.

COMSOL. 2007. *COMSOL Multiphysics User's Guide*. Version 3.4.

Corcoran, J.M., Remillieux, M.C., and R.A. Burdisso. 2012. "Prediction of high frequency sonic boom noise transmission into buildings using a hybrid analytical-ray tracing approach." *Proceedings of Internoise 2012/ASME NCAD meeting*. New York City, NY, August 19-22.

Cotoni, V., Le Bot, A., and L. Jezequel. 2002. "Sound transmission through a plate by an energy flow approach." *Acta Acustica united with Acustica*. **88** (6): 827-836.

Cumpsty, N.A. and D.S. Whitehead. "The excitation of acoustic resonances by vortex shedding." *Journal of Sound and Vibration*. **18** (3): 353-369.

Davies, B. and B. Martin. 1979. "Numerical inversion of the Laplace Transform: a survey and comparison of methods." *Journal of Computational Physics*. **33** (1): 1-32.

Escolano, J., Navarro, J.M., and J.J. Lopez. 2010. "On the limitation of a diffusion equation model for acoustic predictions of rooms with homogeneous dimensions." *Journal of the Acoustical Society of America*. **128** (4): 1586-1589.

Farina, A. 1995. "RAMSETE: a new pyramid tracer for medium and large scale acoustic problems." *Proceedings of Euro-Noise 95*. Lyon, France, March 21-23. Vol. I p. 55.

Farina, A. 2000. "Validation of the pyramid tracing algorithm for sound propagation outdoors: comparison with experimental measurements and with the ISO-DIS 9613 standards." *Advances in Engineering Software*. **31** (4): 241-250.

Gibson, A.P., Hebden, J.C., and S.R. Arridge. 2005. "Recent advances in diffuse optical imaging." *Physics in Medicine and Biology*. **50** (4): R1-R43.

Halliwell, R.E., Nightingale, T.R.T., Warnock, A.C.C., and J.A. Birta. 1998. "Gypsum board walls: transmission loss data." National Research Council Canada.

Heckl, M.A. and L.S. Mulholland. "Some recent developments in the theory of acoustic transmission in tube bundles." *Journal of Sound and Vibration*. **179** (1): 37-62.

Incropera, F.P., DeWitt, D.P., Bergman, T.L., and A.S. Lavine. 2007. *Fundamentals of Heat and Mass Transfer*. 6th ed. Hoboken, NJ: John Wiley & Sons, Inc.

Jing, Y. and N. Xiang. 2007. "A modified diffusion equation for room-acoustic predication." *Journal of Acoustical Society of America*. **121** (6): 3284-3287.

Jing, Y. and N. Xiang. 2008. "On boundary conditions for the diffusion equation in room-acoustic prediction: Theory, simulations, and experiments." *Journal of Acoustical Society of America*. **123** (1): 145-153.

Kinsler, L.E., Frey A.R., Coppens, A.B., and J.V. Sanders. 2000. *Fundamentals of Acoustics*. 4th ed. New York: John Wiley & Sons, Inc.

Kohler, W.E. and L.W. Johnson. 2006. *Elementary Differential Equations*. 2nd ed. Boston, MA: Pearson Education, Inc.

Kuttruff, H. 1973. *Room Acoustics*. London: Applied Science Publishers, Ltd.

Le Bot, A. 1998. "A vibroacoustic model for high frequency analysis." *Journal of Sound and Vibration*. **211** (4): 537-554.

Le Pollès, T., Picaut, J., Bérengier, M., and C. Bardos. 2004. "Sound field modeling in a street canyon with partially diffusely reflecting boundaries by the transport theory." *Journal of Acoustical Society of America*. **116** (5): 2969-2983.

Liggett, J.A., and P.L-F. Liu. 1983. *The Boundary Integral Equation Method for Porous Media Flow*. London: George Allen & Unwin (Publishers) Ltd.

Lighthill, M.J. 1958. *An introduction to Fourier analysis and generalised functions*. Cambridge, United Kingdom: Cambridge University Press.

London, A. 1950. "Transmission of reverberant sound through double walls." *Journal of the Acoustical Society of America*. **22** (2): 270-279.

Marsh, J.A. 1971a. "The airborne sound insulation of glass: part 1." *Applied Acoustics*. **4** (1): 55-70.

Marsh, J.A. 1971b. "The airborne sound insulation of glass: part 2." *Applied Acoustics*. **4** (2): 131-154.

Marsh, J.A. 1971c. "The airborne sound insulation of glass: part 3." *Applied Acoustics*. **4** (3): 175-191.

Mulholland, K.A., Parbrook, H.D., and A. Cummings. 1967. "The transmission loss of double panels." *Journal of Sound and Vibration*. **6** (3): 324-334.

Nefske, D.J. and S.H. Sung. 1989. "Power flow finite element analysis of dynamic systems: basic theory and application to beams." *Journal of Vibration, Acoustics, Stress, and Reliability in Design*. **111** (1): 94-100.

Papoulis, A. 1955. "A new method of inversion of the Laplace transform." *Quarterly of Applied Mathematics*. **14** (4): 405-414.

Philibert, J. 2005. "One and a Half century of Diffusion: Fick, Einstein, before and beyond." *Diffusion Fundamentals 2*.

Picaut, J., Simon, L., and J.D. Polack. 1997. "A mathematical model of diffuse sound field based on a diffusion equation." *Acta Acustica.* **83** (4): 614-621.

Picaut, J., Simon, L., and J. Hardy. 1999a. "Sound field modeling in streets with a diffusion equation." *Journal of Acoustical Society of America.* **106** (5): 2638-2645.

Picaut, J., Simon, L., and J.D. Polack. 1999b. "Sound field in long rooms with diffusely reflecting boundaries." *Applied Acoustics.* **56** (4): 217-240.

Picaut, J. 2002. "Numerical modeling of urban sound fields by a diffusion process." *Applied Acoustics.* **63** (9): 965-991.

Quirt, J.D. 1982. "Sound transmission through windows I. Single and double glazing." *Journal of the Acoustical Society of America*. **72** (3): 834-844.

Quirt, J.D. 1983. "Sound transmission through windows II. Double and triple glazing." *Journal of the Acoustical Society of America*. **74** (2): 534-542.

Remillieux, M.C., Burdisso, R.A., and G. Reichard. "Transmission of sonic booms into a rectangular room with a plaster-wood wall using a modal-interaction model." *Journal of Sound and Vibration.* **327** (3-5): 529-556.

Schroeder, M.R. 1965. "New method of measuring reverberation time." *Journal of the Acoustical Society of America*. **37** (3): 409-412.

Sesler, J. 2003. *Implementation of Refractory Foam Technology for Silencing Small IC Engines*. M.S. Thesis. Virginia Tech: U.S.

Stewart, J. 2003. *Calculus: Early Transcendentals*. 5th ed. Belmont, CA: Brooks/Cole, Thomson Learning, Inc.

Ultramet. Ultramet Advanced Materials Solutions. May 20, 2013. <www.ultramet.com>.

Valeau, V., Picaut, J., and M. Hodgson. 2006. "On the use of a diffusion equation for room-acoustic prediction." *Journal of Acoustical Society of America.* **119** (3): 1504-1513.

Wu, T.W. (Editor). 2000. *Boundary Element Acoustics: Fundamentals and Computer Codes*, Southampton, UK: WIT Press.

Appendix A: Basic Review of Diffusion Theory

Diffusion is the process describing the random spreading of particles from regions of high concentration to region of low concentration. Figure A.1 shows the simple example of a group of particles in a glass. The particles are initially all concentrated in the same area, and then diffuse in the whole glass. In other words, the particles, as a result of their random movement, eventually spread themselves uniformly in the whole medium.
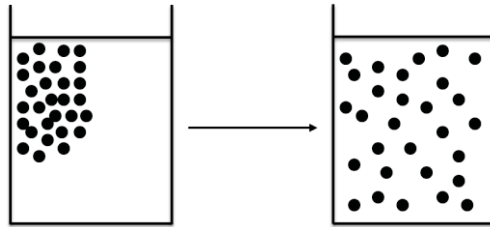
Figure A.1: Schematic demonstrating the diffusion of particles in a glass [fair use].

The mathematical and physical concept of diffusion was first developed by Joseph Fourier in 1822 in his work on heat conduction. The time rate of heat transfer through a material (local heat flux) is defined as proportional to the negative gradient of temperature and the coefficient of proportionality is called the material's conductivity. Analogous laws are known in electricity (charge transport) as Ohm's law and in fluid dynamics (hydraulic flow) as Darcy's law.

The general laws of diffusion were derived in 1855 by Adolf Fick, introducing the diffusion coefficient. Here, a variable with an under bar denotes a vector quantity. Fick's first law states that the diffusive flux, $\mathbf{J}$, at position, $\mathbf{r}$, and time, t, is proportional to the negative gradient of concentration field, Φ, with ∇ denoting the gradient operator. That is

$$\mathbf{J}(\mathbf{r},t) = -D(\mathbf{r},t)\nabla\Phi(\mathbf{r},t) \qquad \text{A.1}$$

where $\mathbf{J}$ is expressed generally as have units of an amount of substance per m^2 per s and Φ is the amount of substance per m^3, D is the diffusion coefficient, also called diffusivity, expressed in SI units of m^2 per s, which depends on the nature of the substance. At that time, the diffusion coefficient could only be determined experimentally but Fick still observed that its value increased with temperature.

Fick's second law describes how the concentration field varies in time. Let us first consider the mass balance of a closed system, i.e. the rate of accumulation of mass in the system, $\dfrac{\partial \Phi}{\partial t}$, exactly equals the rate of mass leaving the system, $-\nabla \mathbf{J}$, where the negative sign is present due to the conventional definition of the diffusive flux. Mathematically stated, this is

$$\frac{\partial \Phi(\mathbf{r},t)}{\partial t} = -\nabla \mathbf{J}(\mathbf{r},t).$$

A.2

Substituting Fick's first law, eq. A.1, into the mass balance of eq. A.2 leads to the expression of the second law as

$$\frac{\partial \Phi(\mathbf{r},t)}{\partial t} = \nabla \cdot \left[D(\mathbf{r},t) \nabla \Phi(\mathbf{r},t) \right].$$

A.3

If the diffusion coefficient is a constant, then eq. A.3 becomes

$$\frac{\partial \Phi(\underline{r},t)}{\partial t} = D \nabla^2 \Phi(\underline{r},t).$$

A.4

where ∇^2 is the Laplacian operator.

In 1905, Einstein, considering the random walk of the diffusing particles, established a mathematical description of the diffusion coefficient in liquids. He stated that D depends on the mean square value of the displacement of the particles in a given time period (Philibert, 2005).

These expressions have largely been used in heat transfer to describe the conduction of heat or the variation of temperature in a given region over time (Incropera et al., 2007). The diffusion of photons has also been used in optics for medical imaging in the brain, referred to as diffuse optical imaging (Gibson et al., 2005). Application of the laws of conservation of energy had also been extensively used in acoustics to predict the sound pressure level due to sound sources inside rooms (Bies and Hansen, 2003). However, these applications always assumed the uniformity of the sound density and the energy flow. Recent research has been performed to model the sound field in rooms following Fick's laws (Picaut et al., 1997; Picaut et al., 1999b; Billon et al., 2006; Valeau et al., 2006; Jing and Xiang, 2007; Billon et al., 2008a; Billon et al., 2008b; Billon et al., 2008c; Jing and Xiang, 2008). Even more recently, efforts have been put in using the diffusion theory to predict sound outdoors, more specifically in streets canyons (Picaut et al., 1999a; Picaut, 2002; Le Pollès et al., 2004; Billon et al., 2009). The next section focuses on applications

of the conservation of energy and the diffusion equation in acoustics, for both indoor and outdoor propagation.

Appendix B: Numerical Formulation of Boundary Elements

Now, the BEM is applied to the Laplace domain integral equation as a method of solving the surface integral. The BEM is applied to the general case with the understanding that the solution of the steady state surface integral is obtained simply by setting $s = 0$. Let the surface integral, $I_S(\mathbf{r}', s)$, be defined as

$$I_S(\mathbf{r}', s) = \int_{S'} \Psi(\mathbf{r}, s) \left[\frac{h(\mathbf{r})}{D} G(\mathbf{r} \mid \mathbf{r}', s) + \frac{\partial G(\mathbf{r} \mid \mathbf{r}', s)}{\partial \mathbf{n}} \right] dS .$$

B.1

The bounding surface is discretized into J elements, ΔS_j, made up of I nodes each. Equation B.1 can then be written as

$$I_S(\mathbf{r}', s) = \sum_{j=1}^{J} \int_{\Delta S_j'} \Psi(\mathbf{r}, s) \left[\frac{h_j}{D} G(\mathbf{r} \mid \mathbf{r}', s) + \frac{\partial G(\mathbf{r} \mid \mathbf{r}', s)}{\partial \mathbf{n}_j} \right] d(\Delta S_j)$$

B.2

where $h_j = \dfrac{c}{4} \dfrac{\alpha_j}{2[2 - \alpha_j]}$ and each element is assumed to have a constant absorption coefficient, α_j. The acoustic energy density at any position on the surface can be found by a linear superposition of the nodal energy density values, $\Psi_i(s)$, as

$$\Psi(\mathbf{r}, s) = \sum_{i=1}^{I} N_i(\mathbf{r}) \Psi_i(s)$$

B.3

where i is the node index and $N_i(\mathbf{r})$ are the shape functions for the element. A schematic of a typical flat triangular element is shown in Figure B.1(a) with its geometry, features, and properties labeled and a typical triangular mesh used for a numerical example later is shown in Figure B.1(b). Although the element is drawn triangular, no specification has been made on the shape of the element at this point in the formulation of the BEM solution.
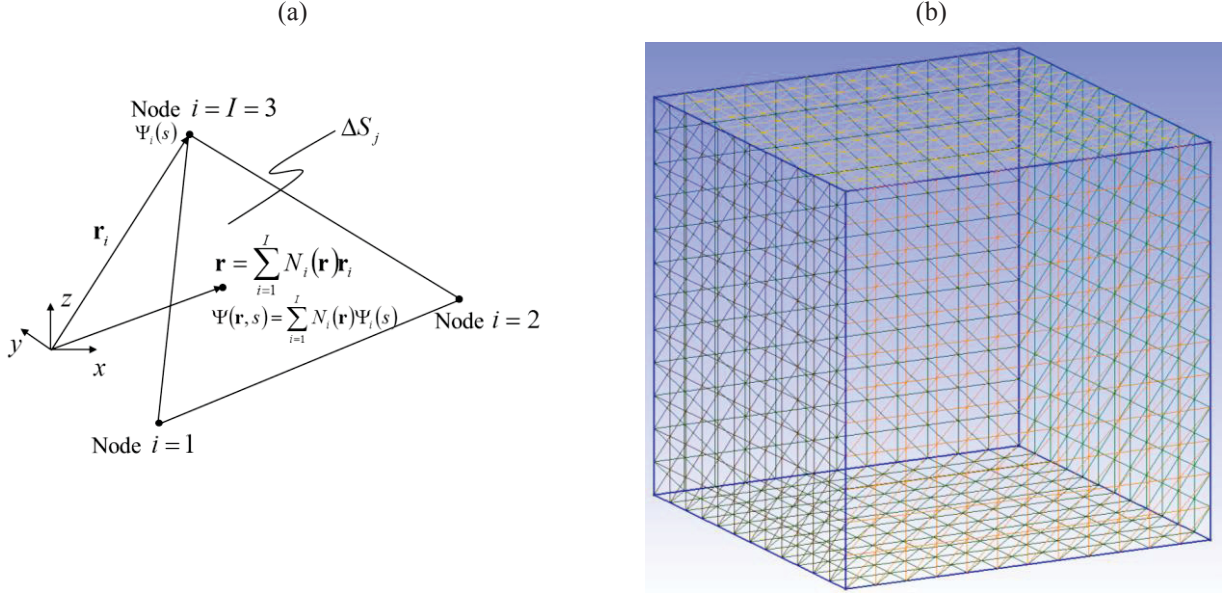
Figure B.1: Schematic showing (a) a typical, arbitrary element with features, geometry, and properties labeled and (b) a typical structured triangular mesh of a 10 x 10 x 10 m cubic volume.

Substituting eq. B.3 into eq. B.2 gives

$$I_S(\mathbf{r}',s) = \sum_{j=1}^{J}\sum_{i=1}^{I}\Psi_{ij}(s)\int_{\Delta S_j'} N_{ij}(\mathbf{r})\left[\frac{h_j}{D}G(\mathbf{r}\,|\,\mathbf{r}',s) + \frac{\partial G(\mathbf{r}\,|\,\mathbf{r}',s)}{\partial \mathbf{n}_j}\right]d(\Delta S_j) \qquad \text{B.4}$$

where $\Psi_{ij}(s)$ is the energy density at the ith node of the jth element.

The next step in the BEM formulation is to set up the numerical integration of the discrete elements. In this formulation, the boundary elements are assumed to be linear, 2D isoparametric elements. The position, $\mathbf{r} = x\hat{i} + y\hat{j} + z\hat{k}$ where $\hat{i}$, $\hat{j}$, and $\hat{k}$ are the unit vectors in three orthogonal directions, at any point inside an element can be found using the shape functions as in

$$x = \sum_{i=1}^{I} x_i N_i(\xi_1,\xi_2)$$

$$y = \sum_{i=1}^{I} y_i N_i(\xi_1,\xi_2) \qquad \text{B.5}$$

$$z = \sum_{i=1}^{I} z_i N_i(\xi_1,\xi_2)$$

163

where (x_i, y_i, z_i) are the nodal positions and (ξ_1, ξ_2) are the isoparametric coordinates of the master element. For a triangular master element shown in Figure B.2 (Wu, 2000), the shape functions are given by

$$N_1(\xi_1, \xi_2) = \xi_1$$
$$N_2(\xi_1, \xi_2) = \xi_2$$
$$N_3(\xi_1, \xi_2) = 1 - \xi_1 - \xi_2$$

B.6
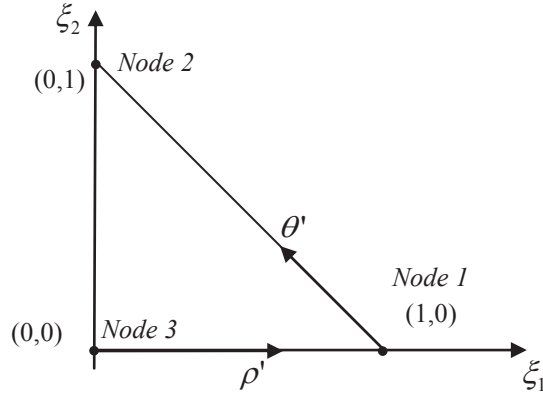
Figure B.2: Isoparametric triangular master element geometry.

The elemental area, $d(\Delta S_j)$, can be found using the relation

$$d(\Delta S_j) = |\mathbf{v}_j| d\xi_1 d\xi_2$$

B.7

where

$$\mathbf{v} = \frac{\partial \mathbf{r}}{\partial \xi_1} \times \frac{\partial \mathbf{r}}{\partial \xi_2} = \begin{bmatrix} \dfrac{\partial y}{\partial \xi_1}\dfrac{\partial z}{\partial \xi_2} - \dfrac{\partial z}{\partial \xi_1}\dfrac{\partial y}{\partial \xi_2} \\[2mm] \dfrac{\partial z}{\partial \xi_1}\dfrac{\partial x}{\partial \xi_2} - \dfrac{\partial x}{\partial \xi_1}\dfrac{\partial z}{\partial \xi_2} \\[2mm] \dfrac{\partial x}{\partial \xi_1}\dfrac{\partial y}{\partial \xi_2} - \dfrac{\partial y}{\partial \xi_1}\dfrac{\partial x}{\partial \xi_2} \end{bmatrix}.$$

B.8

Let the Jacobian, $J = |\mathbf{v}|$. Then, using eq. B.8,

$$J = \sqrt{\left(\frac{\partial y}{\partial \xi_1}\frac{\partial z}{\partial \xi_2} - \frac{\partial z}{\partial \xi_1}\frac{\partial y}{\partial \xi_2}\right)^2 + \left(\frac{\partial z}{\partial \xi_1}\frac{\partial x}{\partial \xi_2} - \frac{\partial x}{\partial \xi_1}\frac{\partial z}{\partial \xi_2}\right)^2 + \left(\frac{\partial x}{\partial \xi_1}\frac{\partial y}{\partial \xi_2} - \frac{\partial y}{\partial \xi_1}\frac{\partial x}{\partial \xi_2}\right)^2}$$

B.9

and

$$d(\Delta S_j) = J_j d\xi_1 d\xi_2.$$

B.10

164

The unit normal vector to the jth element can be found using

$$\mathbf{n}_j = \frac{\mathbf{v}_j}{J_j}.$$

For triangular elements, the x derivatives defining the vector, $\mathbf{v}$, are determined using eqs. B.5 and B.6 to be

$$\frac{\partial x}{\partial \xi_1} = \sum_{i=1}^{I} x_i \frac{\partial N_i(\xi_1, \xi_2)}{\partial \xi_1} = x_1 - x_3$$
$$\frac{\partial x}{\partial \xi_2} = \sum_{i=1}^{I} x_i \frac{\partial N_i(\xi_1, \xi_2)}{\partial \xi_2} = x_2 - x_3$$

Similarly, the derivatives can be evaluated for y and z. Focusing on the element integral of eq. B.4, let

$$C_{ij}(\mathbf{r}',s) = \int_{\Delta S_j'} N_{ij}(\mathbf{r}) \left[\frac{h_j}{D} G(\mathbf{r}|\mathbf{r}',s) + \frac{\partial G(\mathbf{r}|\mathbf{r}',s)}{\partial \mathbf{n}_j} \right] d(\Delta S_j).$$

Using the geometry of the master element shown in Figure B.2 to obtain integral limits and substituting eq. B.10 into B.12 results in

$$C_{ij}(\mathbf{r}',s) = \int_0^1 \int_0^{1-\xi_2} \left[\frac{h_j}{D} G(\mathbf{r}|\mathbf{r}',s) + \frac{\partial G(\mathbf{r}|\mathbf{r}',s)}{\partial \mathbf{n}_j} \right] N_{ij}(\xi_1, \xi_2) J_j d\xi_1 d\xi_2$$

where $\mathbf{r} = \begin{bmatrix} x & y & z \end{bmatrix}^T = f(\xi_1, \xi_2)$. To apply Gaussian quadrature to the triangular master element, it must first converted to a unit square as shown in Figure B.3 using the ρ' and θ' isoparametric coordinates shown for both master elements in Figure B.2 and Figure B.3 (Wu, 2000).
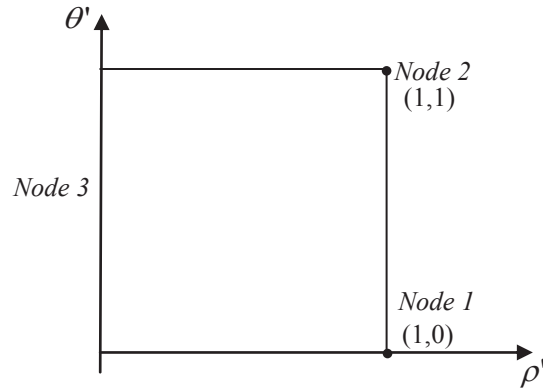
Figure B.3: Isoparametric unit square element geometry.

The coordinates and Jacobian for this transformation are given by (Wu, 2000)

$$\xi_1 = \rho'(1-\theta')$$
$$\xi_2 = \rho'\theta'$$
$$J' = \rho'$$

0.15

Thus,

$$d\xi_1 d\xi_2 = J' d\rho' d\theta' .$$

B.16

Substituting eq. B.16 into eq. 0.14 gives

$$C_{ij}(\mathbf{r}',s) = \int_0^1 \int_0^1 \left[\frac{h_j}{D} G(\mathbf{r}|\mathbf{r}',s) + \frac{\partial G(\mathbf{r}|\mathbf{r}',s)}{\partial \mathbf{n}_j} \right] N_{ij}(\xi_1,\xi_2) J_j \rho' d\rho' d\theta' .$$

0.17

In the next step required to directly apply Gaussian quadrature to the element, the unit square is converted to a 2x2 square with geometry shown in Figure B.4 (Wu, 2000).
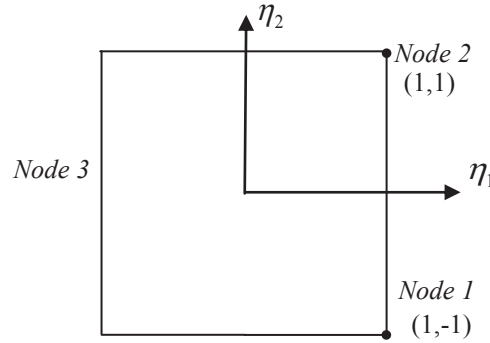
Figure B.4: Isoparametric 2x2 square element geometry.

The coordinates and Jacobian for this transformation are given by (Wu, 2000)

$$\rho' = \frac{1}{2} + \frac{1}{2}\eta_1$$
$$\theta' = \frac{1}{2} + \frac{1}{2}\eta_2$$
$$J'' = \frac{1}{4}$$

B.18

The elemental areas between the two square elements are related by

$$d\rho' d\theta' = \frac{1}{4} d\eta_1 d\eta_2 .$$

B.19

Substituting eq. B.19 into eq. 0.17 gives

$$C_{ij}(\mathbf{r}',s) = \frac{1}{4}\int_{-1}^{1}\int_{-1}^{1}\left[\frac{h_j}{D}G(\mathbf{r}\mid\mathbf{r}',s)+\frac{\partial G(\mathbf{r}\mid\mathbf{r}',s)}{\partial \mathbf{n}_j}\right]N_{ij}(\xi_1,\xi_2)J_j\rho'd\eta_1 d\eta_2 \;.$$ B.20

Now, an exact solution of the integral for the linear interpolation of the integrand can be found by application of a Gaussian quadrature by evaluation of the shape functions at M^2 Gauss integration points, $\left(\xi_1^{(m)},\xi_2^{(n)}\right)$, given by

$$C_{ij}(\mathbf{r}',s) = \frac{1}{4}\sum_{m=1}^{M}\sum_{n=1}^{M}w_m w_n\left[\frac{h_j}{D}G(\mathbf{r}\mid\mathbf{r}',s)+\frac{\partial G(\mathbf{r}\mid\mathbf{r}',s)}{\partial \mathbf{n}_j}\right]N_{ij}\left(\xi_1^{(m)},\xi_2^{(n)}\right)J_j\rho'$$ B.21

where m and n are the indices of the Gauss point in each direction and w_m and w_n are the weights associated with the Gauss integration points.

For elements in which $\mathbf{r}=\mathbf{r}'$ at one of the nodes, the integrand becomes singular but the integral will converge using the numerical integration procedure discussed. For quicker convergence in this special case, the origin of the local $\xi_1-\xi_2$ coordinate system is placed on the singular node and a more general transformation to the local $\rho'-\theta'$ coordinate system is used (Wu, 2000). For example, if the first node of the element is singular, the coordinate transformation becomes

$$\begin{aligned}\xi_1 &= \xi_1^{(1)} + \rho'\left[\xi_1^{(2)} - \xi_1^{(1)} - \theta'\left(\xi_1^{(3)} - \xi_1^{(2)}\right)\right] \\ \xi_2 &= \xi_2^{(1)} + \rho'\left[\xi_2^{(2)} - \xi_2^{(1)} - \theta'\left(\xi_2^{(3)} - \xi_2^{(2)}\right)\right]\end{aligned}$$ B.22

where superscripts in parentheses indicate node numbers.

Equation B.21 can be used to evaluate the integral, $C_{ij}(\mathbf{r}',s)$, for linear, triangular boundary elements. For other types of elements, a different numerical integration scheme must be developed.

Appendix C: Statistical Energy Analysis Review and Coupled Volume Derivation

Consider a subsystem (acoustic or structural) of resonant modes, all with equal energy, over a frequency band, $\Delta\omega$. Next, consider a similar subsystem coupled to the first forming a system. Now, it is assumed that all the resonating modes in the frequency band transfer energy from one subsystem to the other similarly and that the modes between subsystems are uncorrelated. The power transmitted from one subsystem 1 to 2, W_{12}', is

$$W_{12}' = E_1\omega\tau_{12} \tag{C.1}$$

where E_1 is the total energy of all resonant modes in subsystem 1, ω is the center frequency of the band, and τ_{12} is called the coupling loss factor (Beranek and Vér, 1992). Since the modes are assumed uncorrelated, the total power transmitted between the two subsystems, W_{12}, is written as (Beranek and Vér, 1992)

$$W_{12} = W_{12}' - W_{21}' = E_1\omega\tau_{12} - E_2\omega\tau_{21}. \tag{C.2}$$

Next, a modal energy, E_{m1}, is defined as the average energy per mode of the subsystem in the frequency band. The modal energy is

$$E_{m1} = \frac{E_1(\Delta\omega)}{n_1(\omega)\Delta\omega} \tag{C.3}$$

where $n_1(\omega)$ is the modal density of the subsystem (Beranek and Vér, 1992). A consistency relationship can be found considering the modal energy and the assumptions made as (Beranek and Vér, 1992)

$$\frac{\tau_{21}}{\tau_{12}} = \frac{n_1(\omega)}{n_2(\omega)}. \tag{C.4}$$

Substituting eq. C.4 into eq. C.2 gives

$$W_{12} = \omega\tau_{12}n_1(\omega)\left[\frac{E_1}{n_1(\omega)} - \frac{E_2}{n_2(\omega)}\right]. \tag{C.5}$$

An energy balance is performed in each subsystem including power input and dissipated by the subsystem and the power transferred to coupled subsystems, W_{12}. Using previously derived relationships for different types of subsystems, the coupling loss factors and modal densities are calculated. Then, an algebraic system of equations is written with one equation for each subsystem. The total energy in each subsystem is solved for giving a uniform value for each component subsystem (Beranek and Vér, 1992).

The coupling loss factor of a plate (2) coupled to an acoustic volume (1), for example, is

$$\tau_{21} = \frac{\rho_1 c_1}{\omega \rho_2 h} \sigma_{rad} \tag{C.6}$$

where ρ_2 is the density of the plate, h is the plate thickness, and σ_{rad} is the plate radiation efficiency. Modal density for typical system components can also be derived. For an acoustic volume,

$$n_1(\omega) = \frac{\omega^2 V_1}{2\pi^2 c_1^3} \tag{C.7}$$

where V_1 is the volume. For a plate,

$$n_2(\omega) = \frac{\sqrt{12} S_2}{4\pi c_2 h} \tag{C.8}$$

where S_2 is the plate area and c_2 is the group speed of flexural waves in the plate (Beranek and Vér, 1992).

As an example, the SEA formulation for two acoustic volumes coupled through a plate is derived. The formulation is used later in a numerical example for comparison with the diffusion model. The source acoustic volume, subsystem 1, contains an input power, W and its energy balance is written as

$$W = W_{1d} + W_{12} \tag{C.9}$$

where W_{1d} is the power dissipated by absorption of the surfaces, α_1. This term is easily found to be

$$W_{1d} = \frac{S_1 c_1 \alpha_1}{4V_1} E_1 \qquad\qquad\text{C.10}$$

Equation C.5 can be rewritten as

$$W_{12} = -W_{21} = -\omega \tau_{21} n_2(\omega) \left[\frac{E_2}{n_2(\omega)} - \frac{E_1}{n_1(\omega)} \right]. \qquad\qquad\text{C.11}$$

Substituting eq. C.6into eq. C.11 gives the net power transmitted from subsystem 1 to the plate, subsystem 2, as

$$W_{12} = \frac{\rho_1 c_1}{\rho_2 h} \sigma_{rad} \frac{n_2(\omega)}{n_1(\omega)} E_1 - \frac{\rho_1 c_1}{\rho_2 h} \sigma_{rad} E_2 \qquad\qquad\text{C.12}$$

Substituting eqs. C.7 and C.8 gives

$$W_{12} = \frac{\pi\sqrt{12}}{2} \frac{\rho_1 c_1^4}{\omega^2 \rho_2 c_2} \frac{S_2}{h^2 V_1} \sigma_{rad} E_1 - \frac{\rho_1 c_1}{\rho_2 h} \sigma_{rad} E_2 . \qquad\qquad\text{C.13}$$

Substituting eqs. C.10 and C.13 into eq. C.9 gives the first of the system of equations in the SEA formulation:

$$\left(\frac{S_1 c_1 \alpha_1}{4V_1} + \frac{\pi\sqrt{12}}{2} \frac{\rho_1 c_1^4}{\omega^2 \rho_2 c_2} \frac{S_2}{h^2 V_1} \sigma_{rad} \right) E_1 - \frac{\rho_1 c_1}{\rho_2 h} \sigma_{rad} E_2 = W . \qquad\qquad\text{C.14}$$

The power balance of the plate, subsystem 2, is

$$W_{12} = W_{2d} + W_{23} \qquad\qquad\text{C.15}$$

where W_{2d} is the energy dissipated due to damping in the plate and W_{23} is the net power transmitted from the plate to the receiving acoustic volume, subsystem 3. The dissipated power is written in terms of a structural loss factor, η_2, as

$$W_{2d} = \omega \eta_2 E_2 . \qquad\qquad\text{C.16}$$

The net power transmission from plate to receiving volume is

$$W_{23} = \omega \tau_{23} n_2(\omega) \left[\frac{E_2}{n_2(\omega)} - \frac{E_3}{n_3(\omega)} \right]. \qquad\qquad\text{C.17}$$

Substituting eqs. C.6, C.7, and C.8 with the appropriate subsystem subscripts into eq. C.17 gives

$$W_{23} = \frac{\rho_3 c_3}{\rho_2 h} \sigma_{rad} E_2 - \frac{\pi\sqrt{12}}{2} \frac{\rho_3 c_3^4}{\omega^2 \rho_2 c_2} \frac{S_2}{h^2 V_3} \sigma_{rad} E_3 . \qquad\qquad\text{C.18}$$

Substituting eq. C.13, C.16, and C.17 into eq. C.15 gives the second equation in the SEA formulation:

$$-\frac{\pi\sqrt{12}}{2}\frac{\rho_1 c_1^{\,4}}{\omega^2 \rho_2 c_2}\frac{S_2}{h^2 V_1}\sigma_{rad}E_1 + \left[\omega\eta_2 + 2\frac{\rho_1 c_1}{\rho_2 h}\sigma_{rad}\right]E_2 - \frac{\pi\sqrt{12}}{2}\frac{\rho_3 c_3^{\,4}}{\omega^2 \rho_2 c_2}\frac{S_2}{h^2 V_3}\sigma_{rad}E_3 = 0 \,. \quad\text{C.19}$$

The power balance in the receiving acoustic volume, subsystem 3, is

$$W_{23} = W_{3d} \qquad\qquad\qquad \text{C.20}$$

where W_{3d} is the power dissipated by the surface absorption, α_3, given by

$$W_{3d} = \frac{S_3 c_3 \alpha_3}{4V_3}E_3 \qquad\qquad\qquad \text{C.21}$$

Substituting eqs. C.18 and C.21 into eq. C.20 gives the final equation for the SEA formulation:

$$\frac{\rho_3 c_3}{\rho_2 h}\sigma_{rad}E_2 - \left(\frac{S_3 c_3 \alpha_3}{4V_3} + \frac{\pi\sqrt{12}}{2}\frac{\rho_3 c_3^{\,4}}{\omega^2 \rho_2 c_2}\frac{S_2}{h^2 V_3}\sigma_{rad}\right)E_3 = 0 \,. \qquad \text{C.22}$$

Using the radiation efficiency for a thin plate surrounded by a rigid baffle (Beranek and Vér, 1992), eqs. C.14, C.19, and C.22 can be solved simultaneously for the total energy in each subsystem. The total energy can then be related to the spatially averaged mean square pressure in acoustic subsystems and the spatially averaged mean square velocity in structural subsystems (Beranek and Vér, 1992).

Appendix D: Energy Finite Element Method Derivation

A power flow model for structural analysis was proposed by Nefske and Sung (1989). In the paper, they consider a small control volume inside of a structural system, e.g. a vibrating plate. Applying a power balance on this volume results in the governing differential equation for the power flow model as

$$\frac{\partial \varphi(\mathbf{r},t)}{\partial t} = -\nabla \cdot \mathbf{J}(\mathbf{r},t) - W_{diss}(\mathbf{r},t) \tag{D.1}$$

where $\varphi(\mathbf{r},t)$ is the energy density in the volume, $\mathbf{J}(\mathbf{r},t)$ is the intensity through the volume, and $W_{diss}(\mathbf{r},t)$ is the power dissipated inside the volume. The power dissipated through damping and/or acoustic radiation in the structure is proportional to the energy density as

$$W_{diss}(\mathbf{r},t) = \omega \eta \varphi(\mathbf{r},t) \tag{D.2}$$

where ω is the angular frequency and η is the loss factor. Nefske and Sung (1989) propose a form of the intensity as

$$\mathbf{J}(\mathbf{r},t) = -\lambda_{\varphi} \nabla \big[\kappa \varphi(\mathbf{r},t) \big] \tag{D.3}$$

where λ_{φ} and κ are termed vibration conduction coefficients whose value must be determined. Substituting eqs. D.2 and D.3 into D.1 gives the general power flow model for structures:

$$\frac{\partial \varphi(\mathbf{r},t)}{\partial t} = \nabla \cdot \big\{ \lambda_{\varphi} \nabla \big[\kappa \varphi(\mathbf{r},t) \big] \big\} - \omega \eta \varphi(\mathbf{r},t). \tag{D.4}$$

To determine the arbitrary coefficients, consider the far field energy density as the sum of positive and negative propagating waves whose energy densities can be separated into $\varphi^{+}(\mathbf{r},t)$ and $\varphi^{-}(\mathbf{r},t)$, respectively. The total energy density is then

$$\varphi(\mathbf{r},t) = \varphi^{+}(\mathbf{r},t) + \varphi^{-}(\mathbf{r},t). \tag{D.5}$$

The intensity propagating through this point is

$$\mathbf{J}(\mathbf{r},t) = \mathbf{J}^{+}(\mathbf{r},t) - \mathbf{J}^{-}(\mathbf{r},t). \tag{D.6}$$

Since the intensity of a wave can be written as a product of the energy density and group velocity,

$$\mathbf{J}^+(\mathbf{r},t) = c_g \varphi^+(\mathbf{r},t) \frac{\mathbf{r}}{|\mathbf{r}|}$$

$$\mathbf{J}^-(\mathbf{r},t) = c_g \varphi^-(\mathbf{r},t) \frac{\mathbf{r}}{|\mathbf{r}|}$$

D.7

this gives

$$\mathbf{J}(\mathbf{r},t) = \left[c_g \varphi^+(\mathbf{r},t) - c_g \varphi^-(\mathbf{r},t) \right] \frac{\mathbf{r}}{|\mathbf{r}|}.$$

D.8

Next, a power balance is applied to equate the gradient of the intensity to the energy dissipated as

$$\nabla \cdot \mathbf{J}^+(\mathbf{r},t) = -\omega \eta \varphi^+(\mathbf{r},t)$$

$$\nabla \cdot \mathbf{J}^-(\mathbf{r},t) = \omega \eta \varphi^-(\mathbf{r},t)$$

D.9

Multiplying eq. D.9 by $c_g/(\omega \eta)$ and adding gives

$$\frac{c_g}{\omega \eta} \left[\nabla \cdot \mathbf{J}^+(\mathbf{r},t) + \nabla \cdot \mathbf{J}^-(\mathbf{r},t) \right] = -c_g \varphi^+(\mathbf{r},t) + c_g \varphi^-(\mathbf{r},t).$$

D.10

Substituting eq. D.10 into eq. D.8 gives

$$\mathbf{J}(\mathbf{r},t) = -\frac{c_g}{\omega \eta} \left[\nabla \cdot \mathbf{J}^+(\mathbf{r},t) + \nabla \cdot \mathbf{J}^-(\mathbf{r},t) \right].$$

D.11

Next, eq. D.7 is substituted into eq. D.11 to give

$$\mathbf{J}(\mathbf{r},t) = -\frac{c_g}{\omega \eta} \left[\nabla c_g \varphi^+(\mathbf{r},t) + \nabla c_g \varphi^-(\mathbf{r},t) \right].$$

D.12

which can be rewritten as

$$\mathbf{J}(\mathbf{r},t) = -\frac{c_g}{\omega \eta} \nabla \left[c_g \varphi(\mathbf{r},t) \right].$$

D.13

Comparing eq. D.13 to D.3 gives

$$\lambda_\varphi = \frac{c_g}{\omega \eta}$$

D.14

and

$$\kappa = c_g.$$

D.15

The power flow model for structures can now be written as

$$\frac{\partial \varphi(\mathbf{r},t)}{\partial t} = \nabla \cdot \left\{ \frac{c_g}{\omega \eta} \nabla \left[c_g \varphi(\mathbf{r},t) \right] \right\} - \omega \eta \varphi(\mathbf{r},t). \qquad \text{D.16}$$

Assuming the group velocity and loss factor do not change with position gives

$$\frac{\partial \varphi(\mathbf{r},t)}{\partial t} = \frac{c_g^{\,2}}{\omega \eta} \nabla^2 \varphi(\mathbf{r},t) - \omega \eta \varphi(\mathbf{r},t). \qquad \text{D.17}$$

This equation forms the basis of the energy finite element method (EFEM) formulated by Bitsie (1997). Using essentially the same method, the power flow model of the acoustic system is given by

$$\frac{\partial \psi(\mathbf{r},t)}{\partial t} = \frac{c^2}{\omega \eta} \nabla^2 \psi(\mathbf{r},t) - \omega \eta \psi(\mathbf{r},t). \qquad \text{D.18}$$

Next, EFEM is extended to coupled systems where it provides significant advantages over other techniques in the analysis of complex built-up structures. For two coupled systems, the power flow from one system to the next over the coupling surface, S_c, must be conserved. This can be expressed in terms of intensity as

$$\int_{S_{c1}} \mathbf{J}_1(\mathbf{r},t) \cdot \mathbf{n}_1 dS + \int_{S_{c2}} \mathbf{J}_2(\mathbf{r},t) \cdot \mathbf{n}_2 dS = 0 \qquad \text{D.19}$$

where S_{ci} is the ith system's side of the coupling surface with unit normal, $\mathbf{n}_i$, and $\mathbf{J}_i$ is the net intensity. Each integral can be split into the intensity of an incident wave, $\mathbf{J}_{inc,i}(\mathbf{r},t)$, a reflected wave, $\mathbf{J}_{ref,i}(\mathbf{r},t)$, and a transmitted wave, $\mathbf{J}_{trans,i}(\mathbf{r},t)$, as in

$$\int_{S_{ci}} \mathbf{J}_i(\mathbf{r},t) \cdot \mathbf{n}_i dS = \int_{S_{ci}} \mathbf{J}_{inc,i}(\mathbf{r},t) \cdot \mathbf{n}_i dS + \int_{S_{ci}} \mathbf{J}_{ref,i}(\mathbf{r},t) \cdot \mathbf{n}_i dS + \int_{S_{ci}} \mathbf{J}_{trans,i}(\mathbf{r},t) \cdot \mathbf{n}_i dS. \qquad \text{D.20}$$

The magnitude of the net intensity of the ith system integrated over the coupling surface can be written in terms of incident intensities only with the use of power reflection, r_{ii}, and transmission coefficients, τ_{ij}, as

$$\int_{S_{ci}} \left| \mathbf{J}_i(\mathbf{r},t) \right| dS = \int_{S_{ci}} \left| \mathbf{J}_{inc,i}(\mathbf{r},t) \right| dS - \int_{S_{ci}} r_{ii} \left| \mathbf{J}_{inc,i}(\mathbf{r},t) \right| dS - \int_{S_{cj}} \tau_{ij} \left| \mathbf{J}_{inc,j}(\mathbf{r},t) \right| dS \qquad \text{D.21}$$

where the ith system is coupled to the jth system and $j \neq i$. The total net intensity in the direction of the normal to the coupling surface becomes

$$\int_{S_{ci}} \mathbf{J}_i(\mathbf{r},t)\cdot\mathbf{n}_i dS = (1-r_{ii})\int_{S_{ci}} |\mathbf{J}_{inc,i}(\mathbf{r},t)|dS - \tau_{ij}\int_{S_{cj}} |\mathbf{J}_{inc,j}(\mathbf{r},t)|dS .$$

D.22

For the simplest case of two systems, 1 and 2, eq. D.22 can be written in matrix form as

$$\begin{Bmatrix} \int_{S_{c1}} \mathbf{J}_1(\mathbf{r},t)\cdot\mathbf{n}_1 dS \\ \int_{S_{c2}} \mathbf{J}_2(\mathbf{r},t)\cdot\mathbf{n}_2 dS \end{Bmatrix} = \begin{bmatrix} 1-r_{11} & -\tau_{12} \\ -\tau_{21} & 1-r_{22} \end{bmatrix} \begin{Bmatrix} \int_{S_{c1}} |\mathbf{J}_{inc,1}(\mathbf{r},t)|dS \\ \int_{S_{c2}} |\mathbf{J}_{inc,2}(\mathbf{r},t)|dS \end{Bmatrix} .$$

D.23

The energy density multiplied by the group speed of the ith system, c_i, can also be written in terms of the magnitudes of the intensities of the three waves as

$$\int_{S_{ci}} c_i\psi_i(\mathbf{r},t)dS = -\int_{S_{ci}} |\mathbf{J}_{inc,i}(\mathbf{r},t)|dS + \int_{S_{ci}} |\mathbf{J}_{ref,i}(\mathbf{r},t)|dS + \int_{S_{ci}} |\mathbf{J}_{trans,i}(\mathbf{r},t)|dS .$$

D.24

Using power reflection and transmission coefficients,

$$\int_{S_{ci}} c_i\psi_i(\mathbf{r},t)dS = -(1+r_{ii})\int_{S_{ci}} |\mathbf{J}_{inc,i}(\mathbf{r},t)|dS - \tau_{ij}\int_{S_{cj}} |\mathbf{J}_{inc,j}(\mathbf{r},t)|dS .$$

D.25

Again, for a two system coupling, eq. D.25 in matrix form is

$$\begin{Bmatrix} \int_{S_{c1}} c_1\psi_1(\mathbf{r},t)dS \\ \int_{S_{c2}} c_2\psi_2(\mathbf{r},t)dS \end{Bmatrix} = -\begin{bmatrix} (1+r_{11}) & \tau_{12} \\ \tau_{21} & (1+r_{22}) \end{bmatrix} \begin{Bmatrix} \int_{S_{c1}} |\mathbf{J}_{inc,1}(\mathbf{r},t)|dS \\ \int_{S_{c2}} |\mathbf{J}_{inc,2}(\mathbf{r},t)|dS \end{Bmatrix} .$$

D.26

Solving for the magnitude of the intensity gives

$$\begin{Bmatrix} \int_{S_{c1}} |\mathbf{J}_{inc,1}(\mathbf{r},t)|dS \\ \int_{S_{c2}} |\mathbf{J}_{inc,2}(\mathbf{r},t)|dS \end{Bmatrix} = -\begin{bmatrix} (1+r_{11}) & \tau_{12} \\ \tau_{21} & (1+r_{22}) \end{bmatrix}^{-1} \begin{Bmatrix} \int_{S_{c1}} c_1\psi_1(\mathbf{r},t)dS \\ \int_{S_{c2}} c_2\psi_2(\mathbf{r},t)dS \end{Bmatrix} .$$

D.27

Substituting eq. D.27 into eq. D.26 gives the intensity normal to the coupling surface in terms of the energy density on the surface as

$$\begin{Bmatrix} \int_{S_{c1}} \mathbf{J}_1(\mathbf{r},t)\cdot\mathbf{n}_1 dS \\ \int_{S_{c2}} \mathbf{J}_2(\mathbf{r},t)\cdot\mathbf{n}_2 dS \end{Bmatrix} = -\begin{bmatrix} 1-r_{11} & -\tau_{12} \\ -\tau_{21} & 1-r_{22} \end{bmatrix}\begin{bmatrix} (1+r_{11}) & \tau_{12} \\ \tau_{21} & (1+r_{22}) \end{bmatrix}^{-1} \begin{Bmatrix} \int_{S_{c1}} c_1\psi_1(\mathbf{r},t)dS \\ \int_{S_{c2}} c_2\psi_2(\mathbf{r},t)dS \end{Bmatrix} .$$

D.28

From conservation of energy, the power reflected and transmitted must equal the incident power, or

$$r_{ii} + \tau_{ji} = 1 .$$

D.29

Substituting eq. D.29 into eq. D.28 gives the coupling condition for the EFEM,

$$
\left\{ \begin{array}{c} \int\limits_{S_{c1}} \mathbf{J}_1(\mathbf{r},t)\cdot\mathbf{n}_1 dS \\ \int\limits_{S_{c2}} \mathbf{J}_2(\mathbf{r},t)\cdot\mathbf{n}_2 dS \end{array} \right\} = \frac{1}{2-\tau_{12}-\tau_{21}} \left[\begin{array}{cc} \tau_{21} & -\tau_{12} \\ -\tau_{21} & \tau_{12} \end{array} \right] \left\{ \begin{array}{c} \int\limits_{S_{c1}} c_1\psi_1(\mathbf{r},t) dS \\ \int\limits_{S_{c2}} c_2\psi_2(\mathbf{r},t) dS \end{array} \right\}.
$$

D.30

Using the relationship between the intensity and the gradient of the energy density gives

$$
\left\{ \begin{array}{c} \int\limits_{S_{c1}} \left[-\frac{c_g}{\eta\omega}\nabla\psi_1(\mathbf{r},t) \right]\cdot\mathbf{n}_1 dS \\ \int\limits_{S_{c2}} \left[-\frac{c_g}{\eta\omega}\nabla\psi_2(\mathbf{r},t) \right]\cdot\mathbf{n}_2 dS \end{array} \right\} = \frac{1}{2-\tau_{12}-\tau_{21}} \left[\begin{array}{cc} \tau_{21} & -\tau_{12} \\ -\tau_{21} & \tau_{12} \end{array} \right] \left\{ \begin{array}{c} \int\limits_{S_{c1}} c_1\psi_1(\mathbf{r},t) dS \\ \int\limits_{S_{c2}} c_2\psi_2(\mathbf{r},t) dS \end{array} \right\}.
$$

D.31

Equations D.18 and 6.2 are written for each system with appropriate boundary conditions and coupled through eq. D.31. The total system is then solved with the FEM to formulate the EFEM.

Appendix E: Full Derivation of the Diffusion BE-LTS with Simple Structural Coupling

In this section, the Laplace domain BEM solution to the acoustic diffusion model for multiple acoustic volumes coupled through a known transmission coefficient, as shown in Figure E.1, is developed. The case shown in the schematic is two coupled volumes, but this formulation can be used for any number or configuration of volumes and coupling surfaces. The domain of the vth acoustic volume is referred to as V_v. The domains of the bounding surfaces of each volume are split into two sub-surfaces each. The domain of the boundary exclusive to the vth volume is S_v, while the domain of the boundary on the coupling surface is S_{cv}. The unit normal vector pointing outward from S_v or S_{cv} is $\mathbf{n}_v$. The position vector can be in any of these defined domains.
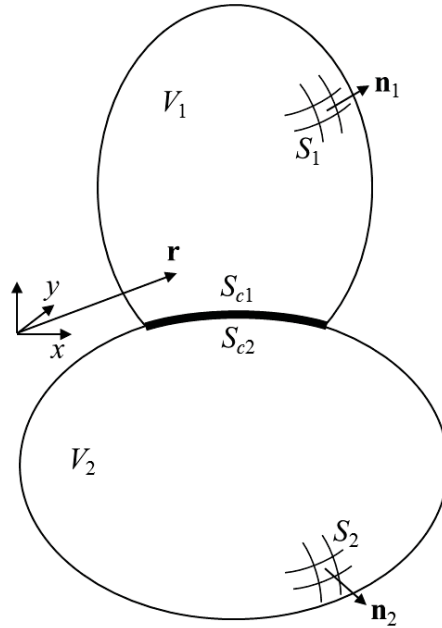

Figure E.1: Schematic demonstrating the geometry for two coupled volumes.

The diffusion equation in the vth volume is given by (Billon et al., 2008a)

$$\frac{\partial \psi_v(\mathbf{r},t)}{\partial t} - D_v \nabla^2 \psi_v(\mathbf{r},t) + mc\psi_v(\mathbf{r},t) = f_v(\mathbf{r},t) \qquad \text{E.1}$$

where ψ_v represents the energy density in the volume or on its bounding surface, D_v the diffusion coefficient, and f_v the supplied acoustic power per unit volume. The boundary conditions are given by (Billon et al., 2008a)

$$\begin{cases} D_v \dfrac{\partial \psi_v(\mathbf{r},t)}{\partial \mathbf{n}_v} + h_{\alpha v}(\mathbf{r})\psi_v(\mathbf{r},t) = 0, & \mathbf{r} \in S_v \\[3mm] D_v \dfrac{\partial \psi_v(\mathbf{r},t)}{\partial \mathbf{n}_v} + h_{\alpha v}(\mathbf{r})\psi_v(\mathbf{r},t) + h_{\tau v}(\mathbf{r})\psi_v(\mathbf{r},t) = h_{\tau u}(\mathbf{r})\psi_u(\mathbf{r},t), & \mathbf{r} \in S_{cv} \end{cases} \qquad \text{E.2}$$

where $h_{\alpha v}(\mathbf{r}) = \dfrac{c}{4}\dfrac{\alpha(\mathbf{r})}{2[2-\alpha(\mathbf{r})]}$ is the absorption exchange coefficient, $h_{\tau v}(\mathbf{r}) = c\tau(\mathbf{r})/4$ is the transmission exchange coefficient, $\alpha_v(\mathbf{r})$ is the absorption coefficient of the bounding surface, $\tau_v(\mathbf{r})$ is the transmission coefficient of the coupling partition associated with energy flowing *out of* the vth volume, and the uth volume is coupled to the vth through S_{cv} and S_{cu} and $u \neq v$. Equations E.1 and E.2 with an initial condition form a well-posed problem that can be solved with a numerical technique such as the FEM or FD technique.

Moving towards the development of the BEM solution, the Laplace Transform of eq. E.1 is

$$s\Psi_v(\mathbf{r},s) - \psi_v(\mathbf{r},0) - D_v\nabla^2\Psi_v(\mathbf{r},s) = F_v(\mathbf{r},s), \quad \mathbf{r} \in V_v \qquad \text{E.3}$$

where $\Psi_v(\mathbf{r},s) = \mathcal{L}[\psi_v(\mathbf{r},t)]$ and $F_v(\mathbf{r},s) = \mathcal{L}[f_v(\mathbf{r},t)]$. This can be rearranged to give

$$\nabla^2\Psi_v(\mathbf{r},s) = \frac{s}{D_v}\Psi_v(\mathbf{r},s) - \frac{1}{D_v}\psi_v(\mathbf{r},0) - \frac{1}{D_v}F_v(\mathbf{r},s), \mathbf{r} \in V_v. \qquad \text{E.4}$$

Taking the Laplace Transform of eq. E.2 gives

$$\begin{cases} D_v \dfrac{\partial \Psi_v(\mathbf{r},s)}{\partial \mathbf{n}_v} + h_{\alpha v}(\mathbf{r})\Psi_v(\mathbf{r},s) = 0, & \mathbf{r} \in S_v \\[3mm] D_v \dfrac{\partial \Psi_v(\mathbf{r},s)}{\partial \mathbf{n}_v} + h_{\alpha v}(\mathbf{r})\Psi_v(\mathbf{r},s) + h_{\tau v}(\mathbf{r})\Psi_v(\mathbf{r},s) = h_{\tau u}(\mathbf{r})\Psi_u(\mathbf{r},s), & \mathbf{r} \in S_{cv} \end{cases} \qquad \text{E.5}$$

Solving for the normal derivative of the energy density in eq. E.5 results in

$$
\begin{cases}
\dfrac{\partial \Psi_v(\mathbf{r},s)}{\partial \mathbf{n}_v} = -\dfrac{h_{\alpha v}(\mathbf{r})}{D_v}\Psi_v(\mathbf{r},s), & \mathbf{r}\in S_v \\[3mm]
\dfrac{\partial \Psi_v(\mathbf{r},s)}{\partial \mathbf{n}_v} = -\dfrac{h_{\alpha v}(\mathbf{r})}{D_v}\Psi_v(\mathbf{r},s) - \dfrac{h_{\tau v}(\mathbf{r})}{D_v}\Psi_v(\mathbf{r},s) + \dfrac{h_{\tau u}(\mathbf{r})}{D_v}\Psi_u(\mathbf{r},s), & \mathbf{r}\in S_{cv}
\end{cases}
\qquad \text{E.6}
$$

which is needed later. The multiple volume diffusion equation in terms of its Green's function is given by

$$
\frac{\partial g_v(\mathbf{r}\,|\,\mathbf{r}',t)}{\partial t} - D_v\nabla^2 g_v(\mathbf{r}\,|\,\mathbf{r}',t) = \delta(\mathbf{r}-\mathbf{r}')\delta(t), \qquad \mathbf{r},\mathbf{r}'\in V_v \qquad \text{E.7}
$$

where $g_v(\mathbf{r}\,|\,\mathbf{r}',t)$ is the free field 3-D Green's function. The initial condition for the Green's function equation is given by $g_v(\mathbf{r}\,|\,\mathbf{r}',0)=0$. The Laplace Transform of the Green's function equation is

$$
sG_v(\mathbf{r}\,|\,\mathbf{r}',s) - D_v\nabla^2 G_v(\mathbf{r}\,|\,\mathbf{r}',s) = \delta(\mathbf{r}-\mathbf{r}'), \qquad \mathbf{r},\mathbf{r}'\in V_v \qquad \text{E.8}
$$

where $G_v(\mathbf{r}\,|\,\mathbf{r}',s) = \mathcal{L}[g_v(\mathbf{r}\,|\,\mathbf{r}',t)]$. Equation E.8 can be rearranged into

$$
\nabla^2 G_v(\mathbf{r}\,|\,\mathbf{r}',s) = \frac{s}{D_v}G_v(\mathbf{r}\,|\,\mathbf{r}',s) - \delta(\mathbf{r}-\mathbf{r}'), \qquad \mathbf{r},\mathbf{r}'\in V_v \qquad \text{E.9}
$$

The Green's function is given by (Butkovskiy, 1982)

$$
G_v(\mathbf{r}\,|\,\mathbf{r}',s) = \frac{1}{4\pi|\mathbf{r}-\mathbf{r}'|}e^{-\sqrt{\frac{s}{D_v}}|\mathbf{r}-\mathbf{r}'|}, \qquad \mathbf{r},\mathbf{r}'\in V_v\cup S_v\cup S_{cv} \qquad \text{E.10}
$$

and its normal derivative on the boundary is

$$
\frac{\partial G_v(\mathbf{r}\,|\,\mathbf{r}',s)}{\partial \mathbf{n}_v} = -\frac{1}{4\pi|\mathbf{r}-\mathbf{r}'|}e^{-\sqrt{\frac{s}{D_v}}|\mathbf{r}-\mathbf{r}'|}\left[\sqrt{\frac{s}{D_v}}+\frac{1}{|\mathbf{r}-\mathbf{r}'|}\right]\frac{(\mathbf{r}-\mathbf{r}')\cdot\mathbf{n}_v}{|\mathbf{r}-\mathbf{r}'|}, \qquad \mathbf{r},\mathbf{r}'\in S_v\cup S_{cv}. \qquad \text{E.11}
$$

The mathematical statement of Green's Second Identity is

$$
\int_{V_v'}\left[G_v(\mathbf{r}\,|\,\mathbf{r}',s)\nabla^2\Psi_v(\mathbf{r},s) - \Psi_v(\mathbf{r},s)\nabla^2 G_v(\mathbf{r}\,|\,\mathbf{r}',s)\right]dV =
$$

$$
\int_{S_v'+S_{cv}'}\left[G_v(\mathbf{r}\,|\,\mathbf{r}',s)\frac{\partial \Psi_v(\mathbf{r},s)}{\partial \mathbf{n}_v} - \Psi_v(\mathbf{r},s)\frac{\partial G_v(\mathbf{r}\,|\,\mathbf{r}',s)}{\partial \mathbf{n}_v}\right]dS, \qquad \mathbf{r}'\in V_v\cup S_v\cup S_{cv} \qquad \text{E.12}
$$

Substituting eqs. E.4 and E.9 gives

$$\int_{V_v'} \left[\Psi_v(\mathbf{r},s)\delta(\mathbf{r}-\mathbf{r}') - \frac{1}{D_v}G_v(\mathbf{r}|\mathbf{r}',s)\psi_v(\mathbf{r},0) - \frac{1}{D_v}G_v(\mathbf{r}|\mathbf{r}',s)F_v(\mathbf{r},s) \right]dV =$$

$$\int_{S_v'+S_{cv}'} \left[G_v(\mathbf{r}|\mathbf{r}',s)\frac{\partial\Psi_v(\mathbf{r},s)}{\partial\mathbf{n}_v} - \Psi_v(\mathbf{r},s)\frac{\partial G_v(\mathbf{r}|\mathbf{r}',s)}{\partial\mathbf{n}_v} \right]dS, \quad \mathbf{r}' \in V_v \cup S_v \cup S_{cv}$$

. E.13

Carrying out the integration over the delta function and rearranging gives

$$\beta\Psi_v(\mathbf{r}',s) = \frac{1}{D_v}\int_{V_v'}G_v(\mathbf{r}|\mathbf{r}',s)\psi_v(\mathbf{r},0)dV + \frac{1}{D_v}\int_{V_v'}G_v(\mathbf{r}|\mathbf{r}',s)F_v(\mathbf{r},s)dV +$$

$$\int_{S_v'+S_{cv}'} \left[G_v(\mathbf{r}|\mathbf{r}',s)\frac{\partial\Psi_v(\mathbf{r},s)}{\partial\mathbf{n}_v} - \Psi_v(\mathbf{r},s)\frac{\partial G_v(\mathbf{r}|\mathbf{r}',s)}{\partial\mathbf{n}_v} \right]dS, \quad \mathbf{r}' \in V_v \cup S_v \cup S_{cv}$$

. E.14

The surface integral can be split into one integral over S_v and another over S_{cv} which gives

$$\beta\Psi_v(\mathbf{r}',s) = \frac{1}{D_v}\int_{V_v'}G_v(\mathbf{r}|\mathbf{r}',s)\psi_v(\mathbf{r},0)dV + \frac{1}{D_v}\int_{V_v'}G_v(\mathbf{r}|\mathbf{r}',s)F_v(\mathbf{r},s)dV +$$

$$\int_{S_v'} \left[G_v(\mathbf{r}|\mathbf{r}',s)\frac{\partial\Psi_v(\mathbf{r},s)}{\partial\mathbf{n}_v} - \Psi_v(\mathbf{r},s)\frac{\partial G_v(\mathbf{r}|\mathbf{r}',s)}{\partial\mathbf{n}_v} \right]dS +$$

$$\int_{S_{cv}'} \left[G_v(\mathbf{r}|\mathbf{r}',s)\frac{\partial\Psi_v(\mathbf{r},s)}{\partial\mathbf{n}_v} - \Psi_v(\mathbf{r},s)\frac{\partial G_v(\mathbf{r}|\mathbf{r}',s)}{\partial\mathbf{n}_v} \right]dS, \quad \mathbf{r}' \in V_v \cup S_v \cup S_{cv}$$

E.15

where β is given by eq. 3.17. Substituting the appropriate relations of eq. E.6 into eq. E.15 gives the integral equation as

$$\beta\Psi_v(\mathbf{r}',s) = \frac{1}{D_v}\int_{V_v'}G_v(\mathbf{r}|\mathbf{r}',s)\psi_v(\mathbf{r},0)dV + \frac{1}{D_v}\int_{V_v'}G_v(\mathbf{r}|\mathbf{r}',s)F_v(\mathbf{r},s)dV -$$

$$\int_{S_v'+S_{cv}'} \Psi_v(\mathbf{r},s)\left[\frac{h_{av}(\mathbf{r})+h_{\tau v}(\mathbf{r})}{D_v}G_v(\mathbf{r}|\mathbf{r}',s) + \frac{\partial G_v(\mathbf{r}|\mathbf{r}',s)}{\partial\mathbf{n}_v} \right]dS +$$

. E.16

$$\frac{1}{D_v}\int_{S_{cv}'}h_{\tau u}(\mathbf{r})\Psi_u(\mathbf{r},s)G_v(\mathbf{r}|\mathbf{r}',s)dS, \quad \mathbf{r}' \in V_v \cup S_v \cup S_{cv}$$

Note that the integral equation is nearly the same as in the single volume case with the addition of one more integral of the energy density transmitted from the coupled volume over the coupling surface and another term devoted to carrying energy out of the volume in a similar manner as the absorption.

The steady state integral equations can be derived using the FVT as done previously. Multiplying eq. E.16 by s and taking the limit as $s \to 0$ results in

$$\beta \bar{\psi}_v(\mathbf{r}') = \frac{1}{D_v} \int_{V_v'} G_v(\mathbf{r}|\mathbf{r}',0) \bar{f}_v(\mathbf{r}) dV -$$

$$\int_{S_v'+S_{cv}'} \bar{\psi}_v(\mathbf{r}) \left[\frac{h_{\alpha v}(\mathbf{r}) + h_{\tau v}(\mathbf{r})}{D_v} G_v(\mathbf{r}|\mathbf{r}',0) + \frac{\partial G_v(\mathbf{r}|\mathbf{r}',0)}{\partial \mathbf{n}_v} \right] dS +$$

$$\frac{1}{D_v} \int_{S_{cv}'} h_{\tau u}(\mathbf{r}) \bar{\psi}_u(\mathbf{r}) G_v(\mathbf{r}|\mathbf{r}',0) dS, \qquad \mathbf{r}' \in V_v \cup S_v \cup S_{cv}$$

E.17

where

$$\bar{\psi}_v(\mathbf{r}) = \lim_{t \to \infty} \psi_v(\mathbf{r},t)$$

E.18

and

$$\bar{f}_v(\mathbf{r}) = \lim_{t \to \infty} f_v(\mathbf{r},t).$$

E.19

Next, the bounding surfaces are discretized and integrated numerically forming a matrix equation which can be solved for the energy on the bounding surfaces. Focusing only on the surface integrals of eq. 6.3, let

$$I_{S_v}(\mathbf{r}',s) = \int_{S_v'+S_{cv}'} \Psi_v(\mathbf{r},s) \left[\frac{h_{\alpha v}(\mathbf{r}) + h_{\tau v}(\mathbf{r})}{D_v} G_v(\mathbf{r}|\mathbf{r}',s) + \frac{\partial G_v(\mathbf{r}|\mathbf{r}',s)}{\partial \mathbf{n}_v} \right] dS -$$

$$\frac{1}{D_v} \int_{S_{cv}'} h_{\tau u}(\mathbf{r}) \Psi_u(\mathbf{r},s) G_v(\mathbf{r}|\mathbf{r}',s) dS, \qquad \mathbf{r}' \in V_v \cup S_v \cup S_{cv}$$

E.20

Discretizing the bounding surfaces, S_v and S_{cv}, into J_v and J_{cv} 2-D elements ΔS_j, respectively, with I nodes each gives

$$I_{S_v}(\mathbf{r}',s) = \sum_{j=1}^{J_v+J_{cv}} \int_{\Delta S_j'} \Psi_v(\mathbf{r},s) \left[\frac{h_{\alpha v}(\mathbf{r}) + h_{\tau v}(\mathbf{r})}{D_v} G_v(\mathbf{r}|\mathbf{r}',s) + \frac{\partial G_v(\mathbf{r}|\mathbf{r}',s)}{\partial \mathbf{n}_v} \right] d(\Delta S_j) -$$

$$\frac{1}{D_v} \sum_{j=1}^{J_{cv}} \int_{\Delta S_j'} h_{\tau u}(\mathbf{r}) \Psi_u(\mathbf{r},s) G_v(\mathbf{r}|\mathbf{r}',s) d(\Delta S_j), \qquad \mathbf{r}' \in V_v \cup S_v \cup S_{cv}$$

E.21

Considering that the energy density at any point inside of the jth element can be found by a linear superposition of the nodal values (denoted with the subscript i) of the energy density, $\Psi_{v,ij}(s)$, multiplied by the chosen shape function, $N_{ij}(\mathbf{r})$, eq. E.21 becomes

$$I_{S_v}(\mathbf{r}',s) = \sum_{j=1}^{J_v+J_{cv}}\sum_{i=1}^{I}\Psi_{v,ij}(s)\int_{\Delta S_j'} N_{ij}(\mathbf{r})\left[\frac{h_{\alpha v}(\mathbf{r})+h_{\tau v}(\mathbf{r})}{D_v}G_v(\mathbf{r}|\mathbf{r}',s)+\frac{\partial G_v(\mathbf{r}|\mathbf{r}',s)}{\partial \mathbf{n}_v}\right]d(\Delta S_j)$$

$$-\frac{1}{D_v}\sum_{j=1}^{J_{cv}}\sum_{i=1}^{I}\Psi_{u,ij}(s)\int_{\Delta S_j'} h_{\tau u}(\mathbf{r})N_{ij}(\mathbf{r})G_v(\mathbf{r}|\mathbf{r}',s)d(\Delta S_j), \qquad \mathbf{r}'\in V_v\cup S_v\cup S_{cv}. \tag{E.22}$$

Equation E.22 can be rewritten as

$$I_{S_v}(\mathbf{r}',s) = \sum_{j=1}^{J_v+J_{cv}}\sum_{i=1}^{I}C_{vv,ij}(\mathbf{r}',s)\Psi_{v,ij}(s)+\sum_{j=1}^{J_{cv}}\sum_{i=1}^{I}C_{vu,ij}(\mathbf{r}',s)\Psi_{u,ij}(s), \quad \mathbf{r}'\in V_v\cup S_v\cup S_{cv} \tag{E.23}$$

where

$$C_{vv,ij}(\mathbf{r}',s) = \int_{\Delta S_j'} N_{ij}(\mathbf{r})\left[\frac{h_{\alpha v}(\mathbf{r})+h_{\tau v}(\mathbf{r})}{D_v}G_v(\mathbf{r}|\mathbf{r}',s)+\frac{\partial G_v(\mathbf{r}|\mathbf{r}',s)}{\partial \mathbf{n}_v}\right]d(\Delta S_j),$$

$$\mathbf{r}'\in V_v\cup S_v\cup S_{cv} \tag{E.24}$$

and

$$C_{vu,ij}(\mathbf{r}',s) = -\frac{1}{D_v}\int_{\Delta S_j'} h_{\tau u}(\mathbf{r})N_{ij}(\mathbf{r})G_v(\mathbf{r}|\mathbf{r}',s)d(\Delta S_j), \qquad \mathbf{r}'\in V_v\cup S_v\cup S_{cv}. \tag{E.25}$$

The integral equation, eq. E.16, can now be rewritten as

$$\beta\Psi_v(\mathbf{r}',s) = \frac{1}{D_v}\int_{V_v'} G_v(\mathbf{r}|\mathbf{r}',s)\psi_v(\mathbf{r},0)dV+\frac{1}{D_v}\int_{V_v'} G_v(\mathbf{r}|\mathbf{r}',s)F_v(\mathbf{r},s)dV-$$

$$\sum_{j=1}^{J_v+J_{cv}}\sum_{i=1}^{I}C_{vv,ij}(\mathbf{r}',s)\Psi_{v,ij}(s)-\sum_{j=1}^{J_{cv}}\sum_{i=1}^{I}C_{vu,ij}(\mathbf{r}',s)\Psi_{u,ij}(s), \qquad \mathbf{r}'\in V_v\cup S_v\cup S_{cv} \tag{E.26}$$

The coefficients, $C_{vv,ij}(\mathbf{r}',s)$ and $C_{vu,ij}(\mathbf{r}',s)$, can be solved using numerical integration as discussed in Appendix B. Letting the position vector assume the value of the kth node of the bounding surface, $\mathbf{r}'=\mathbf{r}_k'$, where there are a total of K_v unique nodes, eq. E.26 becomes

$$\frac{1}{2}\Psi_{v,k}(s)+\sum_{j=1}^{J_v+J_{cv}}\sum_{i=1}^{I}C_{vv,kij}(s)\Psi_{v,ij}(s)+\sum_{j=1}^{J_{cv}}\sum_{i=1}^{I}C_{vu,kij}(s)\Psi_{u,ij}(s)=$$

$$\frac{1}{D_v}\int_{V_v'} G_v(\mathbf{r}|\mathbf{r}_k',s)\psi_v(\mathbf{r},0)dV+\frac{1}{D_v}\int_{V_v'} G_v(\mathbf{r}|\mathbf{r}_k',s)F_v(\mathbf{r},s)dV \tag{E.27}$$

where $C_{vv,kij}(s)=C_{vv,ij}(\mathbf{r}_k',s)$ and $C_{vu,kij}(s)=C_{vu,ij}(\mathbf{r}_k',s)$. Assuming the volume integrals can be solved using methods discussed previously, let

$$B_{v,k}(s) = \frac{1}{D_v} \int_{V_v'} G_v(\mathbf{r}|\mathbf{r}_k',s)\psi_v(\mathbf{r},0)dV + \frac{1}{D_v} \int_{V_v'} G_v(\mathbf{r}|\mathbf{r}_k',s)F_v(\mathbf{r},s)dV \qquad \text{E.28}$$

Substituting eq. E.28 into E.27 gives

$$\frac{1}{2}\Psi_{v,k}(s) + \sum_{j=1}^{J_v+J_{cv}}\sum_{i=1}^{I} C_{vv,kij}(s)\Psi_{v,ij}(s) + \sum_{j=1}^{J_{cv}}\sum_{i=1}^{I} C_{vu,kij}(s)\Psi_{u,ij}(s) = B_{v,k}(s). \qquad \text{E.29}$$

In matrix form, eq. E.29 can be written as

$$\frac{1}{2}[\mathbf{I}]_{K_v \times K_v}\,\Psi_v(s)_{K_v \times 1} + \left[\mathbf{C}_{vv}(s)\right]_{K_v \times K_v}\,\Psi_v(s)_{K_v \times 1} +$$
$$\left[\mathbf{C}_{vu}(s)\right]_{K_v \times K_u}\,\Psi_u(s)_{K_u \times 1} = \mathbf{B}_v(s)_{K_v \times 1} \qquad \text{E.30}$$

where $\Psi_v(s) = \{\Psi_{v,1}(s) \quad \Psi_{v,2}(s) \quad \cdots \quad \Psi_{v,K_v}(s)\}^T$ and

$\mathbf{B}_v(s) = \{B_{v,1}(s) \quad B_{v,2}(s) \quad \cdots \quad B_{v,K_v}(s)\}^T$. The matrix of coefficients, $\left[\mathbf{C}_{vv}(s)\right]_{K_v \times K_v}$, is given

by

$$\left[\mathbf{C}_{vv}(s)\right] = \begin{bmatrix} \sum_{j=1}^{J_{ev,1}} C_{vv,1ij}(s) & \sum_{j=1}^{J_{ev,2}} C_{vv,1ij}(s) & \cdots & \sum_{j=1}^{J_{ev,K_v}} C_{vv,1ij}(s) \\ \sum_{j=1}^{J_{ev,1}} C_{vv,2ij}(s) & \sum_{j=1}^{J_{ev,2}} C_{vv,2ij}(s) & \ddots & \vdots \\ \vdots & \ddots & \ddots & \vdots \\ \sum_{j=1}^{J_{ev,1}} C_{vv,K_vij}(s) & \cdots & \cdots & \sum_{j=1}^{J_{ev,K_v}} C_{vv,K_vij}(s) \end{bmatrix} \qquad \text{E.31}$$

where $J_{ev,l}$ is the number of elements the lth node belongs to in volume v; the index, i, takes on

only one value for each of these elements as each unique node will correspond to a single node

of the jth element. The matrix of coefficients, $\left[\mathbf{C}_{vu}(s)\right]_{K_v \times K_u}$, is given by

$$\left[\mathbf{C}_{vu}(s)\right] = \begin{bmatrix} \sum_{j=1}^{J_{ev,1}} C_{vu,1ij}(s) & \sum_{j=1}^{J_{ev,2}} C_{vu,1ij}(s) & \cdots & \sum_{j=1}^{J_{ev,K_u}} C_{vu,1ij}(s) \\ \sum_{j=1}^{J_{ev,1}} C_{vu,2ij}(s) & \sum_{j=1}^{J_{ev,2}} C_{vu,2ij}(s) & \ddots & \vdots \\ \vdots & \ddots & \ddots & \vdots \\ \sum_{j=1}^{J_{ev,1}} C_{vu,K_vij}(s) & \cdots & \cdots & \sum_{j=1}^{J_{ev,K_u}} C_{vu,K_vij}(s) \end{bmatrix}. \qquad \text{E.32}$$

Individually, eq. E.30 represents an underdetermined linear system of equations with K_v in $K = K_v + K_u$ unknowns. However, writing one for each volume, $v = 1, 2, ..., N_V$, gives

$$\frac{1}{2}[\mathbf{I}]_{K \times K} \begin{Bmatrix} \boldsymbol{\Psi}_1(s) \\ \boldsymbol{\Psi}_2(s) \\ \vdots \\ \boldsymbol{\Psi}_{N_V}(s) \end{Bmatrix}_{K \times 1} + \begin{bmatrix} \mathbf{C}_{11}(s) & \mathbf{C}_{12}(s) & \cdots & \mathbf{C}_{1N_V}(s) \\ \mathbf{C}_{21}(s) & \mathbf{C}_{22}(s) & & \\ \vdots & & \ddots & \\ \mathbf{C}_{N_V 1}(s) & & & \mathbf{C}_{N_V N_V}(s) \end{bmatrix}_{K \times K} \begin{Bmatrix} \boldsymbol{\Psi}_1(s) \\ \boldsymbol{\Psi}_2(s) \\ \vdots \\ \boldsymbol{\Psi}_{N_V}(s) \end{Bmatrix}_{K \times 1} = \begin{Bmatrix} \mathbf{B}_1(s) \\ \mathbf{B}_2(s) \\ \vdots \\ \mathbf{B}_{N_V}(s) \end{Bmatrix}_{K \times 1} . \quad \text{E.33}$$

More compactly,

$$[\mathbf{A}(s)]_{K \times K} \, \boldsymbol{\Psi}(s)_{K \times 1} = \mathbf{B}(s)_{K \times 1} \quad \text{E.34}$$

where $\{\boldsymbol{\Psi}(s)\} = \{\boldsymbol{\Psi}_1(s) \quad \boldsymbol{\Psi}_2(s) \quad \cdots \quad \boldsymbol{\Psi}_{N_V}(s)\}^T$, $\{\mathbf{B}(s)\} = \{\mathbf{B}_1(s) \quad \mathbf{B}_2(s) \quad \cdots \quad \mathbf{B}_{N_V}(s)\}^T$, and

$$[\mathbf{A}(s)] = \frac{1}{2}[\mathbf{I}] + \begin{bmatrix} \mathbf{C}_{11}(s) & \mathbf{C}_{12}(s) & \cdots & \mathbf{C}_{1N_V}(s) \\ \mathbf{C}_{21}(s) & \mathbf{C}_{22}(s) & & \\ \vdots & & \ddots & \\ \mathbf{C}_{N_V 1}(s) & & & \mathbf{C}_{N_V N_V}(s) \end{bmatrix}. \quad \text{E.35}$$

The structure of the coefficient matrix in the complete system of equations of eq. E.35 is as follows. The matrices $[\mathbf{C}_{vv}(s)]$ are fully populated because the energy at one node is dependent upon the energy integrated over the entire surface of its volume; these matrices represent the energy flow out of the vth volume and are the equal to the matrices that are calculated if each volume is isolated and considered independently. The off-diagonal matrices, $[\mathbf{C}_{vu}(s)]$ represent the flow of energy transmitted into the vth volume from the uth volume. Thus, these matrices have full columns of values multiplying the energy at nodes on the coupling surfaces; all other columns multiplying energy at nodes not on the coupling surfaces are zero. Equation E.34 can be solved for the energy density at each node of the bounding surfaces of both volumes. Then, eq. E.26 can be solved to calculate the energy at any point in the vth volume.

A similar matrix equation can be set up to solve the steady state integral equations. Once the steady state energy is calculated and eq. E.34 is solved for several discrete values of the Laplace

variable, the energy at any point of interest can be numerically inverted back into the time domain using one of the numerical Laplace inversions discussed previously.

Appendix F: Transmission Loss of Plates with Known Acoustic Impedance

Transmission coefficients of typical building components have been calculated and measured for applications in room acoustics for many years (Berendt et al., 1967; Halliwell et al., 1998; London, 1950; Mulholland et al., 1967; Marsh, 1971a; Marsh, 1971b; Marsh, 1971c; Quirt, 1982; Quirt, 1983). The transmission coefficient, τ, is usually expressed in terms of an acoustic transmission loss (TL) given by

$$TL(f) = -10\log_{10}[\tau(f)] \qquad\qquad \text{F.1}$$

as a function of frequency, f.

To use the coupled volume acoustic diffusion model in other fields of acoustics where transmission coefficients are not as well documented, e.g. muffler analysis, an equivalent transmission coefficient is derived from known properties. The equivalent transmission coefficient is now derived for the transmission through any layer with known specific acoustic impedance.

Consider a plane wave incident upon a thin absorptive layer with complex pressure, p_i, particle velocity, $\mathbf{v}_i$, and angle, θ_i, as shown in Figure F.1. The presence of the obstacle will cause a reflected wave with pressure, p_r, particle velocity, $\mathbf{v}_r$, and angle, θ_r, and a transmitted wave with pressure, p_t, particle velocity, $\mathbf{v}_t$, and angle, θ_t.
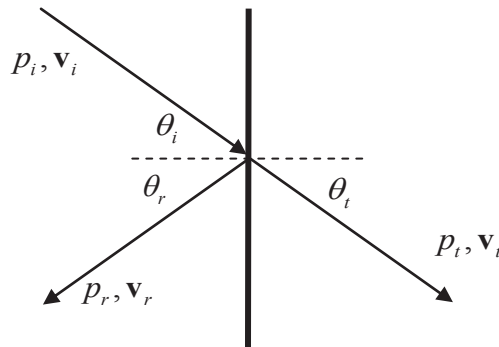

Figure F.1: Schematic of a plane wave incident upon an absorptive layer with reflected and transmitted waves.

Assuming that the layer is thin and rigid, the particle velocity in the direction normal to the layer must be continuous as in

$$\mathbf{v}_i \cos\theta_i + \mathbf{v}_r \cos\theta_r = \mathbf{v}_t \cos\theta_t. \tag{F.2}$$

If the medium on either side of the thin layer is the same, then it can be shown that all angles are equal, $\theta_i = \theta_r = \theta_t = \theta$ (Kinsler et al., 2000), and eq. F.2 becomes

$$\mathbf{v}_i + \mathbf{v}_r = \mathbf{v}_t. \tag{F.3}$$

The relations

$$p_i = \rho c \mathbf{v}_i, \, p_r = -\rho c \mathbf{v}_r, \, p_t = \rho c \mathbf{v}_t \tag{F.4}$$

relate pressure and particle velocity for all three plane waves. Multiplying eq. F.3 by the density and speed of sound, and substituting eq. F.4 gives

$$p_i - p_r = p_t \tag{F.5}$$

which can be rearranged into

$$\frac{p_r}{p_i} = 1 - \frac{p_t}{p_i}. \tag{F.6}$$

Assuming a known specific acoustic impedance of an absorptive layer, z, the relation can be written (Wu, 2000)

$$p_i + p_r - p_t = \rho c z \mathbf{v}_t \cos\theta. \tag{F.7}$$

Rearranging and substituting eq. F.4, eq. F.7 becomes

$$1 + \frac{p_r}{p_i} = \frac{p_t}{p_i}(1 + z\cos\theta). \tag{F.8}$$

Substituting eq. F.6 into eq. F.8 and solving for the ratio of transmitted to incident pressure gives

$$\frac{p_t}{p_i} = \left(1 + \frac{1}{2}z\cos\theta\right)^{-1}. \tag{F.9}$$

Taking the absolute value and squaring eq. F.9 gives the transmission coefficient of the absorptive layer as

$$\tau(\theta) = \left(\left|1 + \frac{1}{2}z\cos\theta\right|^2\right)^{-1}. \tag{F.10}$$

Let $z = a + ib$ and eq. F.10 reduces to

$$\tau(\theta) = \frac{1}{\left(1 + \frac{1}{2}a\cos\theta\right)^2 + \left(\frac{1}{2}b\cos\theta\right)^2}.$$

F.11

Because the acoustic diffusion model assumes a diffuse field with incident waves arriving from all angles, the diffuse transmission coefficient, τ_d, must be derived. The diffuse transmission coefficient is defined as the integral of the transmission coefficient over a hemispherical surface given by (Bies and Hansen, 2003)

$$\tau_d = \frac{1}{\pi}\int_0^{2\pi}\int_0^{\pi/2} \tau(\theta,\phi)\cos\theta\sin\theta\, d\theta\, d\phi$$

F.12

where ϕ is the azimuthal angle of incidence. Substituting eq. F.11 into eq. F.12 gives

$$\tau_d = \frac{1}{\pi}\int_0^{2\pi}\int_0^{\pi/2} \frac{\cos\theta\sin\theta}{\left(1 + \frac{1}{2}a\cos\theta\right)^2 + \left(\frac{1}{2}b\cos\theta\right)^2} d\theta\, d\phi.$$

F.13

Let $u = \cos\theta$ to get

$$\tau_d = -\frac{1}{\pi}\int_0^{2\pi}\int_1^0 \frac{u}{\frac{1}{4}|z|^2 u^2 + au + 1} du\, d\phi.$$

F.14

Carrying out the integration with respect to u with the help of any integration table yields

$$\tau_d = -\frac{1}{\pi}\int_0^{2\pi}\left\{\frac{2}{|z|^2}\left[\ln\left|\frac{1}{4}|z|^2 u^2 + au + 1\right| - \frac{2a}{b}\tan^{-1}\left(\frac{\frac{1}{2}|z|^2 u + a}{b}\right) - \right]\right\}_1^0 d\phi.$$

F.15

Evaluating at the limits of integration gives

$$\tau_d = \frac{1}{\pi}\int_0^{2\pi}\frac{2}{|z|^2}\left[\frac{2a}{b}\tan^{-1}\left(\frac{a}{b}\right) + \ln\left|\frac{1}{4}|z|^2 + a + 1\right| - \frac{2a}{b}\tan^{-1}\left(\frac{\frac{1}{2}|z|^2 + a}{b}\right)\right]d\phi.$$

F.16

Since the transmission coefficient is independent of the azimuthal angle of incidence, the last integral is trivially evaluated and the diffuse transmission coefficient is

$$\tau_d = \frac{4}{|z|^2}\left[\frac{2a}{b}\tan^{-1}\left(\frac{a}{b}\right) - \frac{2a}{b}\tan^{-1}\left(\frac{\frac{1}{2}|z|^2 + a}{b}\right) + \ln\left|\frac{1}{4}|z|^2 + a + 1\right|\right].$$

F.17

A very simple empirical expression to calculate the impedance of a perforated sheet as a function of frequency, f, is given by (Wu, 2000)

$$z(f) = \frac{1}{\rho c \sigma}(2.40 + i0.02f)$$

where σ is the porosity or ratio of the total area of the holes to the total area of the sheet. The resistance and reactance, or real part and imaginary part of the impedance, respectively, are plotted for a few different values of porosity in Figure F.2. Based on eq. F.18, it comes as no surprise that the resistance of the perforated sheet is constant and the reactance is linear in frequency. As the porosity of the perforated sheet increases, or more hole area is introduced compared to the sheet area, the resistance decreases and the slope of the reactance decreases.
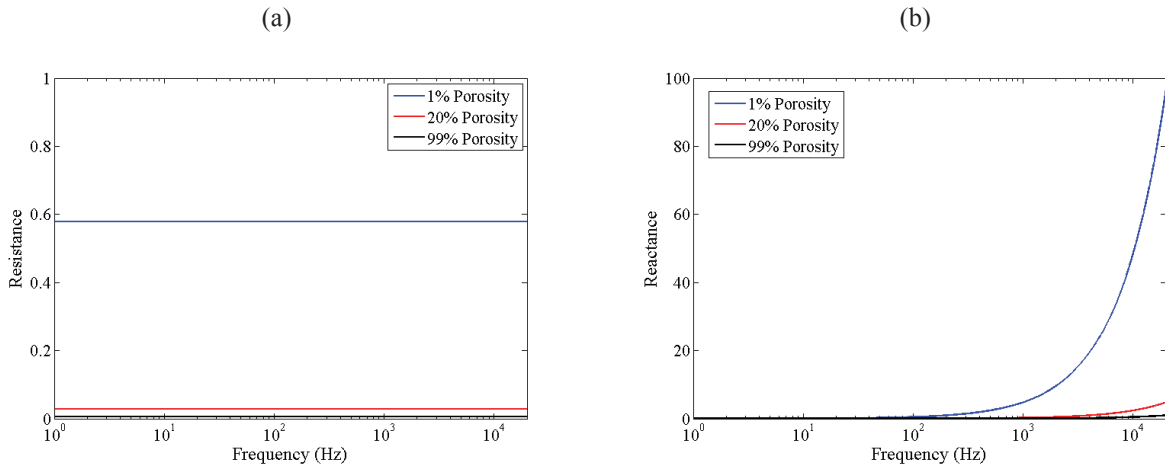
(a)   (b)

Figure F.2: (a) Resistance and (b) reactance of perforated sheets with different porosity as a function of frequency.

The transmission coefficients and transmission losses (TL) of the perforated sheets with different porosity with the impedance given by eq. F.18 are plotted in Figure F.3 against frequency. At low frequencies, the acoustic transmission through each perforated sheet is dominated by the resistive part of its impedance being fairly flat in frequency. At high frequencies, the reactive part of the impedance dominates the transmission greatly reducing the amplitude of the transmitted wave. The transition frequency where the reactance begins to dominate the resistance varies with the porosity of the perforated sheet occurring around 100 Hz for very low porosity, 1000 Hz for a more standard (20%), and 5000-6000 Hz for a very high porosity.
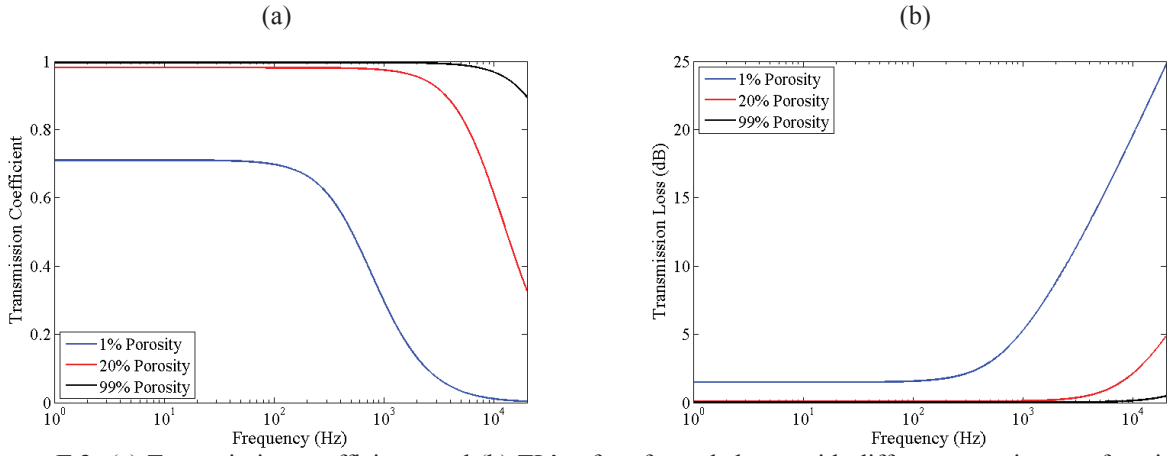
Figure F.3: (a) Transmission coefficients and (b) TL's of perforated sheets with different porosity as a function of frequency.

Appendix G: Coupled Volume Statistical Formulation

An energy balance formulation will now be presented using statistical theory and its underlying assumptions for a two volume interior transmission problem such as the one shown in Figure 6.9. Assuming the energy in each volume is uniform, a steady state energy balance can be written as

$$E_{source} - E_{abs} - E_{trans} = 0 \qquad \text{G.1}$$

for either volume where E_{source} is the energy emitted by the source, E_{abs} is the energy absorbed by the surfaces, and E_{trans} is the energy transmitted to another volume. The balance of power for Volume 1 is

$$W_1 - \frac{c}{4}(\alpha_1 A_1 + \alpha_{c1} A_c)\psi_1 - \frac{c}{4} A_c (\tau_2 \psi_1 - \tau_1 \psi_2) = 0 \qquad \text{G.2}$$

where W_1 is the acoustic power of the source in Volume 1, ψ_1 and ψ_2 are the uniform energy densities in Volumes 1 and 2, respectively, A_1 is area of the exclusive surfaces bounding Volume 1 with α_1 being the uniform absorption of these surfaces, A_c is the area of the coupling surface, α_c is the absorption of the coupling surface, τ_1 is the transmission coefficient of the coupling surface for energy flowing into Volume 1 from Volume 2, and τ_2 is the transmission coefficient for energy flowing into Volume 2 from Volume 1. The power balance in Volume 2 is

$$W_2 - \frac{c}{4}(\alpha_2 A_2 + \alpha_{c2} A_c)\psi_2 - \frac{c}{4} A_c (\tau_1 \psi_2 - \tau_2 \psi_1) = 0 \qquad \text{G.3}$$

where W_2 is the acoustic source power in Volume 2 and A_2 and α_2 are the surface area and absorption coefficients of the surfaces exclusive to Volume 2, respectively. Rewriting eqs. G.2 and G.3 as a linear system of equations gives

$$\begin{cases} (\alpha_1 A_1 + \alpha_{c1} A_c + \tau_2 A_c)\psi_1 - \tau_1 A_c \psi_2 = \dfrac{4}{c} W_1 \\ -\tau_2 A_c \psi_1 + (\alpha_2 A_2 + \alpha_{c2} A_c + \tau_1 S_c)\psi_2 = \dfrac{4}{c} W_2 \end{cases} \qquad \text{G.4}$$

In matrix form, eq. G.4 is

$$\begin{bmatrix} \alpha_1 A_1 + \alpha_{c1} A_c + \tau_2 A_c & -\tau_1 A_c \\ -\tau_2 A_c & \alpha_2 A_2 + \alpha_{c2} A_c + \tau_1 S_c \end{bmatrix} \begin{Bmatrix} \psi_1 \\ \psi_2 \end{Bmatrix} = \frac{4}{c} \begin{Bmatrix} W_1 \\ W_2 \end{Bmatrix} \qquad \text{G.5}$$

which can be solved for the uniform, steady state energy in each volume.

The rate of change of the total diffuse energy in a volume, E_v, is equal to the acoustic power supplied by a source, $W_{v,source}$, less the power absorbed in the volume, $W_{v,abs}$, and transmitted to another volume, $W_{v,trans}$. Stated mathematically

$$\frac{dE_v(t)}{dt} = W_{v,source}(t) - W_{v,abs}(t) - W_{v,trans}(t) \qquad\qquad \text{G.6}$$

Now, this formulation is specialized for the problem in Chapter 6, i.e. a source and receiving volume with uniform absorption coupled through a partition with a known TL. Assuming a uniform distribution of energy density in the source volume (denoted with subscript 1), eq. E.1 can be written as

$$\frac{\partial \psi_1(t)}{\partial t} = -\frac{c}{4V_1}(\alpha A_1 + \tau A_c)\psi_1(t) + \frac{c}{4V_1}A_c\tau_2\psi_2(t) + \frac{W_1}{V_1} \qquad\qquad \text{G.7}$$

where ψ_1 is the energy density in the source volume and ψ_2 the energy density in the receiving volume; V_1 is the volume of the source room, A_1 the surface area of the non-coupling surfaces, and A_c is the surface area of the coupling partition; α is the absorption coefficient of the non-coupling surfaces; τ is the transmission coefficient of the coupling partition; W_1 is the source power. In the receiving volume, eq. E.1 becomes

$$\frac{\partial \psi_2(t)}{\partial t} = \frac{c}{4V_2}A_c\tau\psi_1(t) - \frac{c}{4V_2}(\alpha A_2 + \tau A_c)\psi_2(t) \qquad\qquad \text{G.8}$$

where V_2 is the volume and A_2 is the surface area of the non-coupling surfaces in the receiving volume.

The homogeneous solutions to two coupled first order ordinary differential equations take the form

$$\psi_{1h}(t) = C_1 v_{11}\exp(\lambda_1 t) + C_2 v_{12}\exp(\lambda_2 t) \qquad\qquad \text{G.9}$$

and

$$\psi_{2h}(t) = C_1 v_{21}\exp(\lambda_1 t) + C_2 v_{22}\exp(\lambda_2 t) \qquad\qquad \text{G.10}$$

where C_1 and C_2 are constants to be determined by initial conditions, λ_1 and λ_2 are the eigenvalues of the system matrix, and $\mathbf{v}_1 = \{v_{11} \quad v_{21}\}^T$ and $\mathbf{v}_2 = \{v_{12} \quad v_{22}\}^T$ are the eigenvectors.

The fundamental matrix, $\mathcal{G}(t)$, for this system is

$$\mathcal{G}(t) = \begin{bmatrix} v_{11}\exp(\lambda_1 t) & v_{12}\exp(\lambda_2 t) \\ v_{21}\exp(\lambda_1 t) & v_{22}\exp(\lambda_2 t) \end{bmatrix}.$$ G.11

The forcing vector, $\mathbf{b}(t)$, is

$$\mathbf{b}(t) = \left\{ \begin{matrix} W_1/V_1 \\ 0 \end{matrix} \right\}.$$ G.12

The total solution to the system is the linear superposition of the homogeneous solution and the particular solution which is (Kohler and Johnson, 2006)

$$\left\{ \begin{matrix} \psi_1(t) \\ \psi_2(t) \end{matrix} \right\} = \mathcal{G}(t) \left\{ \begin{matrix} C_1 \\ C_2 \end{matrix} \right\} + \mathcal{G}(t) \int_0^t \mathcal{G}^{-1}(t')\mathbf{b}(t')dt'.$$ G.13

Substitution and some matrix calculations gives the transient solutions for the energy density in the source and receiving volumes as

$$\psi_1(t) = C_1 v_{11}\exp(\lambda_1 t) + C_2 v_{12}\exp(\lambda_2 t) +$$
$$\frac{1}{v_{11}v_{22} - v_{12}v_{21}} \frac{W_1}{V_1} \left(-\frac{v_{11}v_{22}}{\lambda_1} + \frac{v_{11}v_{22}}{\lambda_1}\exp(\lambda_1 t) + \frac{v_{12}v_{21}}{\lambda_2} - \frac{v_{12}v_{21}}{\lambda_2}\exp(\lambda_2 t) \right)$$ G.14

and

$$\psi_2(t) = C_1 v_{21}\exp(\lambda_1 t) + C_2 v_{22}\exp(\lambda_2 t) +$$
$$\frac{v_{21}v_{22}}{v_{11}v_{22} - v_{12}v_{21}} \frac{W_1}{V_1} \left(-\frac{1}{\lambda_1} + \frac{1}{\lambda_1}\exp(\lambda_1 t) + \frac{1}{\lambda_2} - \frac{1}{\lambda_2}\exp(\lambda_2 t) \right).$$ G.15

For the buildup of energy due to the source with zero initial energy,

$$C_1 = C_2 = 0$$ G.16

and the solutions are

$$\psi_1(t) = \frac{1}{v_{11}v_{22} - v_{12}v_{21}} \frac{W_1}{V_1} \left(-\frac{v_{11}v_{22}}{\lambda_1} + \frac{v_{11}v_{22}}{\lambda_1}\exp(\lambda_1 t) + \frac{v_{12}v_{21}}{\lambda_2} - \frac{v_{12}v_{21}}{\lambda_2}\exp(\lambda_2 t) \right)$$ G.17

and

$$\psi_2(t) = \frac{v_{21}v_{22}}{v_{11}v_{22} - v_{12}v_{21}} \frac{W_1}{V_1} \left(-\frac{1}{\lambda_1} + \frac{1}{\lambda_1} \exp(\lambda_1 t) + \frac{1}{\lambda_2} - \frac{1}{\lambda_2} \exp(\lambda_2 t) \right).$$

G.18

Appendix H: Numerical Convergence in the Simple Uniform Coupled Volumes

Convergence in the multiple volume BEM solution due to mesh size is studied for the two extreme values of the coupling partition TL (1 dB and 50 dB), i.e. for varying strengths of the coupling between the two volumes. The initial boundary mesh of 12 elements per volume is created by placing one element side along each edge of the volumes. The mesh refinement strategy places consecutively increasing numbers of element sides along each edge of the volumes. The average steady state energy density in the source volume is plotted against the total number of elements, on the bounding surface of both volumes, and the number of elements per MFPL in Figure H.1. The average steady state energy density in the receiving volume is plotted in the same way in Figure H.2. Both volumes demonstrate a converging trend in energy density.
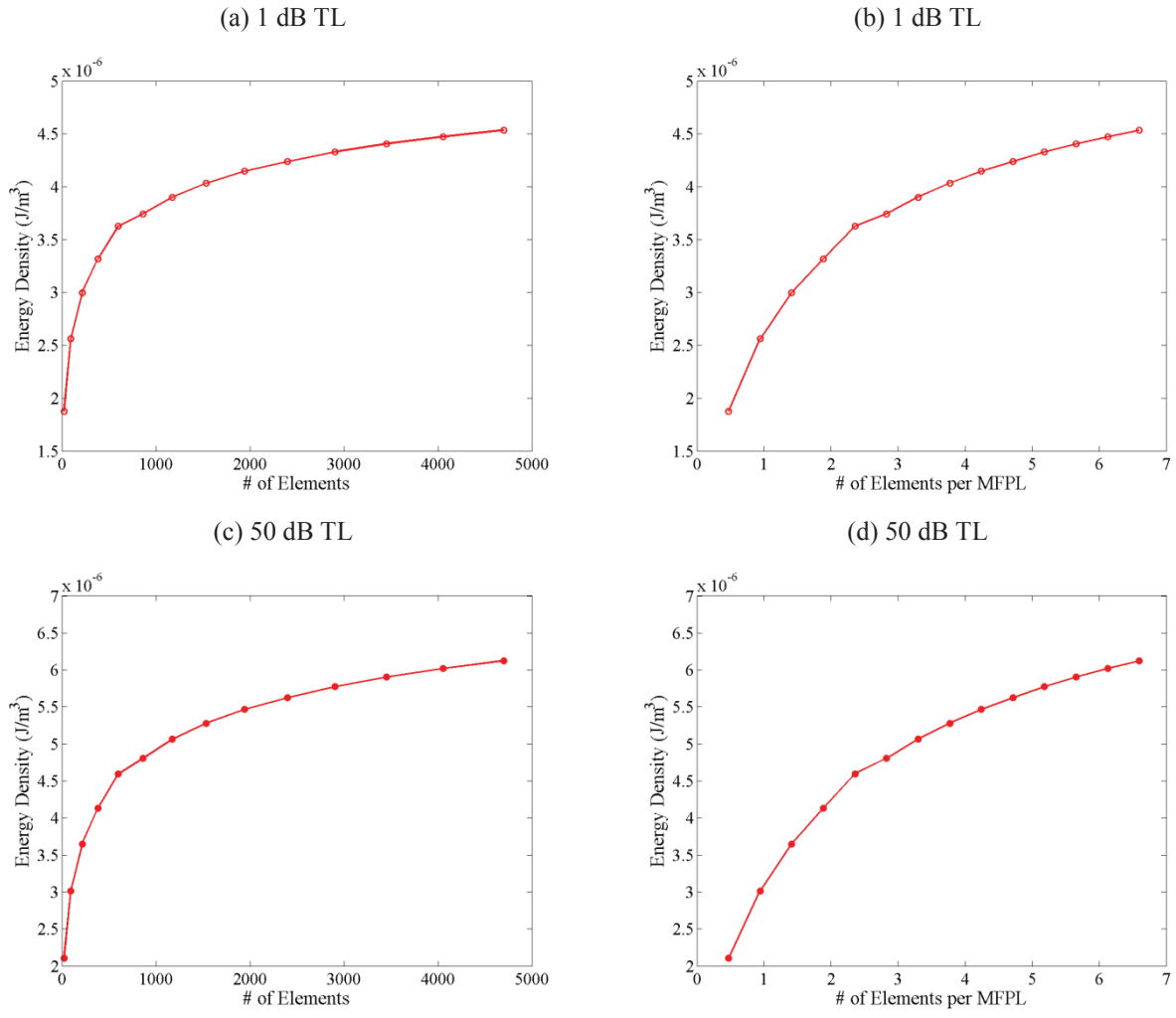
Figure H.1: Convergence in the steady state average energy density in the source volume against (a,c) number of elements and (b,d) number of elements per mean free path length for (a,b) 1 dB TL and (c,d) 50 dB TL of the coupling partition.
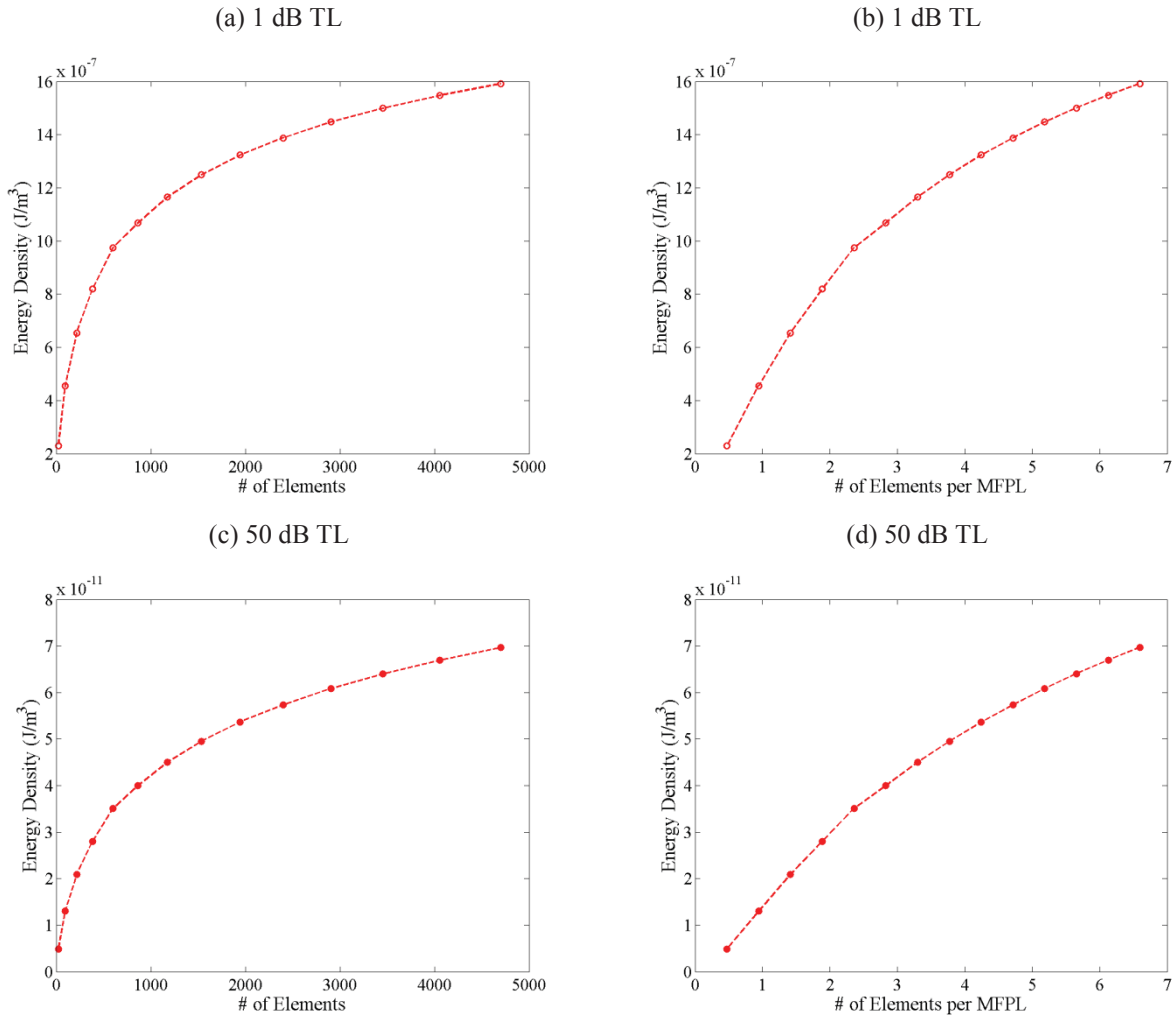
(a) 1 dB TL   (b) 1 dB TL

(c) 50 dB TL   (d) 50 dB TL

Figure H.2: Convergence in the steady state average energy density in the receiving volume against (a,c) number of elements and (b,d) number of elements per mean free path length for (a,b) 1 dB TL and (c,d) 50 dB TL of the coupling partition.

Next, the percent difference in average steady state energy density is plotted in Figure H**.**3. There are two general features to note about the convergence in this example. First, convergence in the receiving volume takes about twice as many elements per MFPL than in the source volume. This is because the acoustic energy must encounter at least one collision in the source volume, i.e. travel one MFPL, before it can be transmitted into the receiving volume. Second, a higher coupling partition TL takes longer to converge than a lower TL, especially significant in the receiving volume whose average energy is most affected by the TL. This is due to the significantly smaller amounts of energy transmitted into the receiving volume being more affected by the change in mesh size. For a coupling partition with 1 dB TL, convergence to

197

within 5 % difference is obtained with a mesh of 864 elements (2.8 per MFPL) in the source volume and 2400 elements (4.8 per MFPL) in the receiving volume. For a coupling partition with 50 dB TL, meshes of 1536 elements (3.8 per MFPL) in the source volume and 4056 elements (6.1 per MFPL) provide convergence to within 5 % difference. The results presented are computed using the finest mesh with 4056 elements.
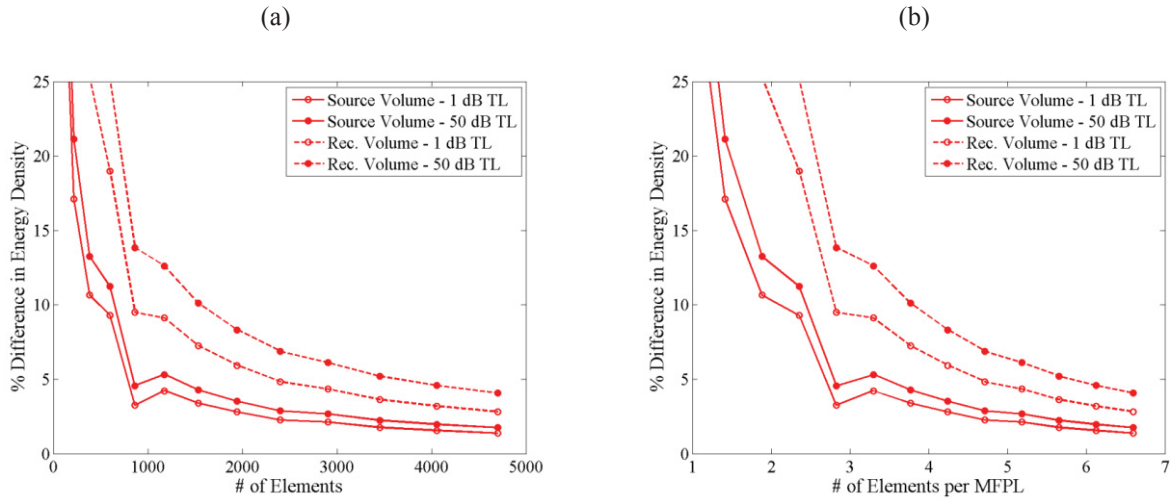

(a) (b)

Figure H.3: Percent difference in the steady state average energy density for increasingly refined meshes of the receiving volume against (a) number of elements and (b) number of elements per mean free path length.

The diffusion model is also solved using the FEM for the simple transmission model. The point source is modeled as a spherical volume with a radius of 17 cm. The source volume is discretized using three perpendicular circles divided into quarter-circular segments. Initially, two element edges are placed along each of these segments and each of the bounding volume edges. This mesh is refined by consecutively increasing the number of element edges along the source segments. The average steady state energy density in the source volume is plotted in Figure H.4 and in the receiving volume in Figure H.5 against the number of elements and number of elements per MFPL for coupling partition TL's of 1 dB and 50 dB. A converging trend is demonstrated in each of the plots.
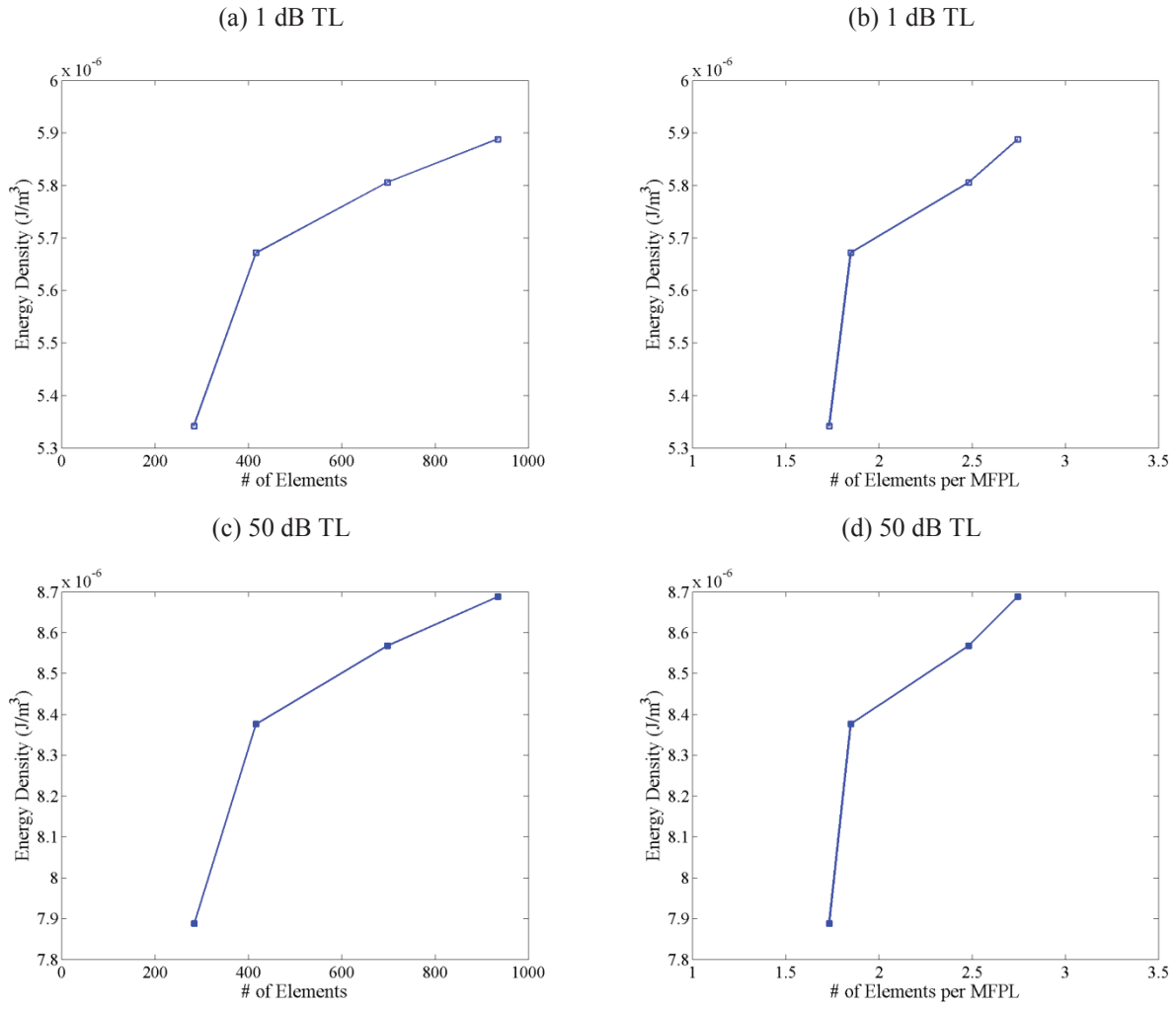
Figure H.4: Convergence in the steady state average energy density in the source volume against (a,c) number of elements and (b,d) number of elements per mean free path length for (a,b) 1 dB TL and (c,d) 50 dB TL of the coupling partition.
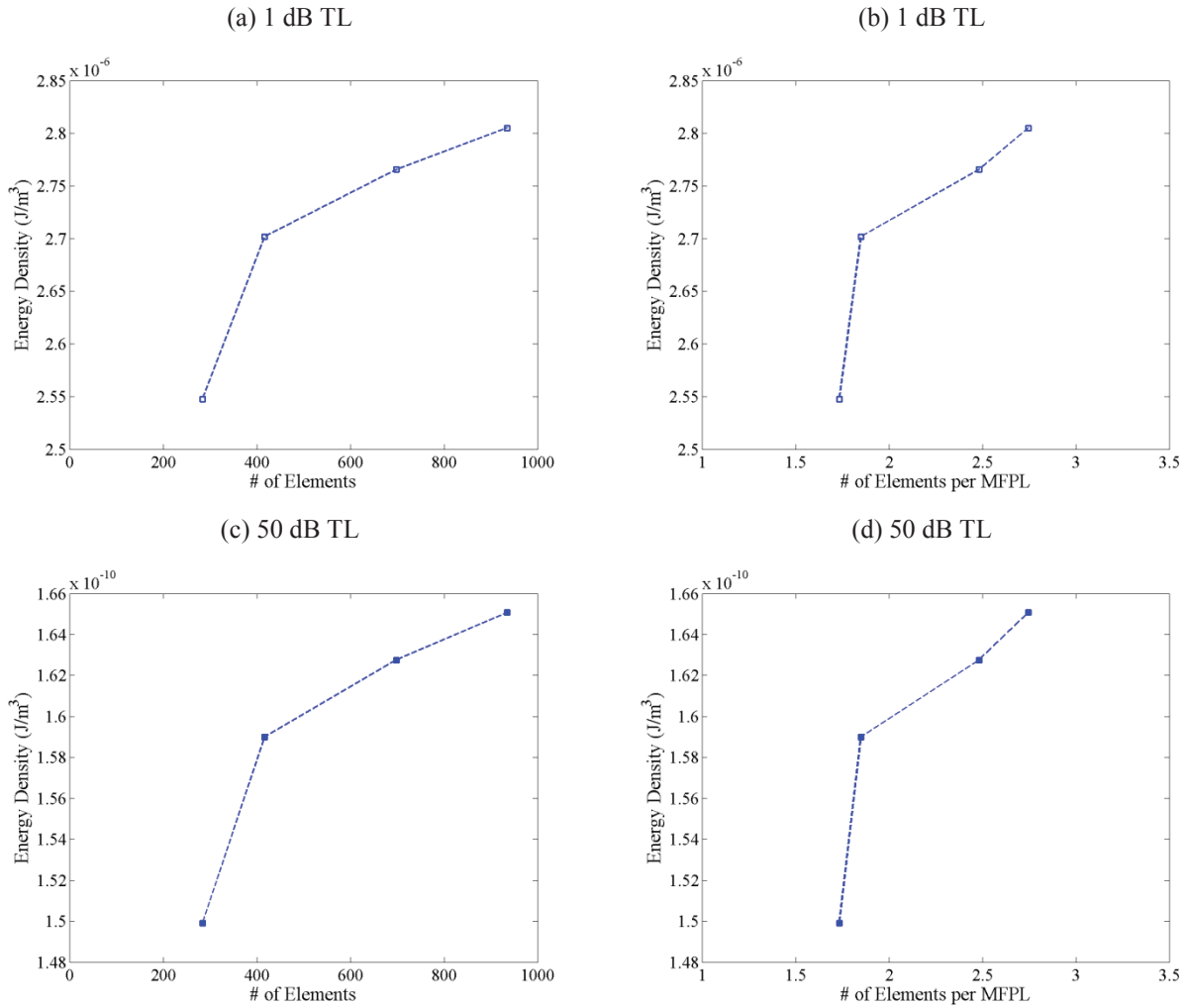
Figure H.5: Convergence in the steady state average energy density in the receiving volume against (a,c) number of elements and (b,d) number of elements per mean free path length for (a,b) 1 dB TL and (c,d) 50 dB TL of the coupling partition.

The percent difference in average steady state energy density is plotted in Figure H.6. As shown in this plot, the convergence is independent of the TL and both volumes converge at the same rate when using the FEM to solve the diffusion model. Convergence to within 2 % difference is guaranteed in three refinements using a mesh of 935 elements (2.7 elements per MFPL); this mesh is used to compute the results presented later.

(a)   (b)
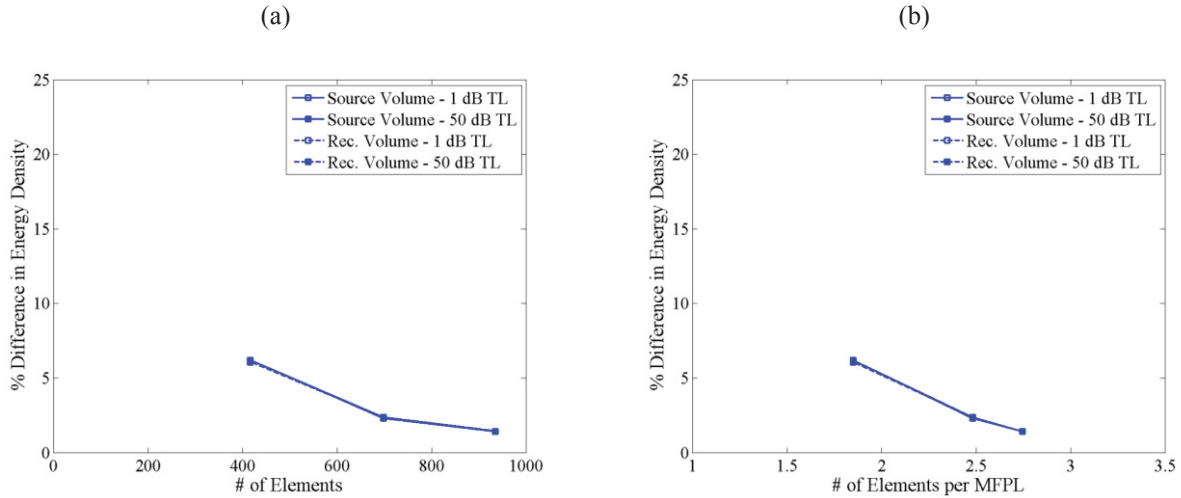
Figure H.6: Percent difference in the steady state average energy density for increasingly refined meshes of the receiving volume against (a) number of elements and (b) number of elements per mean free path length.

The final numerical technique used to solve the simple transmission example is ray tracing. Rays encountering the coupling partition are allowed to propagate through the surface without changing direction but the energy is lessened by the defined reflection, scattering, and transmission coefficients. Rays are traced for three seconds; the steady state value is taken to be the energy after three seconds have passed. Convergence in the ray tracing solution is studied by increasing the level of source division as in previous examples. The average steady state energy density in each volume is plotted for coupling partitions of 1 dB and 50 dB TL for increasing numbers of rays in Figure H.**7**. A converging trend is demonstrated in each case.
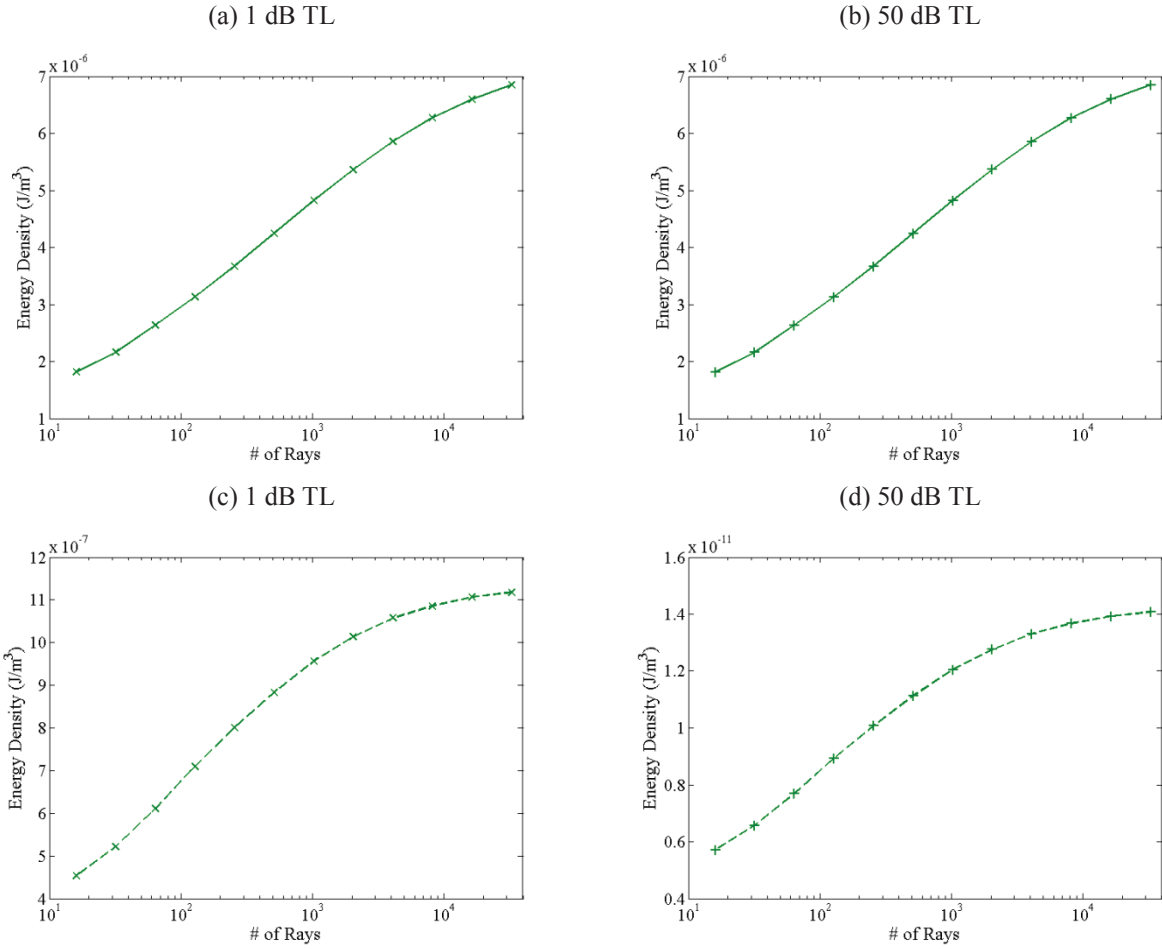
Figure H.7: Convergence in the steady state average energy density in the (a,b) source volume and (c,d) receiving volume against the number of rays for (a,c) 1 dB TL and (b,d) 50 dB TL of the coupling partition.

The percent difference in average steady state energy density is plotted in Figure H.8. Due to the geometric nature of the ray tracing technique, convergence is independent of the TL of the coupling partition as demonstrated in the plot. Another interesting feature of this convergence study is that the energy converges faster in the receiving volume than in the source volume, opposite what was demonstrated in the diffusion BEM solution. The average energy density converges to within 5 % difference in the receiving volume using only 4096 rays, while 32768 rays are required for convergence to within 5 % difference in the source volume. The steady state results plotted later are computed using 32768 rays.
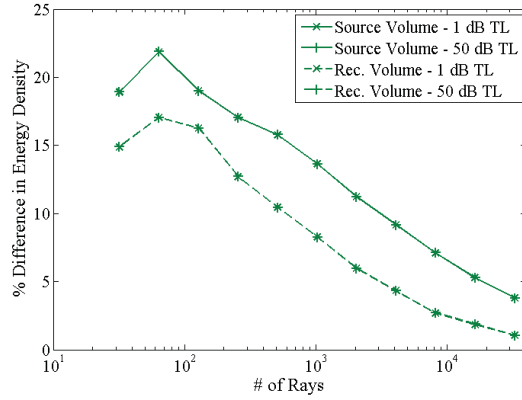
Figure H.8: Percent difference in the steady state average energy density for an increasing number of rays.

To study the convergence of the numerical solutions to the transient problem, the average energy density in the source volume at 0.5 s and in the receiving volume at 0.7 s is computed for partition TL's of 1 dB and 50 dB. Using the same meshing strategy as the steady state problem, the transient average energy density computed using the BEM solution to the diffusion model is plotted in Figure H.9 for the source volume and in Figure H.10 for the receiving volume. Again, both demonstrate the expected converging trend.
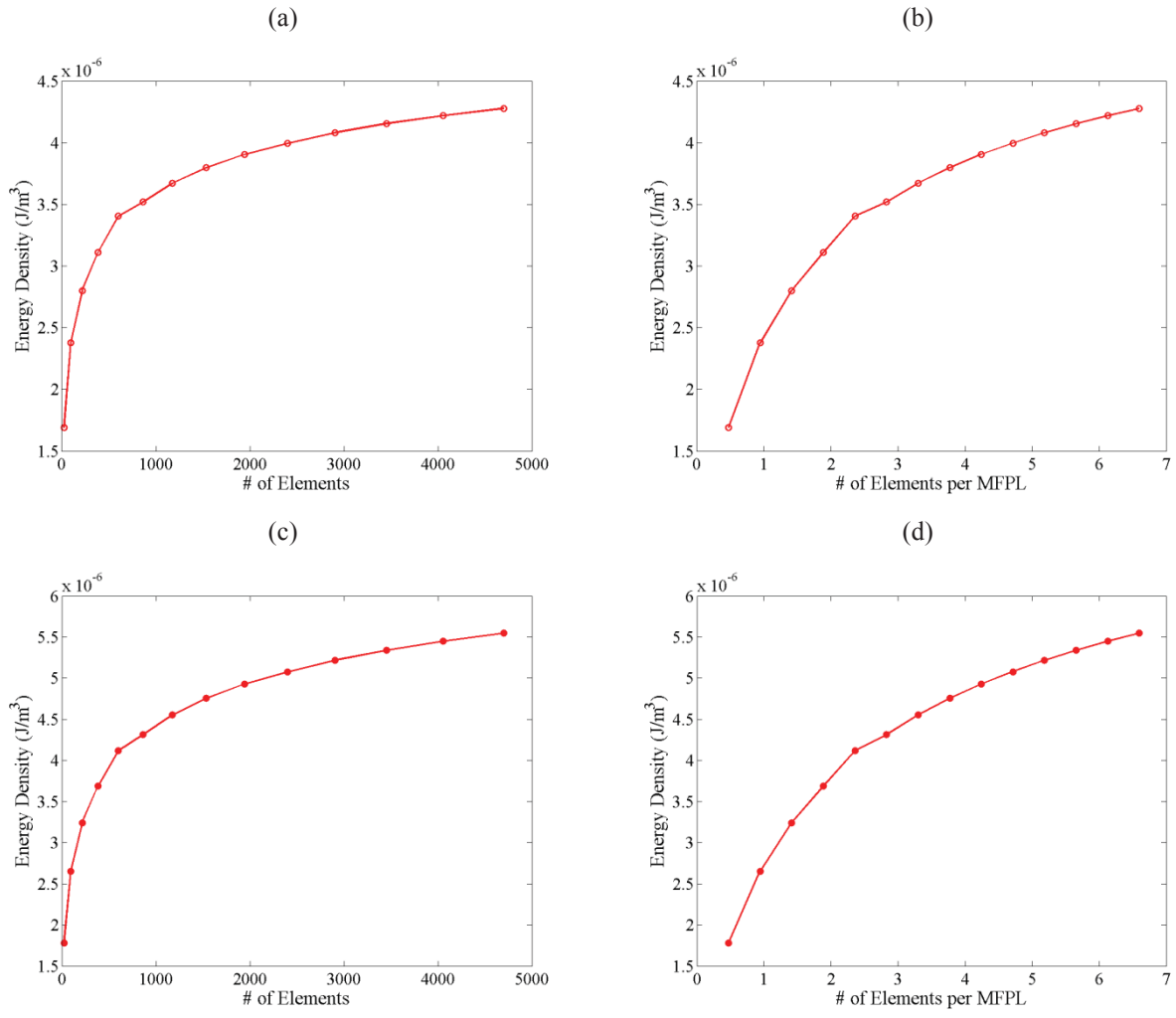
Figure H.9: Convergence in the transient average energy density in the source volume against (a,c) number of elements and (b,d) number of elements per mean free path length for (a,b) 1 dB TL and (c,d) 50 dB TL of the coupling partition.
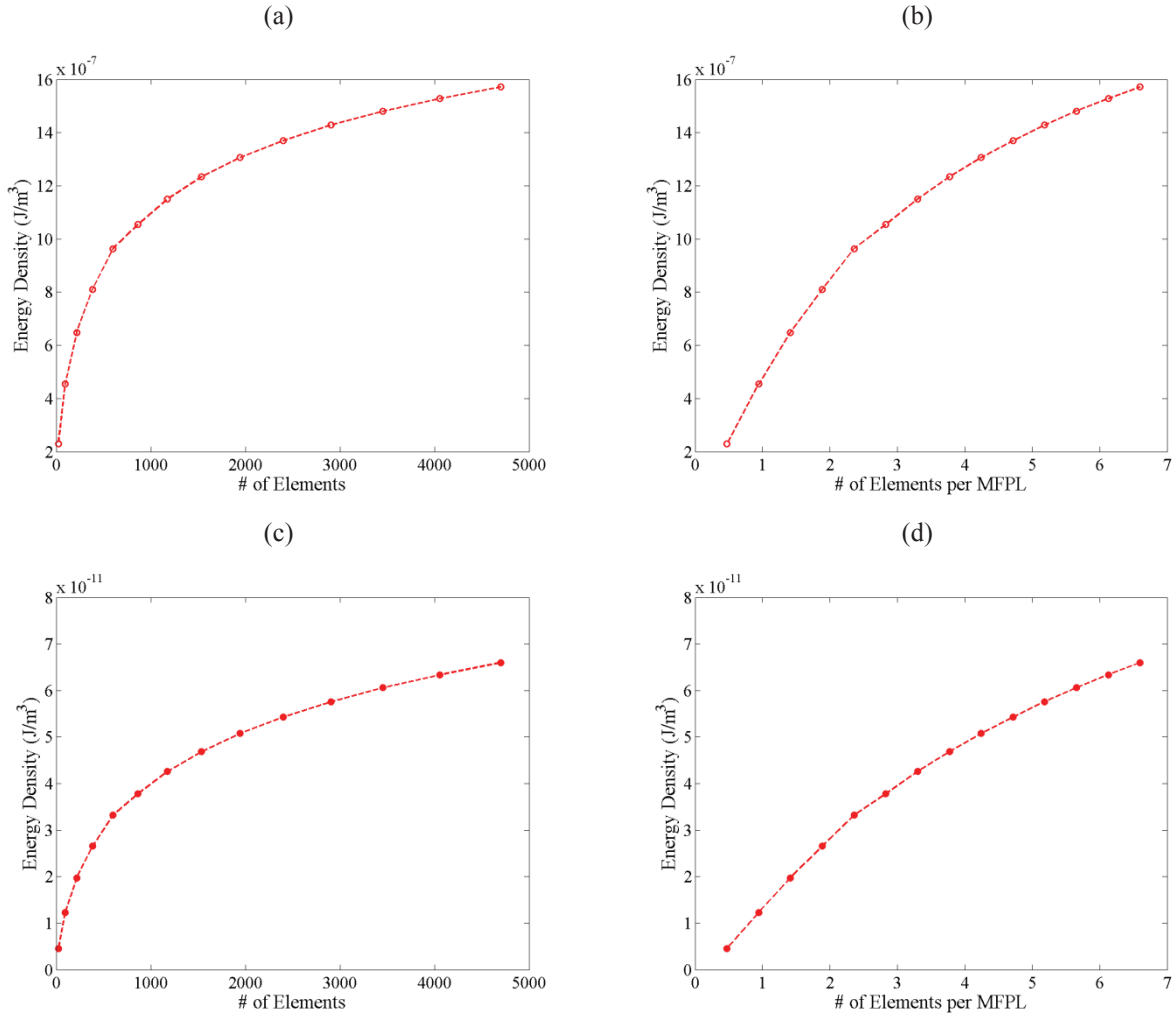
Figure H.10: Convergence in the transient average energy density in the receiving volume against (a,c) number of elements and (b,d) number of elements per mean free path length for (a,b) 1 dB TL and (c,d) 50 dB TL of the coupling partition.

The percent difference in average transient energy density is plotted in Figure H.11. The convergence in the transient solution is basically the same as in the steady state case. For a coupling partition with 1 dB TL, convergence to within 5 % difference is obtained with a mesh of 864 elements (2.8 per MFPL) in the source volume and 2400 elements (4.8 per MFPL) in the receiving volume. For a coupling partition with 50 dB TL, meshes of 1536 elements (3.8 per MFPL) in the source volume and 4056 elements (6.1 per MFPL) provide convergence to within 5 % difference. The results presented are computed using the finest mesh with 4056 elements, the same as the steady state mesh.
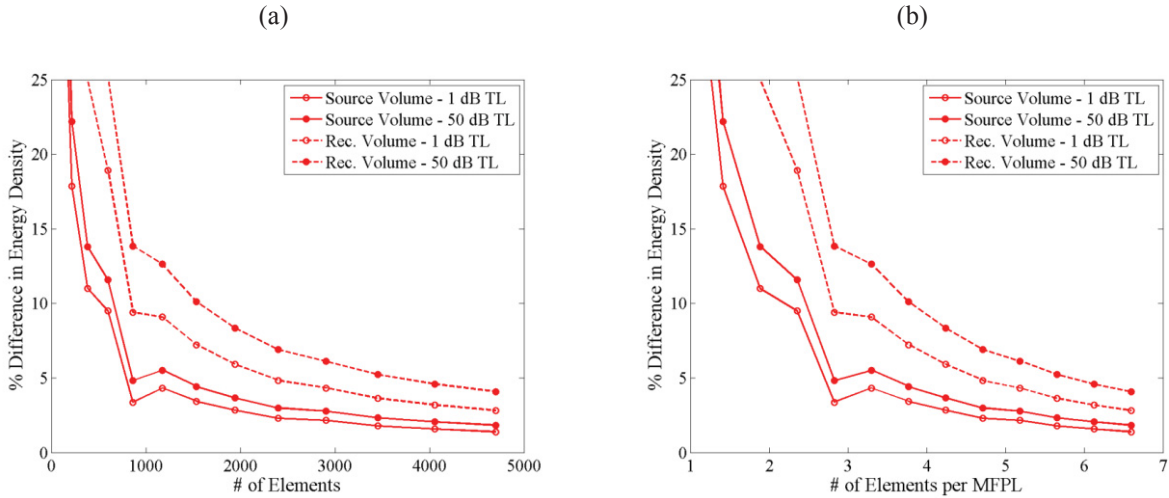
Figure H.11: Percent difference in the transient average energy density for increasingly refined meshes of the receiving volume against (a) number of elements and (b) number of elements per mean free path length..

The average transient energy density in the source volume computed with the diffusion FEM is plotted in Figure H.12 and in the receiving volume in Figure H.13 against the number of elements and number of elements per MFPL for coupling partition TL's of 1 dB and 50 dB. The same meshing strategy as in the steady state case is used. A converging trend is demonstrated in each of the plots.
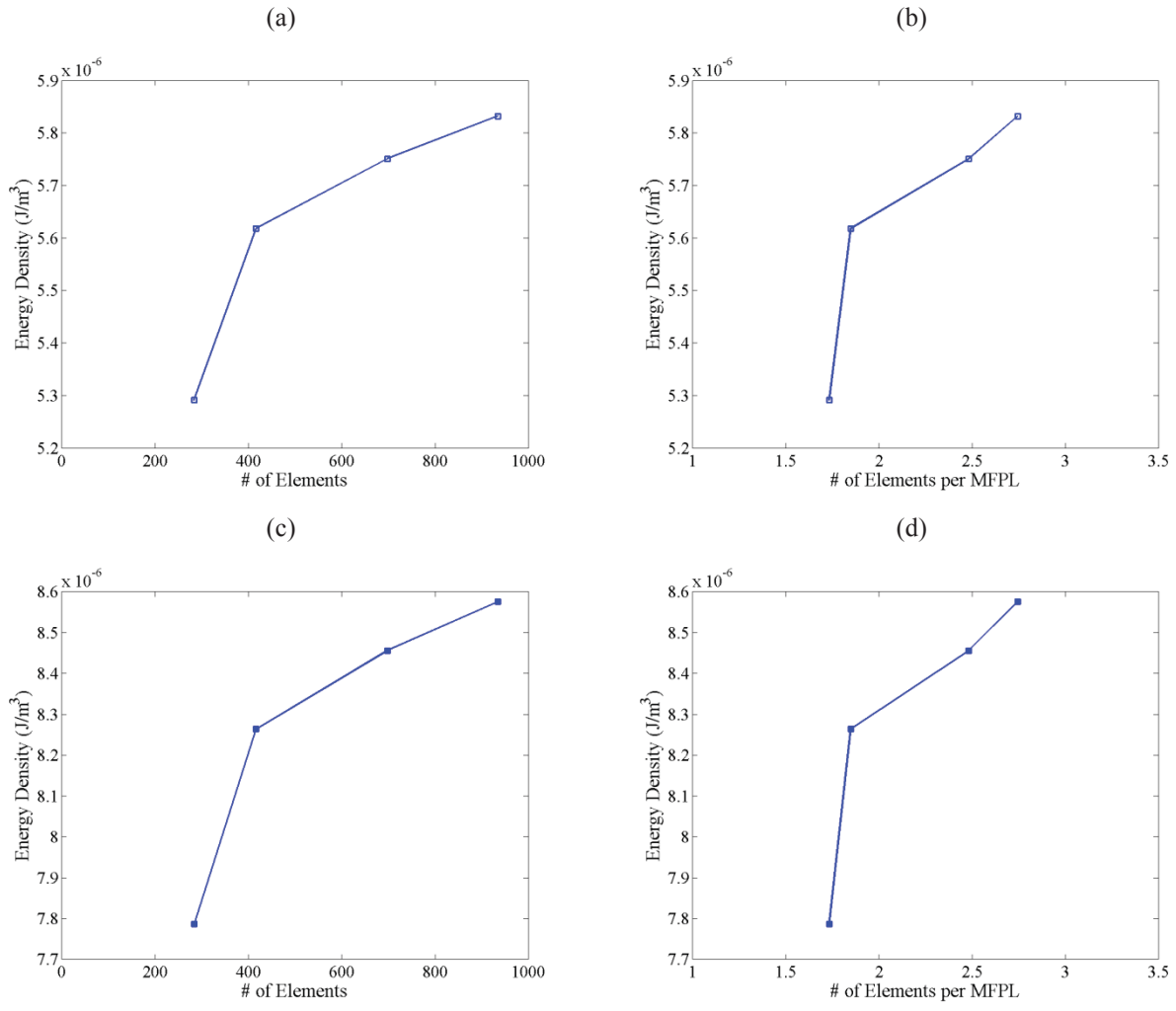
Figure H.12: Convergence in the transient average energy density in the source volume against (a,c) number of elements and (b,d) number of elements per mean free path length for (a,b) 1 dB TL and (c,d) 50 dB TL of the coupling partition.
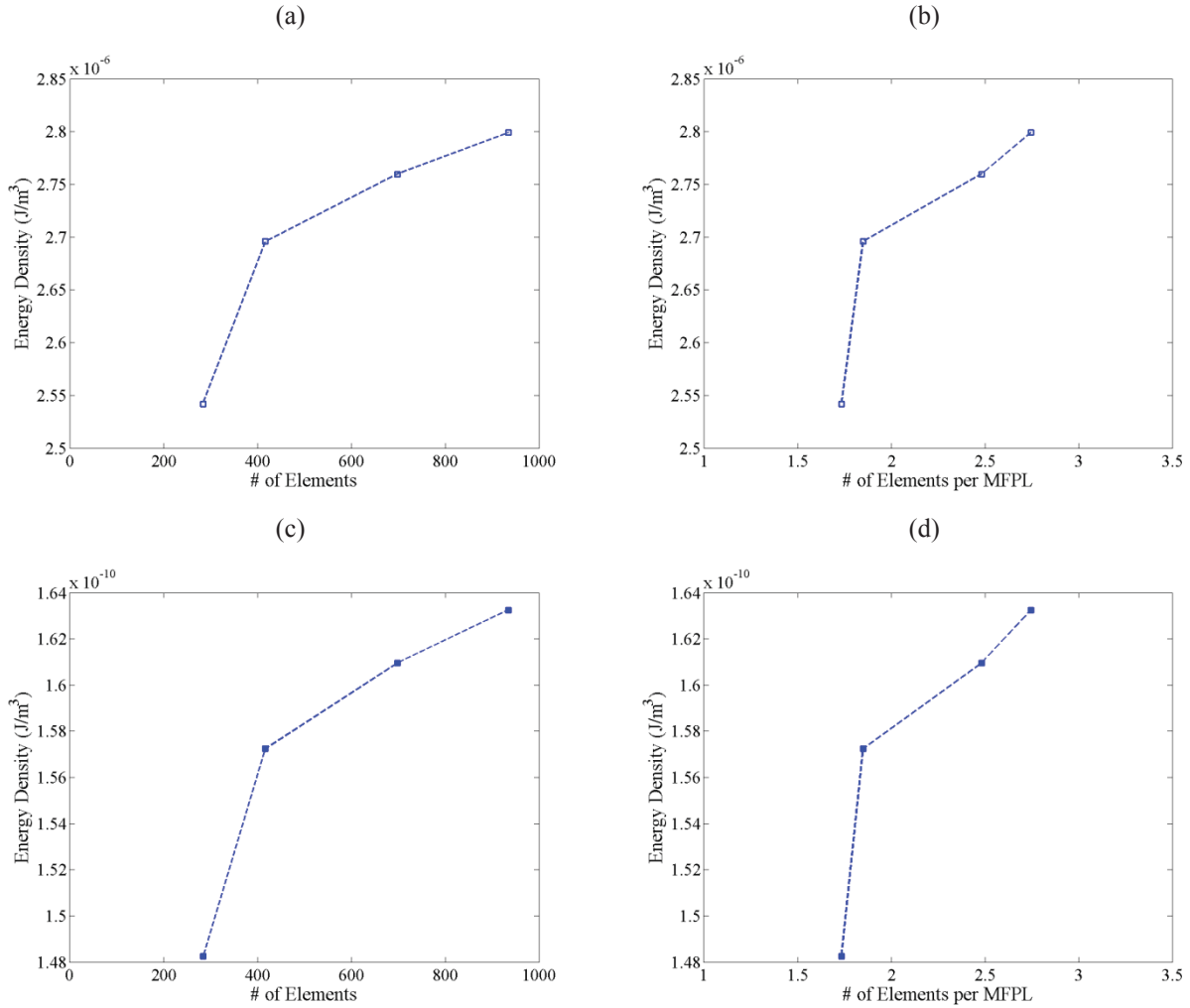
Figure H.13: Convergence in the transient average energy density in the receiving volume against (a,c) number of elements and (b,d) number of elements per mean free path length for (a,b) 1 dB TL and (c,d) 50 dB TL of the coupling partition.

The percent difference in average transient energy density is plotted in Figure H.14. Again, convergence is the same in the transient case as in the steady state problem. Convergence to within 2 % difference is guaranteed in three refinements using a mesh of 935 elements (2.7 elements per MFPL); this mesh, again the same as the steady state mesh, is used to compute the results presented later.
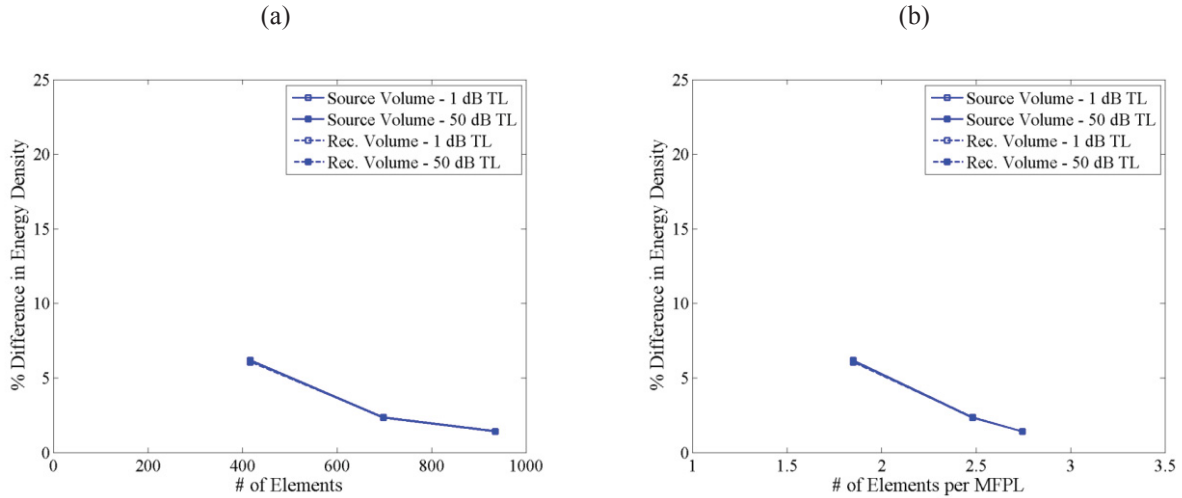
(a)   (b)

Figure H.14: Percent difference in the transient average energy density for increasingly refined meshes of the receiving volume against (a) number of elements and (b) number of elements per mean free path length..

Finally, the average transient energy density in each volume computed using the ray tracing technique is plotted for coupling partitions of 1 dB and 50 dB TL for increasing numbers of rays in Figure H.15. A converging trend is demonstrated in each case.
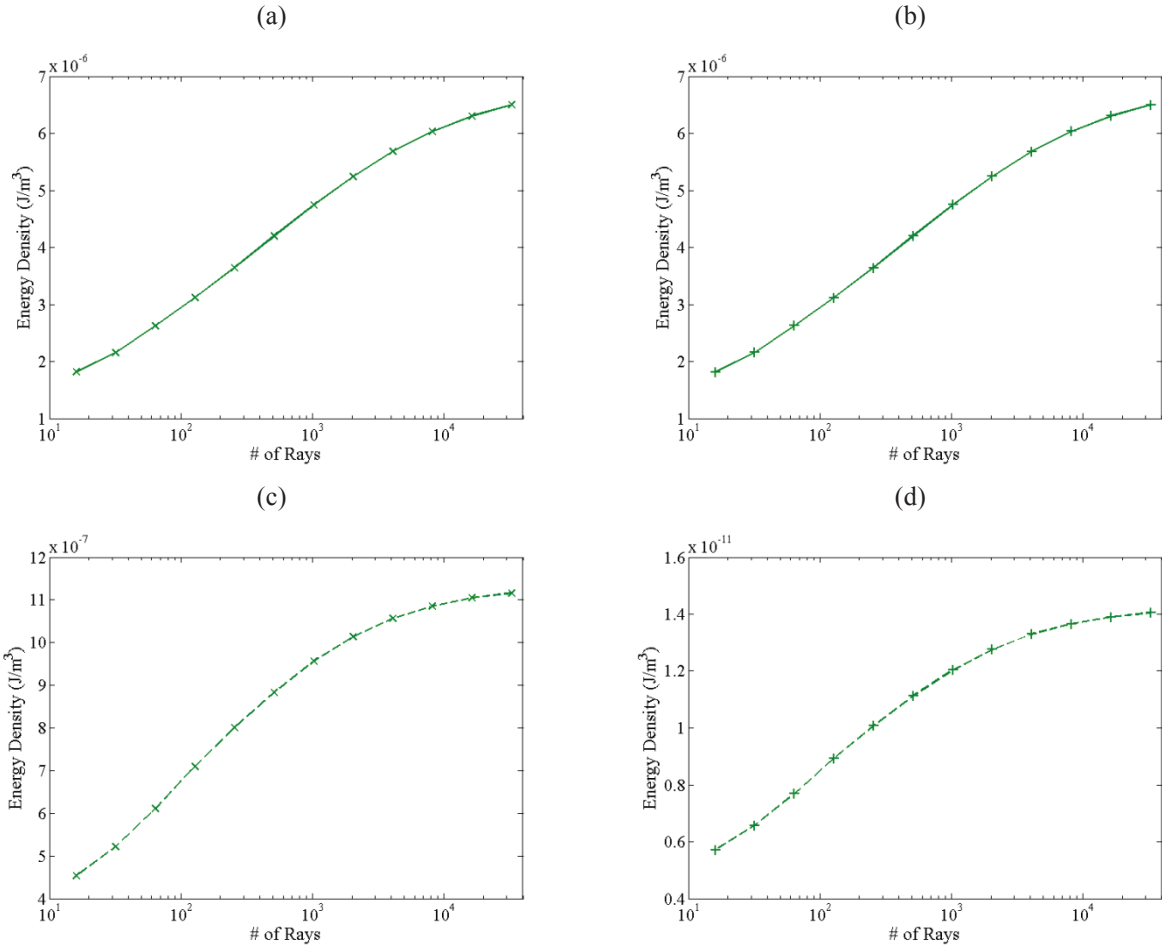
Figure H.15: Convergence in the transient average energy density in the (a,b) source volume and (c,d) receiving volume against the number of rays for (a,c) 1 dB TL and (b,d) 50 dB TL of the coupling partition.

The percent difference in average transient energy density is plotted in Figure H.16. As with the other numerical methods, the convergence of the transient ray tracing solution is almost identical to the steady state convergence. The average energy density converges to within 5 % difference in the receiving volume using only 4096 rays, while 16384 rays are required for convergence to within 5 % difference in the source volume, slightly faster than the steady state problem. The transient results plotted later are computed using 32768 rays, the same number used to compute the steady solution.
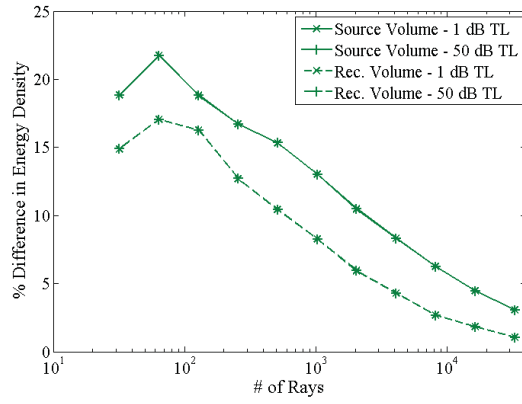
Figure H.16: Percent difference in the transient average energy density for an increasing number of rays.